Optimizing the dielectric response of PVDF-Based Copolymer Films : insights from ink formulation and printing process optimization

Jean-David Isasa

université de BORDEAUX

THÈSE PRÉSENTÉE

POUR OBTENIR LE GRADE DE

DOCTEUR DE L'UNIVERSITÉ DE BORDEAUX

ÉCOLE DOCTORALE DES SCIENCES CHIMIQUES

SPECIALITÉ : POLYMÈRES

Par Jean-David ISASA

« Optimisation des propriétés diélectriques de copolymères à base de PVDF : étude de la formulation d'encres et optimisation de procédés d'impression »

"Optimizing the dielectric response of PVDF-Based Copolymer Films: insights from ink formulation and printing process optimization"

SOUS LA DIRECTION DE : Georges HADZIIOANNOU et Guillaume FLEURY

Soutenance réalisée le

21/02/2024

Membres du jury :

Mme. Annie COLIN, Professeure, ESPCI- Paris PSL	Présidente du jury
Mme. Sophie BARRAU, Professeure, UMET-Université de Lille	Rapporteur
M. Eric DANTRAS, Maître de conférences, CIRIMAT- Université de Toulouse	Rapporteur
M. Hamid KELLAY, Professeur, LOMA-Université de Bordeaux	Examinateur
M. Georges HADZIIOANNOU, Professeur, LCPO-Université de Bordeaux	Directeur de Thèse
M. Guillaume FLEURY, Professeur, LCPO-Université de Bordeaux	Directeur de Thèse

Remerciements :

Il me sera très difficile de remercier tout le monde, car c'est grâce à l'aide de nombreuses personnes que j'ai pu mener à bien cette thèse.

Je voudrais tout d'abord remercier l'ensemble des membres du jury qui ont accepté d'évaluer mes travaux de thèse, pour leur présence lors de la soutenance ainsi que pour les échanges et discussions scientifiquement enrichissants.

Je voudrais remercier grandement mes directeurs de thèse, le professeur Hadziioannou et le professeur Fleury, pour toute leur aide dans la réalisation de ces travaux ainsi que pour leur expertise scientifique.

Je voudrais aussi remercier les différents partenaires industriels de la chaire SMILE qui ont contribué à l'avancement de ce projet.

Il m'est impossible de ne pas mentionner l'entièreté de l'équipe SMILE, pour sa cohésion et son implication dans la perspective de mener à bien des travaux de recherche multidisciplinaires.

Ces remerciements vont de pair avec l'ensemble des personnes du LCPO, du solide cœur du B8 et de mes compagnons de bureau qui, professionnellement et personnellement, se sont révélés être un facteur majeur de réussite dans l'aboutissement de ces trois années.

Je remercie également l'équipe d'Arkema Piezotech et plus particulièrement Dr. Chevalier pour son expertise et son aide dans la réalisation des dispositifs par impression.

Je tiens aussi à remercier le soutien technique de la plateforme ELORPrintTec dans la réalisation de différentes expérimentations pertinentes durant ces trois années.

Ces années de dur labeur ont aussi été l'occasion de faire de nouvelles rencontres qui, selon moi, m'ont permis de façonner positivement la personne que je suis.

Finalement, ces derniers remerciements vont directement aux membres de ma famille, à mes amis et aux personnes qui me sont chères, qui ont été présents dans les moments difficiles mais aussi joyeux de cette étape.

Optimisation des propriétés diélectriques de copolymères à base de PVDF : étude de la formulation d'encres et optimisation de procédés d'impression

Résumé :

Les polymères fluorés fortement polaires tels que le P(VDF-TrFE) sont des matériaux émergents dans le domaine de l'électronique organique flexible en raison de leurs nombreuses applications en tant qu'actionneurs, capteurs ou récupérateurs d'énergie. En raison de la forte polarité des liaisons C-F, une orientation dipolaire coopérative dans les domaines cristallins peut être induite et est principalement responsable des propriétés électroactives de ces polymères. Le dépôt de ces matériaux en films minces peut être réalisé par impression ou déposition par voie liquide, offrant une méthode de mise en œuvre polyvalente et évolutive pour la production de couches hautement fonctionnelles. Néanmoins, la mise en œuvre de telles couches dans des dispositifs pratiques est directement liée aux propriétés rhéologiques des encres électroactives qui déterminent les régimes d'impression conduisant à des couches électroactives stables et fonctionnelles. Dans cette étude, nous avons évalué le comportement viscoélastique de solutions de P(VDF-TrFE) et P(VDF-TrFE-CTFE) pour des solvants de polarité différente, allant du régime dilué au régime concentré. À partir de ces mesures, nous avons extrait, en utilisant une approche basée sur des lois d'échelles, plusieurs paramètres polymère-solvant fortement dépendants de la composition du polymère et de la polarité du solvant. Des mesures complémentaires de diffusion de la lumière ont également corrélé les changements de conformation du polymère avec l'affinité polymère-solvant extraite de l'analyse rhéologique. Enfin, nous avons examiné l'impact de la formulation des encres sur la fabrication de dispositifs organiques à base de PVDF par la méthode de sérigraphie afin d'établir une corrélation entre les paramètres rhéologiques de l'encre et la résistance au claquage par court circuits pendant les cycles de polarisation. Ainsi, cette étude fournit une compréhension approfondie de l'influence de la solvatation du polymère sur les régimes d'impression afin d'obtenir des couches électroactives de haute performance.

Mots clés : polymères, ferroélectricité, impression, viscosité

Optimizing the dielectric response of PVDF-Based Copolymer Films: Insights from ink formulation and printing process optimization

Abstract:

Highly polar fluorinated polymers such as P(VDF-TrFE) are emerging materials in the field of flexible organic electronics because of their numerous applications as actuators, sensors, or energy harvesters. Due to the high polarity of C-F bonds, cooperative dipole orientation in crystalline domains can be induced and are primarily responsible for the electroactive properties of these polymers. The processing of these materials into thin films can be performed by solution printing or casting, offering a versatile and scalable method for the production of highly functional layers. Nevertheless, the implementation of such layers in practical devices is directly related to the rheological properties of the electroactive inks that determine the printability regimes leading to stable and functional electroactive layers.

In this study, we evaluated the viscoelastic behavior of P(VDF-TrFE) and P(VDF-TrFE-CTFE) solutions for solvents of different polarity, ranging from the dilute to the concentrated regime. From these measurements, we extracted using a scaling approach several polymer-solvent parameters that are highly dependent on the polymer composition and solvent polarity. Complementary light scattering measurements further correlated the polymer conformational changes with the polymer-solvent affinity extracted from the rheological analysis. Finally, we examined the impact of the ink formulation on the fabrication of PVDF-based organic devices by the screen-printing method in order to establish a correlation between the rheological parameters of the ink and the resistance to breakdown during the polarization cycles. Therefore, this study provides a deeper understanding on the influence of the polymer solvation on the printability regimes in order to obtain high performance electroactive layers.

Keywords: polymers, ferroelectricity, printing, viscosity

Unité de recherche

Laboratoire de Chimie des Polymères Organiques (LCPO) – UMR5629

Team 4: “Polymer electronic Materials and Devices”

16 Av. Pey Berland, 33600 Pessac

List of abbreviations:

%χ	Percentage Of Crystallinity
$\dot{\gamma}$	Shear Rate
[η]	Intrinsic Viscosity
$<R^2>$	Contour Length
ΔH	Enthalpy
2θ	Diffraction Angle
A_2	Second Virial Coefficient
AFM	Atomic Force Microscopy
b	Kuhn Length
B_g	Parameter For Concentration Range $c^* \leq c \leq c_{th}$
B_{th}	Parameter For Concentration Range $c_{th} \leq c \leq c^{**}$
c	Concentration Of Monomers In Solution
c*	Chain Overlap Concentration
c**	Critical Concentration Of The Concentrated Regime
Cp_1	Plateau Value For The Calculation Of The B_g Parameter
Cp_2	Plateau Value For The Calculation Of The B_{th} Parameter
CTFE	Chlorotrifluoroethylene
c_{th}	Thermal Blob Overlap Concentration
D	Apparent Diffusion Coefficient
Đ	Dispersity
DFE	Defective Ferroelectric
DLS	Dynamic Light Scattering
dn/dc	Refractive Index Increment
D_R	Rotational Diffusion Coefficient
DSC	Differential Scanning Calorimetry
D_T	Translational Diffusion Coefficient
E	Electric Field
E_c	Coercive Field
FE	Ferroelectric
FE*	Probable Defective Ferroelectric Phase
F_{EA}	Fraction of Electroactive Material
FTIR	Fourier Transform Infrared Spectroscopy
g	Number Of Monomers Per Correlation Blob
$\tilde{g}$	Number Of Monomer Per Normalization Blob
G’	Storage Modulus

G''	Loss Modulus
g_{th}	Number Of Monomers Per Thermal Blob
HH	Head to Head
HT	Head to Tail
I	Current
I(q)	Scattered Intensity at q Wavenumber
K	Optical Parameter
kt	Thermal Energy
l	Monomer Projection Length
LS	Light Scattering
MA-DLS	Multi-Angle Dynamic Light Scattering
MC	Mesh Count
M_n	Number Averaged Molar Mass
M_w	Weight Average Molar Mass
Ne	Number Of Monomers Between Entanglements
$\tilde{N}_e$	Apparent Number Of Monomer Between Entanglements
NMR	Nuclear Magnetic Resonance
N_w	Weight Average Degree Of Polymerization
N_W	Weight Average Degree Of Polymerization
OA	Open Area
P	Polarization
P(VDF-TrFE)	Poly(Vinylidene Fluoride-Trifluoroethylene)
P(VDF-TrFE-CTFE)	Poly(Vinylidene Fluoride-Trifluoroethylene-Chlorotrifluoroethylene)
PE	Paraelectric
$\tilde{P}_{e,RC}$	Apparent Number Of Entanglements Per Tube Diameter
PET	Polyethylene Terephthalate
P_m	Maximum polarization
ppm	Parts Per Million
P_r	Remanent Polarization
P_{sat}	Saturation Polarization
PTFE	Poly(Tetrafluoroethylene)
PVDF	Poly(Vinylidene Fluoride)
R	Excess Intensity Of Scattered Light
R0	Radius Of The Solubility Sphere
RFE	Relaxor Ferroelectric
R_g	Radius Of Gyration
R_H	Hydrodynamic Radius

RT	Room Temperature
SEC	Size-Exclusion Chromatography
SEM	Scanning Electron Microscopy
SLS	Static Light Scattering
T	Temperature
T_c	Curie Transition Temperature
tg	Trans-Gauche Chain Conformation
T_g	Glass transition temperature
T_m	Melting Temperature
TrFE	Trifluoroethylene
TT	Tail to Tail
U_e	Volumetric energy density
UV	Ultra Violet
V	Voltage
VDF	Vinylidene Fluoride
WAXS	Wide Angle X-Ray Scattering
α	Expansion Coefficient
β	Coefficient Representing The Number Of Monomers Between Entanglements
Γ	Relaxation Frequency
δ_D	Dispersive Solubility Parameter
δ_H	Protic Solubility Parameter
δ_p	Polar Solubility Parameter
ε_0	Vacuum permittivity
εr	Relative permittivity
η	Viscosity
η*	Complex Viscosity
η_0	Viscosity Of The Pure Solvent
$\eta_{17\%wt}$	Apparent Viscosity At 17% Concentration
η_{red}	Reduced Viscosity
η_{rel}	Relative Viscosity
η_s	Specific Viscosity
λ_g	Rescaling Factor For θ Conditions
ν	Flory Exponent
ξ	Correlation Length
ξ_{th}	Thermal Blob Length
ρ	Form Factor
ϕ	Torsion Angle

ω	Angular Frequency
ΔH_m	Enthalpy Of Melting
ΔH_{s-s}	Enthalpy Of Solid-To-Solid Transition

Vibration abbreviations:

τ	Torsion
ρ	Rocking
w	Wagging
δ	Deformation
ν	Stretching

Solvent abbreviations:

Ac	Acetone
ACN	Acetonitrile
GBL	γ-Butyrolactone
CH	Cyclohexanone
CP	Cyclopentanone
DMAC	Dimethyl Acetamide
DMF	Dimethyl Formamide
DMSO	Dimethylsulfoxide
EA	Ethyl Acetate
MEK	Methyl Ethyl Ketone
MIBK	Methylisobutylketone
NMP	N−Methyl−2−Pyrrolidinone
PC	Propylene Carbonate
PGMEA	Propylene Glycol Methylethercetate
THF	Tetrahydrofuran
TEP	Triethylphosphate
EGDA	Ethylene Glycol Diacetate

Table of contents

CHAPTER 1:

General Introduction

Chapter 1: General Introduction

1.1 State of the Art

1.1.1 Basic Concept of Ferroelectricity

1.1.1.A Brief History of Ferroelectricity

Talking about ferroelectricity is not possible without mentioning the detection of this phenomenon by Prof. Joseph Vasalek who discovered the remanent polarization and reversible polarization of Rochelle salt.[1] Contrary to linear dielectric materials, under the application of an electric field, the response of the material is non-linear and leads to a hysteresis of the polarization behavior (**Figure 1**). This peculiar response is due to the inner structuration of the material; *i.e.,* a particular crystalline structure. The symmetry and polarity of the crystal determine whether the material is ferroelectric or not (see **Figure 1**c for the classification of the crystal classes depending on their dielectric behaviors). More precisely, ferroelectric materials are a subcategory of piezoelectric and pyroelectric materials that are non-centrosymmetric and whose spontaneous polarization can be reversed.[2]

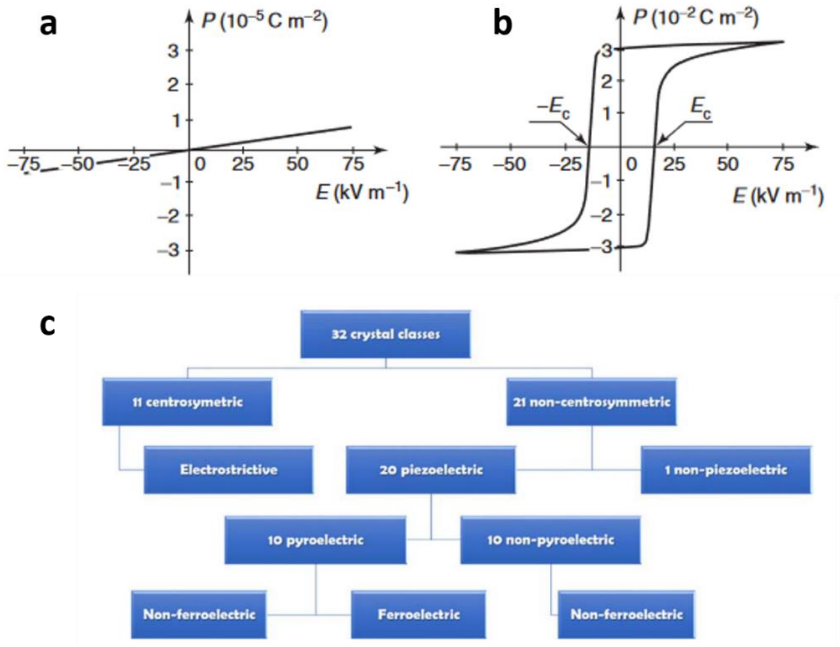

Figure 1. *Dependence of the polarization (P) as a function of the electric field (E) for (a) a linear dielectric and (b) ferroelectric triglycine sulfate reproduced from Levanyuk et al.[3] The values of the coercive field and spontaneous polarization are E_c = 15 KV m^{-1} and P = 3.1x10^{-2} C m^{-2}, respectively. (c) Classification of the different crystal classes reproduced from Costa et al.[4]*

1.1.1.B Theory of Ferroelectricity

There are two types of ferroelectric materials: “displacive” in which the polarization switching is accomplished by shifting the position of ions in the unit cell, and “order/disorder” in which the material exhibits a transition from non-oriented dipoles (the paraelectric phase) to oriented dipoles (the ferroelectric phase). Indeed, the presence of opposite charges or the asymmetry of the crystal can lead through the application of an external stimulus; *i.e.,* mechanical strain or electric field, to a polarization of the crystal (**Figure 2**a).

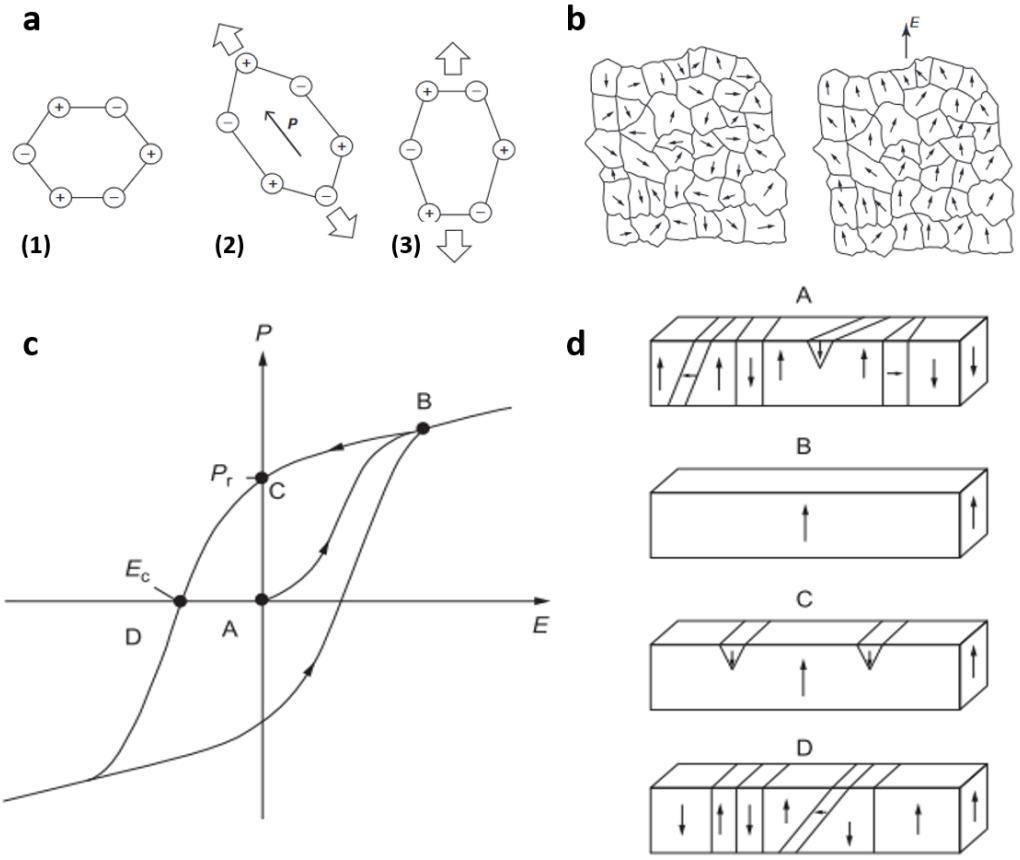

Figure 2. *(a) (1) Unstressed and (2, 3) stressed structures containing positive and negative ions, under external stimuli. A separation of positive and negative charge centers is achieved in (2) but not in (3), reproduced from Newhman et al.*[2] *(b) Schematic of the poling (dipole alignment) process of ferro-piezoelectric ceramics reproduced from Pardo et al.*[5]*(c,d) Typical P=f(E) hysteresis loop and schematics of dipolar domain configurations that correspond to the points (A–D) marked in (c), to illustrate the “switching” process (reproduced from Pardo et al.*[5]*)*

A ferroelectric material is first of all a dielectric material, which acts as a barrier for free charges to flow when an electric field is applied. In a parallel plate capacitor geometry, when a voltage V is applied, charges, '*Q*', are stored at the surface with

$$Q = C\,V, \tag{I.1}$$

'C' is the capacitance that is defined as:

$$C = (\varepsilon\,A)/\,d = (\varepsilon_0\,\varepsilon_r\,A)/d, \tag{I.2}$$

Where 'ε_0' is the vacuum permittivity (8.854 10^{-12} F m^{-1}), and 'ε_r' is the relative dielectric permittivity of the material. When an electric field is applied, the response of the materials depends on the frequency of the field. Indeed, the dielectric permittivity, 'ε_r' is a function of the frequency of the applied electric field and is defined as a complex function:

$$\varepsilon_r = \varepsilon'_r + i\varepsilon''_r \tag{I.3}$$

where ε_r' represents the real part of the relative permittivity and is related to the energy stored in the dielectric and ε_r'' represents the imaginary part of the relative permittivity and relates to the energy loss in the material. The applied electric field $\vec{E}$ induces a spatial displacement of charges:

$$\vec{D} = \varepsilon_0\vec{E}+\vec{P}. \tag{I.4}$$

The macroscopic polarisation $\vec{P}$ is the density of charges created at the surface, corresponding to the total amount of charges per unit area ($P = Q\,A^{-1}$), and is defined as:

$$\vec{P} = \varepsilon_0\chi\vec{E}. \tag{I.5}$$

At the macroscale, the polarization heads to the orientation and the relaxation of the dipoles more or less uniformly (**Figure 2**b) resulting in the hysteresis response of the material following the well-known P=f(E) hysteresis loop (**Figure 2**c,d). From this polarization curve, remarkable values can be extracted such as the remanent polarization (P_r) value of P at zero field after polarization, the coercive field (E_c) which represents the value of E in which the polarization returns to zero (minimum energy needed allowing dipoles orientation), and the maximum value polarization (P_m).

The energy storage efficiency of a dielectric material can be described by the energy density, a numerical quantity indicating the amount of energy stored. The volumetric energy density can be written as:

$$U_e = \int EdD, \tag{I.6}$$

which represents the upper part of the outside area of the hysteresis loop. On the other hand, the energy loss can be represented by the inside part of the hysteresis loop.

The response of a ferroelectric material is temperature-dependent. Above a critical temperature, the so-called Curie Temperature, T_c, both remanent polarization and the polarization hysteresis loop vanishes marking the transition from a ferroelectric (order) to a paraelectric (disorder) behavior. This transition is represented by a maximum value of permittivity (the measure of the electric polarizability of a dielectric material; *i.e.,* its ability to store energy under an applied electric field) at which the maximum mobility for dipole orientation is reached.

a

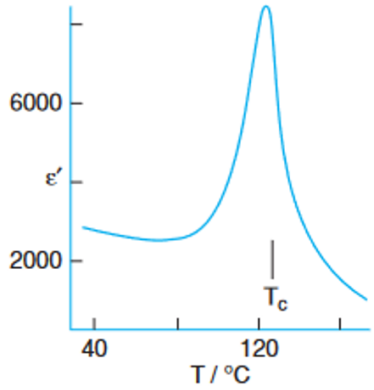

b

Material	T_c/°C
Barium titanate, $BaTiO_3$	120
Rochelle salt, $KNaC_4H_4O_6{\cdot}4H_2O$	Between –18 and +24
Potassium niobate, $KNbO_3$	434
Potassium dihydrogenphosphate, KDP, KH_2PO_4	–150
Lead titanate, $PbTiO_3$	490
Lithium niobate, $LiNbO_3$	1210
Bismuth titanate, $Bi_4Ti_3O_{12}$	675
Gadolinium molybdate, GMO, $Gd_2(MoO_4)_3$	159
Lead zirconate titanate, PZT, $Pb(Zr_xTi_{1-x})O_3$	Depends on x

Figure 3. *(a) Typical evolution of the permittivity as a function of the temperature for a ferroelectric material, (b) recapitulative table of Curie temperature values for well-known inorganic ferroelectrics reproduced from Ropp et al.*[6]

1.1.1.C Relaxor Ferroelectricity

Relaxor ferroelectrics (RFE) are a particular category of ferroelectric materials. Contrary to conventional FE materials, the temperature-dependent dielectric permittivity (ε’) exhibits a

broad and smeared maximum, which is known as a diffuse phase transition.[7] Contrary to FE, the frequency-dependent peak of the real and imaginary parts of the permittivity shifts to higher temperatures with increasing frequency (**Figure 4**a).[8]

This behavior has been explained by the nanometer size domains allowing an easier polarization but counterbalanced by a considerably weakened polarization state. This intrinsic property of RFE can be described by a narrower hysteresis loop (low P_r) with high recoverable energy density and low energy loss (**Figure 4**b).

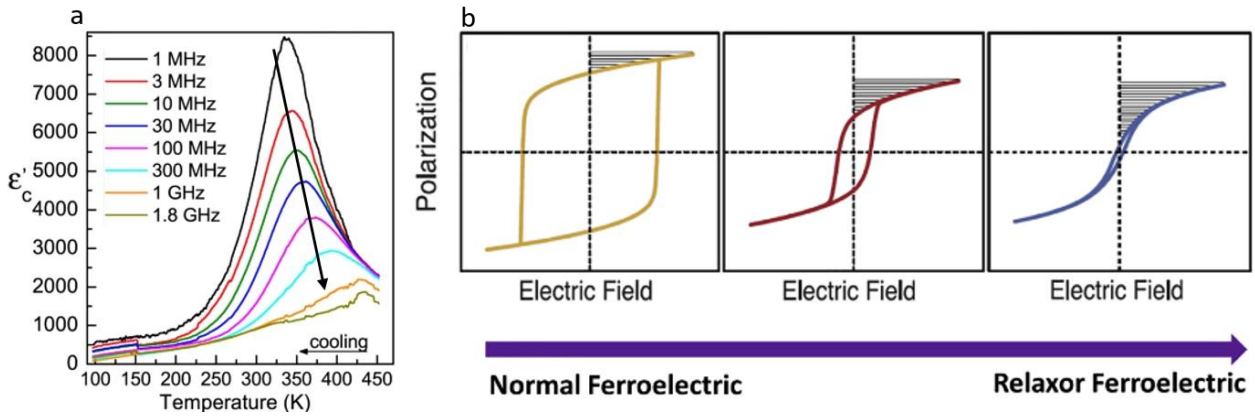

Figure 4. *(a) real part of the relative permittivity as a function of the temperature at different frequencies for an RFE-like material adapted from Zhu et al.*[9] *(b) evolution of the P=f(E) loop according to the nature of the ferroelectricity with dashed lines represents the energy storage density of the material reproduced from Xiaodong et al.*[10]

1.1.2 Polymers as Electroactive Materials

Organic materials have received considerable attention from the industry as a more affordable and environmentally friendlier approach for the fabrication of functional systems.[11–15] This shift is driven by the ever-increasing costs associated with the production of functional devices based on semiconductors and rare-earth elements. The extraction of these materials exhausts the environment, being a source of pollution, and CO_2 emission, along with the associated impacts on biodiversity and human communities. Despite the attractiveness of these functional organic materials, several optimizations are still required, particularly concerning their physical properties, processing methods, and integration in practical devices. The fabrication of thin films

with tailored functionality is crucial for the advent of organic materials, pushing their integration in sensors, actuators, transducers, or even in more complex systems, such as OPVS,[16]OLEDS,[17] OFETs,[18] energy-storage or harvesting,[19] and cooling[20] systems.

1.1.2.A The Case of PVDF

Poly (vinylidene fluoride)-based "P(VDF)" polymers are an example of these types of organic functional materials. These polymers have attractive electroactive properties (ferroelectric, piezoelectric, pyroelectric)[12,21,22] that led to their implementation in a wide range of applications, such as actuation, sensing, ferroelectric tunnel-junctions, energy storage, non-volatile memories, among other examples that are not directly related to electronic applications, *i.e.* membranes[23] or binders[24].

The presence of the two highly electronegative fluorine atoms in opposition with the low electronegativity of the carbon-hydrogen bond effectively creates a permanent dipolar moment. The electroactive properties of these fluorinated polymers are tightly related to their crystalline structure and chain conformation. In addition, these two properties have also been observed to be highly dependent on the thin film fabrication conditions[25,26,27,28], which prompted extensive studies on the crystalline structure of PVDF-based polymers.

1.1.2.A.a The Crystalline Phases in PVDF-based Electroactive Polymers

PVDF is a polymorph presenting different crystalline phases (α, β, γ, δ, and ε) that are intimately related to the chain conformation (**Figure 5**):

- Chains crystallizing in the α phase present an antiparallel *tg+tg-* conformation leading to a paraelectric behavior (the α phase is at ambient conditions the thermodynamically stable polymorph);
- The δ phase is a parallel variant of the α phase and shows a weakly ferroelectric behavior with non-zero net dipolar moment;
- The γ phase results from the chain crystallization in a parallel *ttg+ttg-* conformation yielding a net dipole moment per unit cell;

- The ε phase is an antiparallel variant of the γ phase, presenting no net dipolar moment (paraelectric);
- and finally the β phase for which chains crystallize in an all-*trans* conformation resulting in a net dipole moment per unit cell.

This last polymorph is of particular importance for ferroelectric applications, as the monomeric dipolar moments are aligned creating a non-zero net polarization, with the highest values among all the electroactive phases. Inducing the crystallization of PVDF into the β phase is arduous as the polymer tends to crystallize in more energetically favorable phases (α or γ) that present very little to almost no net polarization.

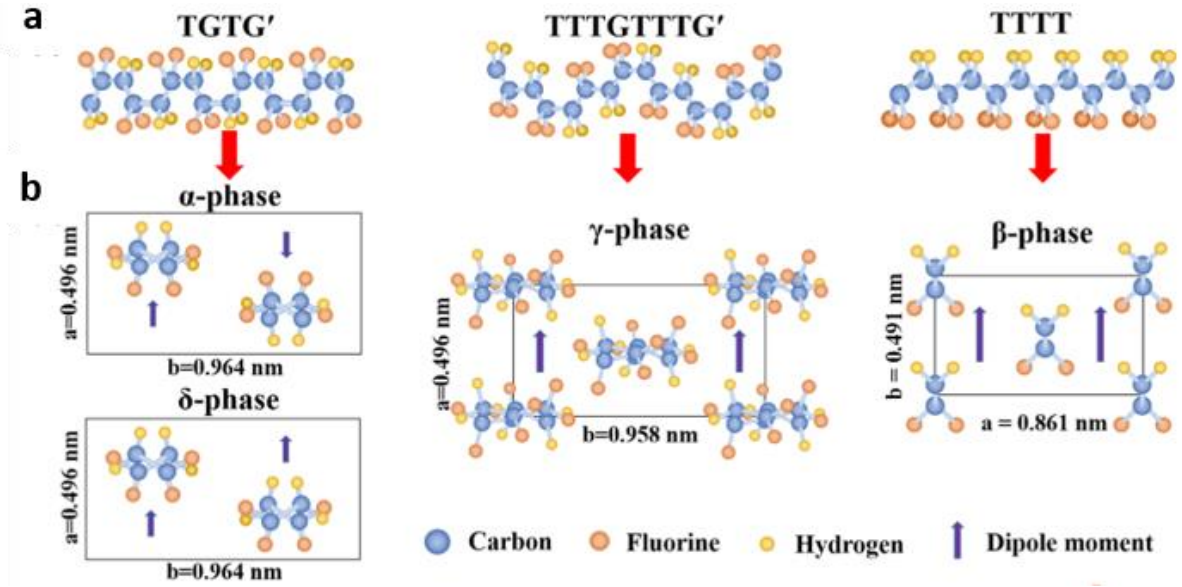

Figure 5. *(a) Representation of the possible PVDF chain conformations and (b) crystalline lattices reproduced from LI et al.*[21]

1.1.2.A.b Tuning of the Electroactive Crystalline Phases in PVDF

i. Post Processing Methods

To crystallize PVDF chains into the more polar β phase, different techniques have been proposed such as thermal annealing, film stretching, or the application of very high electric fields (poling).[29,30] Mechanical stretching results in the extension of the polymeric chains from the center of the spherulites, which transforms the α-phase spherulites into a β-phase crystal (**Figure 6**).

Nevertheless, the stretching of a nanometer to micrometer thick film is a hazardous task to implement at a large scale with a very high reproducibility.

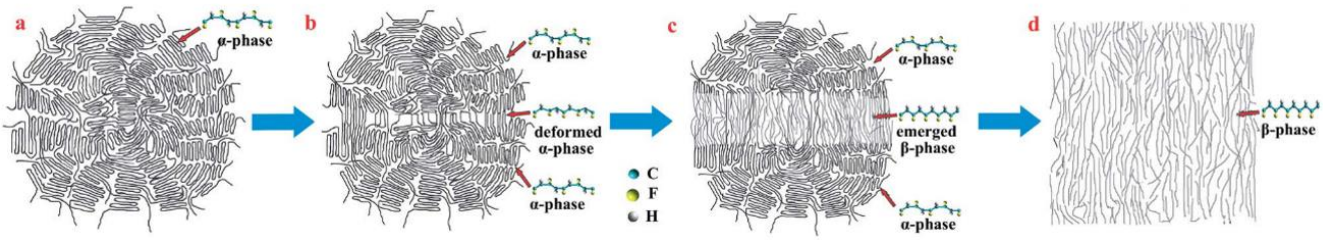

***Figure 6**. Process of transformation of an α-phase crystal to a β-phase crystal by uniaxial drawing reproduced from Li et al.*[30]

ii. Macromolecular Engineering to Induce all-trans Conformation

Polymerization of the PVDF homopolymer is mainly "isoregical" meaning that linear chains are produced following a head-to-tail insertion mechanism during the polymerization process (**Figure 7**).[31]

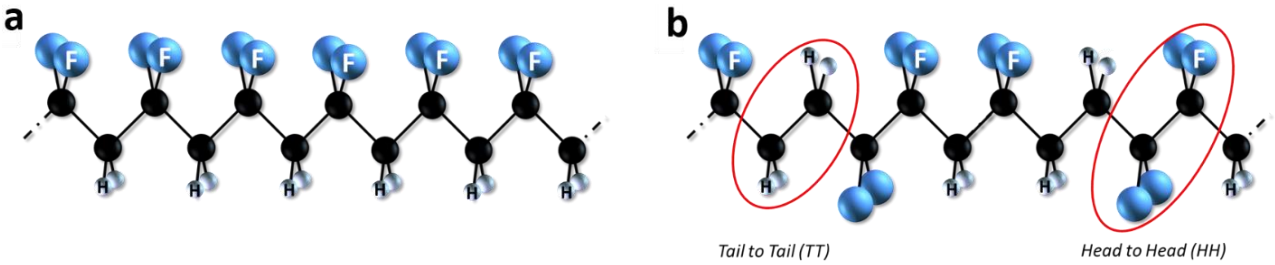

Figure 7. PVDF homopolymer chain sequencing induced by (a) isoregical head-to-tail (HT) polymerization and (b) head-to-head (HH) and tail-to-tail (TT) defects.

Nevertheless, regio-defects inevitably appear with head-to-head (HH) and tail-to-tail (TT) insertions.[32] These defects are usually in a minor proportion (6 mol.%) but this value can increase (up to 23.5 mol.%) via, for instance, the copolymerization of VDF with either 1-chloro-2,2-difluoroethylene or 1-bromo-2,2-difluoroethylene, followed by reductive dechlorination or debromination with tribu-tyltin hydride.[33] Interestingly, it has been shown experimentally and then theoretically that these defects have a strong influence on the PVDF chain conformation.[34] Indeed, the

stabilization of an all-*trans* conformation instead of a *tg+tg-* is dictated by its potential energy. By the mean of theoretical calculations, the all-*trans* conformation is shown to be more energetically stable for a percentage of defects above 11 mol.% (see **Figure 8**).

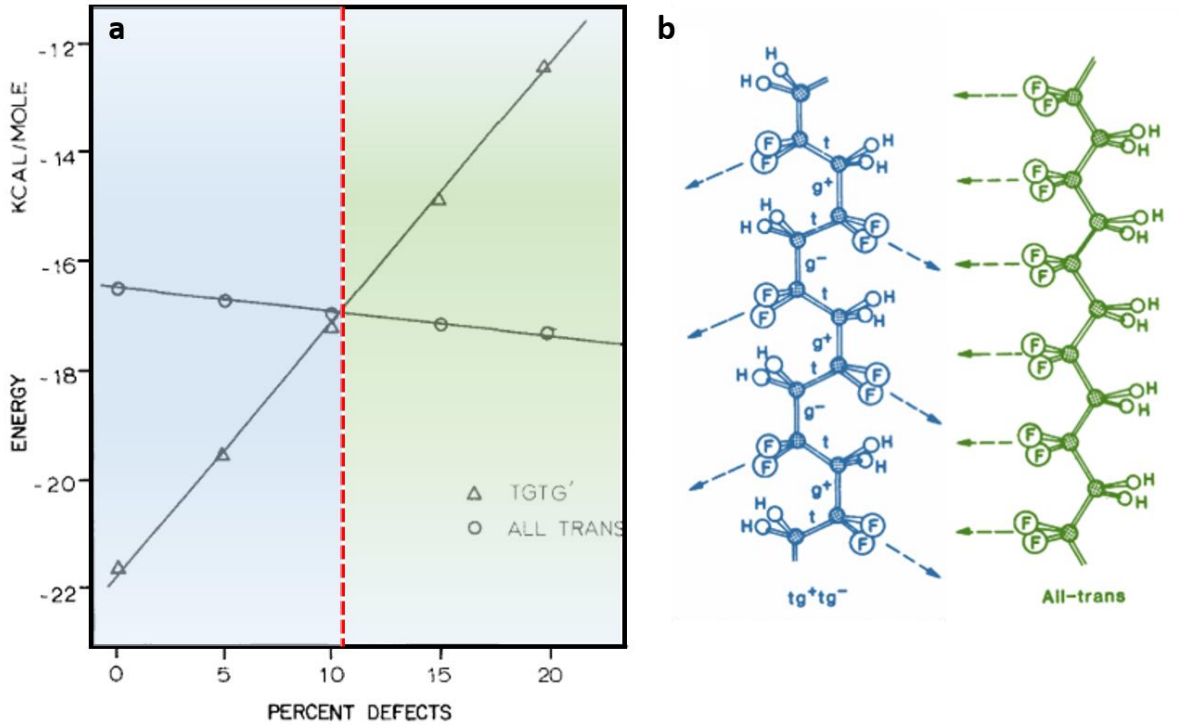

Figure 8. *(a) Evolution of the energy of the chain conformation as a function of percentage of defects (mol.%). The red line at 11 mol.% represents the critical point in which both conformations have the same energy (adapted from Farmer et al.[34]) (b) Conformations of the PVDF chain (adapted from Lovinger[35]). Each color corresponds to the region of the most stable chain conformation.*

1.1.2.B P(VDF-TrFE) as a Native Ferroelectric Polymer

Despite its prime appeal, the electroactive properties of PVDF are capped by its internal structure and the difficulty to induce the crystallization in the β-phase. One of the main advances in the field of fluorinated electroactive polymers has been to incorporate another monomeric unit known as trifluoroethylene (TrFE) to increase the electroactive performance of the material. Numerous applications, previously constrained by limitations imposed by the thermally stable α-phase of PVDF, could now be overcome. Over the past few years, there has been an exponential

increase in the utilization of this material, attributed to its electroactive and chemically inert properties, as shown in **Figure 9** by the number of scientific reports dealing with P(VDF-TrFE).

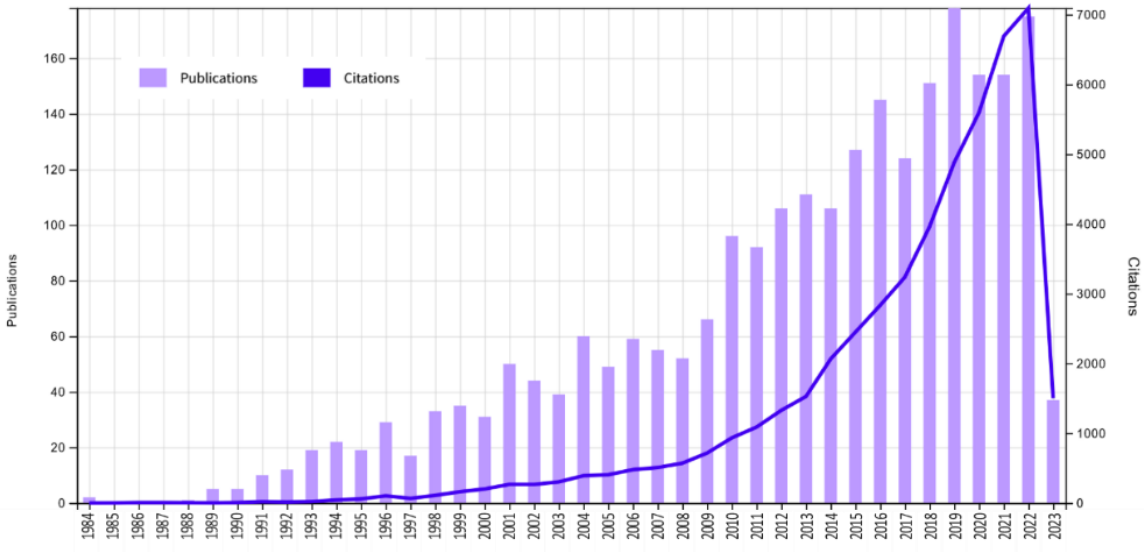

Figure 9. *Evolution of the number of publications and citations of work related to P(VDF-TrFE) extracted from Web of Science (September 2023).*[36]

It is now well established that the addition of the TrFE monomeric units into the polymer chain modifies its internal structure. The direct consequence of this addition is observable in the thermodynamic transitions of the material: the Curie and melting transitions. Through the use of complementary techniques, such as X-ray scattering and dielectric spectroscopy, studies from Lovinger *et al*.[37] and Furukawa *et al.*[38] evidenced the effects of the percentage of TrFE within the polymeric chain on the melting temperature (T_m) and more critically on the Curie temperature (T_c). As shown in **Figure 10**, the increase of VDF content steadily decreases the T_m from 200 °C to 140 °C. On the other hand, T_c undergoes a sharp increase in temperature from 50 mol.% to 80 mol.% of VDF.

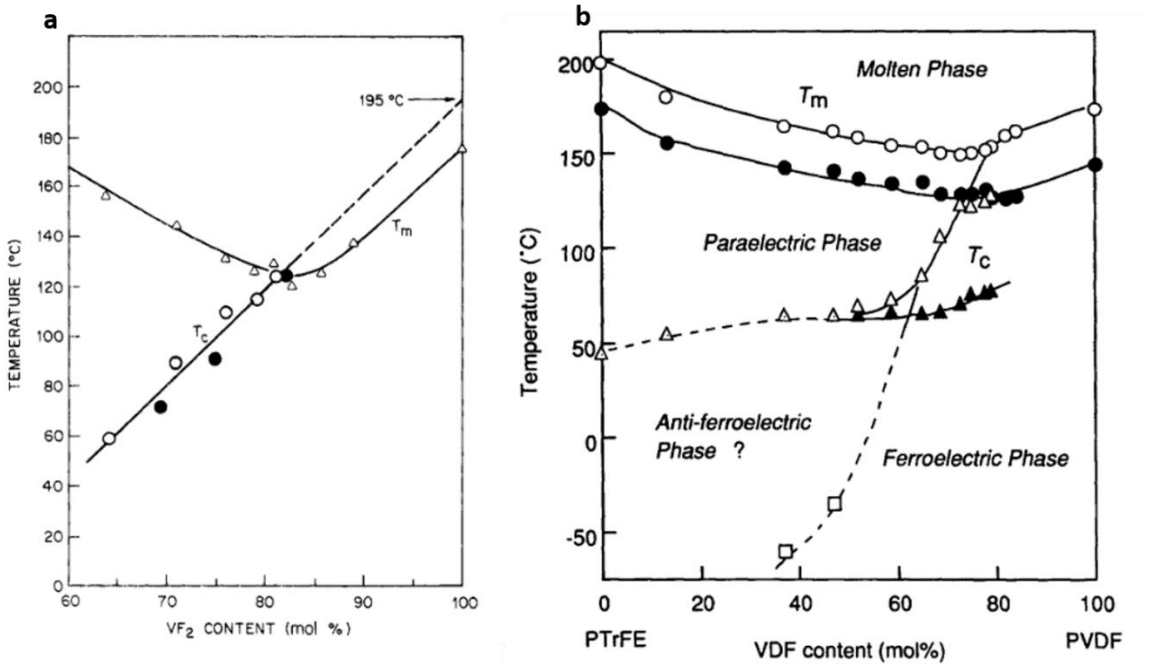

Figure 10. *Evolution of the melting and Curie temperatures as a function of the VDF content within the polymer sequence (a) extracted from Lovinger* [37] *and (b) Furukawa (1997).*[38]

This modification of the material intrinsic properties by adding TrFE units in the chain sequence can be attributed to two contributions. The first one is due to the chemistry used during the fabrication of these copolymers that introduces chain defects while inserting TrFE units. The second one is linked to the modification of the tacticity/conformation of the chains while adding TrFE.[39]

The addition of TrFE units in the chain sequence also introduces regio-defects which, in turn, modifies the more energetically stable conformation. Nevertheless, the presence of a third fluorine atom has a greater impact on chain conformation due to its steric hindrance.[38] The larger size of the fluorine atoms (*versus* the hydrogen atoms) induces the stabilization of the all-*trans* conformation (syndiotactic all-*trans*) in comparison to the *tg+tg-* one (isotactic helix) (**Figure 11**d). As a result, the introduction of the TrFE units considerably increases the proportion of all-*trans* chain segments and consequently the formation of β-phase crystals.[40] This growth of the all-*trans* conformation leading to the appearance of the Curie temperature at the critical composition of 20 mol %.

Besides, the presence of a third fluorine atom has an influence on the chain tacticity with a strong impact of the TrFE content on the isotacticity as shown in **Figure 11**.[41] The energy of all-*trans* (syndiotactic *trans*) conformation for the VDF-TrFE segment is lowered by adding TrFE units (**Figure 11**b). At low TrFE content, the TrFE-TrFE segment also preferably adopts the all-*trans* conformation (**Figure 11**c). However, at higher TrFE contents (*i.e.,* below a critical VDF proportion of 49 mol.%), the *trans* conformation is no longer the most energetically stable and leads to the formation of an isotactic helix conformation. This value of 49 mol.% is known as the morphotropic phase boundary (MPB), at which the composition dictates the conformation and the dielectric properties of the material.

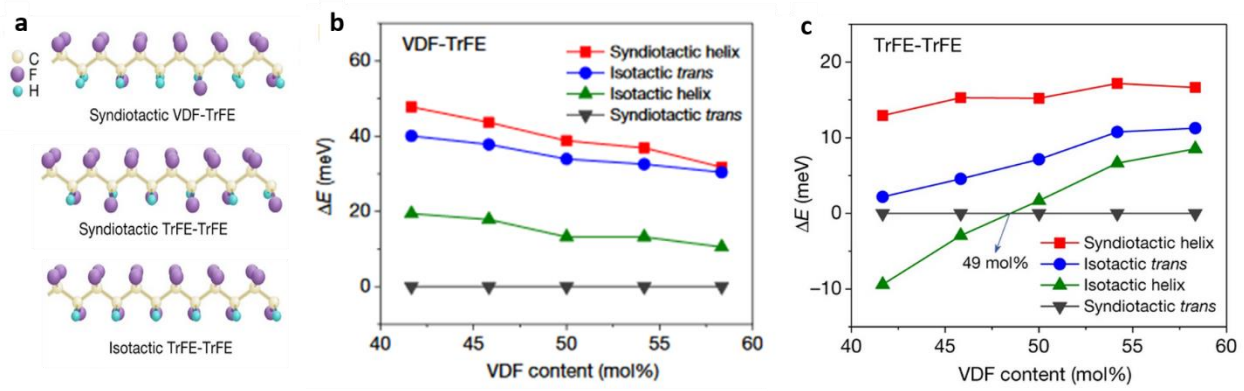

Figure 11. *(a) Schematic representation of the chain tacticity for syndiotactic VDF-TrFE, syndiotactic TrFE-TrFE, and isotactic TrFE-TrFE. Calculated energy difference ΔE between various phases with different tacticities and the syndiotactic trans-planar phase in the (b) VDF-TrFE and (c) TrFE-TrFE segment (adapted from Liu et al.*[41]*).*

1.1.2.C P(VDF-TrFE-CTFE) as a Native Relaxor Ferroelectic Polymer

Recently, PVDF-based terpolymers containing chlorofluoroethylene (CFE) and chlorotrifluoroethylene (CTFE) monomers were demonstrated to present relaxor-ferroelectric properties. In this class of materials, the phase transition that typically takes place at the Curie transition temperature (for a ferroelectric material) is much broader. This enables further opportunities in energy and temperature-management-related applications, as relaxor-ferroelectric materials have a much narrower hysteresis loop with low remanent polarization, greatly decreasing dielectric

loss during polarization cycles. Recently, major advances in the area of solid refrigeration with the use of the electrocaloric effect brought more interest to this material.[42,43]

As well as the steric hindrance effect of the third fluorine atom in the TrFE unit, the addition of a bulkier monomer containing a chlorine atom will have the same effect.

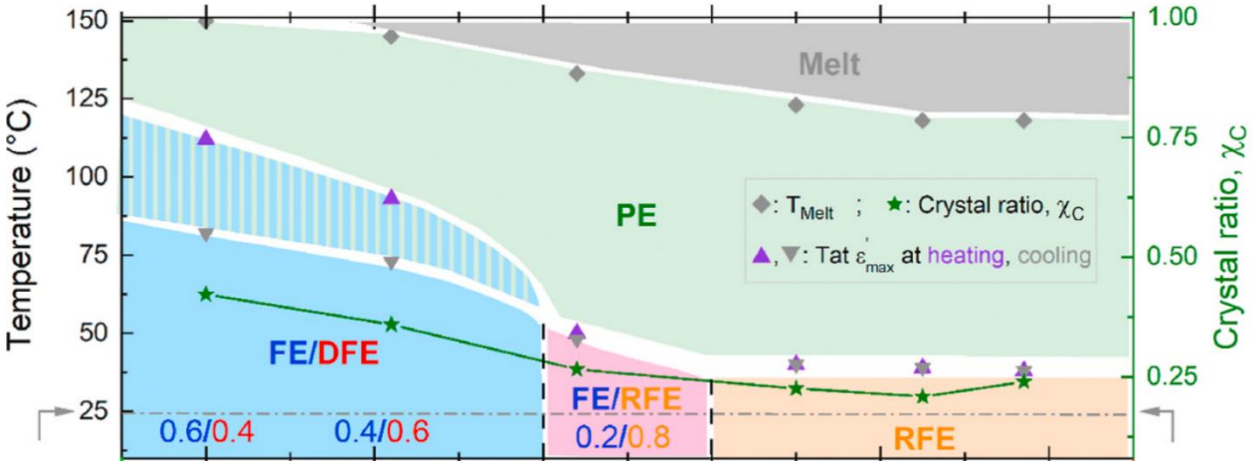

Figure 12. *Temperature versus mol.% CTFE phase diagram of annealed poly(VDF-TrFE-CTFE) terpolymers, where ★ represents the crystal ratio (χ_c) , ◆ the melting temperature (T_{Melt}) , ▲ and ▼ the temperature at maximum permittivity (T at ε_{max}) during heating and cooling respectively. Adapted from Bargain et al.*[44]

As shown in **Figure 12**, the introduction of CTFE has the direct consequence in decreasing the T_{melt} and also the T at ε_{max} of the material. This evolution is readily explainable by a modification of the crystalline lattice from a more to less cohesive crystal. As a result, the material crystals shift from FE to DFE to RFE crystalline structure.

Under an electric field, the pinning induced by the CTFE unit, restrict the rotation of the TrFE and VDF neighboring sites creating local defects.[45] Moreover, studies showed that the CTFE units are excluded from the crystalline unit cell and considered to be included in the material as kinks inducing γ-to-PE transition in a P(VDF-CTFE) copolymer.[45]

1.2 Deciphering Relationship Between Structure and Electroactive Properties

1.2.1 Multiscale Analysis of PVDF-Based Electroactive Materials: Some Case Studies

As discussed previously, the composition affects chain conformation and, consequently, material crystallinity and dielectric response. Progress in synthetic methods leads to the production of P(VDF-TrFE) with on-demand compositions. As shown in **Figure 13**a, Liu *et al*.[41] demonstrated that P(VDF-TrFE) with VDF content from 45 mol.% to 80 mol.% could be synthesized and the determination of the composition was performed by ^{1}H NMR. More precisely, with the help of the signals in the 6 ppm to 5 ppm (chemical shift) region (**Figure 13**a), a precise determination of the TrFE molar content of the copolymer can be performed. More specifically, as the VDF mol.% increases, the integration of the signal between 6 and 5 ppm corresponding to the proton on the TrFE unit increases with respect to the integration of the signal between 3 and 2 ppm that correspond to the protons in a two consecutive VDF units.

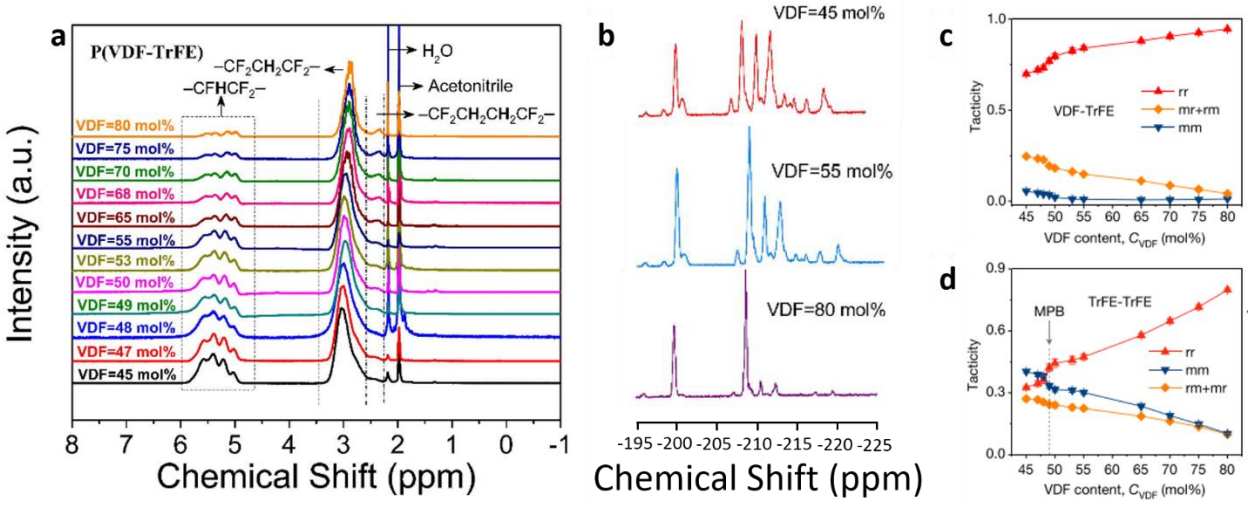

Figure 13. *(a) ^{1}H NMR spectra of P(VDF-TrFE) copolymers with different VDF mol.% content with the assignation of the different signals, (b) ^{19}F NMR spectra of three different compositions, evolution of the tacticity as a function of the VDF content for the (c) VDF-TrFE and (d) TrFE-TrFE segments (adapted from Liu et al.[41]).*

Interestingly, the use of ^{19}F NMR made it possible to determine quantitatively the number of defects within the chain, by using ratios of the integrals of the respective triad peaks of the -CHF- resonance (**Figure 13**b). For the VDF-TrFE segment, the syndiotactic (rr), heterotactic (mr+rm), and isotactic (mm) triad peaks are centered at -199.9, -200.8, and -198.3 ppm, respectively. For the TrFE-TrFE segment, the syndiotactic (rr), heterotactic (mr+rm), and isotactic (mm) triad peaks centers are located at -208.7, -210.5, and -212.4 ppm, respectively.[41] The composition has a direct impact on the value of the number of defects. From the three samples with different compositions presented in **Figure 13**b, the ^{19}F NMR measurements exhibit distinct signals meaning that the three different compositions differ from each other in their tacticity/defects. The signal ratios emphasize a progression in the number of defects with the increase of TrFE as shown in **Figure 13**c,d. These measurements underline the evolution of the tacticity with the mol.% of VDF and more importantly from a syndiotactic to an isotactic conformation for the TrFE-TrFE unit at 49 mol.% of VDF. This is in accordance with the appearance of the so-called morphotropic phase boundary (MPB) located at a composition of around 50 mol.% of VDF.

The evolution of compositions and tacticity has a strong impact on the crystallization behavior as seen in **Figure 14**a. The formation of a specific phase (α, β, γ, δ, and ε) is the direct consequence of the conformation of the chain. Accordingly, the evaluation of the material crystallinity is representative of the chain conformation.

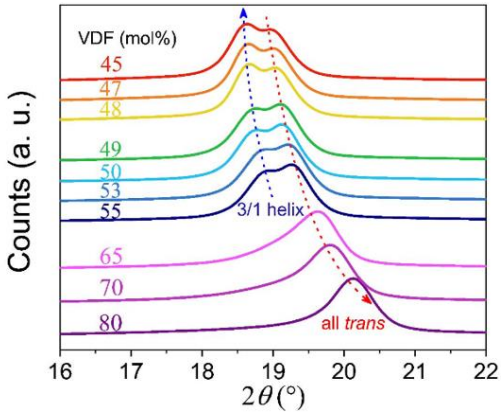

Figure 14. *WAXS measurements for P(VDF-TrFE) copolymer with different VDF mol. % content reproduced from Liu et al.*[41]

The PE phase is based on a hexagonal unit cell which differs from the FE and RFE phases with pseudo-hexagonal/orthorhombic and orthorhombic unit cells, respectively.[22,46] As these phases have different crystalline lattices, it is then possible to deconvolute the WAXS signals to obtain a quantitative polycrystalline composition of the material. From **Figure 14**, WAXS measurements were performed on a wide range of compositions of P(VDF-TrFE), the differences in the diffractograms are noteworthy. The first significant change results in the progressive shifting of the main peak signal to lower 2θ values when the amount of VDF decreases. If we link this information to the lattice spacing, this progression enlightens the transition to a less dense crystalline lattice. When reaching 55 mol.% of VDF, a second peak appears, drawing attention to the appearance of a second major crystalline population within the material. As shown in **Figure 14**, the material progressively shifts from a majority of FE crystalline domains to a combination of less densely packed FE domains with a combination of RFE domains.

The crystallinity as mentioned above, is a direct consequence of the chain conformation. Besides, conformational changes are known to modify the vibrational fingerprint of the material under radiation. FTIR measurements are of particular interest as they can be performed with ease on samples in both the solid and liquid states. Accordingly, FTIR has been widely used to characterize PVDF-based copolymers to access their crystalline composition. By attributing the various signals to the corresponding vibrational modes, the different chain conformations (and thus, crystalline phases) can be determined as shown in Figure 15a.[41,47–50] The α phase associated with the (tg+tg-), and the electroactive (EA) β and γ phases with all-*trans* and *tttg* chain conformations respectively, have been attributed to specific vibrational modes within the FTIR spectra.

- α (*tgtg*): 1430, 1382,1209, 975, 854, 795, 762, 613, 532, 488 cm^{-1}
- β (all-*trans*): 1275, 841, 510 cm^{-1}
- γ (*tttg*): 1234, 812, 431 cm^{-1}

Using this assignment, Xiaomei *et al*. developed an effective method to quantify the electroactive fraction, as well as the β and γ contents using the intensity ratios of specific bands (**Figure 15**c).[47] This technique is thus another tool to identify the influence of the VDF molar content on the chain conformation and the presence of a MPB.[41]

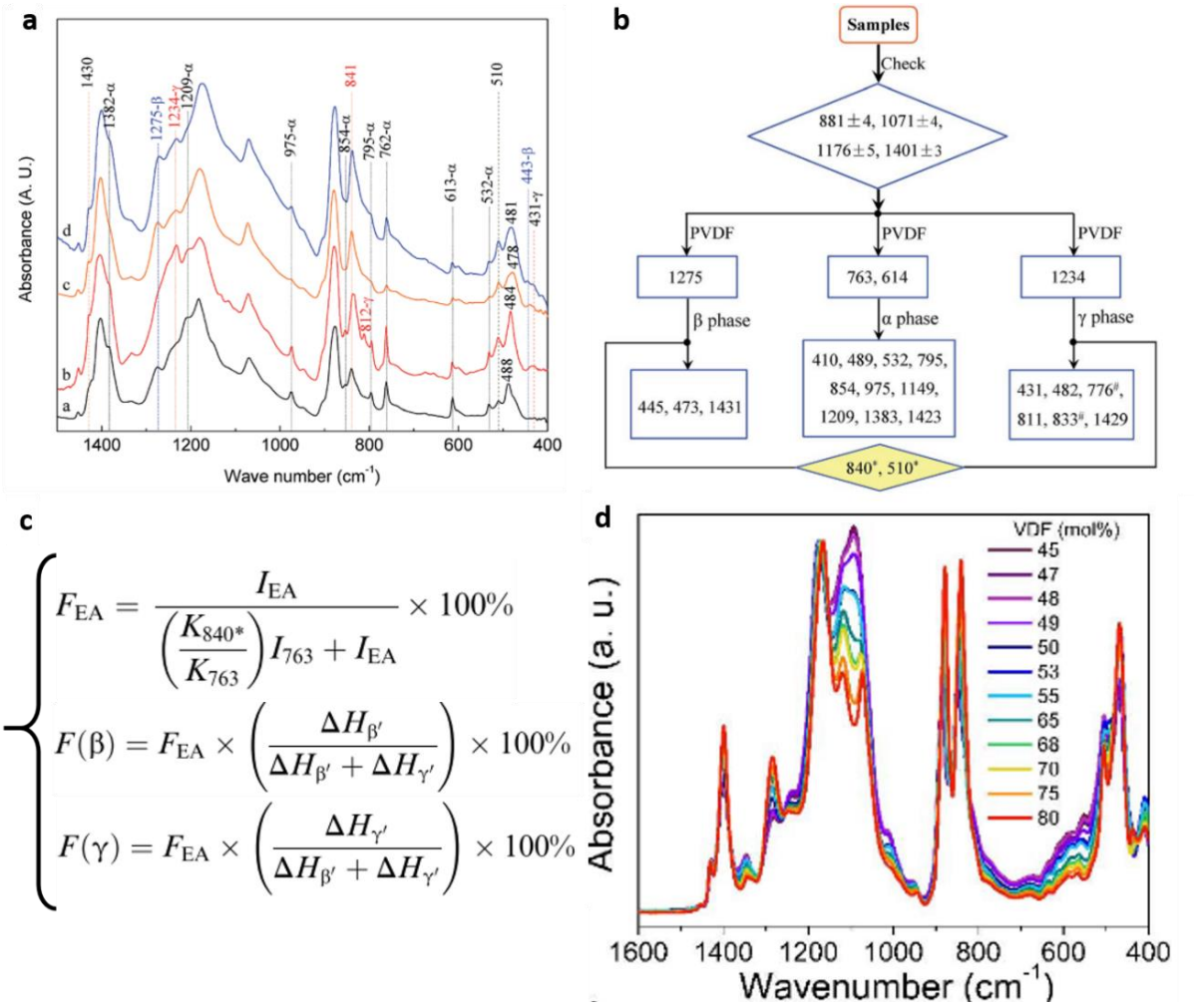

Figure 15. *(a) FTIR spectra with the signal peak attribution of PVDF films with different crystallinities according to the vibration of the respective chain conformations reproduced from Cai et al.*[47] *(b) Flow diagram for the identification of α, β, and γ phases; 840 cm*$^{-1}$ *and 510 cm*$^{-1}$ *represent bands in the range of 837–841 and 508–512 cm*$^{-1}$*, respectively; 776 cm*$^{-1}$ *and 833 cm*$^{-1}$ *reflects possible variations based on specific processes.*[47] *(c) Set of equations for the determination of the fraction of electroactive "*F_{EA}*", beta "F(β)" and gamma "F(γ)" phases, where* I_{EA} *represents the intensity of the peak at 840 cm*$^{-1}$*,* ΔH_{β}*, and* ΔH_{γ}*, are the height differences (absorbance differences) between the peak around 1275 cm*$^{-1}$ *and the nearest valley around at 1260 cm*$^{-1}$*, and the peak around at 1234 cm*$^{-1}$ *and the nearest valley around at 1225 cm*$^{-1}$*, respectively*[47] *(d) Evolution of the FTIR signal of copolymers with different VDF mol % compositions reproduced from Liu et al.*[41]

For various P(VDF-TrFE) compositions, an examination of the intensities (Figure 14c) of the all-*trans* band conformation at approximately 1290 cm^{-1}, *tg+tg-* conformation at around 614 cm^{-1}, and $(tg+)_3$ or $(tg-)_3$ conformation at about 507 cm^{-1} reveals a clear trend. It is evident that the

content of all-*trans* chain conformations increases proportionally with the VDF mol.% content. At lower VDF mol.% content, the majority of all-*trans* conformation switches to a *3/1* helix-type structure further confirming the MPB transitional regime.

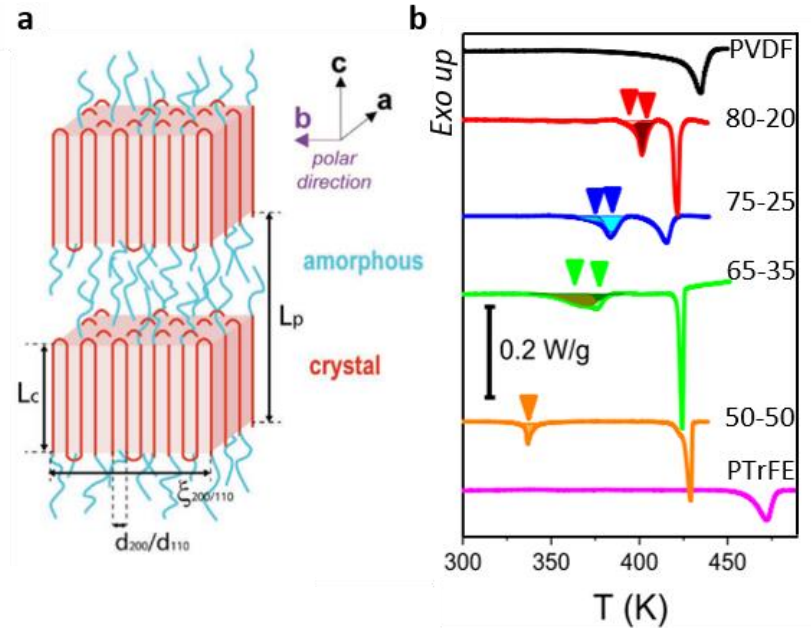

Figure 16. (*a) schematic representation of a 3D lamellar structure with L_c representing the crystal lamellae length and L_p the long period of the structure reproduced from le Goupil et al.*[51] *(b) DSC thermograms of P(VDF-TrFE) copolymers of different compositions reproduced from Pipertzis et al.*[52]

Complementary to the WAXS, Differential Scanning Calorimetry (DSC) measurements offer a way to access crystal features such as cohesiveness and quality of the crystal. In **Figure 16**b, the thermograms exhibit a clear signature with respect to the amount of VDF. The melting temperature represented by the endotherm at high temperatures remains essentially unchanged while the temperature at which the second endotherm (at lower temperatures) progressively decreases. This second endotherm is representative of the Curie transition. This decrease is related to the impact of TrFE on the crystalline structure: as the VDF content decreases, the number of defects increases, and the crystalline arrangement is less dense with a higher characteristic spacing.[51] The observation of a well-defined endotherm for the Curie transition allows its description as a first-order transition where changes occur abruptly and do not have any prior fluctuations.

The “de-densification” is due to the evolution of crystallinity with a transition from FE to an RFE phase. This phase is less cohesive, as seen by a decrease of the 2θ peak in WAXS measurements[39,41,52] (**Figure 14**), thus the energy needed to transition from the electroactive phase to the paraelectric phase is considerably reduced which is transcribed by a temperature shift of the Curie transition. The order-to-disorder transition experienced during the Curie transition is easier to achieve for a less dense system as the movement of the dipoles is less constrained. The enthalpy also relates to this behavior. The transition from an FE phase to a DFE or RFE phase (less cohesive) reduces chain packing.[34,38,48,53,54] Consequently, it then reduces the energy needed to reversibly transform the system at the Curie temperature.

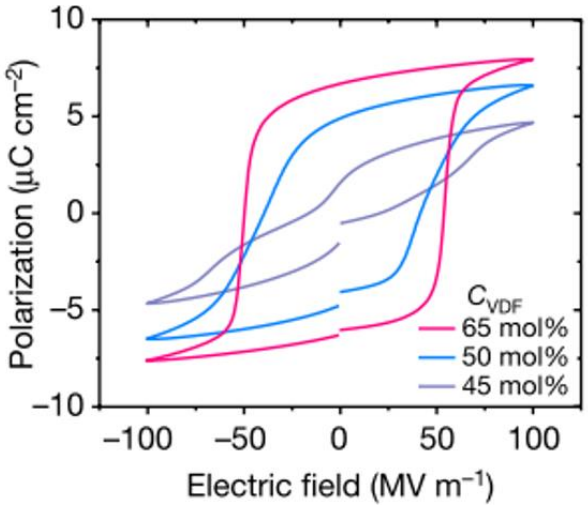

Figure 17. *Polarization versus electric field of (a) P(VDF-TrFE) of different VDF mol.% composition reproduced from Liu et al.*[41]

The material dielectric response is also heavily correlated to the composition of the copolymer (**Figure 17**). At high VDF content (above 50 mol.%), strong cooperative behavior is observable under an electric field. The switching of the dipoles induced by the high ordering results in the wide hysteresis loop (**Figure 17**). Due to the strong dipolar cohesion ordering, the orientation persists upon removal of the electric field resulting in a non-zero polarization at zero electric field reflecting the commonly so-called FE phase. Due to their strong FE behavior, P(VDF-TrFE) copolymers are mostly used for piezoelectric and pyroelectric applications. Those applications take advantage of the order present in the material and the possible reversibility from order to disorder.

The characteristics of the polarization loop such as the remanent polarization, the saturation polarization, the coercive field but also the energy loss and recovery energy density – directly reflect the quality of the crystal order.

We have seen previously that the composition affects the number of defects in the polymer chain; and the potential energy of the different possible chain conformations. By comparing the loops established for a copolymer with a VDF content of 65 mol.% with the one of a copolymer with a VDF content of 45 mol.%, the transition from a typical FE loop to an RFE/DFE loop is easily distinguishable since the main differentiating parameter is the amount of recoverable energy density. The recoverable energy density is higher for an RFE/DFE-like material with lower cohesiveness than for a FE material.

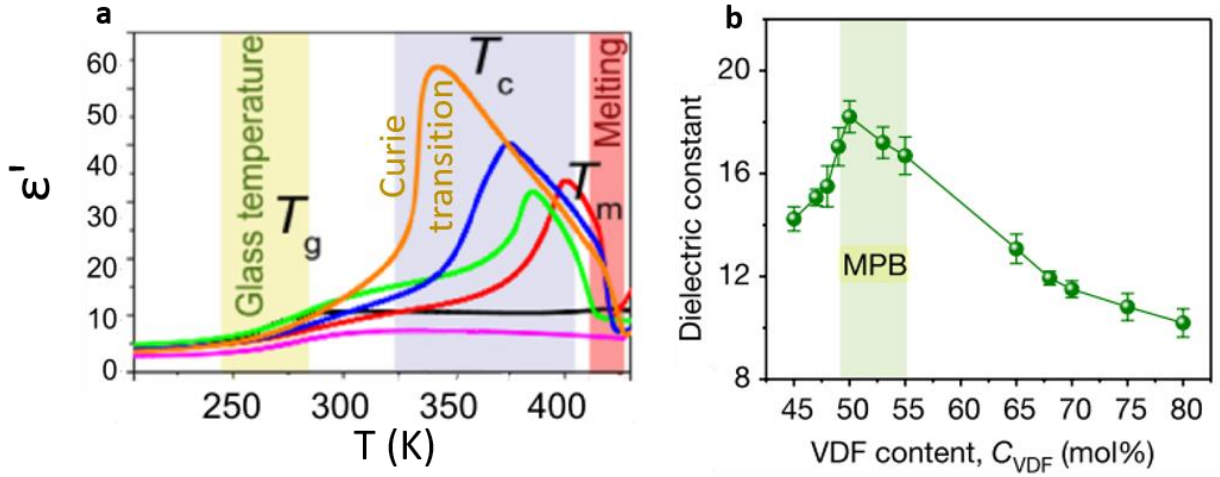

Figure 18. *(a) Dynamic permittivity measurements at 100 kHz as a function of the temperature for P(VDF-TrFE) copolymers with different VDF mol.%: PVDF homopolymer in black, 80 mol.% in red, 75 mol.% in green, 65 mol.% in blue, 50 mol.% in orange and PTrFE in magenta (reproduced from Pipertzis et al.[52]) (b) Maximum permittivity value obtained by dielectric measurements performed at room temperature at 1 kHz as a function of the VDF mol.% (reproduced from Liu et al.[41])*

Another feature is also important while examining the material dielectric properties and efficiency. Values such as relative permittivity (ε‘) and the loss angle (tanδ) dictate the “performance” of the material. A higher ε‘ means that the response of the material under an electric field will be higher. It is of first importance since an optimal material should exhibit high permit-

tivity values while maintaining the losses (reflected by the values of tanδ) at their minimum. Nevertheless, these features are frequency and temperature-dependent and must be characterized to use the material at maximum efficiency. Dielectric spectroscopy (DS) or impedance spectroscopy, is frequently used to study the response of a sample subjected to an applied electric field at fixed or variable frequency and/or temperature.

As shown in **Figure 18**a, the permittivity value is dependent on the VDF mol.% composition. The temperature at which the maximum permittivity is reached and the actual values of ε' depend on the composition. This feature is representative of the Curie transition, *i.e*., a system undergoing an order-to-disorder transition. According to **Figure 18**a, this temperature decreases while decreasing the VDF content, meaning that higher mobility is achieved at lower temperatures. This assessment gives another clue that the composition affects the crystallization of the material and its transformation from an FE to a more RFE behavior. The Curie transition region also widens for lower VDF content illustrating the modification of the material structure and representative of the RFE phase. The glass transition temperature, T_g, is also observable as the mobility of the dipoles drastically increases at the time of the glassy-to-rubbery transition. In the melting temperature region, the material is fully disordered which induces a considerable drop in the permittivity. From measurements performed at room temperature on annealed samples (see **Figure 18**b), the permittivity reaches a maximum for a composition of 50 mol.% in VDF. This transition further corroborates the presence of an MPB at a critical VDF content and the modification of the dielectric behavior from an FE material to an RFE with the decrease of the VDF content. Accordingly, it is of first importance, to establish precisely the composition of the material to access the desired properties.

1.2.2 Tailoring Electroactive Properties with Bulky Monomers Inducing the Relaxor-Ferroelectric Behaviour

P(VDF-TrFE) copolymers presented excellent ferroelectric properties that are directly related to their crystallization behavior. These copolymers naturally crystallize in the β-phase (all-*trans* chain conformation) due to the steric hindrance and "defects" introduced by the TrFE repeating units. Additional research led to the development of PVDF-based terpolymers with the inclusion of CTFE or CFE units which further increased steric hindrance. The presence of CFE/CTFE units along the polymer chain disrupts long-range ordering during the crystallization process, resulting in the formation of crystalline nanodomains and/or defects that have been attributed to the observed relaxor-ferroelectric behavior. Nevertheless, high amounts of CFE/CTFE units in the polymer sequence also decrease the overall crystallinity of the polymer, generating a trade-off between crystallinity and the magnitude of relaxor-ferroelectric behavior.

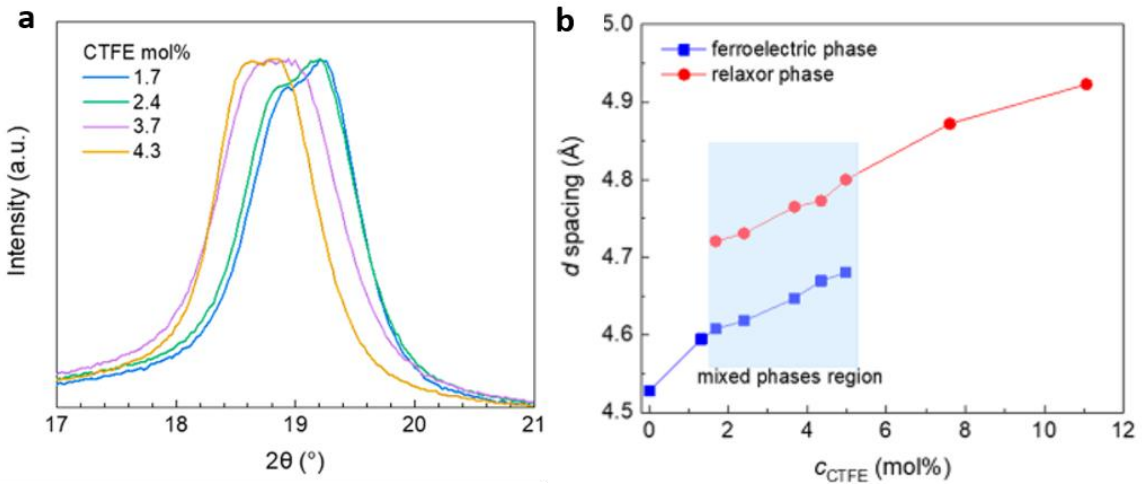

Figure 19. *(a) WAXS diffraction data for several P(VDF-TrFE-CTFE) compositions. (b) Evolution of the lattice spacing "d" as a function of the CTFE content reproduced from Han et al.*[55]

In comparison to WAXS measurements conducted on copolymers, the diffraction angle of the principal signal in the terpolymer is not only shifted to lower 2θ values but is also dependent on composition. As the CTFE content increases, the 2θ values of the main signal consistently decrease. This observation is supported by the *d* spacing values, which steadily increase from a length characteristic of an FE phase to an RFE phase. This evidence strongly indicates that the

incorporation of the bulkier CTFE monomer diminishes the material cohesiveness, ultimately resulting in an RFE structuration of the material.

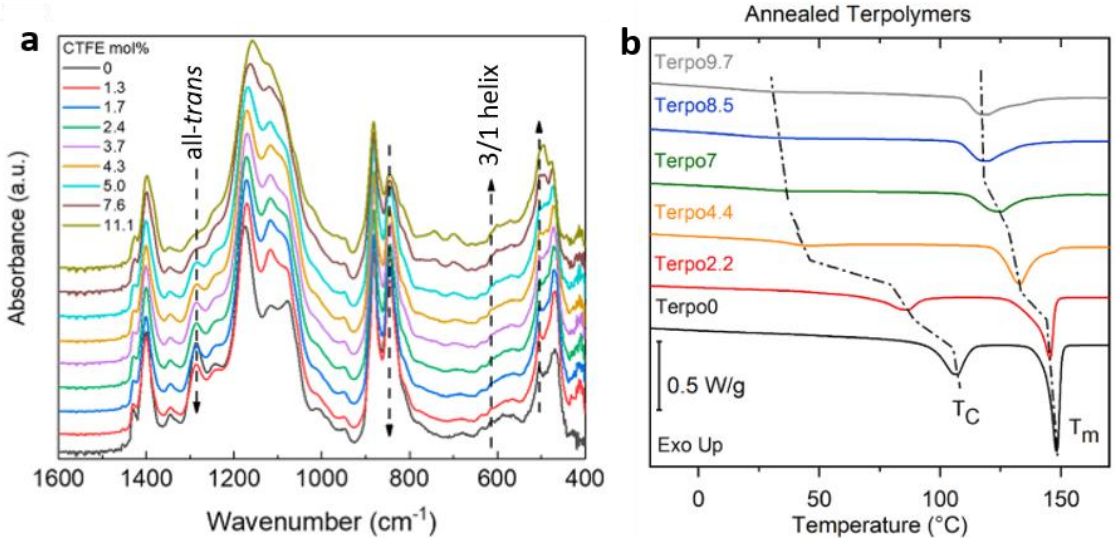

Figure 20. *(a) FTIR spectra of P(VDF-TrFE-CTFE) terpolymers dotted lines correspond to characteristic absorption bands of all-trans (1280 cm^{-1}) and 3/1 helix (510 cm^{-1}) adapted from Han et al.*[55] *(b) First heating DSC experiments on various CTFE terpolymer composition reproduced from Bargain et al.*[44]

The introduction of CTFE units into the copolymer chain shows also a huge composition-structure dependence observable through FTIR. Typical vibrational modes correspond to *all-trans* conformations and the 3/1 helix shows a drastic change with the composition. At zero CTFE content, the P(VDF-TrFE) (here 65/35 mol.%) disposes of the typical vibrational bands representative of the *all-trans* conformation at 1280 cm^{-1} and the 3/1 helix conformation around 510 cm^{-1} as seen and commented in the previous section. Increasing CTFE content massively impacts the FTIR spectra by progressively decreasing the *all-trans* vibrational intensity contrasted by the increase of the 3/1 helix intensity confirming the shift to an RFE-like structuration.

In the DSC traces, the addition of CTFE to P(VDF-TrFE) diminishes the temperature of the two endotherms but also their enthalpy values. The well-defined endotherms describing the melting and the Curie transition of the copolymer are massively impacted by the CTFE incorporation. While adding the CTFE unit, the Curie transition is no longer considered as a first-order transition as the order to disorder is now taking place progressively and is almost undetectable through

DSC. Also, the melting temperature relates to a less dense structure compared to the neat copolymer as the shifting of the endotherms to lower values can be transcribed to a lower crystal lamella length (L_c).[51] This feature evokes the evolution of a less dense crystal structure from FE to DFE/RFE structure and the dielectric properties associated.

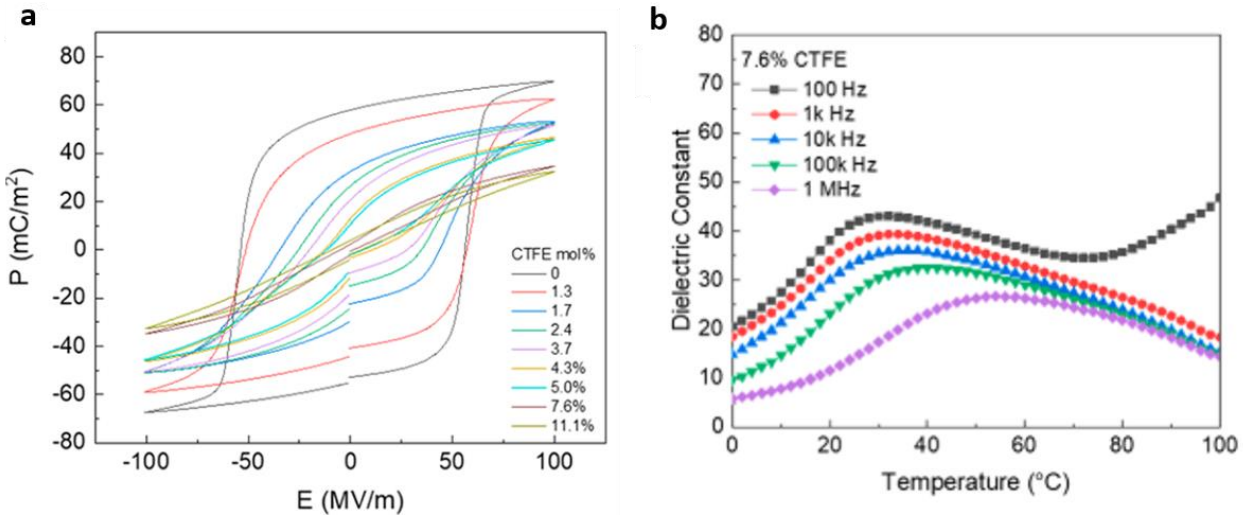

Figure 21. *(a) Polarization versus electric field of different terpolymer compositions, (b) broadband dielectric spectroscopy of a 7.6 mol.% CTFE terpolymer as a function of the temperature and frequency reproduced from Han et al.*[55]

Finally, the dielectric properties are as well representative of the previous conclusions concerning the structuration of the terpolymer. From **Figure 21**a, the dielectric measurement leads to the belief that the initial FE copolymer progressively transforms to an RFE-like material as the PE loops exhibit lower P_r and a higher energy storage density, that both combined result in a thinner hysteresis loop. To corroborate this RFE-like behavior, dielectric spectroscopy was used and established the frequency dependence of a well-defined RFE-like terpolymer (7.6 mol.% CTFE), one of the criteria for assessing an RFE material nature. More precisely, the shift in temperature of the maximum dielectric constant is a typical behaviour of a RFE material (**Figure 21**b).

1.3 Methods to Increase the Formation of the Electroactive Phase

The lack of thermodynamic stability of the β phase within the crystalline PVDF material leads to the development of methodologies to increase the total amount of crystallinity and the electroactive fraction. Indeed, the chemical method previously described involving adding co-monomers has limitations in increasing crystallinity. Accordingly, several processing methods were established to finely tune the structural characteristics of PVDF-based electroactive materials. Thermal annealing[25,26,38,54], solvents casting[56–59], solvent annealing[60,61], stretching[62–64], poling[49,65,66], precipitations[67,68], blending[69,70] (with organic and inorganic materials), and chemical modifications[51,71,72] are some of the methods described to enhance the electroactive properties.

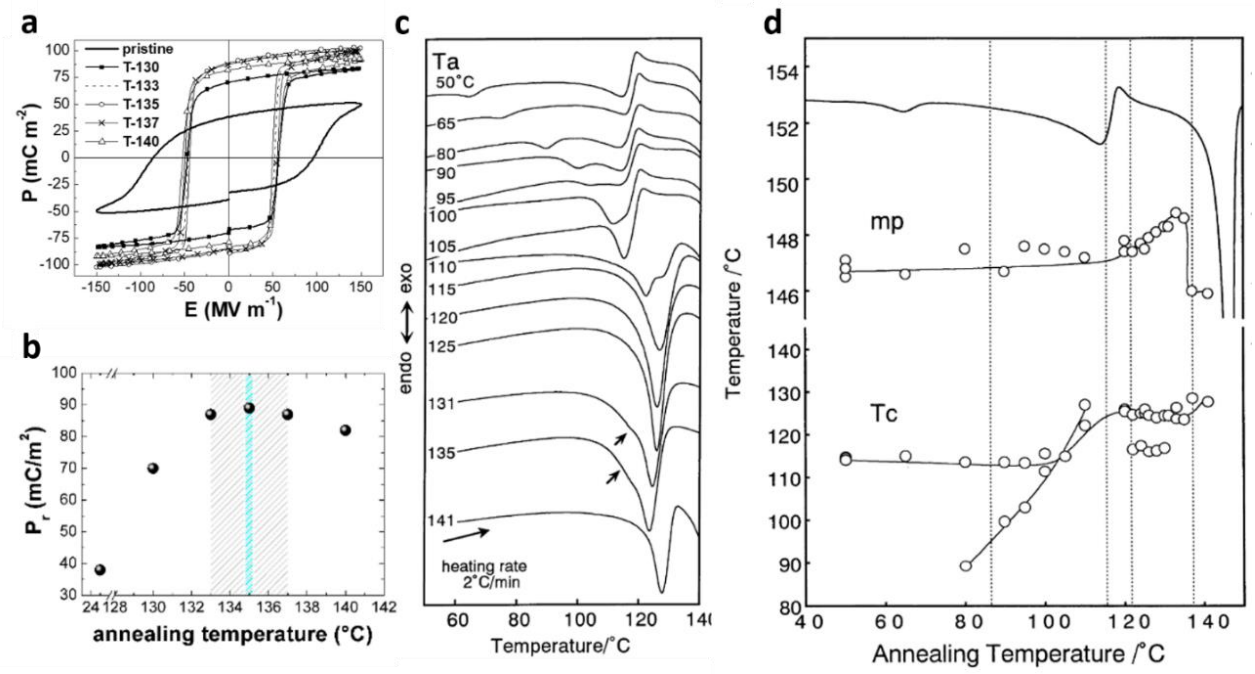

Figure 22. *(a) and (b) Polarization loops and remanent polarization values according to the annealing temperature of a P(VDF-TrFE) copolymer reproduced from Spampinato[73], (c) and (d) DSC thermograms and evolution of the Curie transition temperature (Tc) and the melting point (mp) reproduced from Tanaka et al.*[54]

Thermal annealing is the most used process to increase the electroactive β phase. In **Figure 22**a,b, we can see that the polarization loops and the remanent polarization values are different according to the annealing temperature of the copolymer. Higher values of remanent polarization could be achieved for an optimal temperature that also depends on the copolymer composition. It is then important to optimize the annealing temperature depending on the composition. The work of Tanaka *et al*.[54] describes this effect by annealing copolymer samples at different temperatures. As shown in **Figure 22**c,d, the Curie temperature (Tc) and the melting point (mp) depend on the temperature of annealing. The increase to higher temperature values is consistent with the densification of the crystalline structure to a higher FE crystal quality as the annealing brings enough mobility to the material to allow crystal growth.

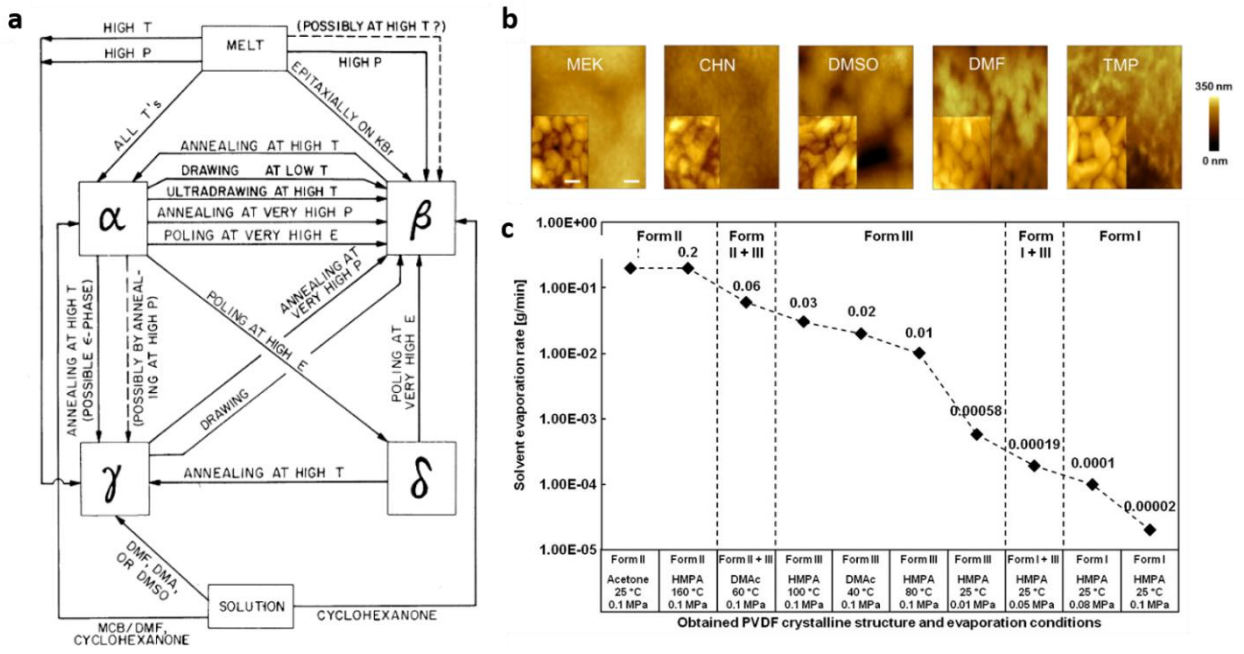

Figure 23. *(a) Schematic summary of crystallization and interconversions of the polymorphic phases of PVDF reproduced from Lovinger et al.*[74] *(b) AFM images of the P(VDF-TrFE) layers using various polar solvents; scale bar: 1 µm. The inset images are the magnified views; scale bar: 100 nm. Reproduced from Sekine et al.*[76] *(c) Relationship between PVDF crystalline phases and solvent evaporation rate. Form I, II, III corresponds to the β, α and γ crystalline phases, respectively. Reproduced from Oribe et al.*[75]

Performing the depositions of PVDF from the melt or solution has an impact on the crystalline structure and has already been commented in literature as seen in **Figure 23**a and **Figure 23**b. From the melt, α, β, and γ are easily accessible by playing with the temperature and/or the pressure. The post processes mentioned above enable an interplay between the phase distribution, which is particularly significant when targeting specific dielectric properties.

Solution casting is also available and demonstrated to favor a crystalline phase according to the solvent nature. In **Figure 23**a, cyclohexanone (1.8D) which has a low dipolar moment increases the β and α content whereas DMF (3.9D) and DMSO (3.7D) with a higher dipolar moment induce γ content. **Figure 23**b. corroborates the fact that the nature of the solvent affects the crystalline structure. Films deposited with different solvent displaying different dipolar moments show a drastic change in film topography. This change was attributed to the fact that solvents with high dipole moments form rougher surfaces because of a slow solvent evaporation. Complementary, the evaporation rate of the solvent after deposition can have major consequences on the film. In the example highlighted in **Figure 23**c, the evaporation rate of hexamethylphosphoramide (HMPA) solvent has an effect on the crystal structure of the PVDF films. PVDF (β) was obtained when the solvent evaporation rate was inferior to 0.0001 $g.min^{-1}$, PVDF (α) was obtained when the solvent evaporation rate superior to 0.2 $g.min^{-1}$, and PVDF (γ) was obtained when the solvent evaporation rate was between 0.00058 $g.min^{-1}$ and 0.03 $g.min^{-1}$.

1.4 Application Prospects

The astonishing electroactive properties of P(VDF) based materials give new possibilities in terms of applications (see **Table 1**). As highlighted in some review papers, PVDF-based copolymers are widely adopted for applications as sensors or actuators.[70,77–81]

Table 1. *Piezoelectric and mechanical properties of various piezoelectric materials adapted from Muralidharan et al.[70] and Stadlober et al.[81]*

Materials	d (10^{-12} C/N) piezoelectric strain constant	g_{33} (10^{-3} mV/N) piezoelectric stress constant	Tc (°C)	Young's Modulus (GPa)
PVDF	d_{33} = −30 d_{31} = 20–30	335	80	2
P(VDF-TrFE)	d_{33} = 30-35		60-130	5
Lead Zirconate Titanate (PZT-4)	d_{33} = 289	26.1	380	11
Barium Titanate ($BaTiO_3$)	d_{33} = 149	14.1	120	120
Quartz	d_{11} = –2.0	50.3	573	31

Their overall physical-chemical properties such as chemical resistance, thermally and atmospheric stability, and high durability associated with their piezoelectric, pyroelectric, or ferroelectric properties make this class of materials a great choice for researchers. **Figure 24** shows a mapping of the different stimuli that can be detected with ferroelectric polymers. Responses to mechanical stimuli are straightforward in their operating mode. Applying a bending, strain, force, pressure or vibrations will induce macro/micro deformations of the material. On the polarized ferroelectric material, the dipoles ordered and aligned will change their orientation subsequently creating a variation of surface charge density inducing a voltage. The exposure to temperature and IR radiation will increase also the mobility and displace the orientation of the dipoles creating a variation in charge density.

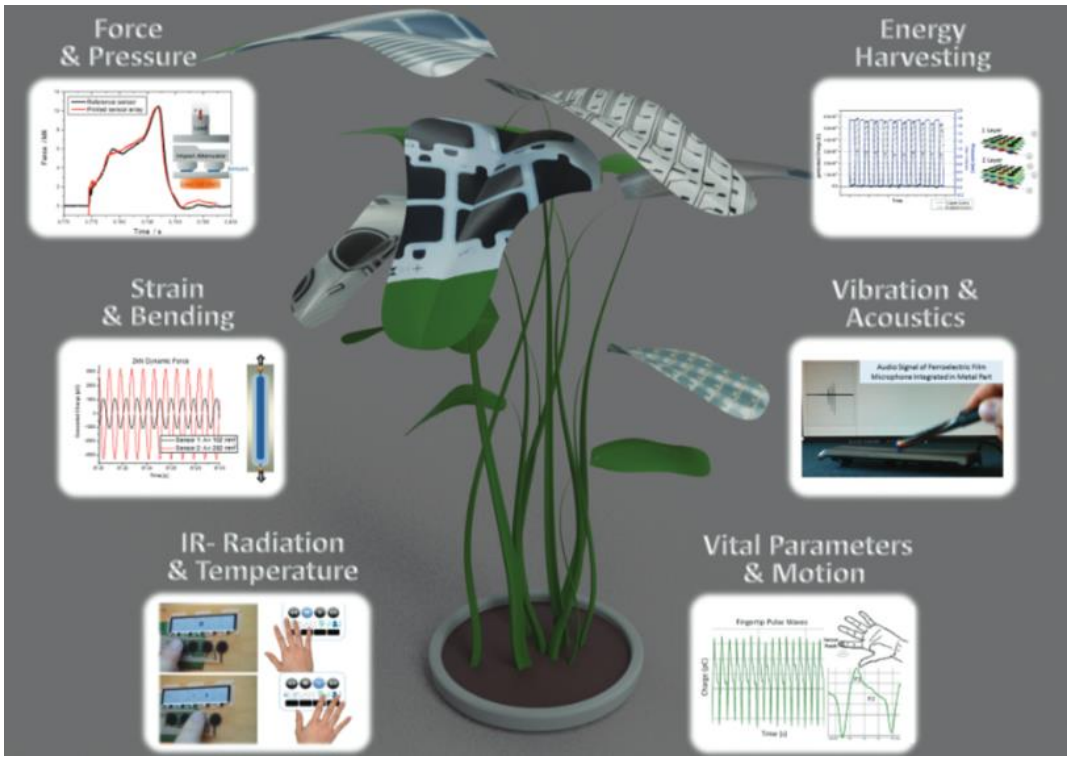

Figure 24. *Physical parameters that can be detected with ferroelectric polymers reproduced from Stadlober et al.*[81]

The electrostrictive properties and electrocaloric effect are also raising interest as these materials could respond to actual environmental concerns.[42,43,82,83] Future works in this field will be to scale up and increase the processability efficiency of these materials via novel ways such as the generation of fully printed devices.[84]

1.5 Printing methods of PVDF-based polymers

From the point of view of cost reduction and process efficiency, the printing technology applied to electroactive polymers could be a considerable advantage. The already well-developed printing industry based on optimized ink formulations is foreseen to trigger the development of electroactive devices, for instance for wearable[63,76,85] or medical applications[86,87]. Nevertheless, the complexity of the VDF-based polymers is an obstacle to the direct implementation of these

materials in such technologies. So far, ink systems containing organic and inorganic compounds for electronic applications demonstrated the necessity to answer specific issues encountered such as homogeneity, roughness, and printability during the deposition process.[88] Indeed, each printing technique has its specific ink requirements for good deposition and, consequently, reliable devices. Applied science is needed to understand and evaluate printability and the underlying mechanisms for all currently known printing technologies (**Figure 25**), such as roll-to-roll[89–91], screen-printing[92–95], blade coating[96–99], and inkjet printing[100–105]. Examples of printed PVDF-based devices have already been presented, showing a real advantage in terms of processing costs and device efficiency.[15,106–111]

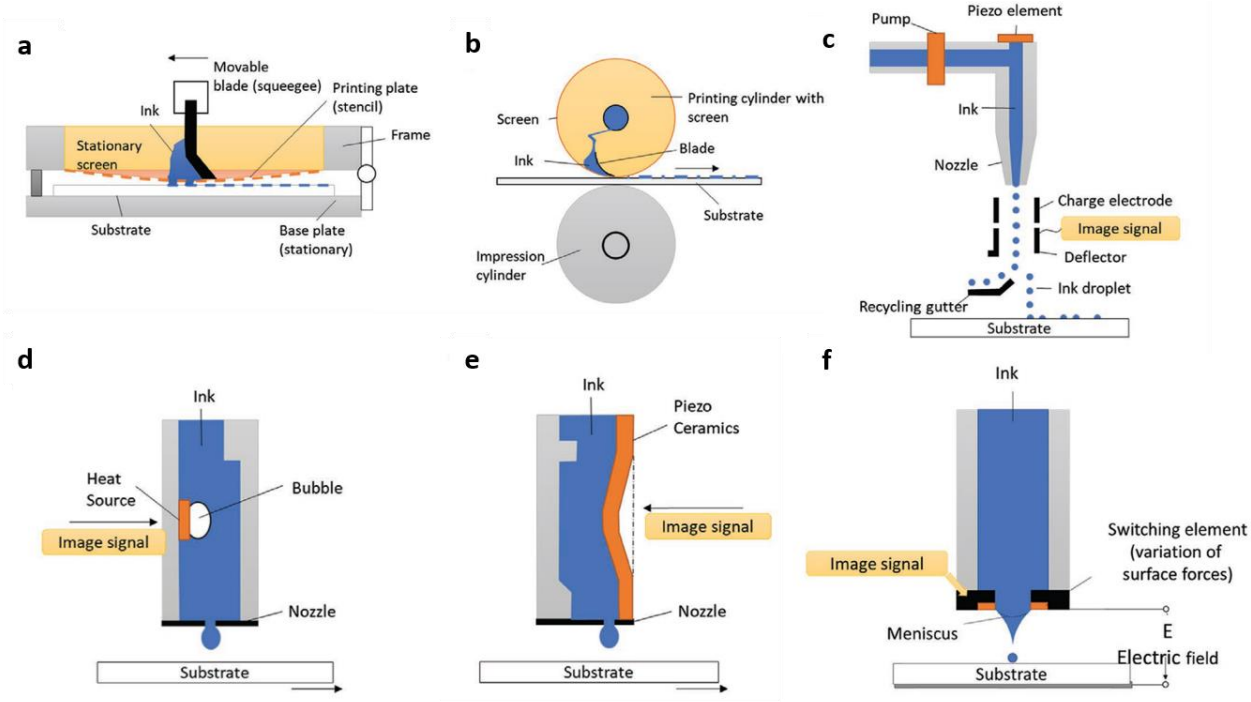

Figure 25. *Simplified views of a) flat-to-flat and b) round-to-round screen-printing mechanics. c) Continuous, d) thermal drop-on-demand (bubble jet), e) piezoelectric drop-on-demand, and f) electrostatic inkjet printing mechanics reproduced from Kipphan et al.*[112] *and Aliqué et al.*[84]

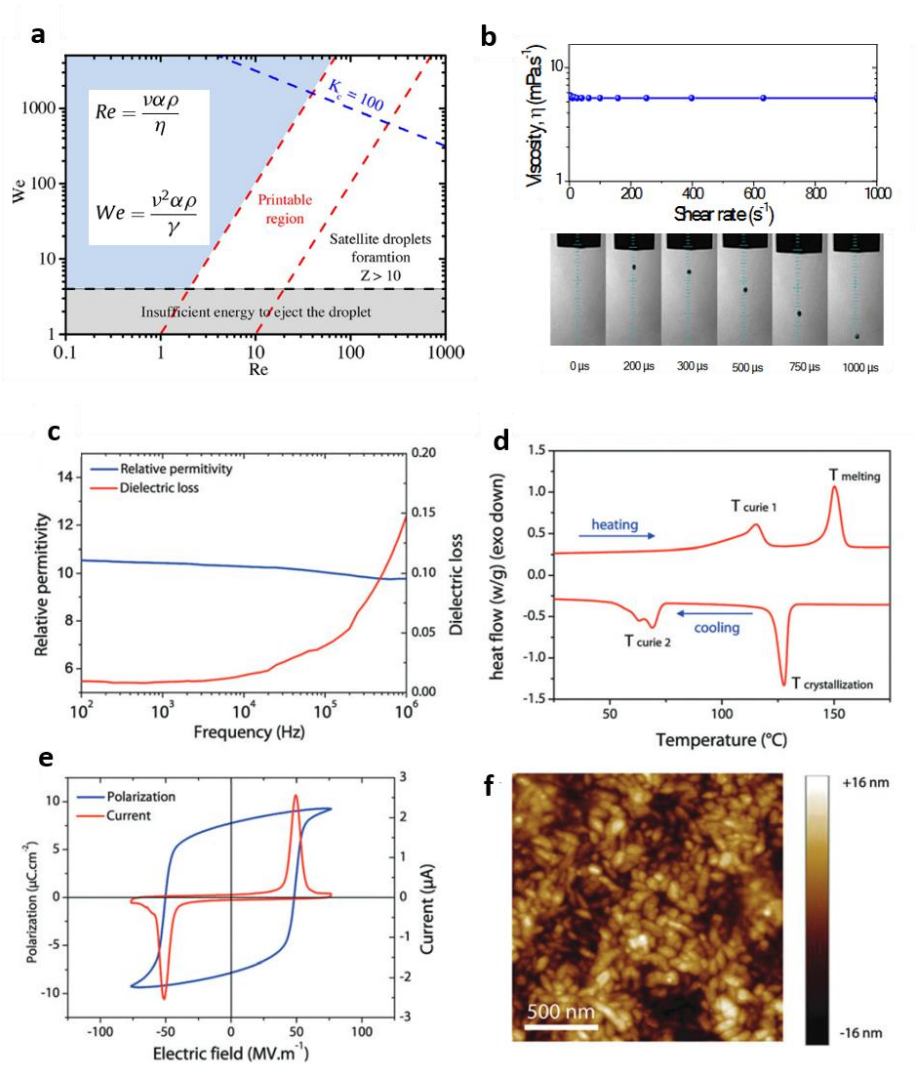

Figure 26. *(a) Printability region of an ink by inkjet printing according to the Reynolds and Weber numbers shown in the inset with v the velocity of the droplet ($m.s^{-1}$), α the nozzle diameter (m), ρ the ink density ($kg.m^{-3}$), η the ink viscosity (Pa.s) and γ the surface tension ($N.m^{-1}$) adapted from Du et al.*[105] *(b) Viscosity as function of the shear for a P(VDF-TrFE) ink and the profile of a droplet ejection with high-speed imaging camera during the ejection of the droplet. (c) Relative permittivity and dielectric loss of the devices printed by inkjet printing. (d) DSC trace and (e) polarization profile of the devices. (f) AFM image of the P(VDF-TrFE) depositions. (b-f) reproduced from Sekine et al.*[76]

The ink requirements are specific to the technique used to perform the deposition. As an example, in the case of a deposition performed through inkjet printing (**Figure 26**), the viscosity of the polymer solution should be Newtonian to comply with proper ink ejection without unwanted satellite droplets interfering with the deposition quality. Reynolds and Weber numbers

related to the droplet velocity, solution viscosity surface tension, and density are used to evaluate the printability of the solution. Figure 26a shows the printability region as a combination of Reynolds and Weber numbers. Efficient devices can be printed with this technique allowing good relative permittivity, crystallinity, and remanant polarization.

Other techniques mentioned above can be accurately used to obtain piezoelectric devices. Each printing technique needs proper ink rheological parameters and imposes a specific stress on the solution. For example, elongation and shearing are imposed on the inks with inkjet and screen printing, respectively. An easy way to tune the rheological properties to fit the requirements is to accurately tune the polymer concentration (**Figure 27**). In most cases, a diluted solution will show Newtonian behavior and low viscosity, while more concentrated solutions will display higher viscosity and in some cases reach a shear-thinning behavior.

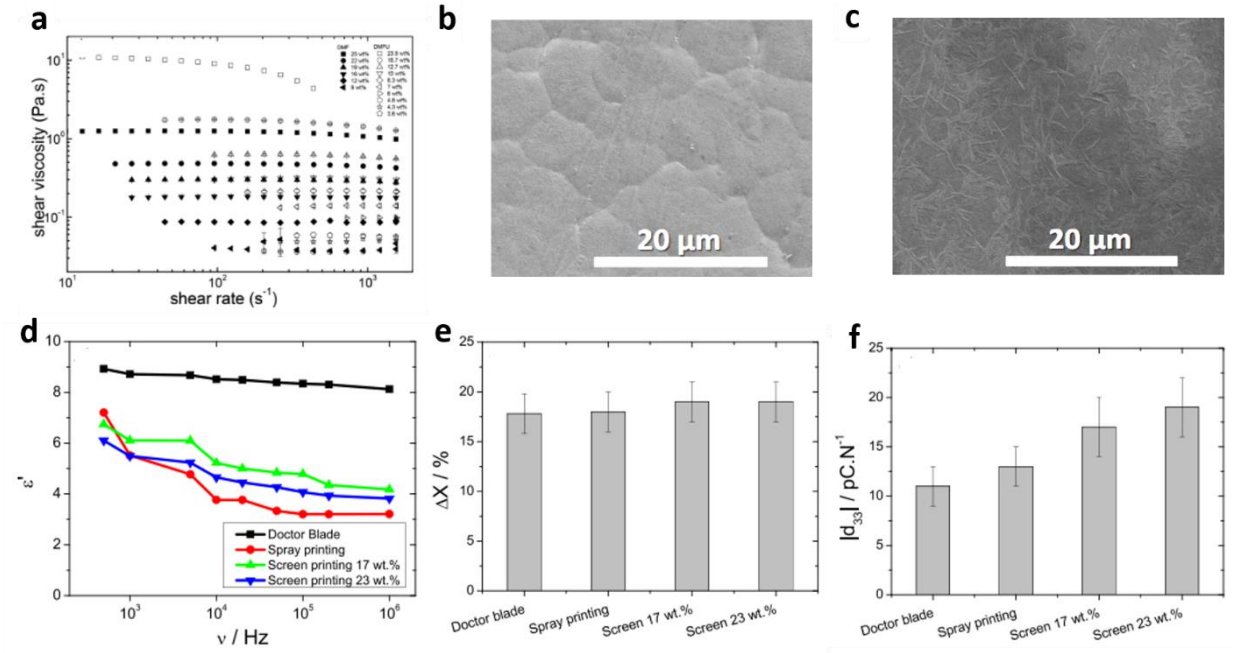

Figure 27. *(a) Shear versus viscosity of P(VDF-TrFE) on a wide range of concentrations in (○) DMF and (●) DMPU. (b) and (c) SEM images of P(VDF-TrFE) obtained by spay-printing and screen-printing respectively. (d) Dielectric constant for different depositions methods and concentrations. (e) Evolution of the crystallinity and (f) the absolute value of the piezoelectric coefficient $|d_{33}|$ for the different depositions methods. (a-f) reproduced from Gonçalves et al.*[110]

These differences in the process can consequently modify the structure of the material according to the deposition technique used. **Figure 27** shows an example of the notable differences that can be obtained in the depositions by using different printing techniques and parameters. The morphologies of the depositions between spray and screen printing are different from spherulitic to rod-like structures. The relative permittivity is also impacted with increased values from 4 to 8. No major differences were attributed to the overall crystallinity but the piezoelectric response evaluated by the d_{33} parameter increased from DR blade to screen printing with different concentrations. In this study, the differences were only attributed to different morphological features among the various samples.

Accordingly, it is essential to formulate PVDF-based inks in order to optimize the dielectric response of printed devices according to the printing techniques.

1.6 Context and objectives of this Ph.D. thesis.

This introductory chapter provides an overview of the relationship between the structural characteristics of P(VDF)-based materials, their electroactive properties and potential high-end applications. It highlights that tuning the dielectric response of these materials can be achieved through various methods such as functionalization, structural modification, or blending. However, the practical application of these functional materials in devices requires adapted processing techniques to meet criteria in terms of geometry, scalability, toxicity, and properties, among other parameters.

This Ph.D. thesis is conducted within the framework of an industrial chair between the LCPO and four industrial partners - ARKEMA, ISORG, SURYS, and VALEO – aiming at the development of P(VDF)-based materials in the emerging field of printed ferrotronics. The SMILE chair (SMILE: Smart Polymer Ferrotronic Materials for Environmental Monitoring and Energy Conversion) aims to address pressing trends and requirements in areas such as autonomous sensing, environmental monitoring, and smart actuation. In particular, it seeks to provide innovative solutions through the use of printing technologies and organic materials.

Accordingly, the main objective of this Ph.D. is to understand the formulation of electroactive inks by studying the solvation of P(VDF)-based materials, chain conformation in solution, ink rheological behaviors, and the resulting properties of deposited layers.

Chapter 2 focuses on the solvation behaviors of P(VDF-TrFE) with different TrFE contents using the Hansen approach. The chapter investigates the conformational state of P(VDF-TrFE) through a scaling approach based on viscosity in different concentration regimes, establishing the fingerprint of the copolymers and demonstrating the relationship between TrFE content and chain conformation.

In **chapter 3**, we then study a particular P(VDF-TrFE) composition (*i.e.*, 80% VDF - 20% TrFE), and studied its solution behavior in various solvents via viscosimetry and light scattering. It was demonstrated that the choice of a solvent can drastically modify and modulate the viscosity of solution with a high copolymer content. We also applied the aforementioned scaling approach

based on viscosity measurements to decipher the change of P(VDF-TrFE) chain conformation as function of the solvent quality and concentration regime.

Chapter 4 focuses on fabricating printed devices using this particular copolymer composition *via* the screen-printing technique. We first settled down the basics of this technique by benchmarking this process modifying only one parameter known as the meshing geometry of the screens used. It has been possible to link the stability of the device under the application of an electric field with the printing process and the ink formulation. An optimization has consequently been proposed to increase the stability of the devices.

Finally, in **chapter 5**, we extend these previous approaches to P(VDF-TrFE-CTFE) terpolymers and studied in particular the deposition of P(VDF-TrFE-CTFE) layers by Blade Coating, emphasising the role of the shear rate on the final material properties.

References

1. Valasek, J. Piezo-electric and allied phenomena in Rochelle salt. *Phys. Rev.* **17**, 475–481 (1921).
2. Newnham, R. E. Ferroelectrics and Other Ferroic Materials. *Struct. Relations* 78–114 (1975) doi:10.1007/978-3-642-50017-6_4.
3. A P Levanyuk, B. A. S. Ferroelectricity. *Elsevier Ltd* 192–201 (2005).
4. Costa, P. *et al.* Recent Progress on Piezoelectric, Pyroelectric, and Magnetoelectric Polymer-Based Energy-Harvesting Devices. *Energy Technol.* **7**, (2019).
5. Pardo, L. Piezoelectric ceramic materials for power ultrasonic transducers. in *Power Ultrasonics* 101–125 (Elsevier Inc., 2015). doi:10.1016/B978-1-78242-028-6.00005-3.
6. Ropp, R. C. *Solid State Chemistry*. *Solid State Chemistry* (2003). doi:10.1016/B978-0-444-51436-3.X5000-7.
7. Pradhan, L. K., Kar, M., Pradhan, L. K. & Kar, M. Relaxor Ferroelectric Oxides: Concept to Applications. in *Multifunctional Ferroelectric Materials* (IntechOpen, 2021). doi:10.5772/INTECHOPEN.96185.
8. Kumar, A., Correa, M., Ortega, N., Kumari, S. & Katiyar, R. S. *Self Assembled Nanoscale Relaxor Ferroelectrics*. (2013). doi:10.5772/54298.
9. Zhu, L. & Wang, Q. Novel ferroelectric polymers for high energy density and low loss dielectrics. *Macromolecules* **45**, 2937–2954 (2012).
10. Xiaodong, J., Xin, C. & Q.M., Z. Relaxor Ferroelectric Capacitors Embrace Polymorphic Nanodomains. *Joule* (2019) doi:10.1016/j.joule.2019.09.008.
11. Schmidt, G. C. *et al.* Fully printed flexible audio system on the basis of low-voltage polymeric organic field effect transistors with three layer dielectric. *J. Polym. Sci. Part B Polym. Phys.* **53**, 1409–1415 (2015).
12. Lu, L., Ding, W., Liu, J. & Yang, B. Flexible PVDF based piezoelectric nanogenerators. *Nano Energy* **78**, 105251 (2020).
13. Liu, K., Ouyang, B., Guo, X., Guo, Y. & Liu, Y. Advances in flexible organic field-effect transistors and their applications for flexible electronics. *npj Flex. Electron. 2022 61* **6**, 1–19 (2022).
14. Klauk, H. Organic Electronics: Materials, Manufacturing and Applications. *Org. Electron. Mater. Manuf. Appl.* 1–428 (2006) doi:10.1002/3527608753.
15. Schmidt, G. C. *et al.* Paper-Embedded Roll-to-Roll Mass Printed Piezoelectric Transducers. *Adv. Mater.* (2021) doi:10.1002/adma.202006437.
16. Zheng, B., Huo, L. & Li, Y. Benzodithiophenedione-based polymers: recent advances in organic photovoltaics. *NPG Asia Mater.* **12**, (2020).
17. Sekine, C., Tsubata, Y., Yamada, T., Kitano, M. & Doi, S. Recent progress of high performance polymer OLED and OPV materials for organic printed electronics. *Sci. Technol. Adv. Mater.* **15**, (2014).
18. Janata, J. & Josowicz, M. Conducting polymers in electronic chemical sensors. *Nat. Mater* **2**, 19–24 (2003).
19. Yang, Y. *et al.* Flexible hybrid energy cell for simultaneously harvesting thermal, mechanical, and solar energies. *ACS Nano* **7**, 785–790 (2013).
20. Qian, J., Jiang, J. & Shen, Y. Enhanced electrocaloric strength in P(VDF-TrFE-CFE) by

decreasing the crystalline size. *J. Mater.* **5**, 357–362 (2019).
21. Li, Q., Zhao, J., He, B. & Hu, Z. Solution processable poly(vinylidene fluoride)-based ferroelectric polymers for flexible electronics. *APL Mater.* **9**, 010902 (2021).
22. Bargain, F. *et al.* Thermal behavior of poly(VDF-ter-TrFE-ter-CTFE) copolymers: Influence of CTFE termonomer on the crystal-crystal transitions. *Polymer (Guildf).* **161**, 64–77 (2019).
23. Kang, G. dong & Cao, Y. ming. Application and modification of poly(vinylidene fluoride) (PVDF) membranes – A review. *J. Memb. Sci.* **463**, 145–165 (2014).
24. Zou, F., Manthiram, A., Zou, F. & Manthiram, A. A Review of the Design of Advanced Binders for High-Performance Batteries. *Adv. energy Mater.* **10**, (2020).
25. Zhao, J., Tan, A. C. & Green, P. F. Thermally induced chain orientation for improved thermal conductivity of P(VDF-TrFE) thin films. *J. Mater. Chem. C* **5**, 10834–10838 (2017).
26. Barique, M. A. & Ohigashi, H. Annealing effects on the Curie transition temperature and melting temperature of poly(vinylidene fluoride/trifluoroethylene) single crystalline films. *Polymer (Guildf).* **42**, 4981–4987 (2001).
27. Lee, J. S., Prabu, A. A. & Kim, K. J. Annealing effect upon chain orientation, crystalline morphology, and polarizability of ultra-thin P(VDF-TrFE) film for nonvolatile polymer memory device. *Polymer (Guildf).* **51**, 6319–6333 (2010).
28. Pouriamanesh, N., Le Goupil, F., Stingelin, N. & Hadziioannou, G. Limiting Relative Permittivity 'Burn-in' in Polymer Ferroelectrics via Phase Stabilization. *ACS Macro Lett.* **11**, 410–414 (2022).
29. Sencadas, V., Gregorio, R. & Lanceros-Méndez, S. α to β Phase Transformation and Microestructural Changes of PVDF Films Induced by Uniaxial Stretch. *http://dx.doi.org/10.1080/00222340902837527* **48**, 514–525 (2009).
30. Li, L., Zhang, M., Rong, M. & Ruan, W. Studies on the transformation process of PVDF from α to β phase by stretching. *RSC Adv.* **4**, 3938–3943 (2013).
31. Cais, R. E. & Sloane, N. J. A. A statistical theory of directional isomerism in polymer chains and its application to polyvinylidene fluoride. *Polymer (Guildf).* **24**, 179–187 (1983).
32. Wilson, C. W. & Santee, E. R. Polymer Analysis by High-Resolution NMR, with Applications to Poly(viny1idene Fluoride) and Poly (vinyl Fluoride). *J. Polym. Sci. part C* **8**, 97–112 (1965).
33. R. E. Cais and J. M. Kometan. Synthesis and Two-Dimensional 19F NMR of Highly Aregic Poly(vinylidenefluoride). *Macromolecules* **18**, 1354–1357 (1985).
34. Farmer, B. L., Hopfinger, A. J. & Lando, J. B. Polymorphism of poly(vinylidene fluoride): potential energy calculations of the effects of head-to-head units on the chain conformation and packing of poly(vinylidene fluoride). *J. Appl. Phys.* **43**, 4293 (1972).
35. Andrew J. Lovinger. Ferroelectric polymers. *Science (80-.).* **220**, 1115–1121 (1983).
36. Web of Science. https://www.webofscience.com/wos/woscc/basic-search.
37. Andrew J. Lovinger; D. D. Davis; J. M. Kometani; R. On the Curie Temperature of Poly(vinylidene fluoride). *Macromolecules* **19**, 1491–1494 (1986).
38. Furukawa, T. Structure and functional properties of ferroelectric polymers. *Adv. Colloid Interface Sci.* **71**–**72**, 183–208 (1997).
39. Liu, Y., Chen, X., Han, Z., Zhou, H. & Wang, Q. Defects in poly(vinylidene fluoride)-based ferroelectric polymers from a molecular perspective. *Appl. Phys. Rev* **9**, (2022).

40. Bohlé, M. & Bolton, K. Conformational studies of poly(vinylidene fluoride), poly(trifluoroethylene) and poly(vinylidene fluoride-co-trifluoroethylene) using density functional theory. *Phys. Chem. Chem. Phys* **16**, 12929 (2014).
41. Liu, Y. *et al.* Ferroelectric polymers exhibiting behaviour reminiscent of a morphotropic phase boundary. *Nature* **562**, 96–100 (2018).
42. Ma, R. *et al.* Highly efficient electrocaloric cooling with electrostatic actuation. *Science (80-.).* **357**, 1130–1134 (2017).
43. Shi, J. *et al.* Electrocaloric Cooling Materials and Devices for Zero-Global-Warming-Potential, High-Efficiency Refrigeration. *Joule* **3**, 1200–1225 (2019).
44. Bargain, F., Thuau, D., Hadziioannou, G., Domingues Dos Santos, F. & Tencé-Girault, S. Phase diagram of poly(VDF-ter-TrFE-ter-CTFE) copolymers: Relationship between crystalline structure and material properties. *Polymer (Guildf).* **213**, 123203 (2021).
45. Tsutsumi, N., Okumachi, K., Kinashi, K. & Sakai, W. Re-evaluation of the origin of relaxor ferroelectricity in vinylidene fluoride terpolymers: An approach using switching current measurements. *Nat. Sci. reports* **7**, (2017).
46. Kobayashi, M., Tashiro, K. & Tadokoro, H. Molecular Vibrations of Three Crystal Forms of Poly(vinylidene fluoride). *Macromolecules* 158 (1974).
47. Cai, X., Lei, T., Sun, D. & Lin, L. A critical analysis of the a, b and g phases in poly(vinylidene fluoride) using FTIR †. *RCS Adv.* **7**, 15382–15389 (2017).
48. Salimi, A. & Yousefi, A. A. Conformational changes and phase transformation mechanisms in PVDF solution-cast films. *J. Polym. Sci. Part B Polym. Phys.* **42**, 3487–3495 (2004).
49. Tashiro, K. *et al.* High-Electric-Field-Induced Hierarchical Structure Change of Poly(vinylidene fluoride) as Studied by the Simultaneous Time-Resolved WAXD/SAXS/FTIR Measurements and Computer Simulations. *Macromolecules* acs.macromol.0c02567 (2021) doi:10.1021/acs.macromol.0c02567.
50. Gregorio, R. Determination of the , and Crystalline Phases of Poly(vinylidene fluoride) Films Prepared at Different Conditions. *J Appl Polym Sci* **100**, 3272–3279 (2005).
51. Florian Le Goupil, Konstantinos Kallitsis, Sylvie Tencé-Girault, Naser Pouriamanesh, Cyril Brochon, Eric Cloutet, Thibaut Soulestin, Fabrice Domingue Dos Santos, Natalie Stingelin, G. H. Enhanced Electroncaloric response of Vinylidene fluoride-based polymers via one-step molecular engineering. *Adv. Funct. Mater.* **31**, (2021).
52. Pipertzis, A., Asadi, K. & Floudas, G. P(VDF-TrFE) Copolymer Dynamics as a Function of Temperature and Pressure in the Vicinity of the Curie Transition. *Macromolecules* **55**, 2746–2757 (2022).
53. Soulestin, T., Ladmiral, V., Dos Santos, F. D. & Améduri, B. Vinylidene fluoride- and trifluoroethylene-containing fluorinated electroactive copolymers. How does chemistry impact properties? *Prog. Polym. Sci.* **72**, 16–60 (2017).
54. Tanaka, R., Tashiro, K. & Kobayashi, M. Annealing effect on the ferroelectric phase transition behavior and domain structure of vinylidene fluoride (VDF)-trifluoroethylene copolymers: a comparison between uniaxially oriented VDF 73 and 65% copolymers. *Polymer (Guildf).* **40**, 3855–3865 (1999).
55. Han, Z., Liu, Y., Chen, X., Xu, W. & Wang, Q. Enhanced Piezoelectricity in Poly(vinylidene fluoride-co-trifluoroethylene-co-chlorotrifluoroethylene) Random Terpolymers with Mixed Ferroelectric Phases. *Macromolecules* **55**, 2703–2713 (2022).

56. Chou, C.-M. & Hong, P.-D. Light Scattering from Birefringent Sphere and Its Aggregation. *Macromolecules* **41**, 6147–6153 (2008).
57. Li, Y.-C. *et al.* Scattering Study of the Conformational Structure and Aggregation Behavior of a Conjugated Polymer Solution. *langmuir* **25**, 4668–4677 (2009).
58. Saiki, E., Nohara, Y., Iwase, H. & Shikata, T. Evidence of Long Two-Dimensional Folding Chain Structure Formation of Poly(vinylidene fluoride) in N-Methylpyrrolidone Solution: Total Form Factor Determination by Combining Multiscattering Data. *ACS omega* **7**, 22825–22829 (2022).
59. Nohara, Y., Saiki, E. & Shikata, T. Long Two-Dimensional Folding Chain Structure Formation of Poly(vinylidene fluoride) in Solutions of a Polar Solvent, N-Methylpyrrolidone. *ACS Appl. Polym. Mater* **4**, 1255–1263 (2022).
60. Cho, Y. *et al.* Enhanced energy harvesting based on surface morphology engineering of P(VDF-TrFE) film. *Nano Energy* **16**, 524–532 (2015).
61. Cho, Y. *et al.* Enhanced Ferroelectric Property of P(VDF-TrFE-CTFE) Film Using Room-Temperature Crystallization for High-Performance Ferroelectric Device Applications. *Adv. Electron. Mater.* **2**, 1600225 (2016).
62. Li, Y. *et al.* Stretching-Induced Relaxor Ferroelectric Behavior in a Poly(vinylidene fluoride-co-trifluoroethylene-co-hexafluoropropylene) Random Terpolymer. *Macromolecules* **50**, 7646–7656 (2017).
63. Ma, S. *et al.* Highly Oriented Electrospun P(VDF-TrFE) Fibers via Mechanical Stretching for Wearable Motion Sensing. *Adv. Mater. Technol.* **3**, 1800033 (2018).
64. Baniasadi, M. *et al.* Effect of thermomechanical post-processing on chain orientation and crystallinity of electrospun P(VDF-TrFE) nanofibers. *Polymer (Guildf).* **118**, 223–235 (2017).
65. Takahashi, Y. Conformationally incommensurate form of poly(vinylidene fluoride) induced by electric field. *J. Appl. Phys.* **67**, 4060–4063 (1990).
66. Scheinbeim, J. I., Newman, B. A. & Sen, A. Field-Induced Crystallization in Highly Plasticized Poly(vinylidene fluoride) Films. *Macromolecules* **19**, 1454–1458 (1986).
67. Lederle, F., Härter, C. & Beuermann, S. Inducing β phase crystallinity of PVDF homopolymer, blends and block copolymers by anti-solvent crystallization. *J. Fluor. Chem.* **234**, (2020).
68. Tu, R., Sprague, E. & Sodano, H. A. Precipitation-Printed High-β Phase Poly(vinylidene fluoride) for Energy Harvesting. *ACS Appl. Mater. Interfaces* (2021) doi:10.1021/acsami.0c16207.
69. Thuau, D. *et al.* High and Temperature-Independent Dielectric Constant Dielectrics from PVDF-Based Terpolymer and Copolymer Blends. *Adv. Electron. Mater.* **6**, (2020).
70. Muralidharan Nivedhitha, D. & Jeyanthi, S. Polyvinylidene fluoride, an advanced futuristic smart polymer material: A comprehensive review. *Polym Adv Technol* **34**, 474–505 (2023).
71. Kallitsis, K. *et al.* Directly Photo-cross-linkable Ferroelectric Polymers Based on P (VDF- co -TrFE).
72. Kallitsis, K. *et al.* Introducing Functionality to Fluorinated Electroactive Polymers. *Macromolecules* **52**, 8503–8513 (2019).
73. N., S. FERROELECTRIC POLYMERS FOR ORGANIC ELECTRONIC APPLICATIONS. (université

de bordeaux, 2018).
74. Lovinger, A. J. Poly(Vinylidene Fluoride). in *Developments in Crystalline Polymers* (1982).
75. Horibe, H. *et al.* Quantification of the solvent evaporation rate during the production of three PVDF crystalline structure types by solvent casting. *Polym. J.* **46**, 104–110 (2014).
76. Sekine, T. *et al.* Fully Printed Wearable Vital Sensor for Human Pulse Rate Monitoring using Ferroelectric Polymer. *Sci. Rep.* **8**, 1–10 (2018).
77. Xia, W. & Zhang, Z. PVDF-based dielectric polymers and their applications in electronic materials. *IET Nanodielectrics* **1**, 17–31 (2018).
78. Saxena, P. & Shukla, P. A comprehensive review on fundamental properties and applications of poly(vinylidene fluoride) (PVDF). *Adv. Compos. Hybrid Mater.* **4**, 8–26 (2021).
79. Ameduri, B. From Vinylidene Fluoride (VDF) to the Applications of VDF-Containing Polymers and Copolymers: Recent Developments and Future Trends †. *chem rev* **109**, 6632–6686 (2009).
80. Bauer, F. Review on the properties of the ferrorelaxor polymers and some new recent developments. *Appl Phys A* **107**, 567–573 (2012).
81. Stadlober, B., Zirkl, M. & Irimia-Vladu, M. Route towards sustainable smart sensors: Ferroelectric polyvinylidene fluoride-based materials and their integration in flexible electronics. *Chem. Soc. Rev.* **48**, 1787–1825 (2019).
82. Bo, Y. *et al.* Electrostatic Actuating Double-Unit Electrocaloric Cooling Device with High Efficiency. *Adv. Energy Mater.* 2003771 (2021) doi:10.1002/aenm.202003771.
83. Hu, H., Zhang, F., Luo, S., Yue, J. & Wang, C. H. Electrocaloric effect in relaxor ferroelectric polymer nanocomposites for solid-state cooling. *Journal of Materials Chemistry A* vol. 8 16814–16830 (2020).
84. Aliqué, M., Delgado Simão, C., Murillo, G. & Moya, A. Fully-Printed Piezoelectric Devices for Flexible Electronics Applications. *Adv. Mater. Technol.* **6**, (2021).
85. Shin, K. Y., Lee, J. S. & Jang, J. Highly sensitive, wearable and wireless pressure sensor using free-standing ZnO nanoneedle/PVDF hybrid thin film for heart rate monitoring. *Nano Energy* **22**, 95–104 (2016).
86. Xi, Y. *et al.* Optimization, characterization and evaluation of ZnO/polyvinylidene fluoride nanocomposites for orthopedic applications: improved antibacterial ability and promoted osteoblast growth. *Drug Deliv.* **27**, 1378–1385 (2020).
87. Zhang, X. *et al.* Nanocomposite Membranes Enhance Bone Regeneration Through Restoring Physiological Electric Microenvironment. *ACS Nano* **10**, 7279–7289 (2016).
88. Glasser, A., Cloutet, E., Hadziioannou, G., Kellay, H. & Cloutet, É. Tuning the rheology of polymer conducting inks for various deposition processes. doi:10.1021/acs.chemmater.9b01387ï.
89. Lee, J., Byeon, J. & Lee, C. Theories and Control Technologies for Web Handling in the Roll-to-Roll Manufacturing Process. *Int. J. Precis. Eng. Manuf. Technol.* **7**, 525–544 (123AD).
90. Park, J., Shin, K. & Lee, C. Roll-to-Roll Coating Technology and Its Applications: A Review. *Int. J. Precis. Eng. Manuf.* **17**, 537–550 (2016).
91. Krebs, F. C., Gevorgyan, S. A. & Alstrup, J. A roll-to-roll process to flexible polymer solar cells: model studies, manufacture and operational stability studies † ‡. *J. Mater. Chem.*

19, 5442–5451 (2009).
92. Ney, L. *et al.* Optimization of fine line screen printing using in-depth screen mesh analysis. *AIP Conf. Proc.* **2156**, 20007 (2019).
93. Potts, S.-J. *et al.* High-speed imaging the effect of snap-off distance and squeegee speed on the ink transfer mechanism of screen-printed carbon pastes. *J. Coatings Technol. Res.* **17**, (1998).
94. Lin, H. W., Chang, C. P., Hwu, W. H. & Ger, M. Der. The rheological behaviors of screen-printing pastes. *J. Mater. Process. Technol.* **197**, 284–291 (2008).
95. Riemer, D. E. The Theoretical Fundamentals of the Screen Printing Process. *hybrid circuits* **18**, (1989).
96. Iliopoulos, I. & Scriven, L. E. A blade-coating study using a finite-element simulation. *Phys. Fluids* **17**, 127101 (2005).
97. Hwang, S. S. Non-Newtonian Liquid Blade Coating Process. *J. Fluids Eng.* **104**, 469–474 (1982).
98. Khaliq, S. & Abbas, Z. Theoretical analysis of blade coating process using simplified Phan-Thien-Tanner fluid model: An analytical study. *Polym. Eng. Sci.* **61**, 301–313 (2021).
99. Davard, F. & Dupuis, D. Flow visualisation experiments in a blade coating process. *J. Nonnewton. Fluid Mech.* **93**, 17–28 (2000).
100. Nallan, H. C., Sadie, J. A., Kitsomboonloha, R., Volkman, S. K. & Subramanian, V. Systematic Design of Jettable Nanoparticle-Based Inkjet Inks: Rheology, Acoustics, and Jettability. *langmuir* **30**, 13470–13477 (2014).
101. Soleimani-Gorgani, A. *Inkjet Printing*. *Printing on Polymers: Fundamentals and Applications* (Elsevier Inc., 2015). doi:10.1016/B978-0-323-37468-2.00014-2.
102. Tekin, E., Smith, P. J. & Schubert, U. S. Inkjet printing as a deposition and patterning tool for polymers and inorganic particles. *Soft Matter* **4**, 703–713 (2008).
103. Xu, D. *et al.* Inkjet printing of polymer solutions and the role of chain entanglement. *J. Mater. Chem.* **17**, 4902–4907 (2007).
104. Du, Z., Yu, X. & Han, Y. Inkjet printing of viscoelastic polymer inks. *Chinese Chem. Lett.* **29**, 399–404 (2018).
105. Derby, B. Inkjet printing of functional and structural materials: Fluid property requirements, feature stability, and resolution. *Annu. Rev. Mater. Res.* **40**, 395–414 (2010).
106. Haque, R. I. *et al.* Inkjet printing of high molecular weight PVDF-TrFE for flexible electronics. *Flex. Print. Electron.* **1**, (2016).
107. Liu, Q. *et al.* Enhanced pseudo-piezoelectric dynamic force sensors based on inkjet-printed electrostrictive terpolymer. *Org. Electron.* **67**, 259–271 (2019).
108. McGinn, C. K. *et al.* Formulation, printing, and poling method for piezoelectric films based on PVDF-TrFE. *J. Appl. Phys* **128**, 225304 (2020).
109. Alique, M. *et al.* Controlled poling of a fully printed piezoelectric PVDF-TrFE device as a multifunctional platform with inkjet-printed silver electrodes. *J. Mater. Chem. C* **10**, 11555–11564 (2022).
110. Gonçalves, S. *et al.* Environmentally Friendly Printable Piezoelectric Inks and Their Application in the Development of All-Printed Touch Screens. *ACS Appl. Electron. Mater.* **1**, 1678–1687 (2019).

111. Migliorini, L., Villa, S. M., Santaniello, T. & Milani, P. Nanomaterials and printing techniques for 2D and 3D soft electronics. *nano Futur.* **6**, (2022).
112. Kipphan, H. Handbook of Print Media. *Springer* 1207 (2014).

CHAPTER 2:

Correlation between solvation, chain conformation, and rheological behavior for P(VDF-TrFE)

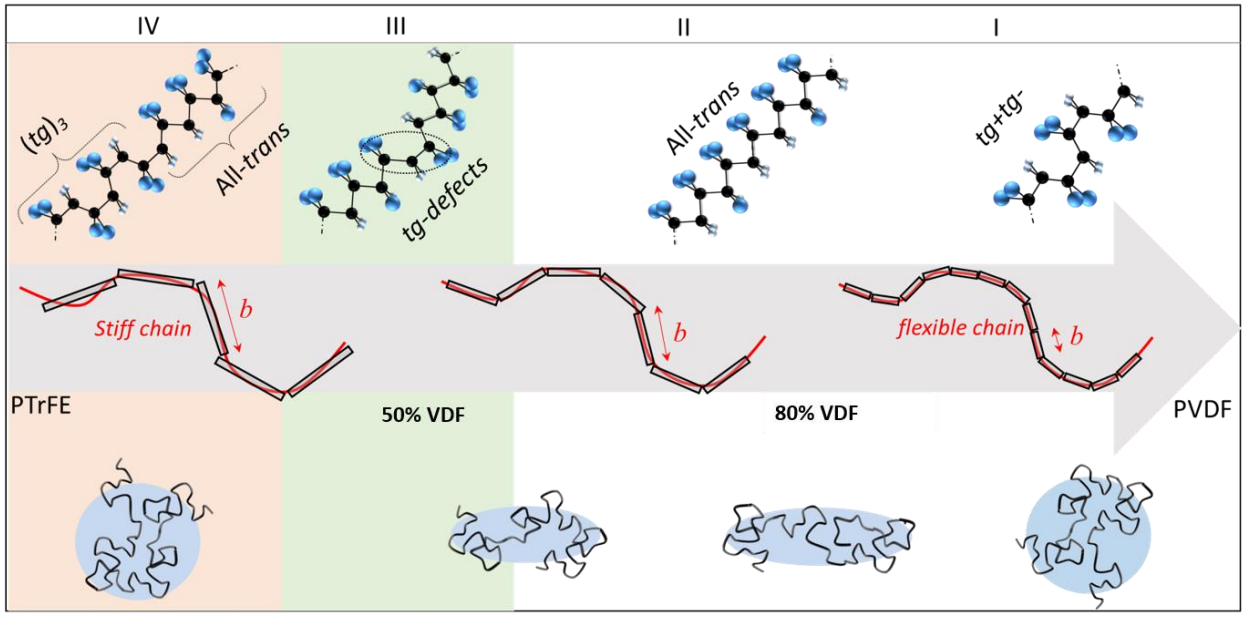

Chapter 2: Correlation between solvation, chain conformation, and rheological behavior for P(VDF-TrFE)

The correlation between solvation, chain conformation, and rheological behavior for P(VDF-TrFE) is a complex interplay that involves understanding how the polymer interacts with the solvent, how these interactions influence the conformation of the polymer chains, and how these factors collectively impact the rheological properties of the polymer solution. This intricate relationship is crucial for gaining insights into the polymer behavior in solution, which, in turn, can have implications for various properties, in particular dielectric properties, and processing techniques.

2.1. Concepts of physical-chemistry of polymers in solution

2.1.1. Polymer chain conformation: ideal chain versus real chain

In order to anticipate the results of this chapter, conceptual notions of polymer physics have to be introduced.[1–3] The conformation of a single polymer chain can be defined following two main paradigms: the ideal chain and the real chain.

An ideal chain, also known as a freely-jointed chain, serves as a fundamental model for describing polymer conformation. This model posits that the monomers within a polymer are positioned akin to the steps of a hypothetical random walker that does not retain memory of its previous steps. By disregarding interactions among monomers, this model assumes that two or more monomers can occupy the same location. The path of the ideal chain is then comparable to a random walk. This chain behavior can be obtained through thermal compensation at the theta temperature in solutions or melts. Such description is usually modelled as a succession of N statistical segments with a precise length, the so-called Kuhn length, b. The mean square end-to-end

distance of the polymer chain is then expressed as follows: $\langle R^2 \rangle = Nb^2$, and the mean square radius of gyration, R_g, representing the average square distance from all monomers to the center of mass of the polymer is then deduced as:

$$\langle R_g^2 \rangle = Nb^2/6 \qquad \text{(II.1)}$$

In the case of a real polymer chain, the constituent monomers interact with each other, behaving as hard cores that cannot be interpenetrated. This characteristic gives rise to a hard-core repulsion between adjacent monomers within the chain. This behavior is related to the concept of excluded volume, and the excluded volume, v, for a spherical Kuhn monomer is then written as $v = b^3$. The chain follows thus a self-avoiding walk on a lattice due to the excluded volume effect.

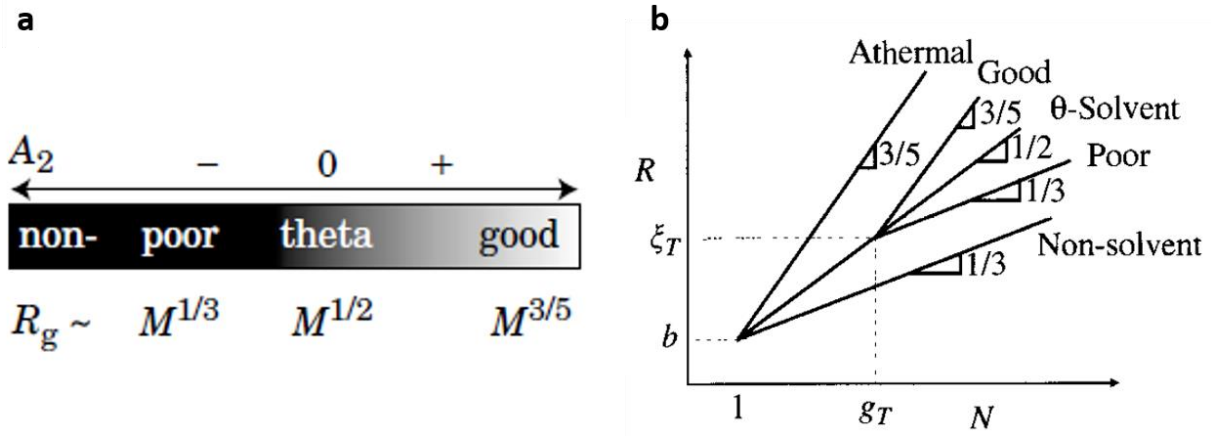

***Figure 28**. (a) Second virial coefficient corresponding to a solvent quality and the power law linking the gyration radius with the molar mass with the Flory exponent reproduced from Teraoka.[1] (b) Evolution of the polymer size as a function of the degree of polymerization in solvents of different quality and the scaling exponent associated reproduced from Rubinstein & Colby.[2]*

Notably, the interactions between solvent and polymer (macro)molecules have a huge contribution to the conformation of the polymer chain. This can be described thermodynamically with the so-called solvent quality that considers the second virial coefficient, A_2, described by the Flory-Huggins mean field theory. Poor solvent quality describes polymer–solvent contacts that become unfavorable ($A_2 < 0$) and can even lead to the precipitation of the polymer chains. On the other hand, good solvent quality exhibits favorable polymer-solvent contacts ($A_2 > 0$). One last case is

when the chain behaves like an ideal chain in solution ($A_2 = 0$) and the solvent can be considered as a theta solvent with equal interactions between polymer repeating units and solvent molecules (**Figure 28**).

Accordingly, the Flory mean-field theory predicts that the polymer size, R, is linked with the number of repeating units through a power law, $R = N^{\nu}$, in which ν is the Flory exponent, representative of the solvent interactions: $\nu = 0.588$ for a good solvent, $\nu = 0.5$ for a theta solvent, and $\nu = 1/3$ for a bad solvent.

- If the attraction between monomers balances the repulsions from the hard cores, the chain can be considered ideal and the excluded volume, v, is equal to zero. These conditions are fulfilled at the θ conditions, *i.e.* at a θ-temperature for a given solvent, and we retrieved the scaling law of an ideal chain:

$$\langle R^2 \rangle = Nb^2 \qquad (II.2)$$

- Provided that the monomer interactions are weaker than the hard-core repulsions, the polymer chains experience swelling, and the excluded volume, v, is greater than zero. This case is representative of a good solvent and it is then possible to express the size of the chain as:

$$R \approx b(\mathrm{v}/b^3)^{2\nu-1}N^{\nu} \approx b(\mathrm{v}/b^3)^{0.18}N^{0.588} \qquad (II.3)$$

- Presuming that the monomer interactions are stronger than the hard-core repulsions, the chain collapses into a dense packing of thermal blobs and the excluded volume is negative. This case is representative of a poor solvent for which the size of the polymer chain is:

$$R = |\mathrm{v}|^{-1/3}b^2N^{1/3} \qquad (II.4)$$

- Equal interactions between monomer/monomer and monomer/solvent are the case of an athermal solvent. In this case, only hard-core repulsions exist and the excluded volume is temperature-independent such as:

$$R = bN^{3/5} \qquad (II.5)$$

2.1.2. Scaling model of a real chain, notion of blobs and influence of the concentration regimes

The main concept behind a scaling approach is to separate a system depending of different length scales. For polymer chain statistics, it is based on the definition of blobs with length scale, ξ, for which the interaction energy between blobs are of the order of the thermal energy kT. On length scale smaller than the blob size, the interactions are negligible and the chain segments contained in the blob behave with unperturbed statistics (ideal chains). On length scale higher than the blob characteristic size, the interaction energy is larger than the thermal energy and the polymer conformations are dictated by interactions. The thermal blob size, ξ_{th}, and the number of monomers in a thermal blob, g_{th}, can be related to the excluded volume, v, such as $\xi_{th} = b^4/|v|$ and $g_{th} = b^6/v^2$. Accordingly, a system can be described based on the evolution of a unique variable, the correlation length, ξ, which defines the distance for which all the interactions of a chain segment are screened from other chains. This length is directly linked to the dimension of the so-called correlation blob. This formalism leads to the representation of a polymer chain *via* a hierarchical blob structure which represented the chain conformation in a solvated state (see **Figure 29**). Accordingly, the size of the correlation blob is closely linked to the concentration of a polymer in solution, and consequently to its viscosity.

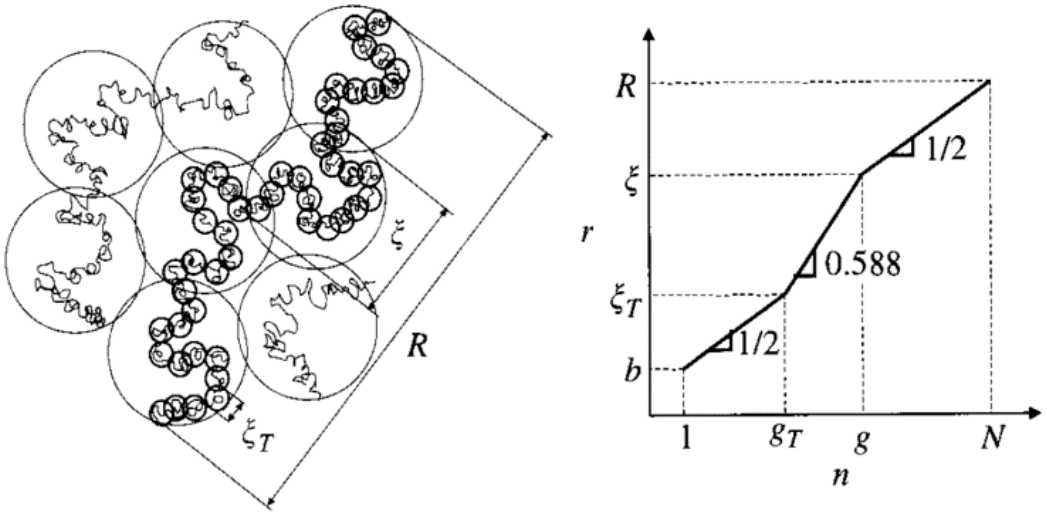

***Figure 29**. Schematic representation of the hierarchical structure of a chain in semi-dilute solution in a good solvent. The plot represents the scaling of the end to end distance r with the number of monomers "n" in a subsection of a chain in a good solvent reproduced from Rubinstein & Colby.[2]*

In the dilute regime, the polymer chain can be considered as a single particle describe by an excluded volume, v. The conformation of a single chain in solution within the dilute concentration regime will directly be dictated by the polymer-solvent interactions and behave as an ideal or a real-chain.

As the polymer concentration increases in the solution, the polymer chains have "less space" and the excluded volume, v, of the chains begins to overlap at a critical concentration, $c = c^*$. This critical concentration marks the transition from a dilute regime to a semi-dilute one where most interactions are represented by a self-avoiding walk. The scaling approach further developed consists in comparing the length, ξ, to the length, $\xi_{th} = b g_{th}^{1/2}$, for which the interactions are at the order of the thermal energy kT. If $\xi < \xi_{th}$, the interactions (mostly excluded volume interactions) are weaker than the thermal energy and the chain behaves as real chains in a self-avoiding walk conformation.

As the concentration further increases, the chains become more densely packed, and the correlation blob is then comparable to the size of the thermal blob. The thermal blob is the minimum volume in which the chain is composed of g_{th} monomers and the chain behaves as ideal

(only subjected to kT), thus highlighting the dominance of solvent-polymer interactions. The critical concentration in question can be identified as a $c = c_{th}$, a concentration in which the thermal blobs overlap but are still in the dilute regime. In this regime, the chain segments inside the correlation blob closely follow an ideal chain statistics and only solvent-polymer interactions are screened.

Next, by increasing further the concentration to $c = c^{**}$, the polymer chains become so densely packed that the correlation length, ξ, is comparable to the Kuhn length, *b*. This marks the transition to a concentrated regime and the description of the chains as "*rod-like*". Furthermore, this description is inherent to the formation of entanglements above c^{**}.

The variation of correlation length, ξ, can then be expressed for the various concentration regimes as:

$$\xi = b(\nu/b)^{2\nu-1}g^{\nu} \qquad (II.6)$$

with g the number of monomers per correlation blob, g can be further derived as:

$$g = (b^3/\nu)^{3(3\nu-1)/(3\nu-1)}c^{-1/(3\nu-1)} \qquad (II.7)$$

The scaling exponents for the three different concentration regimes are 0.558, 0.5, and 1 for the self-avoiding walk, random walk, and rod-like chain behaviors, respectively (see **Figure 30**b). According to the interactions with the solvent, the variation of the correlation length can be written as follow for the Semi-dilute and concentrated regimes in good solvent:

$$\xi = b\,(b^3/\nu)^{(2\nu-1)/(3\nu-1)}\,c^{-\nu/(3\nu-1)} \qquad (II.8)$$

and $\xi = b / c$ in θ-solvent

The evolution of the chain conformation with concentration in polymeric systems has been widely used through the years to characterize solvent quality. Viscosity, light scattering (LS), and osmometric measurements, which probe the polymer conformation in solution, are accordingly valuable tools in order to link polymer-polymer and polymer-solvent interactions.[4–11]

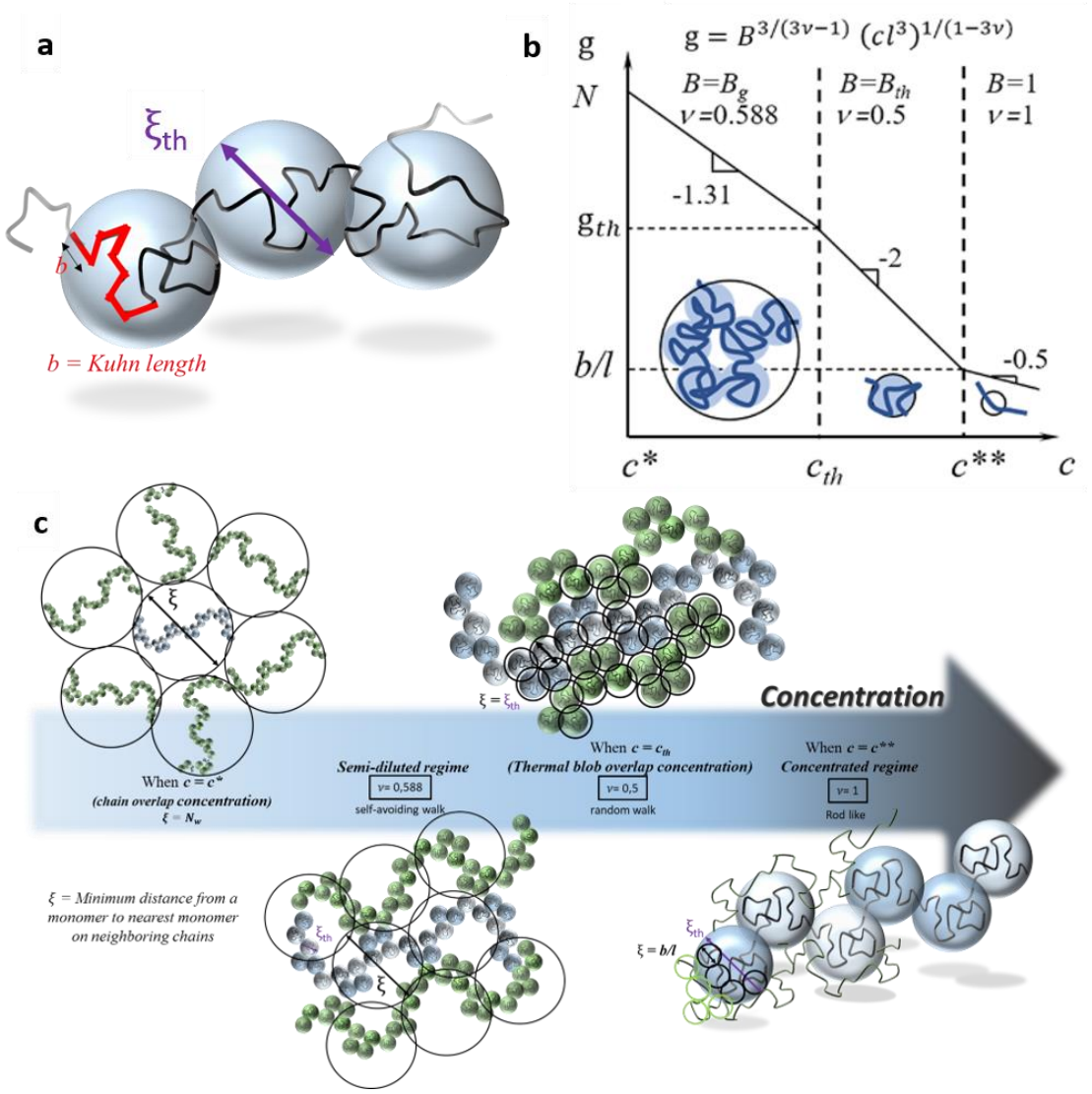

***Figure 30**. (a) Schematic representation of a part of a single polymeric chain composed of a finite number of Kuhn segments of length b and excluded volume of a diameter ξ_{th}. (b) Variation of the size of the correlation blob as a function of the concentration with the slopes representing the scaling exponents reproduced from Dobrynin et al.[4] (c) Graphical representation of the evolution of the correlation length, ξ, as a function of the concentration.*

2.1.3. Polymer Chain Dynamics

In solution, the polymer chains diffuse according to their interaction with solvent molecules and polymer molecules on their surroundings. A way to represent the dynamics of the solutions can be conceptualized by the Zimm and Rouse models.

For the Rouse model, The polymer chain can be represented by beads connected to each other by springs where only thermal agitation and drag forces affect chain dynamics (**Figure 31**a). In this model, there are no excluded interactions between the beads.

In order to take in account interactions mediated by the solvent, the Zimm model can be used as an extension of the Rouse model with the same setup, here the beads are coupled by hydrodynamic interactions. In the dilute regime, the Zimm model is applied and hydrodynamic interactions prevail. In this representation, the motion of the beads is closely linked to the motion of the solvent and the other monomers. As a result, solvent and polymer chains have the same motion.

In the semi-dilute regime, at a length scale larger than the correlation blob, the chain relaxes by a Rouse motion whereas inside the correlation blob, the Zimm relaxation is dominant.

At relatively high concentrations, chains packed together cannot cross each other constraining the motion of a chain to a tube. This tube can be described by a diameter a and is related to the number of monomers in an entanglement strand, N_e, with $a = bN_e^{1/2}$. The motion of this tube is described the reptation theory and consists of a linear Rouse motion along the reptation tube (**Figure 31**b). The viscosity of such a system is then defined for a bulk system as:

$$\eta = KM_w^{3.4}. \qquad \text{(II.9)}$$

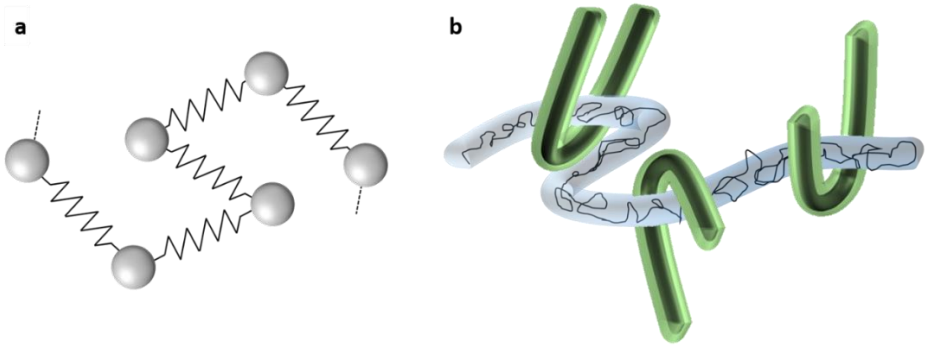

***Figure 31**. (a) Representation of the Rouse model and (b) the reptation tube imposed by entanglements with surrounding chains.*

2.2. Literature overview of the solvation behavior of PVDF-based polymers

PVDF is already used in many applications requiring the use of formulated inks. For instance, membrane formation by inverse phase separation and electrospinning are one of its prime applications. Considering the mechanism involved during their fabrication, several studies aimed to describe the behavior of PVDF in the solvated state. Bottino *et al*.[12] first determined the solubility region of the polymer by using the Hansen cohesive parameters (**Figure 32**a).[13] This first approach led to further studies establishing the impact of the use of different solvent polarities and mixtures, temperatures, and concentrations on the membranes morphologies and architectures prepared by phase inversion[14–16] or electrospinning.[17] In the **Figure 32**c, membranes produced with different solvents are shown. The amount of β phase crystallinity for the different membranes was associated with the decrease of the Hansen solubility values, raising interest in the impact of the solubility of the polymer on the crystallization process. The morphology of the pores was also found to be link to the crystalline structure of the material as the porous superstructure is mainly composed of aggregated spherulites[18] caused by the formation of β phase crystallites.[19] As shown in **Figure 32**c, the solubility is ranked as higher for TEP, then decreases for the DMF, TMP, and HMPA and corroborates the previous statements. Here, the presence of aggregates is linked to the lack of solubility. More aggregation and β crystallinity are then found for a lower solubility and further confirmed by FTIR with the presence of the 840 cm^{-1} peaks (**Figure 32**d).

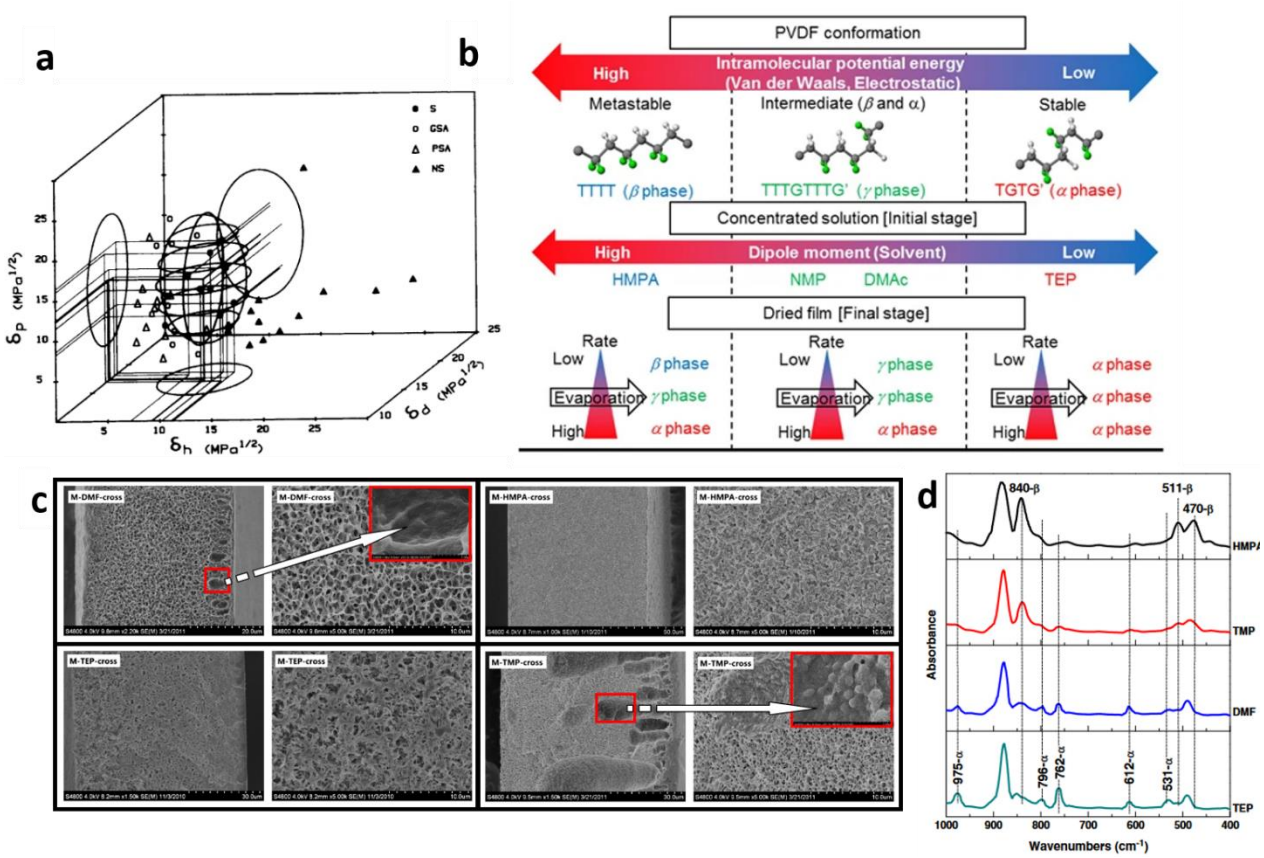

***Figure 32**. (a) PVDF Hansen solubility region represented in the 3D Hansen space reproduced from Bottino et al.[12] (b) Correlation between polymer–solvent interactions and solvent evaporation rates with the PVDF crystalline structures reproduced from Nishiyama et al.[20] (c) SEM images (top and cross-section) of membranes produced with phase inversion in water using DMF, TEP, HMPA, and TMP as solvents and (d) FTIR spectra of the different fabricated membranes with the different solvents reproduced from Tao et al.[18]*

Due to the structure/electroactivity relationships, many studies attempted to establish a correlation between solvent media and crystalline ordering in the deposited material.[20–22] All these studies put in evidence the influence of the solvent interactions on the polymeric chain molecular arrangement, and roughly attributed the changes to the evaporation rate and the dipolar moment of the solvent. According to Nishiyama *et al.*[20] (**Figure 32**b), a solvent with a low dipolar moment will exhibit minimal interaction with the polymeric chain. The chain will consequently be in a shrunken globule state, leading to a twisted chain conformation (α phase). On the other hand, the content of β and γ phases were shown to be dependent on the evaporation rate,

and a slower evaporation led to a majority of β phase for high dipolar moment solvent. Accordingly, the mobility of the chain is a crucial parameter to drive the crystallisation of the PVDF chains towards an electroactive crystalline phase. Nevertheless, it is noteworthy that the effect of the solvent polarity can be overwritten by thermal treatment, often used for the preparation of PVDF films.

Only a limited number of studies provide an in-depth understanding of the chain conformation and behavior of solvated PVDF chains.[23–28] Notably, the work conducted by Lutringer and Weill[23,24] stands out for its direct exploration of polymer-solvent interactions, employing light scattering and viscometric experiments across various molar masses of PVDF in different solvents. This approach enabled the extraction of key parameters such as the mean square of the radius of gyration, intrinsic viscosity, and the second virial coefficient for different systems. The values obtained varied depending on the solvent system, with lower intrinsic viscosity, radius of gyration, and virial coefficient indicating a system behaving in a lower-quality solvent. In **Figure 33**, the variation of these three parameters as a function of the molar mass for the different solvent systems illustrates the previous observations with $< S_r^2 >^{1/2}$, $[\eta]$, A_2 representing the mean square gyration radius, the intrinsic viscosity and the second virial coefficient, respectively. With this methodology, a classification of the different solvents from poor to good is then possible, *i.e.* DMSO < DMF < DMAc < NMP ≈ HMPT ≈ DMPU, with DMSO appearing very close to a θ solvent.

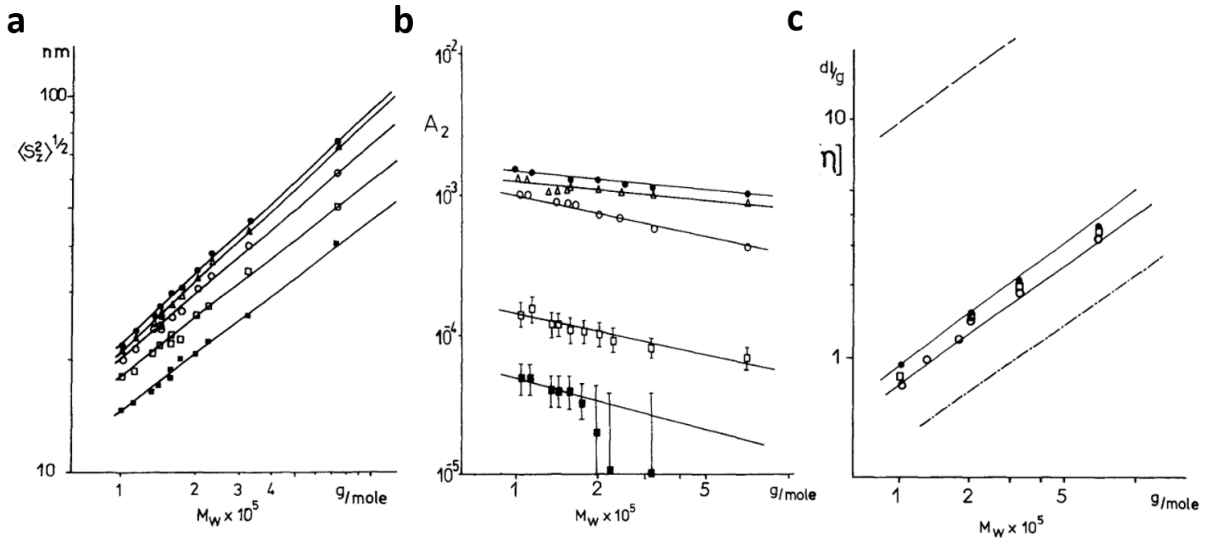

***Figure 33**. Representation of (a) the mean square gyration radius $< S_r^2 >^{1/2}$, (b) the second virial coefficient A_2, and (c) the intrinsic viscosity $[\eta]$, as a function of the PVDF molar mass in various solvents: (●) DMPU, (■)DMSO, (Δ) NMP, (○) DMAc, and (□) DMF. Reproduced from Lutinger and Weill.*[23]

Another recurrent point for PVDF systems is the aggregation, microgel formation, and superstructures that can be triggered by an inappropriate choice of solvents.[25–28] The recent work of Nohara *et al.*[25,26] demonstrated the formation of superstructures in NMP such as rectangular columnar particles. Superstructured aggregates in solution have also been identified during the fabrication of PVDF films,[29] creating defects acting as nucleation points for the generation of a specific crystalline phase.[19] The formation of the insoluble polymer fraction in the case of microgels was also related to the number of defects in the chain sequence occurring during the polymerization process. Indeed, PVDF samples forming microgels are characterized not only by a slightly higher fraction of reverse head-to-head addition but also by a higher probability of not repairing a reverse addition defect by an adjacent tail-to-tail addition.[24]

P(VDF-TrFE) has also been used for the fabrication of membranes, and similar trends as the ones observed for PVDF were demonstrated. In Figure 7, electrospun membranes fabricated from different solvents are shown. The solvent impacts the overall morphology with polar solvents lowering the characteristic size of the structure and increasing β phase content. The solution concentration is also seen to affects the morphology of the membranes. **Figure 34**, shows a

clear modification of the morphology, by a thickening of the fibers composing the membranes as the concentration increases.

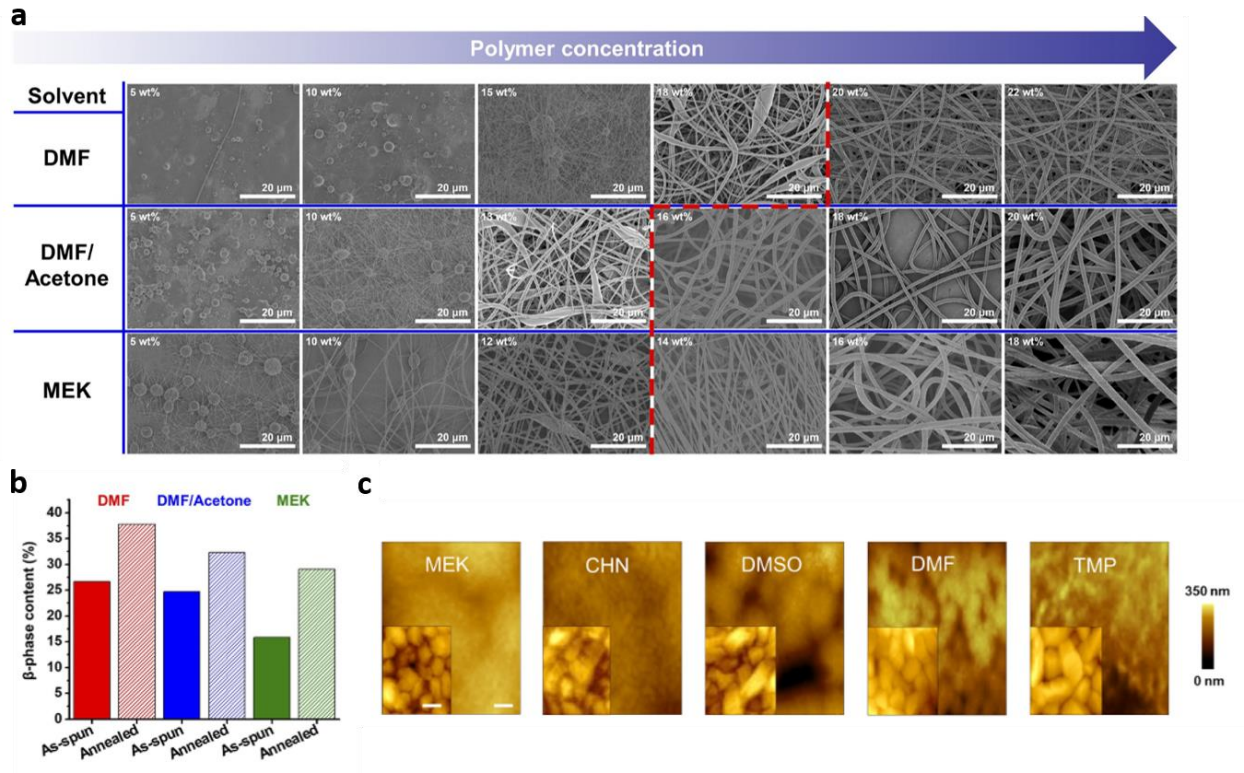

***Figure 34**. (a) SEM images of electrospun membranes as a function of polymer concentration in three different solvents (DMF, DMF/acetone, and MEK), reproduced from Kim et al.[17]; (b) β phase content for as-spun and thermally annealed P(VDF-TrFE) fibers for three different solvents (DMF, DMF/acetone, and MEK), reproduced from Kim et al.[17] (c) AFM images of the P(VDF-TrFE) layers using various solvents of different polarity; scale bar: 1 µm. The inset images are the magnified views; scale bar: 100 nm. Reproduced from Sekine et al.[30]*

2.3. Impact of the P(VDF-TrFE) composition on the chain conformation

In the previous chapter, we demonstrated the complexity and the challenges inherent to the functional use of PVDF-based materials, in terms of processing and applications. The following chapter is dedicated to the understanding of PVDF-based systems in solution. More precisely, this

approach aims to expand our understanding of P(VDF-TrFE) in solution by evaluating the modification of chain conformation with respect to solvent quality and P(VDF-TrFE) composition. Complementary approaches were first used to determine the compatible solvents in which the polymer is soluble. Using Hansen parameters, light scattering experiments, and viscosity measurements, we will demonstrate that it is possible to elucidate the impact of the composition on the conformation of the polymer chain in solution. These experiments also reveal the existence of a conformational change in the solvated state near a critical TrFE composition of 50 mol.%.

2.3.1. Hansen Solubility Approach

To the best of our knowledge, no study has thoroughly examined the solution behavior of P(VDF-TrFE) systems. Bottino *et al.* evaluated the solubility of the P(VDF) homopolymer using the Hansen methodology. We extended this approach to P(VDF-TrFE) systems with various compositions, *i.e.*, ranging from high molar content of VDF to high molar content of TrFE. The idea is to identify changes in the solubility of the copolymer compared with the P(VDF) homopolymer and to establish a possible correlation between TrFE content and solubility.

In this scope, we selected seven P(VDF-TrFE) copolymer compositions and one P(VDF) homopolymer as a reference. To determine the solubility behavior of these systems, the Hansen methodology was used. It consists of performing solubility tests with a set of predefined solvents. Each solvent is described by three cohesive components, δ_D, δ_P, and δ_H, respectively representing the dispersive, polar, and protic (hydrogen bonding) parts in $MPa^{0.5}$. If the solvent can dissolve the material, the cohesive parameters will have close values between the solvent and the polymer. It is then possible, with an large number of solvents, to represent in the 3D Hansen space the solubility region of the material. In the case of our study, the solubility of the PVDF-based materials was probed for 39 solvents. The solubility of the polymer was sorted as a bad solubilizing solvent for non-transparent solutions, and good solvents for all the transparent solutions. Another state could be observed when using solvents with intermediate behavior, characterized by the "swelling" of the polymer. All the data are summarized in **Table 2**.

***Table 2**. Copolymer compositions and solvents used. δ_D, δ_P, and δ_H are the Hansen solubility parameters. Solubility is represented in a ternary system (1 = soluble, 0 = insoluble, *** = swelling).*

	δ_D	δ_P	δ_H	solubility					
Solvent	***MPa$^{0.5}$***			***80-20***	***83-17***	***70-30***	***50-50***	***43-57***	***21-79***
1,3-dioxolane	18.1	6.6	9.3	1	***	1	1	1	1
1,4-Dioxane	17.5	1.8	9	1	0	1	1	1	1
1-Butanol	16	5.7	15.8	***	0	0	0	***	0
Acetone	15.5	10.4	7	1	1	1	1	1	1
Acetonitrile	15.3	18	6.1	1	0	1	1	1	1
Anisole	17.8	6.7	4.1	***	0	0	0	0	0
Benzaldehyde	19.4	7.4	5.3	0	*NA*	*NA*	*NA*	*NA*	*NA*
Benzonitrile	18.8	12	3.3	0	0	***	***	***	0
Benzyl acetate	18.3	5.7	6	0	0	0	0	0	0
Butoxyethyl acetate	16.2	4.7	9.8	1	0	1	1	1	1
Butyl acetate	15.8	3.7	6.3	***	0	1	1	1	1
γ-Butyrolactone	19	16.6	7.4	1	0	1	1	1	1
Cyclohexanol	17.4	4.1	13.5	0	*NA*	0	0	*NA*	*NA*
Cyclohexanone	17.8	6.3	5.1	1	0	1	1	1	1
Cyclopentanone	17.9	11.9	5.2	1	0	1	1	1	1
Diacetone alcohol	15.8	8.2	10.8	***	0	1	1	1	1
Dichloromethane	17	7.3	7.1	0	0	0	0	0	0
Diethyl carbonate	15.1	6.3	3.5	0	0	1	1	1	1
Diethylene glycol	16.6	12	20.7	0	0	0	0	0	0
Dimethyl acetamide	16.8	11.5	9.4	1	1	1	1	1	1
Dimethyl carbonate	15.5	8.6	9.7	1	0	1	1	1	1
Dimethyl formamide	17.4	13.7	11.3	1	1	1	1	1	1
Dimethyl phthalate	18.6	10.8	4.9	0	0	***	***	0	0
Dimethylsulfoxide	18.4	16.4	10.2	1	1	1	1	1	1
Ethanol	15.8	8.8	19.4	0	0	0	0	0	0
Ethyl acetate	15.8	5.3	7.2	1	0	1	1	1	1
Isopropanol	15.8	6.1	16.4	0	0	0	0	***	0
Isopropyl acetate	14.9	4.5	8.2	0	0	1	1	1	1
Methanol	15.1	12.3	22.3	0	0	0	0	0	0
Methyl ethyl ketone	16	9	5.1	1	0	1	1	1	1
Methylisobutylketone	15.3	6.1	4.1	1	0	1	1	1	1
N−methyl−2−pyrrolidinone	18	12.3	7.2	1	1	1	1	1	1
Propylene carbonate	20	18	4.1	1	0	1	1	1	1
Propylene glycol methylethercetate	15.6	5.6	9.8	1	0	1	1	1	1
Styrene	18.6	1	4.1	0	0	0	0	0	0
Terpineol	17	3.6	7.7	0	0	0	0	0	0
Tetrahydrofuran	16.8	5.7	8	1	0	1	1	1	1
Toluene	18	1.4	2	0	0	0	0	0	0
Triethyl phosphate	16.7	11.4	9.2	1	1	1	1	1	1

This dataset was then implemented into the HSPiP software developed by Hansen, Abbot, and Yamamoto. The solubility sphere is then calculated with an iterative algorithm and is displayed in **Figure 35**.[13]

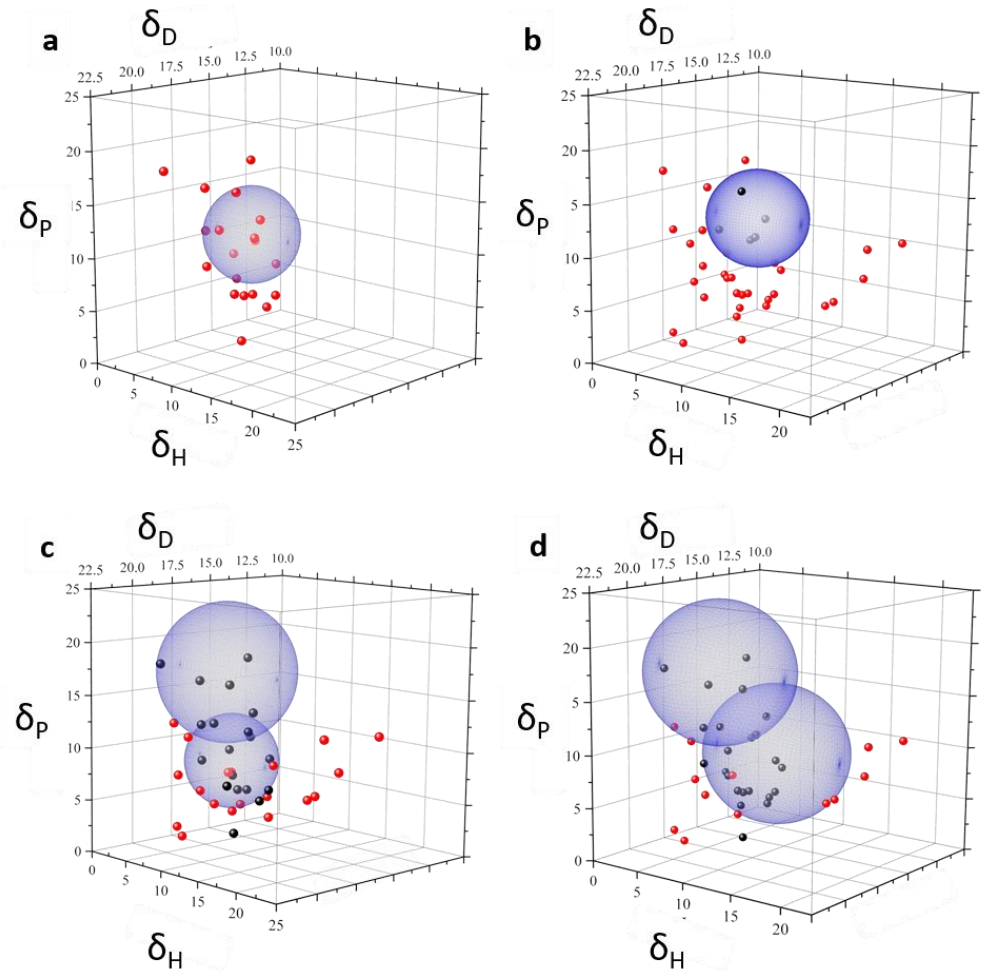

***Figure 35**. Representation of the solubility regions in the 3D Hansen space δ_D, δ_P, and δ_H obtained via the HSPiP software: (a) for P(VDF) obtained from the dataset of Bottino et al.[12], for P(VDF-TrFE) with various compositions, (b) 83-17 (c) 80-20 (d) 75-25 and higher TrFE contents. Black and red dots represent the good and bad solvents, respectively.*

As expected P(VDF) exhibits a narrow solubility region since fluorine atoms in organic molecules depress their ability to establish molecular interactions with solvents.[31] With the addition of TrFE units, no change is noticeable until a critical composition of P(VDF-TrFE)-80:20 where the single solubility region splits into two regions. To strengthen this unconventional double solubility region behavior, the iteration of a unique P(VDF-TrFE)-80:20 solubility sphere in the 3D Hansen

solubility space was also performed by defining its center coordinates (i.e.; δ_D = 14.4, δ_P = 16.7, δ_H = 9 (in $MPa^{0.5}$)), and radius (i.e.; R0 = 11.8) (single sphere presented in annex **FigureS2- 3**). Nevertheless, the resulting "desirability" parameter, d, is low with a value of 0.55. For a fully optimized fitting, the desirability should reach a value of 1, *i.e*., the solubility sphere contains all good solvents while bad solvents are located outside. This observation prompts us to reconsider the relevance of the single-sphere model for the studied materials. Indeed, the chemical nature of electroactive fluoropolymers drives the solubility behavior via two distinct effects. The presence of fluorine atoms with a high electronegativity along the polymer backbone induces a high polarization, which is counterbalanced by a net cancellation of the dipole moments along the polymer backbone inducing a "nonpolar" behavior also known as the fluorophobic effect.[32–35] This complex solubility behavior is retrieved in the 3D Hansen space by the presence of two solubility regions with respective center coordinates (δ_{D1} = 17.5, δ_{P1} = 17.2, δ_{H1} = 7.9 (in $MPa^{0.5}$)) and (δ_{D2} = 16.4, δ_{P2} = 8.2, δ_{H2} = 6.3 (in $MPa^{0.5}$)), and radii R01 = 6.7 and R02 = 4.6. Accordingly, an increased desirability value of 0.92 is retrieved by using a model based on a double sphere. The same methodology was applied to the higher TrFE content copolymers and also resulted in the description of a solubility behavior with two regions. The parameters of the fittings are summarized in **Table 3**. Nevertheless, for compositions with higher TrFE content, the dataset of solvents appears to limit the accurate description of the solubility behavior as more solvents can dissolve the polymer. A larger number of solvents located near this boundary would be a plus for estimating the actual values of the sphere center and radius.

Table 3*. Parameters of the solubility regions for the compositions with δ_D, δ_P, and δ_H center of coordinated of the spheres 1 and 2 with their respective radius R0 and the desirability function d.*

Composition	*δD1*	*δP1*	*δH1*	*R01*	*δD2*	*δP2*	*δH2*	*R02*	*d*
	$MPa^{0.5}$				*$MPa^{0.5}$*				
P(VDF)	17.6	12.3	10.6	4.5					1
P(VDF-TrFE)-83:17	16.7	13.3	9.5	4.6					1
P(VDF-TrFE)-80:20	17.5	17.2	7.9	6.7	16.4	8.2	6.3	4.6	0.92
P(VDF-TrFE)-75:25	18.1	17.5	7.3	6.8	15.3	9.2	9.5	6.7	0.95

This fluorophobic effect resulted in the formation of two solubility spheres is only appearing from the 80:20 critical composition. It is not unremarkable that this effect takes place at the same critical composition where the Curie transition is below the melting temperature in the solid state as shown by Furukawa.[36] This statement guides us to think that the interactions and the conformation of the chain in solution are closely related to the composition of the copolymer and consequently to its properties.

2.3.2. Single chain conformation of P(VDF-TrFE) in DMSO

The solubility of a polymer chain is closely correlated to its molar mass. This is illustrated by polymers exhibiting LCST (lower critical solubility temperature) or UCST (upper critical solubility temperature) behaviors for which the molar mass affects the critical solubility temperature. To consider this contribution, size exclusion chromatography (SEC) experiments were conducted to determine the absolute molar mass by using the refractive index increment *dn/dc* method. To have comparable data between the different systems, a common good solvent, DMSO, was chosen. Indeed, it is a solvent that can easily dissolve all compositions, in a short time, at room temperature.

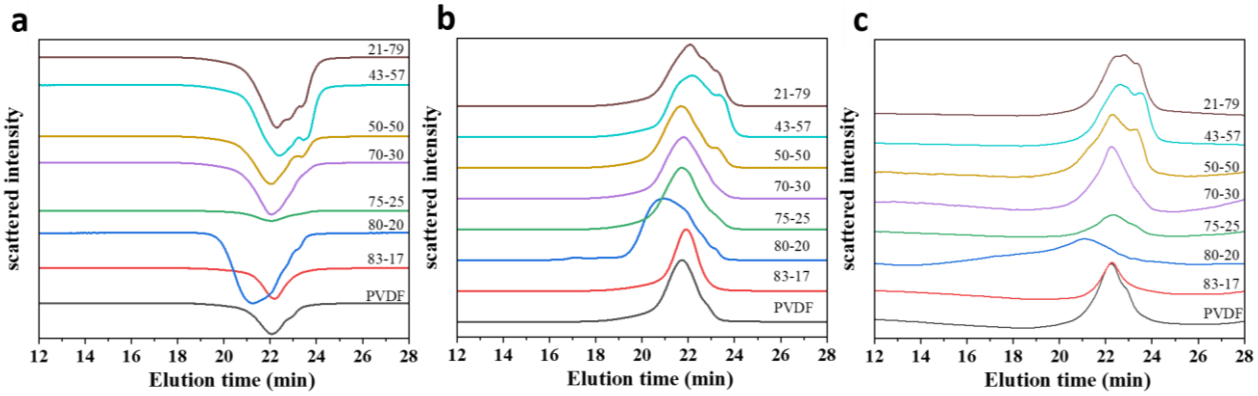

***Figure 36**. SEC chromatograms of the P(VDF-TrFE) copolymers with different compositions in DMSO. Data was collected with the (a) RI detector (b) LS detector and (c) UV detector.*

Figure 36 shows the results obtained for the different compositions in DMSO. The procedure to obtain the absolute molar mass is described in annex **FigureS2- 2**. As a result, the different

molar masses and dispersities are summarized in **Table 4** and **Figure 38**a. All the compositions have comparable molar masses (M_w ≈ 200 kg/mol) and dispersity, except for the 83:17 composition which has a lower molar mass (M_w ≈ 85 kg/mol). Despite this, we can still consider that the solubility behaviors previously established are inherent to the polymer composition, as a lower molar mass should increase the solubility of the polymer.

Using the SEC results, it is also possible to extract the evolution of the gyration radius (R_g), representing the center of mass of a polymeric chain in solution, as a function of their molar mass (**Figure 38**b). Early studies by Benoit and Doty[37] described the impact of the stiffness of the chain on the evolution of the gyration radius with respect to their molar mass. The slopes of the conformational plot (double log plot of R_g *versus* M_w) illustrate the conformation of the chain and its extension. These results on the evolution of the R_g value as a function of the molar mass can be interpreted by using the Mark-Houwink-Kuhn-Sakurada (MHKS) relation $R_g = KM_w^{\alpha}$. The α values stand for the representation of the conformation with the following values: 0.33 corresponds to spheres, 0.5–0.6 to flexible random coils, and 1 to rod-like chains.[38–40]

***Table 4**. Average molar masses in number (M_n) and in weight (M_w), dispersity (Đ), and refractive index increment dn/dc, extracted by SEC for each polymer composition in DMSO.*

Composition	M_n	M_w	**Đ**	***dn/dc***	R_g	α
%VDF:%TrFE	*Kg/mol*			10^{-2}	*nm*	
100	*142.7*	*206.8*	*1.4*	*-5.01*	*21.0*	*0.37*
83:17	*53.8*	*83.7*	*1.6*	*-7.99*	*17.8*	*0.49*
80:20	*183.3*	*206.3*	*1.3*	*-6.68*	*40.7*	*0.6*
75:25	*161.8*	*192.5*	*1.2*	*-7.81*	*29.9*	*0.45*
70:30	*154.0*	*184.8*	*1.2*	*-7.58*	*29.3*	*0.44*
50:50	*219.1*	*206.3*	*1.2*	*-6.41*	*30.7*	*0.43*
43:57	*165.7*	*185.6*	*1.1*	*-7.01*	*26.7*	*0.36*
21:79	*179.3*	*214.6*	*1.2*	*-5.77*	*24.1*	*0.20*

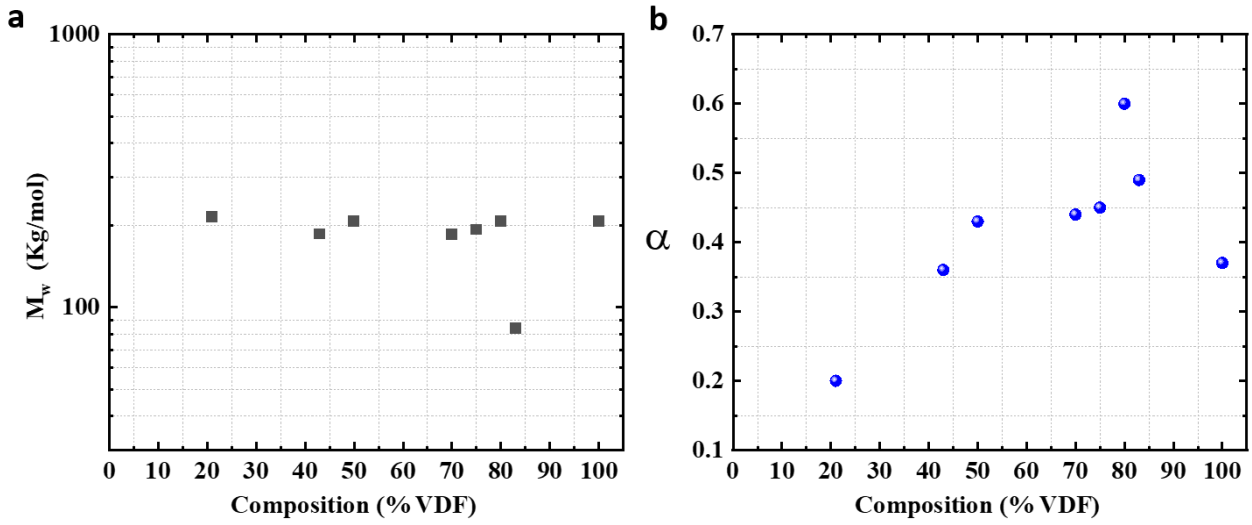

***Figure 37**. (a) M_w and (b) α as a function of the VDF content in mol.% extracted from the SEC traces rectified by the dn/dc method.*

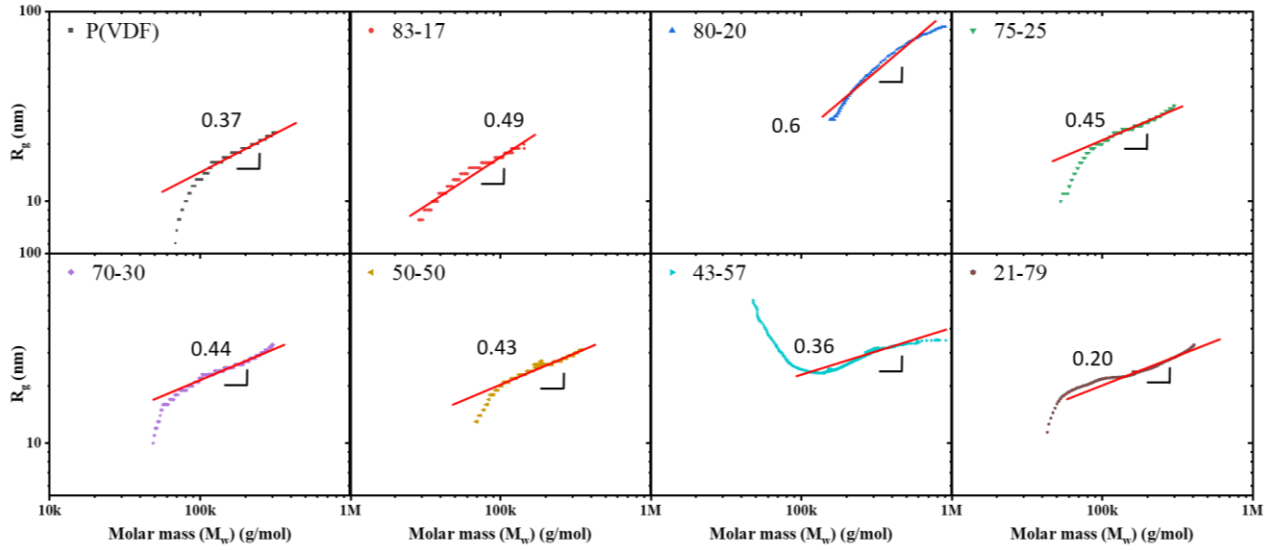

***Figure 38**. Conformational plots: variation of the R_g (nm) as a function of the molar mass for the different compositions. The slopes, α, are extracted from the linear part of the curves in the double log scale representation.*

All the compositions, except the 21:79, displayed slopes with values higher than 0.33, meaning that the copolymer chains behave as flexible random coils in DMSO. Interestingly, this α value is maximum at the 80:20 composition and undergoes a steady decrease while increasing the TrFE amount. This tendency reveals the impact of the composition on the conformation of

the chain. At higher TrFE content (above 50 mol.% TrFE), the chain collapses to more spherical objects. This observation is related to a chain conformational change into a 3/1-helix with the increase of sequence defects which has been recently reported by Resende et al.[41], but is here observable in the solvated state.

The hydrodynamic radius (R_H) was further determined by dynamic light scattering (DLS). This parameter can inform us about the expansion of the chain in the solvent and how this one varies according to the different compositions. From a technical point of view, it is possible to extract R_H by extracting the relaxation time (τ) of the correlation function at one single angle. Nevertheless, we opted to perform multi-angle DLS (MA-DLS), *i.e.*, measurements are performed at various angles allowing the determination of diffusion coefficient (D), by a simple linear regression. **Figure 39**a shows the DLS data performed on the copolymer composition (35:65) and at different angles (from 30° to 150°). From this representation, we can affirm that the object distribution is unimodal as the correlation function is represented by only one population of relaxation times (see **Figure 39**b). Similar measurements were performed on the remaining compositions and are shown in **Figure 39**c (the correlograms for all compositions are presented in annex **FigureS2- 5**). Following the methodology, the relaxation frequency (Γ) extracted for the different compositions is represented in **Figure 39**c, as a function of the scattering wave vector. The R_H of the different compositions in DMSO can be extracted from this representation and are reproduced in **Table 5**. The values of R_H are similar for every composition with an average value around 14 nm. The only exception is for the 83:17 composition for which the R_H value is close to 10 nm. This sudden decrease in size can be attributed to the lower molar mass as attested by the SEC experiments presented previously.

***Table 5**. Summary of the R_H values as a function of the copolymer composition determined by MA-DLS in DMSO.*

Composition *%VDF:%TrFE*	*100*	*83:17*	*80:20*	*75:25*	*70:30*	*50:50*	*43:57*	*21:79*
R_H (nm)	*14.4*	*10.5*	*15.6*	*13.3*	*13.2*	*13.1*	*15.5*	*15.9*

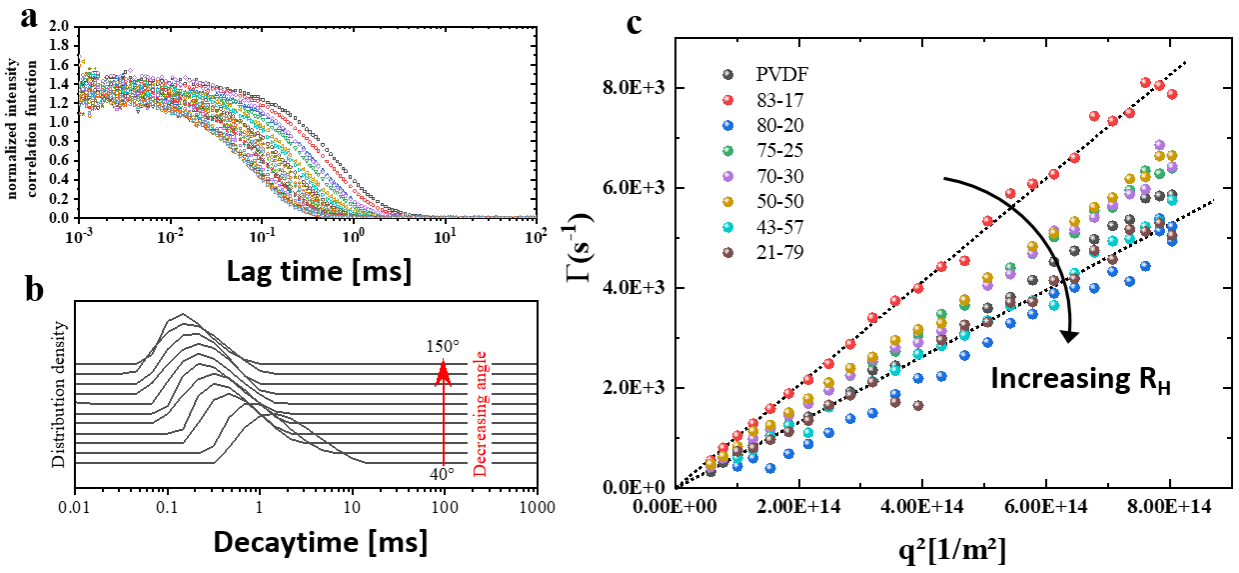

***Figure 39**. (a) Normalized correlation functions as a function of the lag time obtained by MA-DLS for P(VDF-TrFE)-35:65 and (b) the distribution density of the decay time for each diffusion angle. (c) Variation of the frequency of decrease (Γ) as a function of the square of the scattering wave vector (q^2) for the different copolymer compositions. The dotted line represents the linear fitting of the data to extract the parameter D.*

Interestingly, the linear fitting for the 80:20 composition does not pass by the origin. This deviation is due to the dependence of the diffusion coefficient, *D*, following two contributions: the translational (D_T) and rotational (D_R) diffusion coefficients with $D = D_T + D_R$. For a quasi-spherical particle, the rotational part is null and $D = D_T$. This aspect highlights on of the main advantages of MA-DLS compared to the conventional one-angle DLS. In this case, the R_H extracted *via* the Stokes-Einstein relation is intrinsically incorrect and led us to conclude taht the 80:20 polymer chain conformation is non-spherical in DMSO. This further confirms the evolution of R_g with the molar mass obtained by SEC as the high value of the α exponent (0.6) extracted from the conformation plot is representative of an extended random coil.

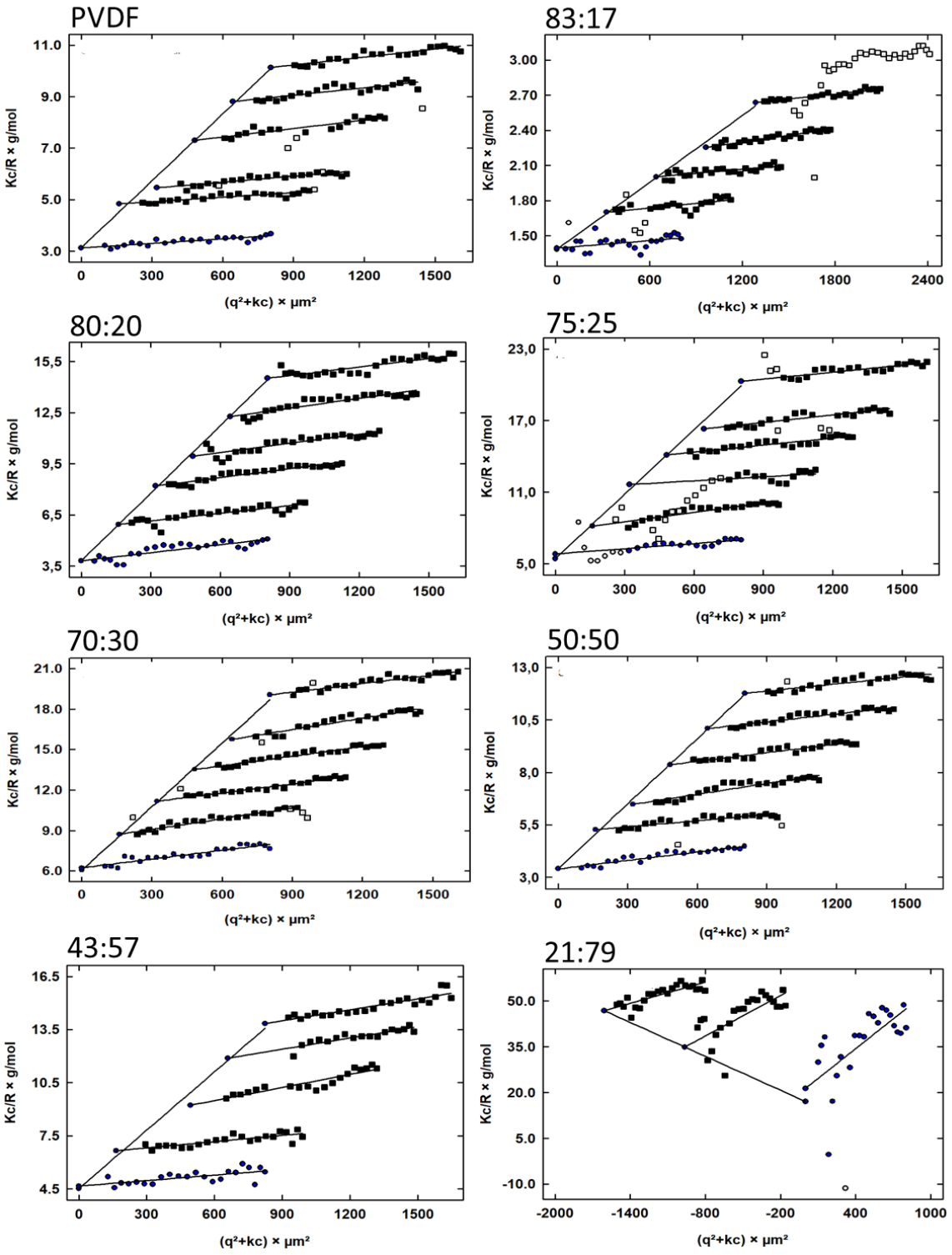

***Figure 40**. (a) Zimm plots extracted from SLS measurements for various P(VDF-TrFE) compositions with 5 concentrations ranging from 1 g/L to 5 g/L in DMSO with (■) measurements at each angle and (●) extrapolated points. The solid lines represent the fittings of the respective datasets.*

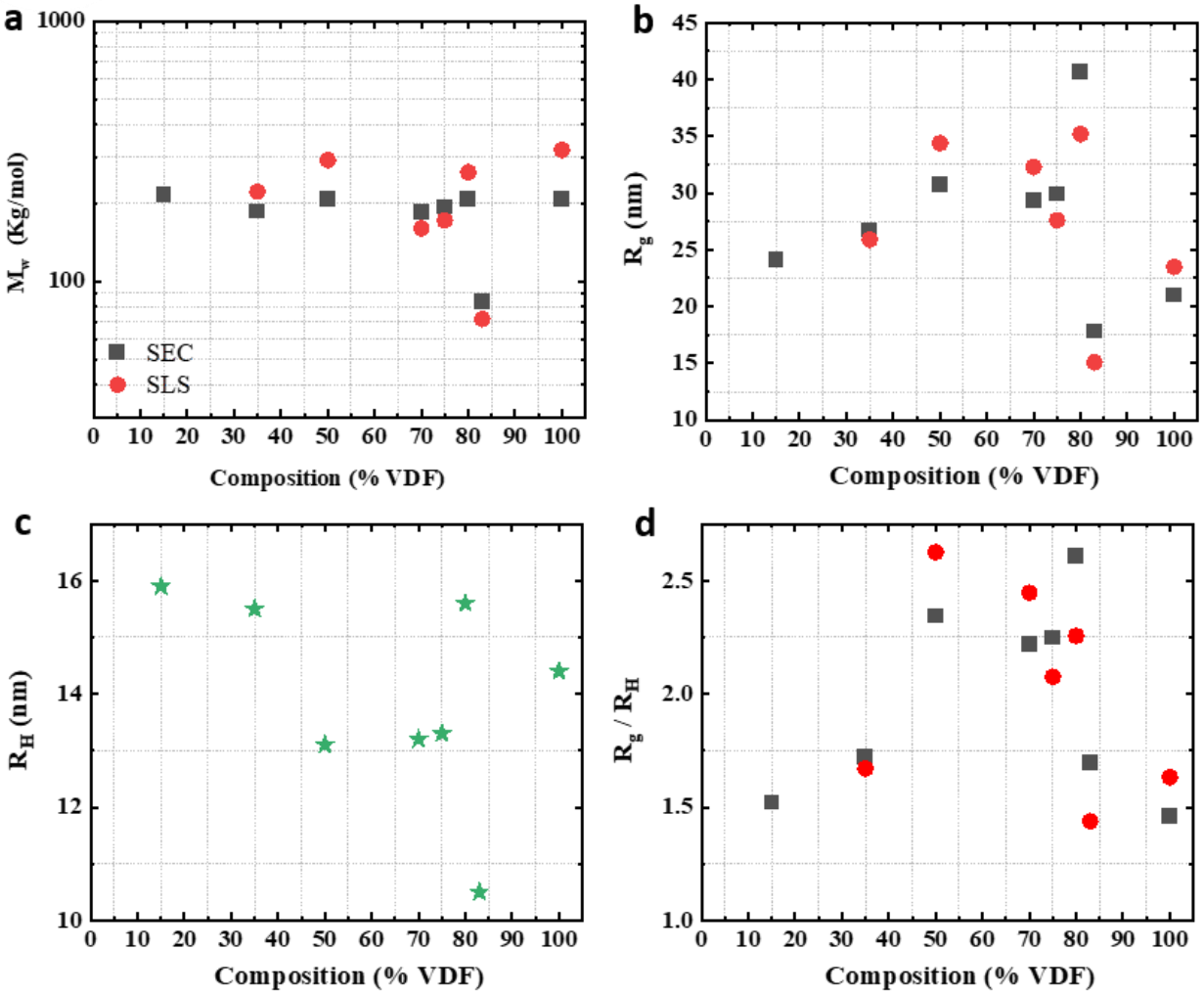

***Figure 41**. Influence of the composition on (a) the molar mass and (b) R_g obtained by (■) SEC and (●) SLS. (c) values of R_H (nm) measured by MA-DLS as a function of the composition in VDF. (d) Variation of the form factor R_g/R_H obtained with (■) SEC and (●) SLS.*

For a full description of the polymer chain conformation in solution, static light scattering (SLS) can provide further information on the polymeric system. By performing SLS, values such as the second Virial coefficient (A_2), M_w, and R_g can be accessed using a Zimm diagram (see **Figure 40**), and these values can be then cross-checked with the values previously determined by SEC. A Zimm diagram consists of extrapolating the values of the scattered intensity, measured for different angles and concentrations, at zero concentration and null angle.

The initial Zimm equation is:

$$\frac{Kc}{\Delta R} = \frac{1}{M_w}\left(1 + \frac{{R_g}^2}{3}\mathrm{q}^2\right) + 2A_2c\ ; \qquad (II.10)$$

Where K is the material constant, c the concentration, M_w the weight averaged molar mass, R_g the radius of gyration, q^2 square of the scattering wave vector, A_2 the second virial coefficient, and ΔR the Rayleigh ratio. At θ = 0, the previous equation becomes:

$$\frac{Kc}{\Delta R} = \frac{1}{M_w} + 2A_2c; \qquad (II.11)$$

and for c = 0 the relation transforms to:

$$\frac{Kc}{\Delta R} = \frac{1}{M_w}\left(1 + \frac{{R_g}^2}{3}\mathrm{q}^2\right). \qquad (II.12)$$

Then it is possible to extract $2A_2$ (q=0), $R_g^2/3$ (c=0), and $1/M_w$ (c=0 and q=0) with the slopes of the different extrapolations represented in **Figure 40**.

To utilize the SLS results for evaluating polymer conformation in solution, the solution must be in a regime where the diffusion of light by the polymer can be attributed to the contribution of a single chain. To meet this criterion, very low concentrations ranging from 1 g/L to 5 g/L were employed, ensuring that the polymer concentration remained below the critical overlap concentration, c* (*vide infra*). These analyses were performed for all polymer compositions and the results are summarized in **Table 8** and **Figure 41**. The molar mass extracted by both SEC and SLS are very similar and are of the same order of magnitude. More discrepancies are observed for the R_g values. Both techniques suggest a maximum value of R_g for the 80:20 composition. Nevertheless, the R_g values strongly depend on the molar mass of the polymeric chain. It is important to consider that the differences observed could mostly be due to the differences in molar masses. Besides, SLS data for the 21:79 composition were inaccessible because of the presence of aggregates that could not be removed through filtration at concentrations higher than 2 g/L.

***Table 6**. Summary of the dimensional parameters extracted from MA-DLS, SEC, and SLS measurements.*

Composition	R_H (nm)	M_w (Kg.mol^{-1})		Rg (nm)		R_g/R_H	
	MA-DLS	SEC	SLS	SEC	SLS	SEC	SLS
PVDF	*14.4*	*206.8*	*319.6*	*21*	*23.5*	*1.46*	*1.63*
83:17	*10.5*	*83.7*	*71.7*	*17.8*	*15.1*	*1.70*	*1.44*
80:20	*15.6*	*206.3*	*262.7*	*40.7*	*35.2*	*2.61*	*2.26*
75:25	*13.3*	*192.5*	*171.6*	*29.9*	*27.6*	*2.25*	*2.08*
70:30	*13.2*	*184.8*	*159.9*	*29.3*	*32.3*	*2.22*	*2.45*
50:50	*13.1*	*206.3*	*292.8*	*30.7*	*34.4*	*2.34*	*2.63*
43:57	*15.5*	*185.6*	*221.4*	*26.7*	*25.9*	*1.72*	*1.67*
21:79	*15.9*	*214.6*	*NA*	*24.1*	*NA*	*1.52*	*NA*

The influence of molar mass on R_g can be circumvented by considering the ratio $\rho = R_g/R_H$, also called the form factor, that can be linked to the shape of a particle in solution. In our study, ρ is superior to unity which is usually associated with elongated objects or extended flexible random coil particles. The overall variation of the form factor with composition can be described as follows: for high VDF content, the form factor goes from a value of 1.5 to 2.5 at the critical composition of 80 mol.% of VDF, then ρ remains almost constant at a value above 2 until the composition of 50 mol.% of VDF where it experienced a drop to values around 1.5. The question of whether such variation in the shape of the polymer chain in solution can be attributed to the defects and modification of tacticity introduced by the addition of TrFE is thus of high interest.

When TrFE units are added to the VDF sequence and reaches values higher than 20 mol.%, the form factor is above 2. As discussed in Chapter 1, the intrinsic ferroelectric properties observed in P(VDF-TrFE)80:20, in comparison to neat PVDF, are attributed to the steric hindrance introduced by TrFE units. This hindrance prompts the polymer chains to adopt an *all-trans* chain conformation. This statement is in agreement with the evolution of the chain expansion extracted from the α coefficient obtained by the SEC experiments as shown in **Figure 38**. After reaching the critical composition of 50:50, ρ and α decrease to reach a more spherical and collapsed conformation that could be linked with the conformational change to a 3/1 helix conformation, recently

reported in literature.[41–43] The observations previously discussed, particularly those related to conformation variations with different solvent polarities, as reported by Nishiyama *et al.*[20], can be reinterpreted in the following manner. Solvents with low polarity were observed to impact the chain in a way that suggested a shrunken conformation, leading to the formation of the *tg+tg-* conformation. Conversely, polar solvents, exhibiting more favorable interactions with the polymer chain, resulted in an expansion of the chain and the formation of the all-*trans* conformation. A similar behavior is observed here, not due to the solvent effect but rather influenced by the composition. The maximal expansion of the chain occurs when the all-*trans* conformation is predominant. As the TrFE content increases, the expansion of the chain diminishes, and beyond the 50 mol.% TrFE composition, the chain collapses in a more spherical shape with fewer interactions with the solvent. The conformational shrinkage leading to the formation of the α-phase observed with solvent polarity can now be associated with a transition in polymer interactions, where composition becomes the primary factor. This transition may correspond to the conversion of the chain conformation into a helical structure, even in the solvated state.

In our study, we have shown that the composition significantly influences interactions with the solvent, consequently affecting chain conformation. Simultaneously, solvent interactions can fine-tune chain stiffness and conformation. Consequently, we anticipate modifications in crystallization behavior and dielectric properties. To enhance our understanding of these interactions and their impact on chain conformation, we employed scaling arguments to establish a "fingerprint" of the chain conformation and quantify polymer interactions in solution.

2.3.3. Fingerprints of P(VDF-TrFE) with different compositions in DMSO using scaling arguments

A scaling approach based on viscosity measurements over a large range of different concentrations can be used to obtain such information. Accordingly, we decided to implement the scaling approach developed recently by Dobrynin *et al.*, which quantitatively ascertains the static and dynamic properties of a polymer/solvent pair from the evolution of solution viscosity in dif-

ferent concentration regimes.[43–47] As reported by the authors, this treatment establishes a polymer/solvent "fingerprint" based on the value of polymer/solvent-specific parameters: B_g - characterizing the conformation of the chains on length scales of the blob size, B_{th} - characterizing the conformation of the chains on length scales of the thermal blob and, P_e - describing the chain packing. These parameters are directly linked to the different concentration regimes (*i.e.*, B_g between the chain overlap concentration, c^*, and the thermal blob overlap concentration, c_{th}; B_{th} between c_{th} and the crossover concentration to the concentrated solution regime, c^{**}; and P_e above c^{**} in the entangled polymer solution regime). Accordingly, this scaling approach extensively describes the scaling relationships between the correlation blob size, ξ, and the number of monomers per correlation blob, g, for polymer chains depending on monomer-monomer and monomer-solvent interactions.[4,5]

The polymer/solvent "fingerprint" can be directly extracted from solution viscosity measurements in the different concentration regimes. **Figure 42**a shows the set of viscosity measurements for the 80:20 composition and its dependence on the concentration. As the concentration of polymer increases, the viscosity at zero shear concomitantly increases. Also, while increasing the concentration, the system goes from a fully Newtonian to a shear-thinning behavior at higher polymer content. As a remark, at high shear, a possible ejection of material from the cone plate geometry can occur, resulting in an abnormally low viscosity. Nevertheless, we decided to report these data to illustrate the behaviour of the different solutions. For all the viscosity measurements, we assess an interval of confidence of viscosity values until a shearing of 300 s^{-1}.

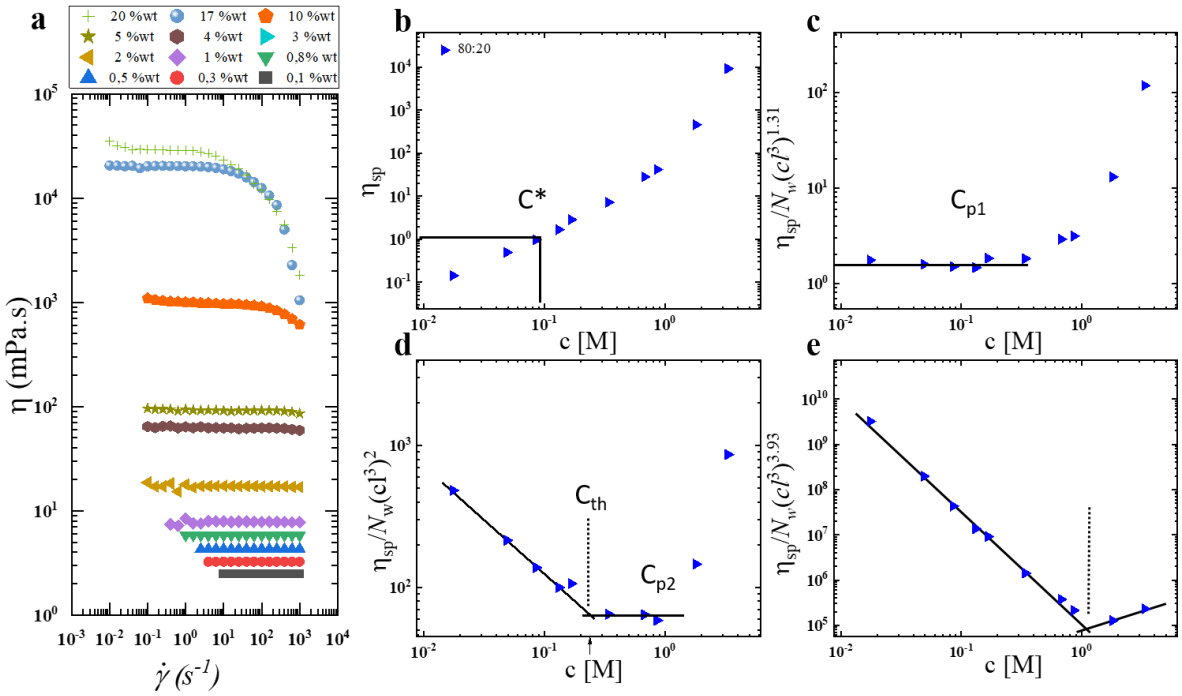

***Figure 42**. (a) Shear-dependent viscosity as a function of the concentration for P(VDF-TrFE)80:20 in DMSO. Influence of the P(VDF-TrFE)80:20 concentration in DMSO for the (b) specific viscosity and normalized specific viscosities according to (c) the self-avoiding walk regime c*<c<c_{th}, (d) the random walk regime c_{th}<c<c**, and (e) the rod-like regime with the respective scaling exponents v = 0.588; v = 0.5; v = 1. Lines represent the graphical determination of parameters such as C_{p1}, C_{p2}, c*, and c_{th} used for the determination of B_g, B_{th}, and P_e.*

Figure 42b-e summarizes the experimental specific viscosity and normalized specific viscosity values according to the concentration regime for the 80:20 composition in DMSO as a function of the monomer concentration. The chain overlap concentration, c*, (*i.e.*, the number of monomers per correlation blob, *g*, is equal to the weight average degree of polymerization, *N*w) was directly extracted from **Figure 42**b; as it is per definition the concentration corresponding to a value of η_{sp} = 1. From the normalized representations displayed in **Figure 42**b-d, the value of the polymer/solvent-specific parameters, B_g and B_{th}, as well as the crossover concentrations, c_{th} and c** were determined and are summarized in **Table 7**. From the representation in **Figure 42**c, the value of the C_{p1} plateau allows to extract B_g from the relationship $B_g = C_{p1}^{-0.255}$. Following, **Figure 42**d allows the extraction of c_{th} and C_{p2} determined with the first crossover and the apparent plateau, respectively. Here, C_{p2} allows the calculation of $B_{th} = Cp_2^{-1/6}$. The final normalization,

as illustrated in **Figure 42**e, serves to confirm that the crossover concentrations obtained are within the Rouse regime. This implies the absence of excluded volume interactions between polymer chains, ensuring that they do not disrupt the concentrated regime.

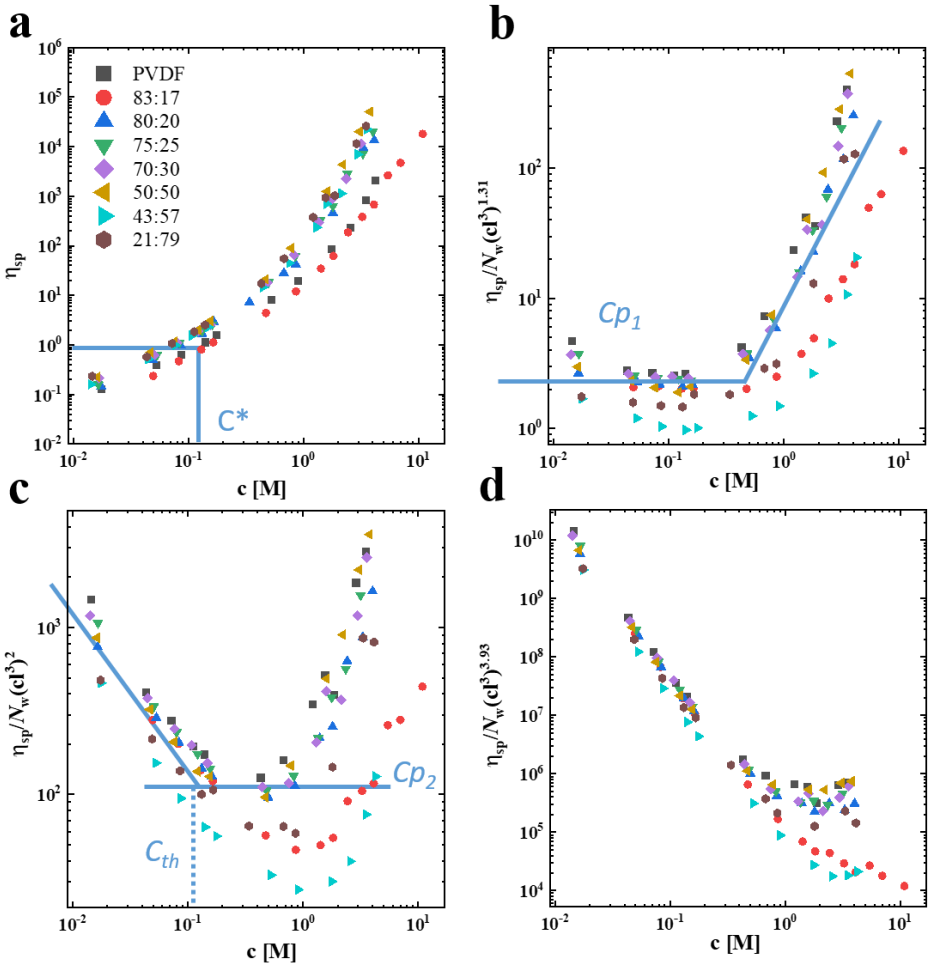

***Figure 43**. Dependence for all copolymer compositions in DMSO of (a) the specific viscosity and the normalized specific viscosities according to (b) a self-avoiding walk regime for $c^* < c < c_{th}$, (c) a random walk regime for $c_{th} < c < c^{**}$, and (d) a rod-like regime with the respective scaling exponents $\nu = 0.588$; $\nu = 0.5$; $\nu = 1$. Lines represent the graphical determination of parameters such as C_{p1}, C_{p2}, c^*, and c_{th}.*

Additional information such as the Kuhn length in solution, *b*, and the number of monomers per thermal blobs, g_{th}, can also be extracted by this treatment and are also regrouped in Table 7. Note that precious information about solvent quality is contained in g_{th} as it immediately

indicates the minimum length of a polymer chain for binary polymer-polymer interactions to occur. The value of the $c_{th}b^3$ criterion (related to the description of entanglements following either the Kavassalis-Noolandi or the Rubinstein-Colby conjectures) is always lower than unity. This means that the system behaves as a polymer in a θ solvent.

The same procedure was reproduced for all P(VDF-TrFE) compositions. Each normalization step according to the concentration regime is displayed in **Figure 43** and the values of interest are as well summarized in **Table 7**. According to **Figure 43**, the evolution of the normalized specific viscosity at the different regimes depends on the composition. The critical concentrations c*, $c_{th,}$ and c** have similar values but are subjected to a sharp decrease above 20 mol.% of TrFE. The higher value of c* observed for 83:17 composition can be explained by the lower molar mass, as the overlap of the correlation blob is directly linked to the size of the chain. Nevertheless, for c_{th} and c**, the same decrease is observed revealing the possible impact of the spherical coil conformation on the values of the overlap concentration.

The observed differences underscore the significant impact of composition on copolymer behaviors in solution. Extracting clear information from the solvent quality parameter, g_{th}, is challenging, as its value is highly dependent on molar mass (and thus N_w). However, regarding the Kuhn length, the composition strongly influences its value. The addition of TrFE appears to reduce the number of statistical segments constituting the chain, thereby enhancing the overall chain rigidity.

The overall variation of the correlation blob for each composition as a function of the concentration can then be established and is represented in **Figure 44**a. With this representation, it is possible to visualize the different concentration regimes and their associated scaling exponents, *i.e.*, the self-avoiding walk, the random walk, and the rod-like regime with the respective scaling exponent values of -0.77, -1, and -0.5. The apparent packing number $\tilde{P}_{e,RC}$ (*i.e.*, the number of entanglement strands per tube diameter) normalized by accounting for the Rubinstein-Colby conjecture can also be extracted with the representation of the normalized specific viscosity, $\lambda\eta_{sp}$, as a function of the number of blobs per chain, $N_w/\tilde{g}$ (**Figure 44**b).

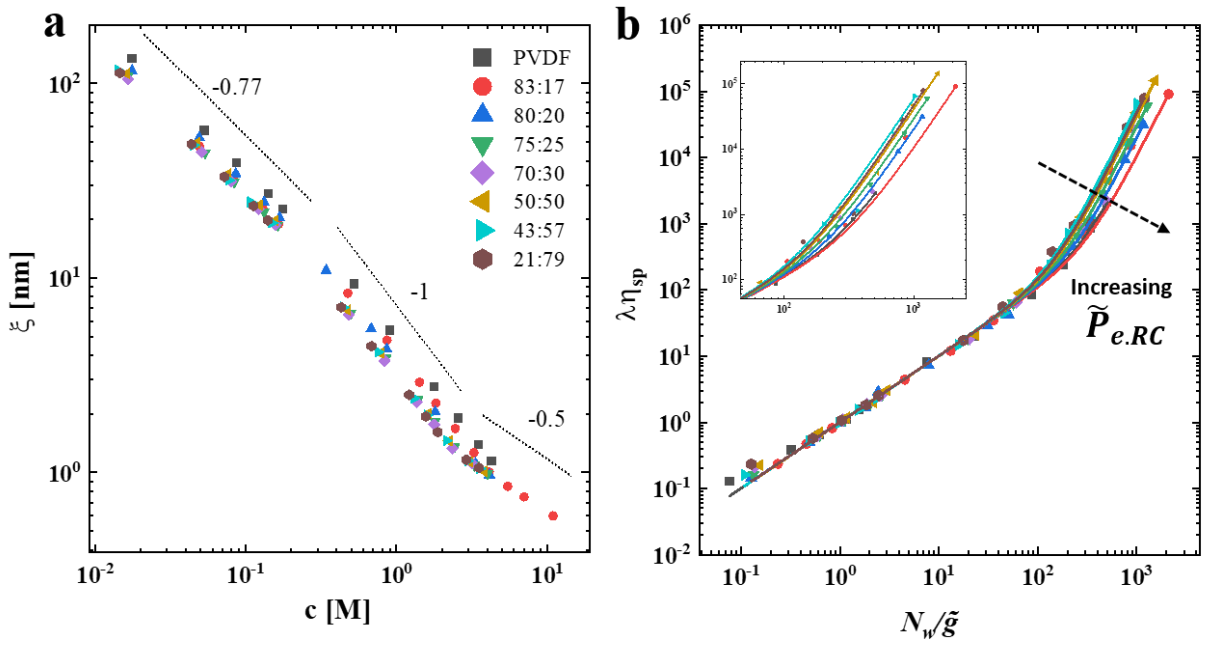

***Figure 44**. (a) Evolution of the size of the correlation blob as a function of the concentration for all the copolymer compositions. The values of the slopes are representative of the different concentration regimes. (b) Dependence of the normalized specific viscosity $\lambda\eta_{sp}$ on the number of blobs per chain $N_w/\tilde{g}$, and the impact of the composition on the apparent normalized packing number $\tilde{P}_{e,RC}$.*

A final representation highlighting the influence of entanglements on the chain conformation is presented in **Figure 45**a, with the dependence of the normalized specific viscosity $\lambda\eta_{sp}/\tilde{P}e_{,RC}^2$ with the number of entanglements per chains $N_w/\tilde{N}_e$. The concentration dependence of the number of monomers between entanglements is correlated to the slope of the curve (β) for higher values of blobs per chain (*i.e.*, at high concentration). Both $\tilde{P}_{e,RC}$ and β values are reproduced in **Table 7**. Through this comprehensive procedure, we now have access to the variation of interaction parameters with the polymer composition, as well as insights into the number of entanglements and chain stiffness, as indicated by the value of the Kuhn length. In **Figure 45**b, representing these two aspects ($\tilde{P}_{e,RC}$ and β), it can be seen that the number of entanglements decreases and the number of monomers between entanglements increases, for compositions under 50 mol.% TrFE content. The observed evolution of β at TrFE content above 50 mol.% suggests that the number of monomers between entanglements slightly decreases, indicating that the entanglements are closer to each other. The change in polymer chain conformation to a 3/1-helix after

crossing the MPB region at 49 mol.% of TrFE may be the cause behind the observed modification in the shape factor. The twisting of the chain as it crosses the MPB could potentially lead to a collapse in conformation, influencing the number of inter-chain interactions. This alteration in structure might be a key factor contributing to the observed changes in the shape factor.

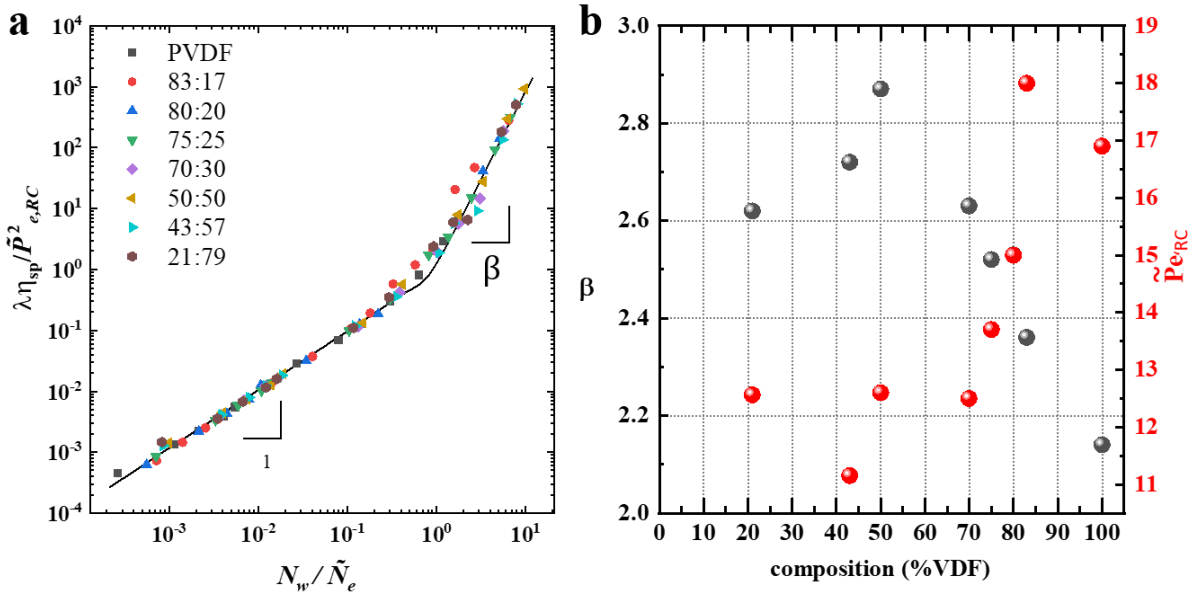

***Figure 45**. (a) Dependence of the normalized specific viscosity $\lambda\eta_{sp}/\tilde{P}e^2_{RC}$ on the number of entanglements per chains $N_w/\tilde{N}_e$. (b) comparison of the number of entanglements and the value of β for the different compositions extracted from the previous data treatments.*

According to **Table 6**, the composition clearly impacts the various parameters extracted from the viscosity measurements. However, the variations in the values of the critical concentrations c*, c_{th}, and c** are not significant enough to draw a strong conclusion. In contrast, the value of the Kuhn length, as shown in **Figure 46**b, consistently increases with the TrFE content. This observation supports the idea that the chain rigidifies as the TrFE content increases, confirming that the chain adopts a more extended conformation induced by the steric hindrance introduced by the TrFe units.

***Table 7**. Recapitulative of the parameters obtained graphically and numerically for each copolymer composition in DMSO. Crossover concentrations: chain overlap (c*), thermal blob overlap (c_{th}), concentrated regime (c**) in mol/L, Kuhn length (b) in nm, the Rubinstein-Colby parameter ($c_{th}b^3$), the apparent packing number $\tilde{P}_{e,RC}$ and β correlated with the number of monomers between two entanglements in the concentrated regime.*

Composition	c* [M].10^{-2}	c_{th} [M]	c** [M]	b [nm]	g_{th}	$c_{th}b^3$	$\widetilde{P}_{e,RC}$	β
PVDF	*13.28*	*0.42*	*6.09*	*0.80*	*656*	*0.22*	*16.9*	2.14
83-17	*15.43*	*0.57*	*4.36*	*0.95*	*212*	*0.49*	*18.0*	2.36
80-20	*8.50*	*0.23*	*3.52*	*1.05*	*897*	*0.28*	*15.1*	2.53
75-25	*7.97*	*0.23*	*2.76*	*1.19*	*653*	*0.39*	*13.7*	2.52
70-30	*7.58*	*0.21*	*2.49*	*1.15*	*709*	*0.41*	*12.5*	2.63
50-50	*7.00*	*0.19*	*2.65*	*1.22*	*887*	*0.35*	*12.6*	2.87
43-57	*7.68*	*0.23*	*2.49*	*1.25*	*608*	*0.44*	*11.4*	2.72
21-79	*6.99*	*0.21*	*2.35*	*1.29*	*656*	*0.47*	*12.1*	2.62

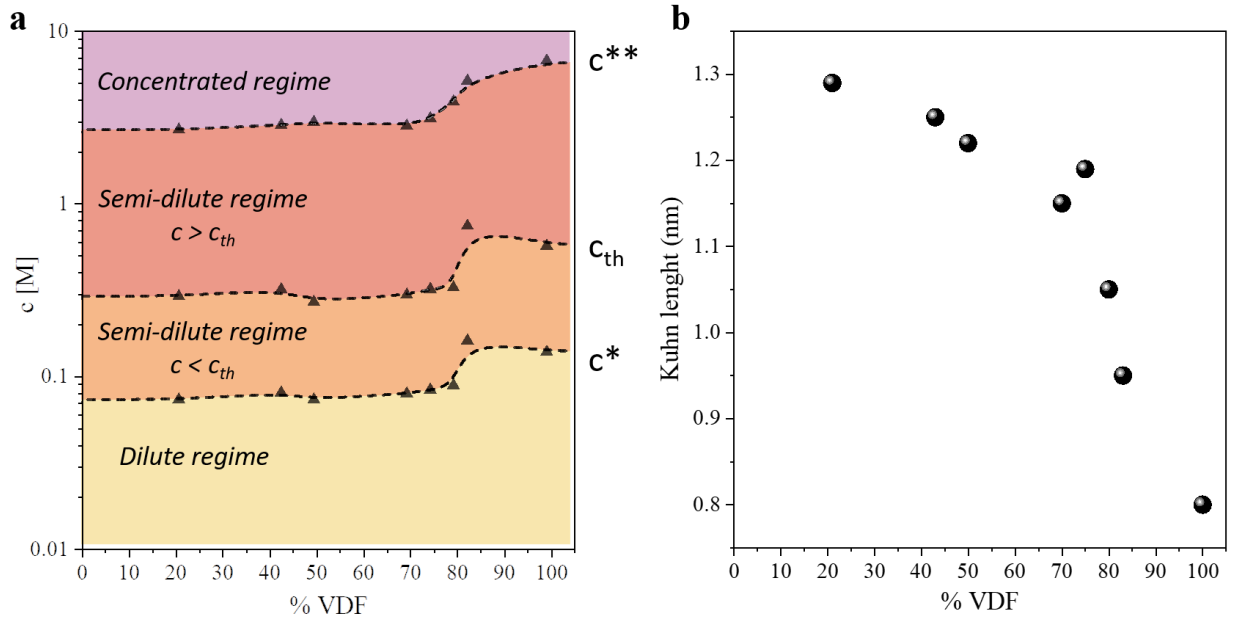

***Figure 46**. (a) Representation of the critical concentrations and regimes according to the copolymer composition. (b) Evolution of the Kuhn length as a function of the copolymer composition.*

2.4 Conclusion

In this chapter, we delved into the challenges associated with fluorinated copolymers in solution, laying the groundwork for further printing by establishing fundamental concepts of polymers in solution. Firstly, to gain insight into the solution behavior of P(VDF-TrFE), we employed the Hansen approach to rationalize the solubility for various copolymer compositions. This initial step revealed the influence of the TrFE monomeric unit on the copolymer solubility and established an initial correlation between composition and chain behavior in solution. Light scattering experiments were then conducted to investigate the chain shape and extension in relation to composition. The results suggested a maximum form factor exceeding 2 for the critical composition of 80:20, with a transition to a form factor below 2 as the composition dropped below 50 mol.% in VDF. This transition was partially explained by the chain conformational shift to a helix induced by the introduction of defects with TrFE.

Subsequently, we employed a scaling approach involving the evolution of viscosity to assess information such as solvent-monomer and monomer-monomer interactions. This comprehensive study highlighted three main points: DMSO can be considered a θ-solvent for all compositions, the Kuhn length increases with the TrFE content, and the number of entanglements in the concentrated regime is inversely proportional to the amount of TrFE. The θ behavior in DMSO suggested that the polymer chain behaves mostly as ideal, canceling monomer attraction that could be induced by the presence of the strong dipolar moment either from the DMSO molecules or the strong electronegativity the Fluorine's atoms along polymer backbone. The increase in the Kuhn length indicated chain stiffening with the addition of TrFE, at the expense of the number of entanglements in solution.

Besides, the complementarity of the techniques used underscored the close relationship between conformation and composition and the impact of defects on the chain conformation. Notably, the twisting effect due to defects was observed to shift the chain conformation from elongated to spherical. As a summary, **Figure 47** illustrates the evolution of the polymer chain shape, conformation and stiffness with the percentage of TrFE. Given the complexity of the system and the

various aspects of chain polymorphism in solution, we chose to explore polymer chain conformation and interactions in one solvent across a broad range of compositions in this chapter. In the subsequent chapter, our focus will shift to a specific composition of interest. Instead of linking composition to interactions, we will impose different interactions (by modifying the solvent for dissolution) on the copolymer and then examine their correlation with chain conformational changes in solution.

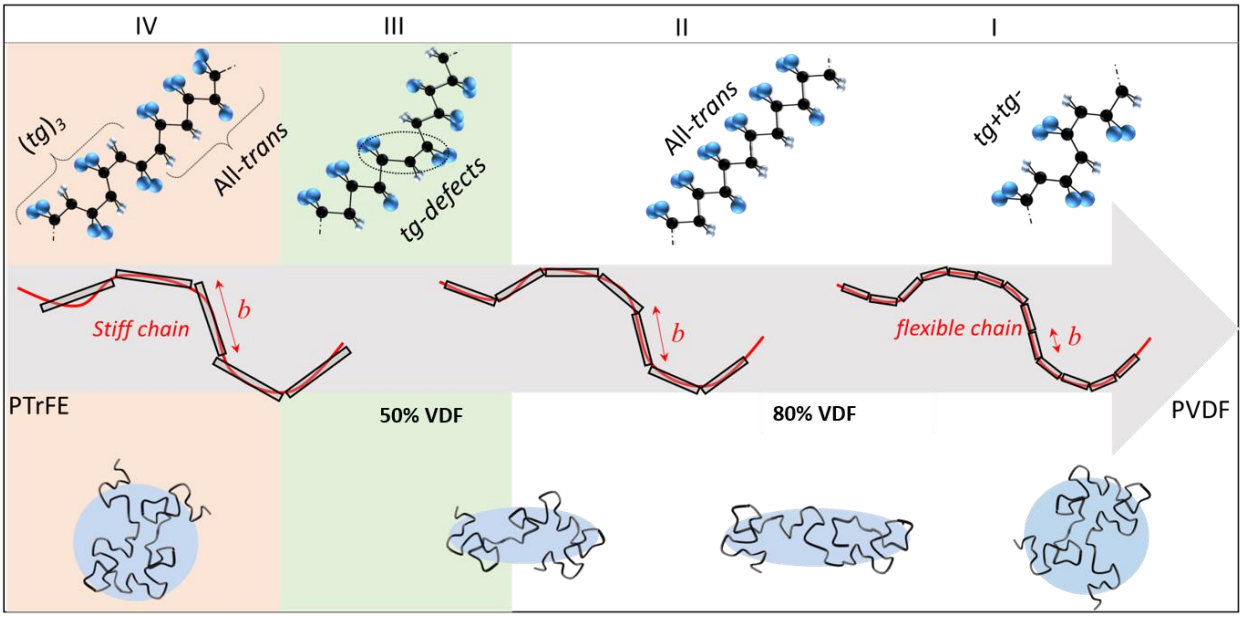

***Figure 47**. graphical representation of the main conclusions established in the Chapter 2. Evolution of the chain conformation in a dilute regime and as function of the Kuhn length and the amount of TrFE in the copolymer. The regions correspond to (I) copolymer with low TrFE content and a majority of tg+tg- (II) The transition regime at the critical concentration of 20% of TrFE where the conformation is in majority* all-*trans (III) Appearance of tg defects around 50% of TrFE (IV) Composition above 50% of TrFE with a combination of 3-1helix $(tg)_3$ and all-trans conformation.*

2.5. Materials and Methods

Poly(vinylidene fluoride-*co*-trifluoroethylene) (P(VDF-TrFE)) was kindly provided by Arkema Piezotech with a VDF/TrFE molar ratio of 83:17, 80:20, 75:25, 70:30, 50:50, 43:57, 21:79 as stated by the manufacturer and confirmed by ^{1}H NMR. All solvents used in this study were purchased from Fisher, Sigma Aldrich, or Thermos Scientific.

2.5.1. Solubility

As a recurrent methodology, 10 mg of copolymer was mixed with 4 mL of solvents. Each mixture was sealed, sonicated at room temperature for 15 minutes, and then stirred at 300 rpm for 2 days. Homogeneity was assessed visually by the transparency of the solution. In the event of non-dissolution after several hours, the temperature was gradually increased from 25 °C to a maximum of 50 °C until dissolution. Transparency was checked again when the samples were cooled to 25 °C. The solvent quality was classified as a poor solvent for non-transparent solutions and as a good solvent for transparent solutions. Another state of solubility has been observed using solvents with intermediate behavior that induce “swelling” of the polymer. All these data are presented in

Table 2. This set of data was then implemented into the HSPiP software developed by Hansen, Abbot, and Yamamoto, leading to the definition of the solubility sphere.[48]

2.5.2. Size-Exclusion Chromatography (SEC)

SEC was employed to estimate the copolymer molecular weight and dispersity (Đ), using dimethylsulfoxide (DMSO) with 1 g/L of LiBr as eluent. SEC measurements were performed on an Ultimate 3000 system (Thermoscientific) equipped with a diode array detector, a multi-angle light

scattering detector, and a differential refractive index detector. Polymers were separated on Tosoh TSK G3000HHR and G2000HHR (7.8×300) columns at a flow rate of 0.5 mL/min. The temperature of the columns was held at 80 °C. Absolute molar masses were determined using the refractive index increment (*dn/dc*) method. The *dn/dc* was evaluated by measuring the refractive index signal while injecting different polymer solution concentrations ranging from 1 to 10 mg/mL. Absolute molar masses were then extracted from the Zimm equation using the ASTRA software.

2.5.3. SLS-MADLS

Each copolymer composition was dissolved in filtered DMSO with PTFE filters (0.1 µm) to obtain a final concentration of 2 g/L. The solutions were first sonicated for 30 min, then magnetically stirred at 50 °C and 300 rpm for 24 hrs. Filtration using a PTFE filter with a pore diameter of 1 µm was then carried out unless otherwise stated. The measuring cells were soaked for 1 day in MEK, then sonicated for about 30 min, before being rinsed with fresh MEK and acetone, and finally dried with compressed dried air. The cells were then soaked for a day in the solvent corresponding to the intended measurement, rinsed with acetone, and dried with compressed dried air. Before filling, the measuring cell was rinsed and filled directly with the corresponding solvent permeate, then sealed with a suitable cap.

For SLS, five solutions with distinct concentrations were prepared through dilution of a mother solution. The preparation of the sample and the measuring cell was performed in the same conditions as for DLS experiments. The toluene and solvent reference cells were also prepared using the same procedure by using a PTFE filter with a pore size of 0.1 µm.

Dynamic Light Scattering (DLS) and Static Light Scattering (SLS) analyses were performed using a compact ALV-CGS3 goniometer with an ALV/LSE-5004 light scattering electronics and an ALV-7004 multi-tau digital correlator with pseudo-cross correlation detection (ALV-Laser, Langen, Germany). The light source was a 22 mW He-Ne laser operating at λ= 632.8 nm. The analysis was carried out at 25 °C. SLS and DLS experiments were performed from 30° to 150° with an increment

step of 5° and 10°, respectively. A total of three measurements of 30 s were performed at each step.

DLS data were evaluated by fitting the normalized time autocorrelation function of the scattered light intensity, $g_{(2)}(t)$ which is related to the normalized electric field autocorrelation function (ACF), $g_{(1)}(t)$ through the Siegert relation: $g_{(2)}(t)=1+\beta|g_{(1)}(t)|^2$ where β is an instrumental constant. The data were fitted with the constrained regularization method (CONTIN), which provides the distribution of relaxation times, A(τ), as the inverse Laplace transform of the electric field ACF: $g_{(1)}(t)=\int_0^\infty A(\tau)\exp(-t/\tau)\ d\tau$. The distribution of relaxation times was converted to an intensity-weighted size distribution by applying the Stokes–Einstein equation.

2.5.4. Rheology

A series of solutions ranging from 0.1 wt.% to 17 wt.% were prepared by dissolving the appropriate quantity of P(VDF-TrFE) into 4 g of a solvent. These solutions were sealed, sonicated, and heated to a maximum temperature of 50 °C for 24 hrs until completely homogeneous, then magnetically stirred at 100 rpm. If necessary, mechanical mixing was carried out to homogenize highly viscous mixtures. Viscosity measurements were performed with an Anton Paar MCR302 rheometer with a cone and plate geometry (50 mm diameter and 1° cone angle). Steady shear viscosity measurements were performed for different shear rates between 0.01 s^{-1} and 1000 s^{-1} at 21 °C. The measurements were carried out under a solvent saturated atmosphere with the help a solvent trap. The linear viscosity data was obtained by extrapolating the Newtonian plateau to get the zero-shear viscosity.

The viscosity of pure solvents was measured at 21 °C at a shear rate of 1000 s^{-1} using a microVISC™ viscometer equipped with an A1 membrane with a flow channel depth of 50 µm.

Annex chapter 2:

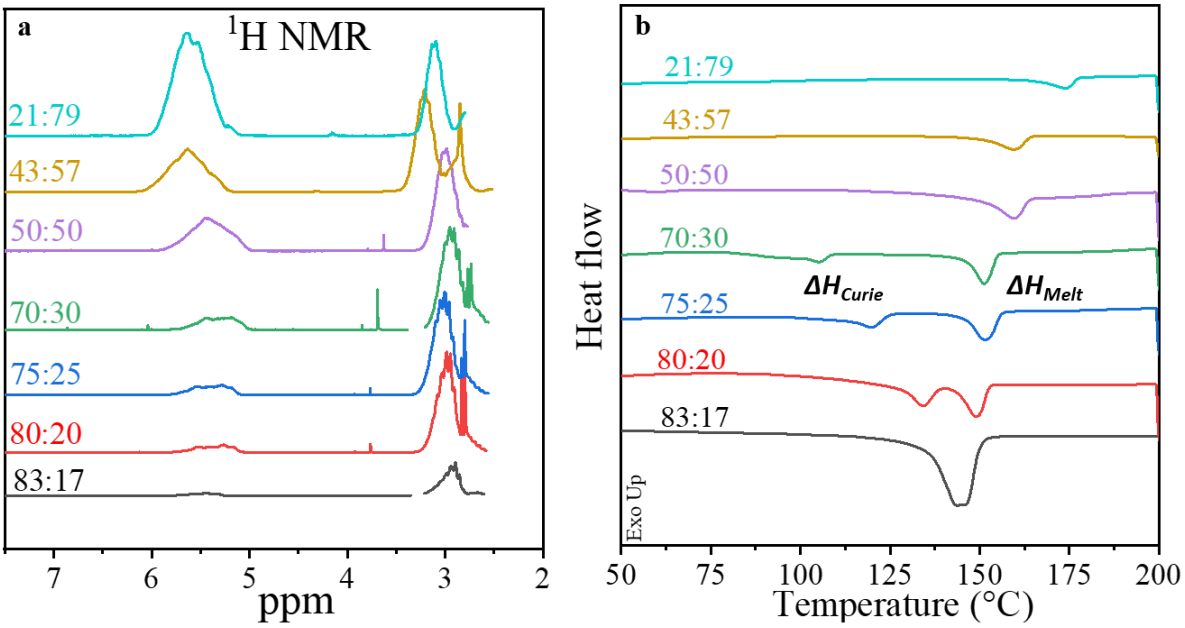

c Composition (VDF:TrFE)	ΔH_{Melt} (J g^{-1})	ΔH_{Curie} (J g^{-1})	ΔH_0 (J g^{-1})	$\%\chi_{tot}$ (%)
21:79	7.5	0	74.7	10
43:57	9.3	0	83.6	11
50:50	14.6	0	86.4	18
70:30	13.8	8.8	94.5	24
75:25	16.6	13.2	96.5	30
80:20	17.5	11.5	98.5	30
83:17	58.0	N/A	99.7	58

FigureS2- 1. (a) *NMR spectra of the different P(VDF-TrFE) compositions* ***(b)*** *DSC thermograms (2nd heating 10 K/min under N_2 athmosphere) for the various copolymer compositions.* ***(c)*** *recapitulative of the values extracted from DSC with ΔH_{melt} and ΔH_{Curie} determined by integrating the corresponding peaks and dividing the areas (W g^{-1} K^{-1}) by the ramp rate (K s^{-1}). ΔH_0 of a 100% crystalline material can be estimated by weighing the respective values of fully crystalline PVDF (106.6 J g^{-1}) and PTrFE (66.3 J g^{-1}) accordingly with copolymer composition.*[49]

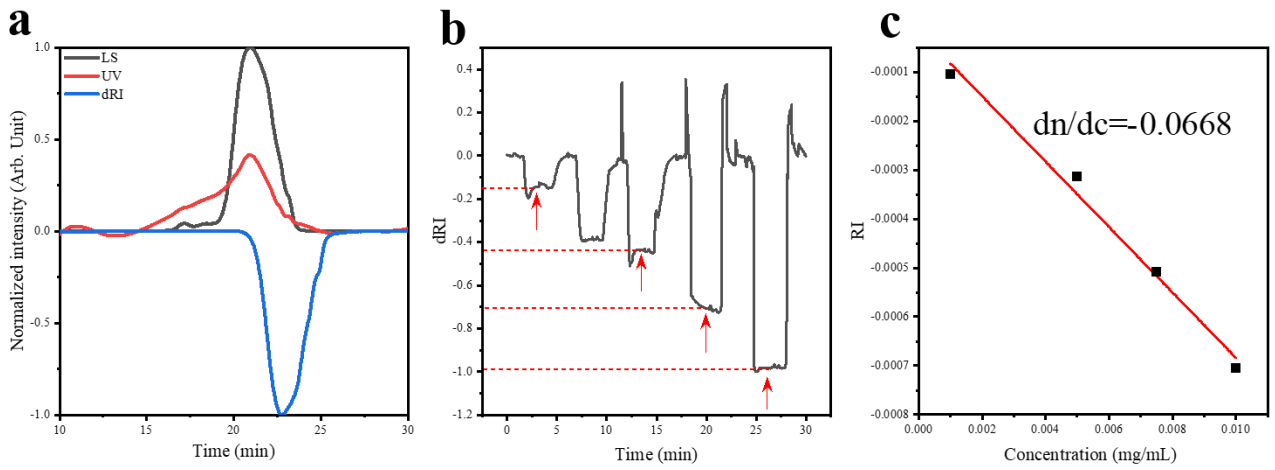

FigureS2- 2. (*a) SEC measurement of the P(VDF-TrFE)-80:20 in DMSO and signal observed with the LS, UV, and dRI detector (b) methodology to measure the refractive index at different concentrations, (c) determination of the refractive index increment dn/dc=-0.0668.*

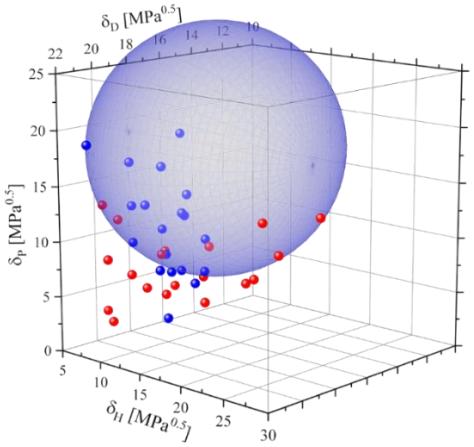

FigureS2- 3. *representation of the P(VDF-TrFE):80-20 solubility with a unique solubility region in the 3D Hansen space with a desirability function of d=0.552*

In this approach, the Hansen solubility parameters (HSP) distance, Ra, between two molecules is defined as:

$$(Ra)^2 = 4(\delta_{D2} - \delta_{D1})^2 + (\delta_{P2} - \delta_{P1})^2 + (\delta_{H2} - \delta_{H1})^2 \qquad (SII\text{-}1)$$

where δ_D, δ_P, and δ_H are the dispersive, polar, and hydrogen-bonding solubility parameters.

$$d = (B_1 * B_2 * ... B_n)^{1/n} \qquad (SII\text{-}2)$$

Desirability function d, where n represents the number of solvents experimentally used for the representation. Optimal representation is reached when d=1 when all good solvents are inside and all bad solvents are outside the sphere.

$$B_i = e^{-(\text{ERROR DISTANCE})} \qquad (SII\text{-}3)$$

B_i desirability function is given for one solvent. B=1 for a good solubilizing solvent inside and a bad solubilizing solvent outside. For non-well-located solvents, B_i is represented by the distance between the location of the solvent and the boundary of the calculated sphere.

$$B_i = e^{+(Ro - Ra)} \qquad (SII\text{-}4)$$

with R_o the radius of the sphere and R_a the distance from the solvent position to the center of the sphere.

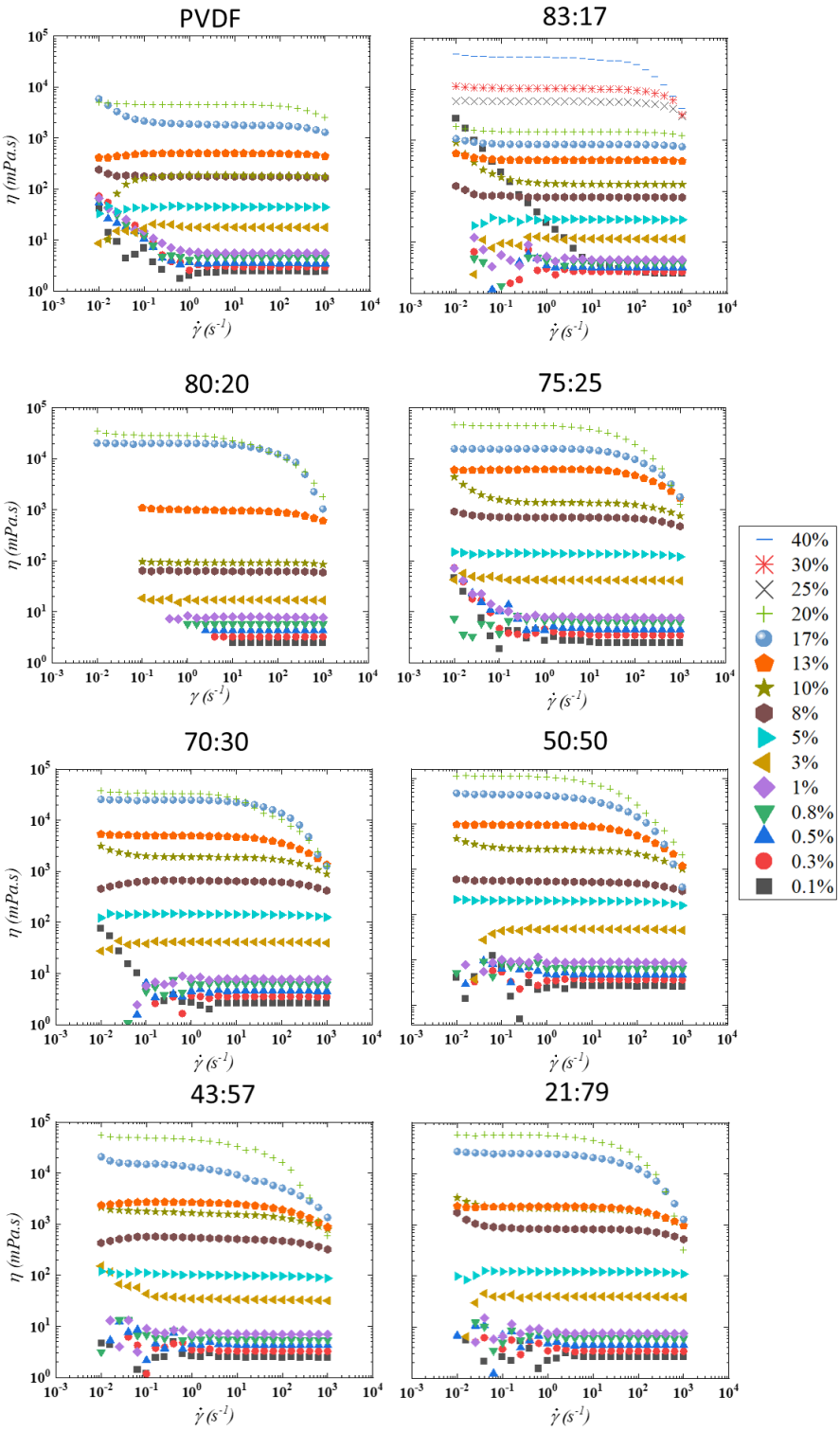

FigureS2- 4. Solution viscosity dependence with respect to the shear rate of PVDF, P(VDF-TrFE)-83:17, 80:20, 75:25, 70:30, 50:50, 43:57, 21:79 at 25°C for concentrations ranging from 0.1 wt.% to 40 wt.%.

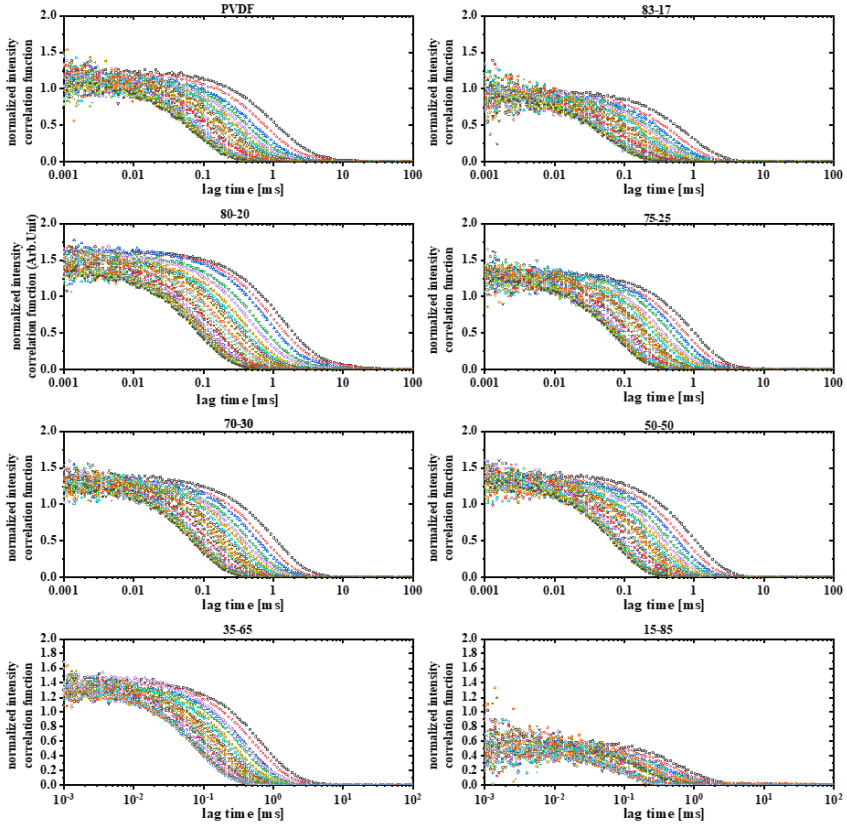

FigureS2- 5. *MA-DLS correlograms for all the copolymer compositions in DMSO at 2 g/L concentration.*

TableS2-1. Recapitulative of the different parameters extracted from the scaling approach of the different P(VDF-TrFE) compositions dissolved DMSO.

Composition	C_{p1}	B_g	C_{p2}	B_{th}	c*	c_{th}	c**	b	g_{th}	$c_{th} b^3$	$\tilde{P}_{e.RC}$
					[M].10^{-2}		[M]	[*nm*]			
PVDF	*1.00*	*0.99*	*27.32*	*0.56*	*13.28*	*0.42*	*6.09*	*0.80*	*656*	*0.22*	*16.9*
83-17	*2.06*	*0.83*	*48.06*	*0.52*	*15.43*	*0.57*	*4.36*	*0.95*	*212*	*0.49*	*18.0*
80-20	*1.54*	*0.89*	*64.21*	*0.49*	*8.50*	*0.23*	*3.52*	*1.05*	*897*	*0.28*	*15.1*
75-25	*2.19*	*0.81*	*95.22*	*0.46*	*7.97*	*0.23*	*2.76*	*1.19*	*653*	*0.39*	*13.7*
70-30	*2.36*	*0.80*	*106.18*	*0.45*	*7.58*	*0.21*	*2.49*	*1.15*	*709*	*0.41*	*12.5*
50-50	*2.06*	*0.83*	*97.19*	*0.46*	*7.00*	*0.19*	*2.65*	*1.22*	*887*	*0.35*	*12.6*
43-57	*2.64*	*0.78*	*124.57*	*0.45*	*7.68*	*0.23*	*2.49*	*1.25*	*608*	*0.44*	*11.4*
21-79	*2.56*	*0.79*	*125.00*	*0.44*	*6.99*	*0.21*	*2.35*	*1.29*	*656*	*0.47*	*12.1*

References

1. Teraoka Iwao. *Polymer Solutions*. (2002). doi:10.4324/9780203809075-32.
2. Rubinstein, M. & Colby, R. H. polymer physics. 442 (2003).
3. Pierre-Gilles Gennes. *Scaling Concepts in Polymer Physics*. (1979).
4. Dobrynin, A. V, Jacobs, M. & Sayko, R. Scaling of Polymer Solutions as a Quantitative Tool. *Macromolecules* **54**, 2288–2295 (2021).
5. Dobrynin, A. V. & Jacobs, M. When Do Polyelectrolytes Entangle? *Macromolecules* **54**, 1859–1869 (2021).
6. Isono, Y. & Nagasawa, M. Solvent Effects on Rheological Properties of Polymer Solutions. *Macromolecules* **13**, 862–867 (1980).
7. Tager, A. A. Effect of solvent quality on the viscosity of flexible-chain and rigid-chain polymers in a wide range of concentrations. *I Rheol. Acta* **13**, 323–332 (2974).
8. Chitrangad, B., Osmers, H. R. & Middleman, S. *for Zero-Shear and Shear-Rate Dependent Viscosity of Polymeric Solutions*.
9. Schnell, M. & Wolf, B. A. Viscosity of polymer/solvent systems: Quantitative description on the basis of molecular surfaces. *Cit. J. Rheol.* **44**, 617 (2000).
10. Somani, S., Shaqfeh, E. S. G. & Prakash, J. R. Effect of Solvent Quality on the Coil-Stretch Transition. *Macromolecules* **43**, 10679–10691 (2010).
11. Bell, S. & Terentjev, E. M. Stretching globular polymers. I. Single chains. *J. Chem. Phys.* **143**, 184902 (2015).
12. Bottino, A., Capannelli, G., Munari, S. & Turturro, A. Solubility parameters of poly(vinylidene fluoride). *J. Polym. Sci. Part B Polym. Phys.* **26**, 785–794 (1988).
13. Charles M.Hansen. *Hansen Solubility Parameters Second edition: A User's Handbook*. (2007).
14. Jung, J. T. *et al.* Understanding the non-solvent induced phase separation (NIPS) effect during the fabrication of microporous PVDF membranes via thermally induced phase separation (TIPS). *J. Memb. Sci.* **514**, 250–263 (2016).
15. Kang, G. dong & Cao, Y. ming. Application and modification of poly(vinylidene fluoride) (PVDF) membranes – A review. *J. Memb. Sci.* **463**, 145–165 (2014).
16. Li, Q., Xu, Z.-L. & Yu, L.-Y. Effects of Mixed Solvents and PVDF Types on Performances of PVDF Microporous Membranes. *J Appl Polym Sci* **115**, 2277–2287 (2009).
17. Kim, M., Lee, S. & Kim, Y. Il. Solvent-controlled crystalline beta-phase formation in electrospun P(VDF-TrFE) fibers for enhanced piezoelectric energy harvesting. *APL Mater.* **8**, (2020).
18. Tao, M. mi, Liu, F., Ma, B. rong & Xue, L. xin. Effect of solvent power on PVDF membrane polymorphism during phase inversion. *Desalination* **316**, 137–145 (2013).
19. Yang, J., Wang, X.-L., Tian, Y. E., Lin, Y. & Tian, F. Morphologies and Crystalline Forms of Polyvinylidene Fluoride Membranes Prepared in Different Diluents by Thermally Induced Phase Separation. *J Polym Sci Part B Polym Phys* **48**, 2468–2475 (2010).
20. Nishiyama, T., Sumihara, T., Sato, E. & Horibe, H. Effect of solvents on the crystal formation of poly (vinylidene fluoride) film prepared by a spin-coating process. *Polym. J.* **49**, 319–325 (2017).

21. Horibe, H. *et al.* Quantification of the solvent evaporation rate during the production of three PVDF crystalline structure types by solvent casting. *Polym. J.* **46**, 104–110 (2014).
22. Tu, R., Sprague, E. & Sodano, H. A. Precipitation-Printed High-β Phase Poly(vinylidene fluoride) for Energy Harvesting. *ACS Appl. Mater. Interfaces* (2021) doi:10.1021/acsami.0c16207.
23. Lutringer, G. & Weill, G. Solution properties of poly(vinylidene fluoride): 1. Macromolecular characterization of soluble samples. *Polymer (Guildf).* **32**, 877–883 (1991).
24. Lutringer, G., Meurer, B. & Weill, G. Solution properties of poly(vinylidene fluoride): 2. Relation between microgel formation and microstructure. *Polymer (Guildf).* **32**, 884–891 (1991).
25. Nohara, Y., Saiki, E. & Shikata, T. Long Two-Dimensional Folding Chain Structure Formation of Poly(vinylidene fluoride) in Solutions of a Polar Solvent, N-Methylpyrrolidone. *ACS Appl. Polym. Mater* **4**, 1255–1263 (2022).
26. Saiki, E., Nohara, Y., Iwase, H. & Shikata, T. Evidence of Long Two-Dimensional Folding Chain Structure Formation of Poly(vinylidene fluoride) in N-Methylpyrrolidone Solution: Total Form Factor Determination by Combining Multiscattering Data. *ACS omega* **7**, 22825–22829 (2022).
27. Chou, C.-M. & Hong, P.-D. Light Scattering from Birefringent Sphere and Its Aggregation. *Macromolecules* **41**, 6147–6153 (2008).
28. Li, Y.-C. *et al.* Scattering Study of the Conformational Structure and Aggregation Behavior of a Conjugated Polymer Solution. *langmuir* **25**, 4668–4677 (2009).
29. Park, I. H., Yoon, J. E., Kim, Y. C., Yun, L. & Lee, S. C. Laser Light Scattering Study on the Structure of a Poly(vinylidene fluoride) Aggregate in the Dilute Concentration State. (2004) doi:10.1021/ma030534v.
30. Sekine, T. *et al.* Fully Printed Wearable Vital Sensor for Human Pulse Rate Monitoring using Ferroelectric Polymer. *Sci. Rep.* **8**, 1–10 (2018).
31. Terziyan, T. V. & Safronov, A. P. Solubility and H-bonding of poly(vinylidene fluoride) copolymers in carbonyl liquids: Experiment and molecular simulation. *J. Mol. Liq.* **275**, 378–383 (2019).
32. Darmanin, T. & ed eric Guittard, F. Fluorophobic Effect for Building up the Surface Morphology of Electrodeposited Substituted Conductive Polymers. *Curr. Opin. Colloid Interface Sci* **44**, 5463–5466 (2005).
33. Percec, V., Johansson, G., Ungar, G. & Zhou, J. Fluorophobic effect induces the self-assembly of semifluorinated tapered monodendrons containing crown ethers into supramolecular columnar dendrimers which exhibit a homeotropic hexagonal columnar liquid crystalline phase. *J. Am. Chem. Soc.* **118**, 9855–9866 (1996).
34. Johansson, G., Percec, V., Ungar, G. & Zhou, J. P. Fluorophobic Effect in the Self-Assembly of Polymers and Model Compounds Containing Tapered Groups into Supramolecular Columns. *J. Am. Chem. Soc.* **119**, 9855–9866 (1996).
35. Jeong, H.-G. *et al.* A Novel Thermally Reversible Soluble-Insoluble Conjugated Polymer with Semi-Fluorinated Alkyl Chains: Enhanced Transistor Performance by Fluorophobic Self-Organization and Orthogonal Hydrophobic Patterning. *Adv. Mater.* **25**, 6416–6422 (2013).

36. Furukawa, T. Structure and functional properties of ferroelectric polymers. *Adv. Colloid Interface Sci.* **71**–**72**, 183–208 (1997).
37. Benoit, H. & Doty, P. M. light scattering from non-gaussian chains. **57**, (1953).
38. Neupane, S., Bittkau, K. S. & Alban, S. Size distribution and chain conformation of six different fucoidans using size-exclusion chromatography with multiple detection. *J. Chromatogr. A* **1612**, 460658 (2020).
39. Wyatt, P. J. Light scattering and the absolute characterization of macromolecules. *Anal. Chim. Acta* **272**, 1–40 (1993).
40. Morris, G. A., Adams, G. G. & Harding, S. E. On hydrodynamic methods for the analysis of the sizes and shapes of polysaccharides in dilute solution: A short review. *Food Hydrocoll.* **42**, 318–334 (2014).
41. Resende, P. M., Isasa, J.-D., Hadziioannou, G. & Fleury, G. Deciphering TrFE Fingerprints in P(VDF-TrFE) by Raman Spectroscopy: Defect Quantification and Morphotropic Phase Boundary. *Macromolecules* (2023) doi:10.1021/ACS.MACROMOL.3C01700.
42. Liu, Y., Chen, X., Han, Z., Zhou, H. & Wang, Q. Defects in poly(vinylidene fluoride)-based ferroelectric polymers from a molecular perspective. *Appl. Phys. Rev* **9**, (2022).
43. Liu, Y. *et al.* Ferroelectric polymers exhibiting behaviour reminiscent of a morphotropic phase boundary. *Nature* **562**, 96–100 (2018).
44. Salimi, A. & Yousefi, A. A. Conformational changes and phase transformation mechanisms in PVDF solution-cast films. *J. Polym. Sci. Part B Polym. Phys.* **42**, 3487–3495 (2004).
45. Tashiro, K. *et al.* High-Electric-Field-Induced Hierarchical Structure Change of Poly(vinylidene fluoride) as Studied by the Simultaneous Time-Resolved WAXD/SAXS/FTIR Measurements and Computer Simulations. *Macromolecules* acs.macromol.0c02567 (2021) doi:10.1021/acs.macromol.0c02567.
46. Gregorio, R. Determination of the , and Crystalline Phases of Poly(vinylidene fluoride) Films Prepared at Different Conditions. *J Appl Polym Sci* **100**, 3272–3279 (2005).
47. Cai, X., Lei, T., Sun, D. & Lin, L. A critical analysis of the a, b and g phases in poly(vinylidene fluoride) using FTIR †. *RCS Adv.* **7**, 15382–15389 (2017).
48. S. Abbott, C., Hansen, M. & H. Yamamoto, R. S. V. Hansen Solubility Parameters in Practice.
49. Roggero, A., Dantras, E., & Lacabanne, C. (2017). Poling influence on the mechanical properties and molecular mobility of highly piezoelectric P(VDF-TrFE) copolymer. Journal of Polymer Science Part B: Polymer Physics, 55(18), 1414–1422. https://doi.org/10.1002/POLB.24396

Chapter 3:

Influence of the solvent quality on P(VDF-TrFE)-80:20 solution behavior

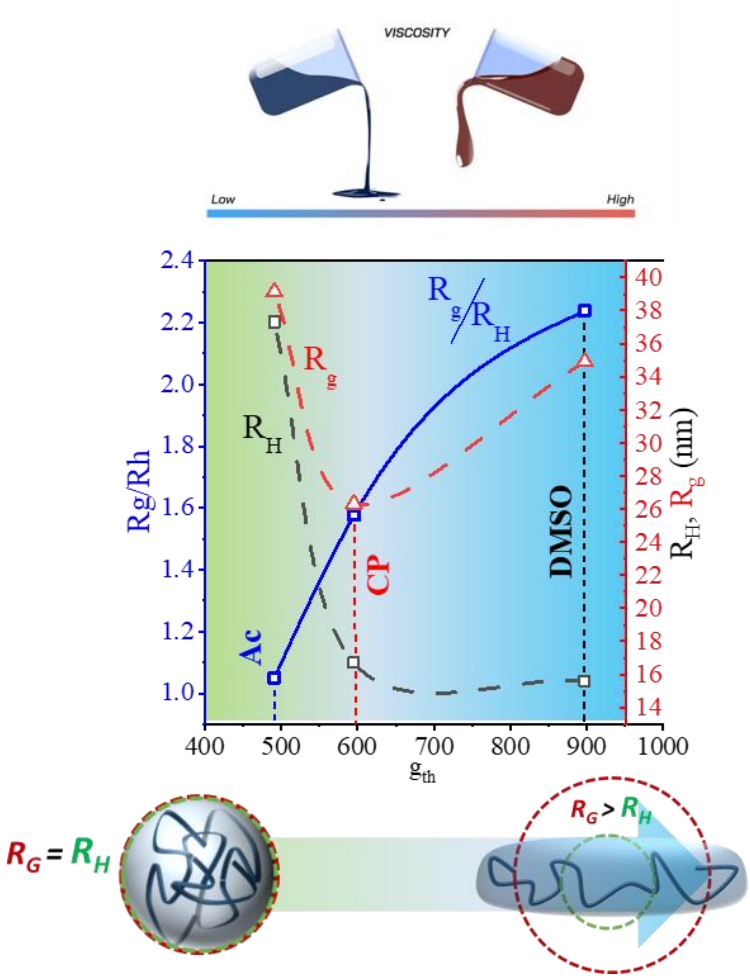

Chapter 3: Influence of the solvent quality on P(VDF-TrFE)-80:20 solution behavior

3.1 Problematic and Motivation

Printing methods enable us to manufacture devices at low cost with fully optimized properties. Nevertheless, new technical challenges have arisen with the utilization of these techniques. For all the wet printing deposition techniques, the viscosity of the solution is a crucial parameter with respect to the feasibility of a specific processing method.[1] For each printing technique, it is mandatory to maintain a viscosity within a specific range to achieve high-quality, uniform, and defect-free films during the deposition process. For instance, inkjet printing and screen printing prerequisites criteria are quite the opposite. For inkjet (drop-on-demand), low viscosities solutions and a minimum of elasticity are needed to fulfill the required Reynolds and Weber numbers.[1–6] On the other hand, screen printing requires higher viscosity and shear thinning behavior of the inks to allow a optimized mass transfer from the mask to the substrate.[7–11] In both cases, these inks require a complete dissolution of the polymer chains into the solvent. For fluorinated polymers, the solubilisation in a solvent of interest can sometimes be a difficult task. Using additives is an effective approach to attain specific rheological properties. However, adding other components can have negative effects on the final dielectric properties of the material, by for example decreasing the breakdown strength.[12] Furthermore, incorporating additional components can introduce additional complexity when attempting to understand fundamental concepts such as the evolution of the viscosity due to interactions with different solvents.

In this chapter, we focused our efforts on the evaluation of the rheological properties of inks based on P(VDF-TrFE)-80:20 as function of the solvents. We first based our work on the Hansen approach to identify the solvents in which our polymer dissolves completely through solubilization studies, and then used the scaling approach developed by Dobrynin *et al*.[13,14] to analyze the interactions between the P(VDF-TrFE)-80:20 chains and the various solvents of interest for printing. This step provides a comprehensive understanding of intra- and inter-molecular interac-

tions for P(VDF-TrFE)-80:20-solvent systems. Additionally, we performed light scattering measurements of the P(VDF-TrFE)-80:20 copolymer in the different solvents in the dilute regime to obtain information on the single chain conformation in solution.

Our results, obtained from an extensive set of solvents, further demonstrates the close relationship between the solvent quality and the variation of the viscosity, while also establishing the influence of polymer-solvent interactions on the fluorinated chain conformation.

3.2 Hansen Solubility Approach and influence of the solvent quality on the viscosity

Based on the methodology presented in Chapter 2, the solubility regions extracted using the Hansen approach, revealed a double-sphere behavior that was mainly attributed to a fluorophobic effect and a change in the polymer chain conformation. This data set enables us to identify the solvent available for total dissolution of the copolymer (see **Figure 48**).

Further rationalization on the solvent quality for P(VDF-TrFE)-80:20 was established through viscosimetric measurements at iso-concentration (*i.e.*, 17 wt.%) for a series of good solvents. Steady shear viscosity measurements were performed following the procedure described in the experimental section to determine the apparent viscosity at zero shear extrapolated from the Newtonian plateau at low shear rates (see **Table 8**). Relative viscosity values taking into account the viscosity of the pure solvent are displayed in **Figure 49**, and clearly show the influence of the solvent quality and in particular its polar contribution on the resulting relative viscosity values, *i.e.*, solvents with an important polar contribution results in P(VDF-TrFE)-80:20 solutions of high relative viscosity.

However, this approach seems limited in terms of correlating the evolution of viscosity with the quality of the solvent. Further treatment using the dipolar moment of the solvents was performed, hypothesizing a weak correlation between apparent viscosity and dipolar moment. Referring to this approach, **Figure 50** suggests that solvents with high dipolar moments, located

in the second solubility sphere, display higher apparent viscosity at the same copolymer concentration. A possible explanation is the interaction of fluorine atoms with the dipoles of the solvent inducing an “anchor” to the polymeric chain, hindering chain mobility.

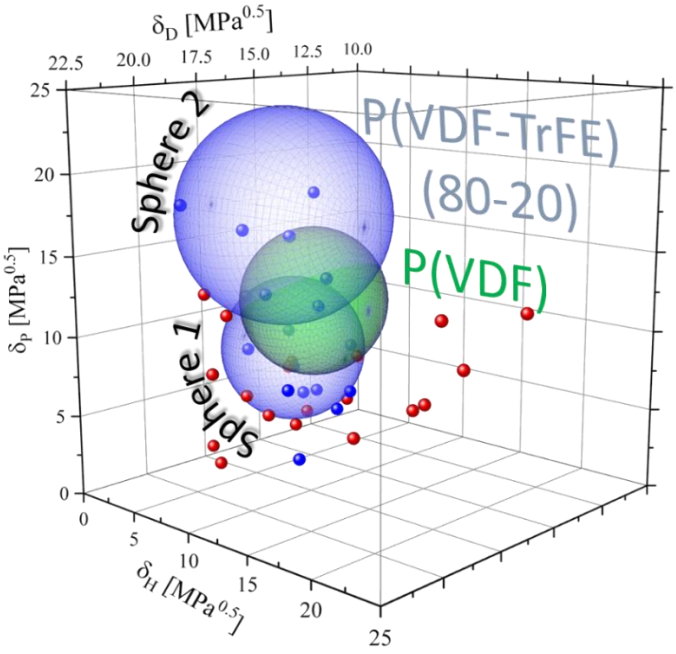

***Figure 48**. Representation of the double sphere solubility region of the P(VDF-TrFE)-80:20 copolymer in the 3D Hansen space with (●) good solubilizing solvents and (●) bad solubilizing solvents.*

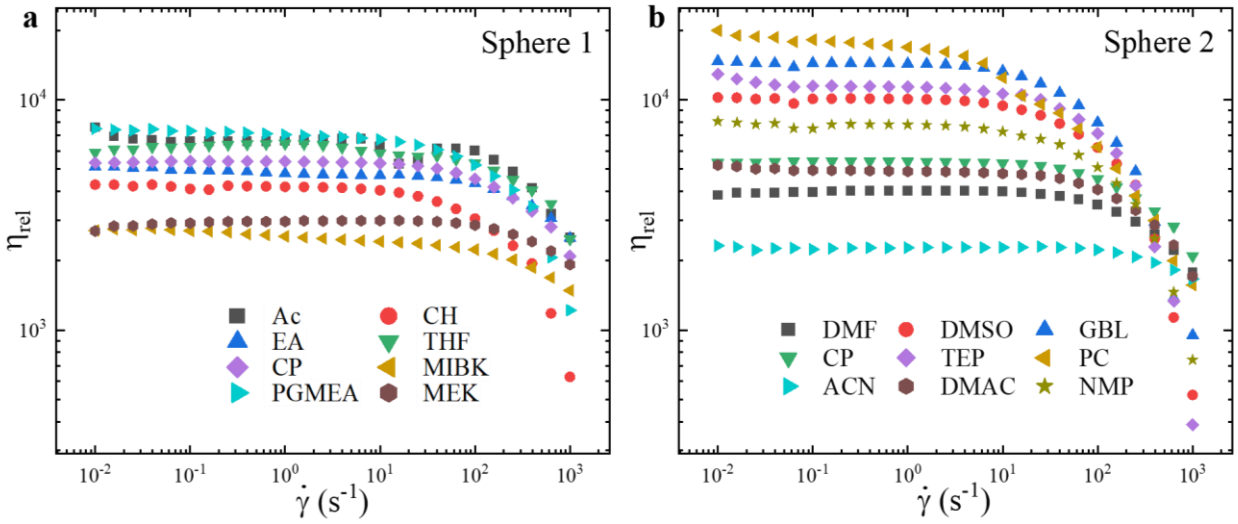

***Figure 49**. Relative viscosity values extracted from steady shear viscosity measurements of the P(VDF-TrFE)-80:20 copolymer at a concentration of 17 wt.% for the solvents present in the solubility (a) sphere 1 and (b) sphere 2.*

Table 8. List of solvents used with their corresponding Hansen solubility parameters, δ_D, δ_P, and δ_H. The apparent viscosity at zero shear of 17 wt.% P(VDF-TrFE)-80:20 solutions ($\eta_{17wt.\%}$) and the viscosity of the pure solvent (η_{solv}) obtained at 21 °C are also given.

Solvent	δ_D	δ_P	δ_H	η_{solv}	$\eta_{17\ wt.\%}$
		$MPa^{0.5}$		$mPa.s$	
Acetone (Ac)	15.5	10.4	7	0.32	2 116
Acetonitrile (ACN)	15.3	18	6.1	0.4	1 002
Cyclohexanone (CH)	17.8	6.3	5.1	2.2	9 224
Cyclopentanone (CP)	17.9	11.9	5.2	1.1	4 319
Dimethyl acetamide (DMAC)	16.8	11.5	9.4	1.1	4 647
Dimethyl formamide (DMF)	17.4	13.7	11.3	0.92	3 697
Dimethylsulfoxide (DMSO)	18.4	16.4	10.2	2.2	20 200
Ethyl acetate (EA)	15.8	5.3	7.2	0.45	2 159
Methyl ethyl ketone (MEK)	16	9	5.1	0.41	1 273
Methylisobutylketone (MIBK)	15.3	6.1	4.1	0.59	1 481
N−methyl−2−pyrrolidinone (NMP)	18	12.3	7.2	1.77	14 728
Propylene carbonate (PC)	20	18	4.1	2.5	20 313
Propylene glycol methyletheracetate (PGMEA)	15.6	5.6	9.8	1.13	7 765
Tetrahydrofuran (THF)	16.8	5.7	8	0.419	3 098
Triethyl phosphate (TEP)	16.7	11.4	9.2	1.67	17 636

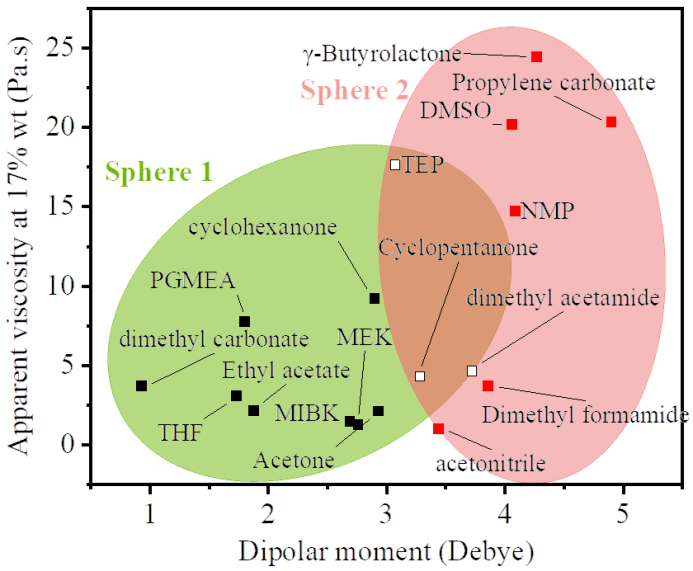

***Figure 50**. Apparent viscosity values at a concentration of 17 wt.% as a function of the dipolar moment of the solvents.*

3.3 Correlation between solvent quality and viscosity using the Huggins and Kraemer regression method

We subsequently attempted to determine the intrinsic viscosity, [η], by using Huggins and Kraemer regression method with an extrapolation of the reduced (η_{red}) and inherent (η_{inh}) viscosities at zero concentration.[16–20] For most of the systems, we can notice a deviation from linearity in the highly diluted solution regime (see **Figure 51**), typically linked to expanded coil dimensions due to electrostatic repulsion between the chain segments making difficult and inaccurate the determination of the [η] by this method.[21,22]

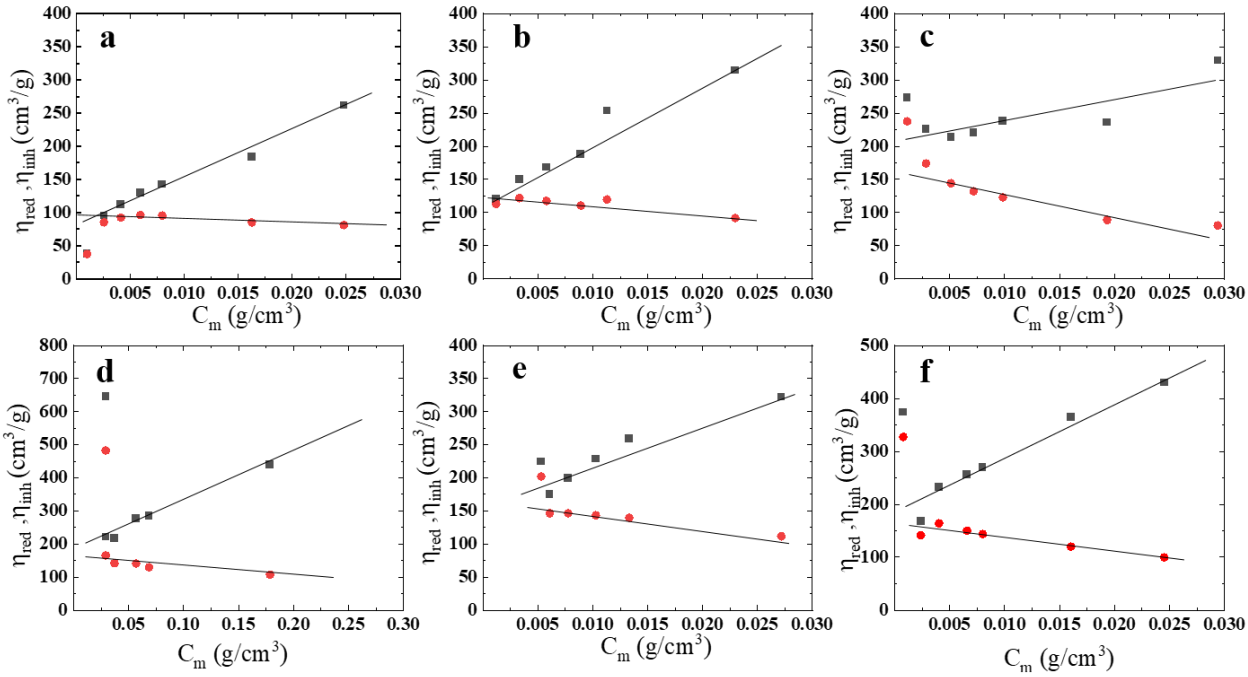

***Figure 51**. Reduced (η_{red}) (■) and inherent (η_{inh}) (●) viscosities as function of the mass concentration for P(VDF-TrFE)-80:20 solutions in (a) ACN, (b) DMSO, (c) CP, (d) TEP, (e) MEK, and (f) Ac. Data are only represented for concentrations below 0.03 g/cm³ to highlight the deviation from linearity in the highly diluted solution regime.*

To account for deviations from linearity in the highly diluted regime, the Fedors method (presented in **Figure 52**) has been applied to extract the intrinsic viscosity [η] from η_{rel}.[23,24] The values for each solvent are reported in **Table 9** and confirm the highly variable solvent quality

with respect to P(VDF-TrFE)-80:20 chains. With the values of [η], it is possible to establish a first ranking of the solvent quality for the P(VDF-TrFE)-80:20, *i.e.*, ACN < DMSO < CP < MEK < TEP < Ac.

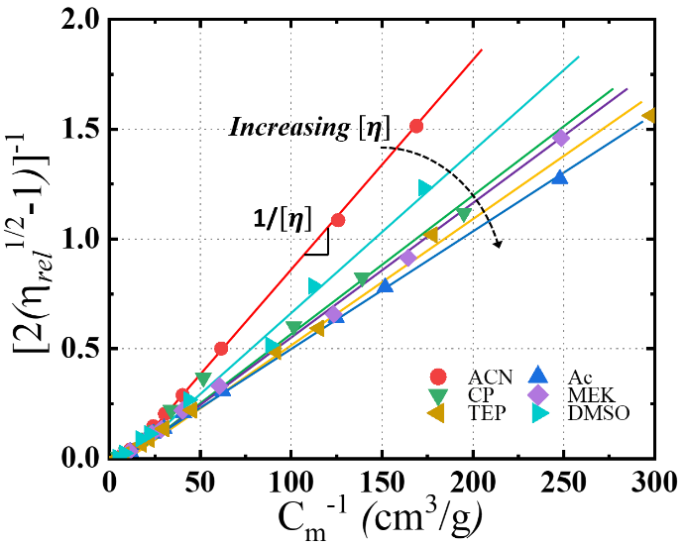

***Figure 52**. Fedors representation of the concentration dependence of the relative viscosity for P(VDF-TrFE)-80:20 in different solvents. The extracted slope represents 1/[η].*

In order to gain additional insights on the solvent quality, we decided to implement the scaling approach described in Chapter 2, which quantitatively ascertains the static and dynamic properties of a polymer/solvent pair from the evolution of solution viscosity in different concentration regimes.[13,14] As reported by the authors, this treatment establishes a polymer/solvent "fingerprint" allowing us to quantify solvent quality and the related modifications of chain conformations.

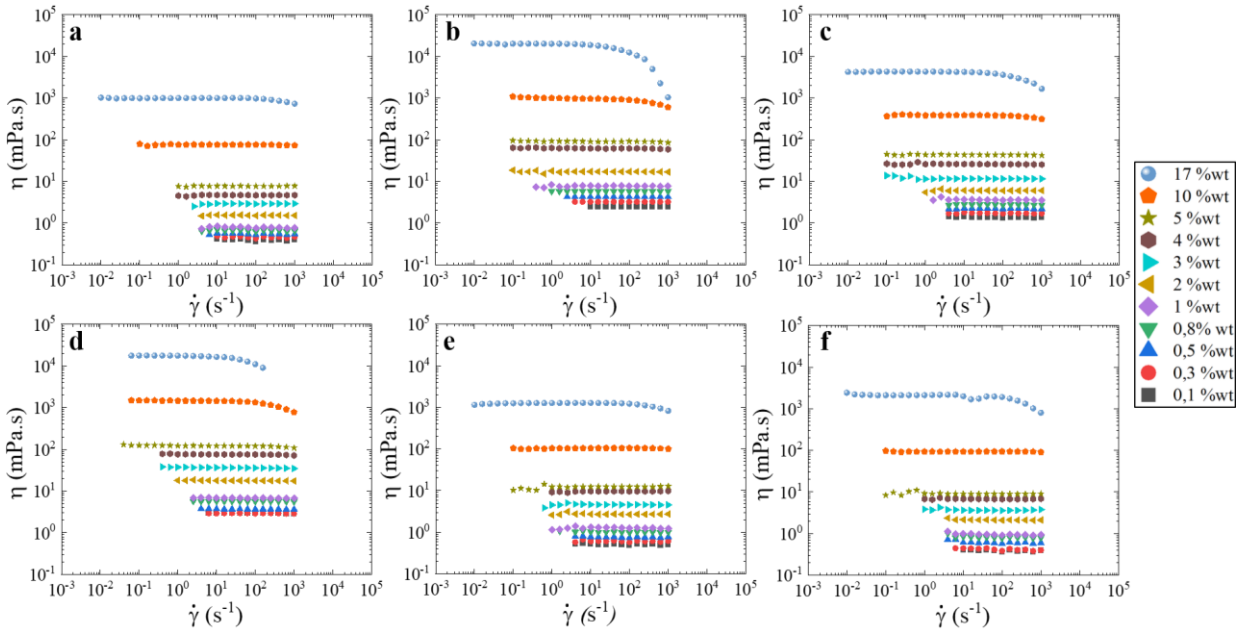

***Figure 53**. Dependence of the viscosity with respect to the shear rate of P(VDF-TrFE)-80:20 polymer solutions at 25 °C in (a) ACN, (b) DMSO, (c) CP, (d) TEP, (e) MEK, (f) Ac, (g) THF for concentrations ranging from 0.1 wt.% to 17 wt.%.*

To do so, P(VDF-TrFE)-80:20 solutions in solvents of various qualities (Ac, ACN, CP, DMSO, MEK, and TEP) were prepared with concentrations ranging from 0.1 wt.% to 17 wt.%. As shown in **Figure 53**, we note that by changing the solvent, the evolution of the viscosity as a function of the concentration is strongly impacted. For all the systems, the viscosity is Newtonian on the range of shear applied under a 5 wt.% concentration. The shear thinning behavior appear at higher concentration for all the systems. Nevertheless, the critical concentration where this shear thinning and the viscosity drop associated appear, is solvent dependent. As an example, at a 17 wt.% concentration, the system dissolved in DMSO exhibits a clear shear thinning around $\dot{\gamma} = 10^2$ s^{-1}, whereas the viscosity decrease in ACN is slightly observable. It is noteworthy that P(VDF-TrFE)-80:20 solutions in different solvents exhibit drastically different absolute values of viscosity for the same solid content: for instance, $\eta_{17\ wt.\%}$ = 20200 mPa.s and $\eta_{17\ wt.\%}$ = 17236 mPa.s in DMSO and TEP, respectively, while $\eta_{17\ wt.\%}$ = 1273 mPa.s and $\eta_{17\ wt.\%}$ = 2116 mPa.s in MEK and Ac, respectively.

3.4 Using scaling arguments to quantify polymer-solvent interactions.

Following the same methodology as described in Chapter 2, **Figure 54** summarizes the experimental apparent viscosity, specific viscosity, and normalized specific viscosity values according to the concentration regimes for all the solvent systems as a function of the monomer concentration, *c*. The chain overlap concentration, *c**, (reached when the correlation blob is equal to the ideal chain size) was directly extracted from **Figure 54**a for the concentration corresponding to η_{sp} = 1. From the normalized representations displayed in **Figure 54**b-d, the value of the polymer/solvent-specific parameters, B_g and B_{th}, as well as the crossover concentrations, c_{th} and *c***, were determined and are summarized in **Table 9**. Additional information such as the Kuhn length in solution, *b*, and the number of monomers per thermal blobs, g_{th}, were also extracted by this treatment and are regrouped in **Table 9** as well. Note that precious information about solvent quality is contained in g_{th} as it immediately indicates the minimum length of a polymer chain for binary polymer-polymer interactions to occur. Accordingly, the best solvents for P(VDF-TrFE)-80:20 are aprotic solvents of medium polarity, *i.e.*, Ac and THF, in accordance with the HSP treatment presented beforehand. Nevertheless, the overall quality of solvents for P(VDF-TrFE)-80:20 only remains θ or "marginally good" as the value of the $c_{th}b^3$ criterion (related to the description of entanglements following either the Kavassalis-Noolandi or the Rubinstein-Colby conjectures) is always lower than 1.

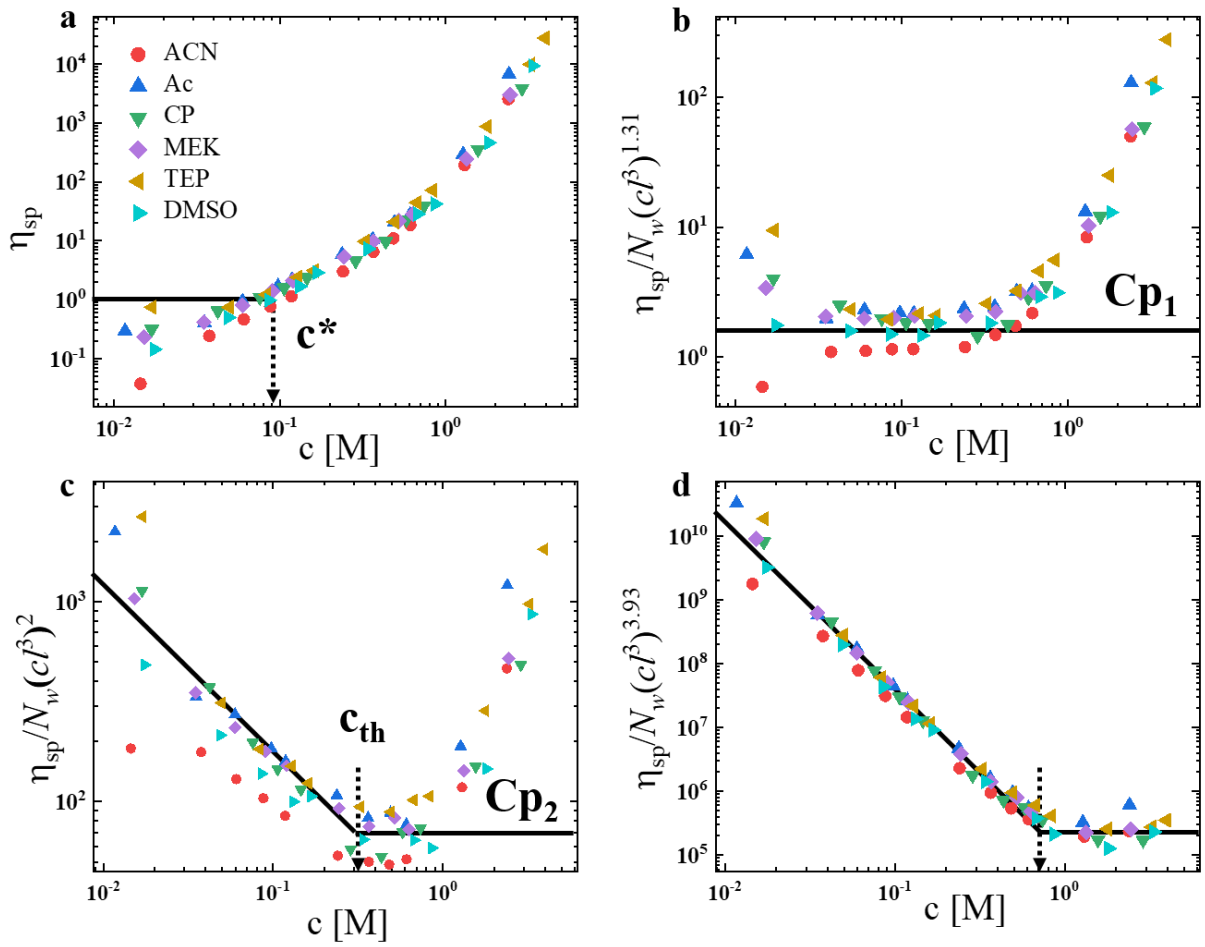

***Figure 54**. Dependence for the P(VDF-TrFE)-80:20 polymer in (●) ACN, (▲) Ac, (▼) CP, (◆) MEK, (◀) TEP, (▶) DMSO, of the (a) specific viscosity and normalized specific viscosity according to the (b) self-avoiding walk regime c*<c<c_{th}, (c) the random walk regime c_{th}<c<c**, and (d) the rod-like regime with the respective scaling exponents ν = 0.588, ν = 0.5 and ν = 1. Lines represent the graphical determination of parameters such as Cp_1, Cp_2, c*, and c_{th} following the treatments explained in Chapter 2.*

***Table 9**. Summary of the parameters extracted for each P(VDF-TrFE)-80:20/solvent couple: cross-over concentrations: chain overlap (c*), thermal blob overlap (c_{th}), concentrated regime (c**) in mol/L [M], Kuhn length (b) in nm, the Rubinstein-Colby parameter ($c_{th}b^3$), the apparent packing number $\tilde{P}_{e,RC}$ and the intrinsic viscosities obtained by the Fedors method.*

Solvent	c*	c_{th}	c**	b	g_{th}	$c_{th}b^3$	$\tilde{P}_{e,RC}$	[η]
	[M].10^{-2}	[M]	[M]	[nm]				[cm^3/g]
Ac	*6.31*	*0.28*	*2.99*	*1.14*	*491*	*0.42*	*12.0*	*190*
MEK	*6.97*	*0.31*	*3.41*	*1.07*	*502*	*0.38*	*13.2*	*171*
CP	*7.11*	*0.29*	*3.6*	*1.04*	*595*	*0.33*	*14.9*	*167*
TEP	*7.54*	*0.21*	*2.70*	*1.20*	*752*	*0.37*	*15.0*	*180*
DMSO	*8.50*	*0.23*	*3.52*	*1.05*	*897*	*0.28*	*15.0*	*135*
ACN	*10.79*	*0.26*	*4.48*	*0.93*	*1056*	*0.21*	*9.6*	*100*

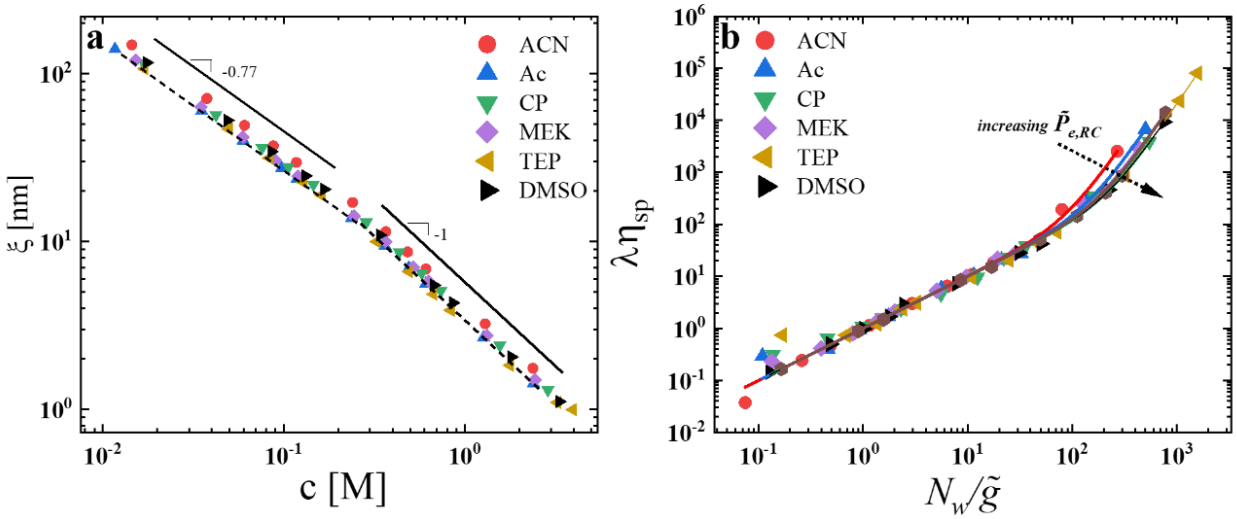

***Figure 55**. (a) variation of the solution correlation length as a function of the concentration in monomer per liter. (b) Dependence of the normalized specific viscosity, $\lambda\eta_{sp}$, on the number of blobs per chain, $N_w/\tilde{g}$, and the impact on the apparent normalized packing number $\tilde{P}_{e,RC}$ in (●) ACN, (▲) Ac, (▼) CP, (♦) MEK, (◀) TEP, and (▶) DMSO.*

These data can then be used to determine the solution correlation length, ξ, as a function of the monomer concentration as shown in **Figure 55**a. Further information can be extracted by determining the apparent packing number (*i.e.*, the number of entanglement strands per tube

diameter) normalized by accounting for the Rubinstein-Colby conjecture, $\tilde{P}_{e,RC}$. Systems presenting a high value of $\tilde{P}_{e,RC}$ are expected to have a large number of entanglements in the concentrated regime, resulting in a higher viscosity at equal concentration. **Figure 55**b shows the normalized specific viscosity, $\lambda\eta_{sp}$, as a function of the number of blobs per chain, $N_w/\tilde{g}$, for the various solvents examined in this study, from which the values of $\tilde{P}_{e,RC}$ can be extracted (see **Table 9**). As anticipated, $\tilde{P}_{e,RC}$ is strongly dependent on the solvent nature with a value close to 15 for DMSO, CP, and TEP, whereas a value as low as 9.6 is retrieved for ACN. Accordingly, systems with high $\tilde{P}_{e,RC}$ display higher viscosity in the concentrated regime, *i.e.*, for c > c^{**}, the regime in which the entanglement state of the polymer solutions predominantly drives the macroscopic viscosity value (with respect to the solvent quality parameter, g_{th}).

3.5 Correlation between polymer-solvent fingerprint and chain conformation

To assess the evolution of the chain conformation and possible co-assembly linked to solvent quality, LS experiments were performed on dilute solutions. Three systems of interest with distinct solvent quality, *i.e.*, Ac, CP, and DMSO, were selected to perform dynamic and static light scattering measurements. **Figure 56**a-c shows DLS correlograms for the three solvents for all the probed angular values (30°-150°) with in insets the density distribution *vs.* decay time. All systems show a rather unique population of objects with a clear angular dependence of the decay time, and it is evident that the scattered intensity is strongly influenced by the solvent quality, with maximum scattered intensity for DMSO. Further treatment of these data yields the extraction of the q^2 dependence of the relaxation rate, Γ, from which the translational diffusion coefficient, D, and the hydrodynamic radius, R_H, were retrieved using the Stokes-Einstein equation (see **Figure 56**d). Significant variations in R_H values were observed for the different solvents with R_H(Ac) = 37.3 nm, R_H(CP) = 16.7 nm, and R_H(DMSO) = 15.6 nm. This can be directly understood by considering the solvent quality and the related change of chain conformation: the low g_{th} value of Ac produces a more extended conformation of the P(VDF-TrFE) chains while the poor quality of DMSO (reflected by a higher g_{th} value) favors chain collapse. However, the presence of larger

objects can be observed in the Ac system as the linearity of q^2 as a function of the relaxation rate Γ is lost at higher q^2 values. The presence of aggregates in the different systems is confirmed by the second relaxation mode at higher lag times. Smaller pore size filter was used to remove aggregates further confirming their presence. Some examples of clear aggregation are displayed in annex (see **FigureS3**- 1). For those systems, the correlograms and the distribution density of the relaxation time show the dispersity of the objects present in the solution. Consequently, the aggregation can be easily observed as long relaxation times are present interpreted as the signature of large objects in solution.

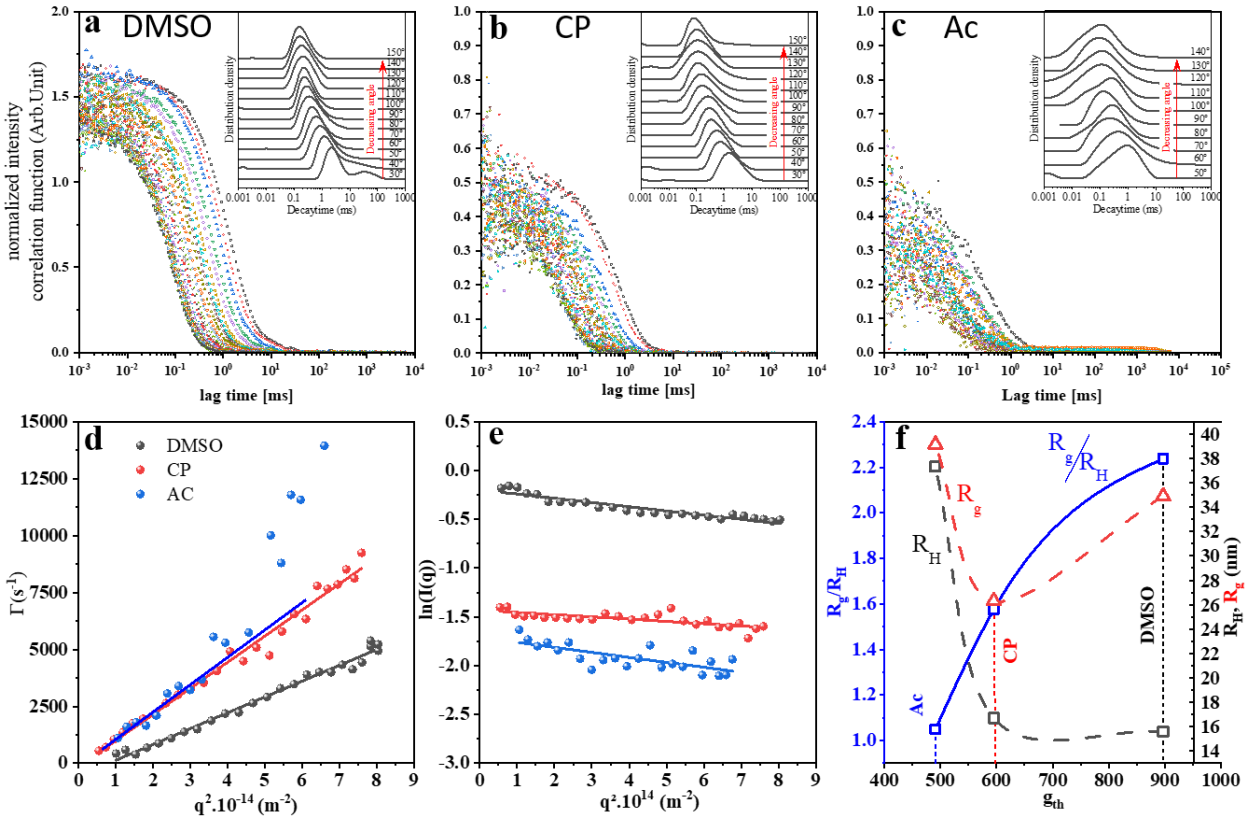

***Figure 56**. DLS correlograms of P(VDF-TrFE)-80:20 solutions in (a) DMSO (b) CP and (c) Ac. The insets represent the distribution density of the decay time (1/Γ) at different angles. (d) q^2 dependence of the relaxation rate Γ for the systems in (●) DMSO, (●) CP, and (●) Ac. The diffusion coefficient has been extracted from the slopes for low q^2 values. (e) Guinier plot and the associated linear fittings for the three different systems. (f) evolution of the ratio (R_g/R_H), R_g and R_H for the three systems as function of the solvent quality represented by the g_{th} parameter.*

SLS data were also acquired for angular values between 30° and 150° and the corresponding Guinier plots are presented in **Figure 56**e, for the three different solvents. The radius of gyration, R_g, was directly extracted from these plots using the Guinier approximation yielding R_g(Ac) = 39.1 nm, R_g(CP) = 26.3 nm and R_g(DMSO) = 34.9 nm. Accordingly, the R_g/R_H ratio shows a strong dependency on the solvent used for the P(VDF-TrFE) solubilisation as depicted in **Figure 56**f. For low g_{th} value (*i.e.*, Ac), R_g/R_H is close to 1 which hints at the formation of spherical objects. As opposed, the high g_{th} value of the P(VDF-TrFE) chain in DMSO is associated with higher R_g/R_H with a value around 2.2. Such value is often associated with the formation of elongated rod-like objects. These observations fully agree with the treatment of the viscosimetric data. From this dataset, the higher viscosity system can be represented as systems in DMSO. A system in DMSO is described as a low solvent quality and having an extended conformation. On the other hand, other behaviour represented by the Ac system displays lower viscosities. In this case, the conformation of the chain is linked to favorable interactions with the solvent leading to a swollen spherical shape of the copolymer in the solvent media.

3.6 Conformational change as function of the P(VDF-TrFE) composition

In this chapter, we mainly focused on the P(VDF-TrFE)-80:20 composition and the evolution of its chain conformation with solvent quality. Nevertheless, we aimed at deciphering the chain conformation behavior for other compositions. Accordingly, two other copolymer compositions (70:30 and 50:50) were selected to repeat the LS measurements in Ac instead of DMSO. Ac solvent was chosen as it showed to behave as a better solvent for the 80:20 composition and displayed a drastic modification of the chain conformation with respect to the one observed in DMSO.

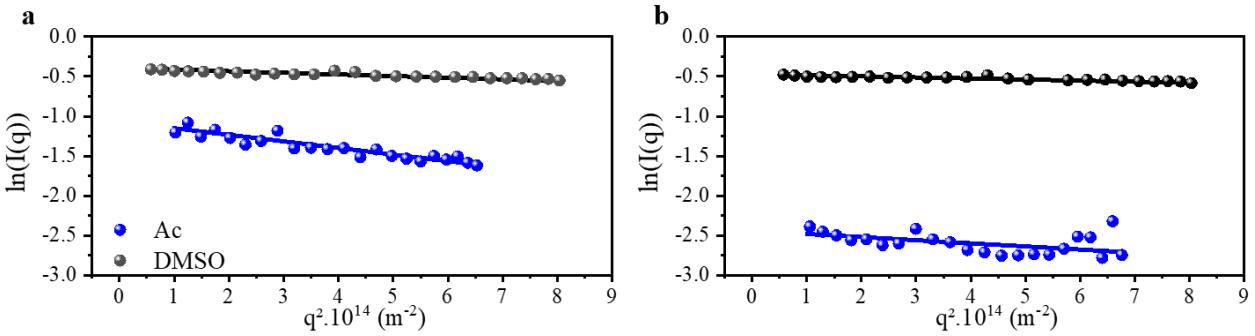

***Figure 57**. (a) and (b) Guinier plots and the associated linear fittings for the compositions P(VDF-TrFE)-70:30 and 50:50 in (●) DMSO and (●) Ac, respectively.*

From **Figure 57**, clear changes are observed in ln($I(q)$)=f(q^2) plot for Ac and DMSO. From the Guinier representation in **Figure 57**, the absolute value of the slope allowing the extraction of the R_g increases for the systems dissolved in Ac. It denotes an increase in the value of R_g with $R_g^{70:30}$(Ac) = 48 nm and $R_g^{50:50}$(Ac) = 36 nm. In DMSO, the Zimm representation allows us to accurately extract the R_g values but such procedure was not applicable to the systems dissolved in Ac as aggregation was detected. This is evidenced as the linearity of Γ was lost at higher q^2 values. The choice has thus been made to compare the R_g values extracted from the Guinier approach for the two systems in DMSO, *i.e*, $R_g^{70:30}$(DMSO) = 21 nm and $R_g^{50:50}$(DMSO) = 17 nm. The values of R_g obtained from the two solvent systems differ, with a R_g(Ac)/R_g(DMSO) > 2, highlighting an expansion of the systems in Ac. That actual expansion of the polymer coil can be linked to the increase of aggregation as more contacts are favored between two polymer chains.

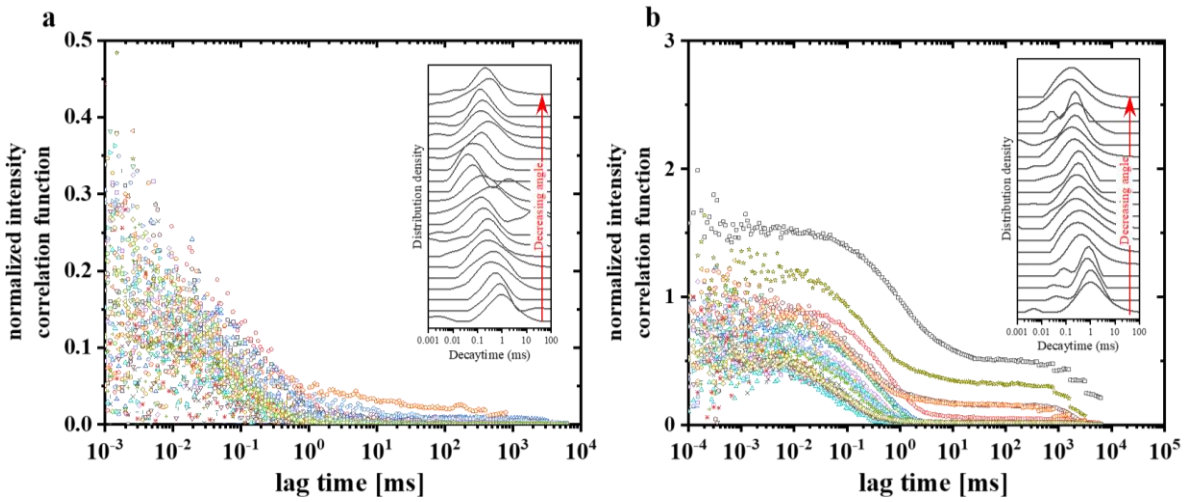

***Figure 58**. DLS correlograms of (a) P(VDF-TrFE)-50:50 and (b) P(VDF-TrFE)-70:30 solutions in Ac. The insets represent the distribution density of the decay time (1/Γ) at different angles.*

The values of the R_H were retrieved using the Stokes-Einstein equation with the dependence of Γ with q^2 (**Figure 59**). The presence of aggregates is further established as the linearity is lost for wavenumbers higher than $q^2 = 6.10^{-14}$ m^{-2}. The Stokes-Einstein relationship was applied to the linear section allowing the determination of $R_H^{70:30}$(Ac) = 101 nm, and $R_H^{50:50}$(Ac) = 47 nm. The values of R_H obtained for these compositions in Ac are higher than in DMSO as $R_H^{70:30}$(DMSO) = 13 nm, and $R_H^{50:50}$(DMSO) = 13 nm. Such differences were also observed for the 80:20 composition, clearly demonstrating that the high solvent quality of Ac leads to a more expanded chain conformation for the range of composition probed in this study.

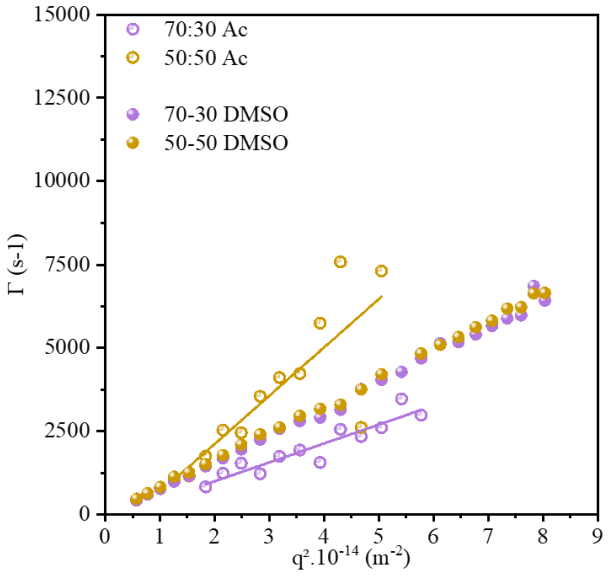

***Figure 59**. q^2 dependence of the relaxation rate Γ for the systems 70:30 and 50:50 dissolved in Ac (hollow sphere) and DMSO (solid sphere). The diffusion coefficient has been extracted from the slopes at low q^2 values. Higher q^2 values are not displayed for clarity.*

However, the high values of R_H obtained by DLS can be misinterpreted as the presence of aggregates was clearly observed as attested by long relaxation times affecting their distribution. In addition, the pronounced expansion of the chain in Ac have been shown to favor aggregation.

***Table 10**. Values of R_g and R_H for the three different copolymer composition 80:20, 70:30, and 50:50 determined by the Guinier approximation and Stokes-Einstein relationship, respectively.*

Composition	**R_H (nm)**		**R_g (nm)**		**R_g/R_H**	
	Ac	**DMSO**	**Ac**	**DMSO**	**Ac**	**DMSO**
80:20	37	15.6	39	35	1.05	2.24
70:30	101	13.2	48	21	0.47	1.59
50:50	47	13.1	36	17	0.76	1.29

The shape factor ($\rho = R_g/R_H$)[25–27] is readily extractable from these data and the values are reported in **Table 10** for the three different copolymers dissolved in Ac and DMSO. For all the

systems, the ratio R_g/R_H is superior to 1 and, as discussed in the previous chapter, it describes an elongated object. Passing from DMSO to Ac, the ρ value dropped from 2.24 to 1 for the 80:20 composition highlighting the transition to a swollen spherical object. The same statement is also applicable for the two other compositions as ρ is higher than 1 in DMSO shifted to a ratio value of $\rho^{70:30}$(Ac) = 0.47 and $\rho^{50:50}$(Ac) = 0.76. Even if the presence of aggregates leading to a possible overestimation of the R_H has to be taken into account, the size expansion and the transition to a spherical object by modifying the solvent quality to Ac is established over the range of compositions.

3.7 Conclusions

In Chapter 2, our investigation underscored the significant impact of incorporating TrFE units on the solubility enhancement of P(VDF-TrFE) in comparison to neat PVDF. The increase of polarizability of the copolymer highlighted the role of dipolar interactions in solution, as initially evidenced by changes in solubility. In this chapter, we conducted viscosity measurements across a diverse set of solvents, pinpointing the substantial influence of solvent nature on the viscosity of P(VDF-TrFE) solutions. Applying a scaling approach based on the evolution of normalized specific viscosities with increasing concentrations, we successfully elucidated the intricate relationship between solvent nature, solvent quality, and key conformational parameters, including the critical and overlap concentrations, the thermal blob size, and packing number. Notably, our findings demonstrated that, regardless of the solvent system, the polymer chain predominantly behaves as polymer chains in θ-conditions.

Further observations of the chain conformation in the dilute regime and in solvents of distinct qualities were performed through LS experiments in three solvents (Ac, CP, and DMSO), and further revealed the evolution of the polymeric chain conformation shape with solvent quality, as previously extracted using the parameter g_{th}. In lower-quality solvents such as DMSO, we observed a reduction in steric repulsion and solvent-mediated attraction between monomers, resulting in the collapse of the chain into an elongated structure. Conversely, in better solvents

such as Ac, the chains swelled, with monomer repulsion prevailing over solvent-induced attraction, leading to a swollen spherical structure.

Remarkably, low-quality solvents exhibited higher viscosities compared to good-quality solvents, shedding light on the dependence of viscosity on solvent quality for printing applications. Accordingly, our study provides valuable insights that could lead to improvements in ink formulation.

3.8 Materials and Methods:

The characteristics of the materials used in this chapter are reported in chapter 2. Furthermore, the details concerning light scattering, viscosity measurements and the scaling approach are also given in chapter 2.

Annex chapter 3:

TableS3- 1. *Recapitulative of the different parameters extracted from the scaling approach and the intrinsic viscosity from Fedors method of the P(VDF-TrFE):80-20 in various solvents.*

Solvent	C_{p1}	B_g	C_{p2}	B_{th}	c^*	c_{th}	c^{**}	b	g_{th}	$c_{th}\,b^3$	$\tilde{P}_{e,RC}$	[η]
					[M].10^{-2}	[M]	[M]	[*nm*]				[cm^3/g]
Ac	*2.23*	*0.81*	*82.89*	*0.47*	*6.31*	*0.28*	*2.99*	*1.14*	*491*	*0.42*	*11.95*	*190*
MEK	*1.95*	*0.84*	*77.00*	*0.48*	*6.97*	*0.31*	*3.41*	*1.07*	*502*	*0.38*	*13.18*	*171*
CP	*1.74*	*0.86*	*54.09*	*0.49*	*7.11*	*0.29*	*3.6*	*1.04*	*595*	*0.33*	*14.90*	*167*
TEP	*2.13*	*0.82*	*97.16*	*0.46*	*7.54*	*0.21*	*2.70*	*1.20*	*752*	*0.37*	*15.00*	*180*
DMSO	*1.54*	*0.89*	*64.21*	*0.49*	*8.50*	*0.23*	*3.52*	*1.05*	*897*	*0.28*	*15.05*	*135*
ACN	*1.15*	*0.96*	*50.57*	*0.52*	*10.79*	*0.26*	*4.48*	*0.93*	*1056*	*0.21*	*9.64*	*100*

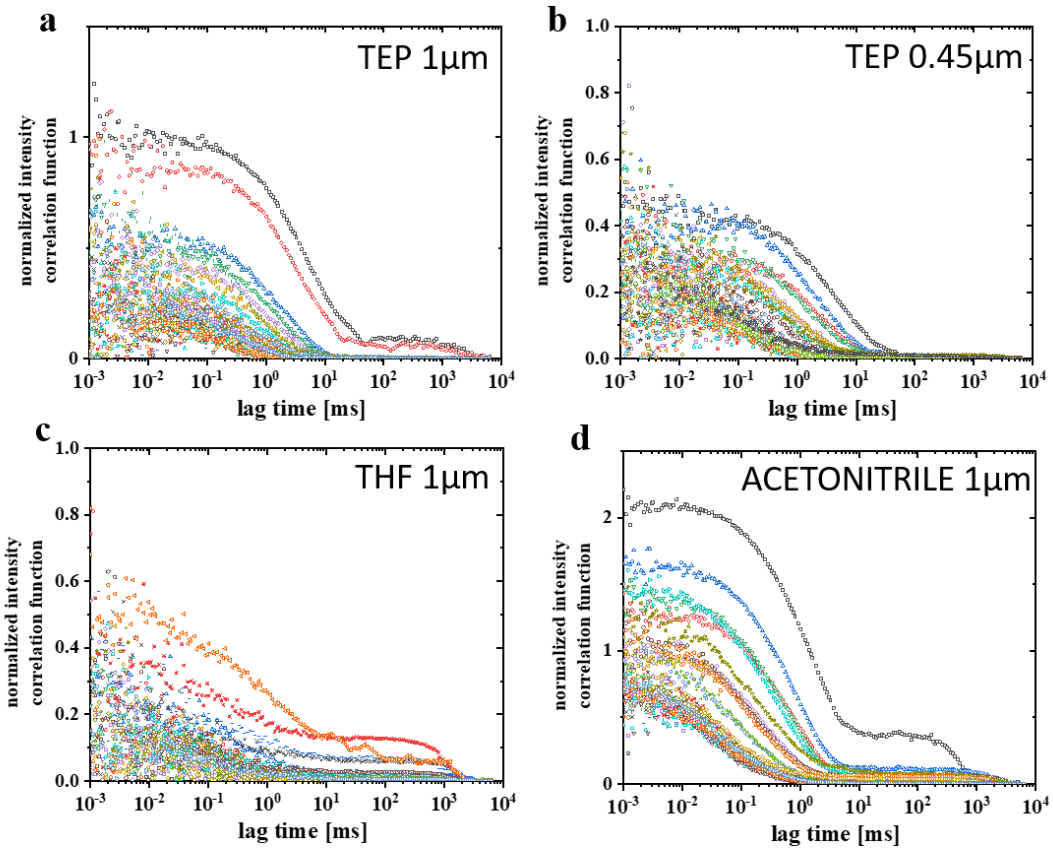

FigureS3*- 1. MA-DLS of the polymer in (a,b) TEP, (c) THF (d) ACN solvents with prior filtration at 1µm and 0.45µm pore size PTFE filter, as indicated.*

References

1. Glasser, A., Cloutet, E., Hadziioannou, G., Kellay, H. & Cloutet, É. Tuning the rheology of polymer conducting inks for various deposition processes. doi:10.1021/acs.chemmater.9b01387ï.
2. Hoath, S. D., Harlen, O. G. & Hutchings, I. M. Jetting behavior of polymer solutions in drop-on-demand inkjet printing. *J. Rheol. (N. Y. N. Y).* **56**, 1109–1127 (2012).
3. Qing, L. *Development of electrostrictive P(VDF-TrFE-CTFE) terpolymer for inkjet printed electromechanical devices*. https://tel.archives-ouvertes.fr/tel-02063349 (2019).
4. Nallan, H. C., Sadie, J. A., Kitsomboonloha, R., Volkman, S. K. & Subramanian, V. Systematic Design of Jettable Nanoparticle-Based Inkjet Inks: Rheology, Acoustics, and Jettability. *langmuir* **30**, 13470–13477 (2014).
5. Derby, B. Inkjet printing of functional and structural materials: Fluid property requirements, feature stability, and resolution. *Annu. Rev. Mater. Res.* **40**, 395–414 (2010).
6. Haque, R. I. *et al.* Inkjet printing of high molecular weight PVDF-TrFE for flexible electronics. *Flex. Print. Electron.* **1**, (2016).
7. Neidert, M., Zhang, W., Zhang, D. & Kipka, A. Screen-printing simulation study on solar cell front side AG paste. *Conf. Rec. IEEE Photovolt. Spec. Conf.* 14–17 (2008) doi:10.1109/PVSC.2008.4922793.
8. Szentgyörgyvölgyi, R., Novotny, E. & Weimert, M. determining and selecting screen printing form parameters for printing on paper textile. (2018) doi:10.24867/grid-2018-p42.
9. Kapur, N., Abbott, S. J., Dolden, E. D. & Gaskell, P. H. Predicting the behavior of screen printing. *IEEE Trans. Components, Packag. Manuf. Technol.* **3**, 508–515 (2013).
10. Xu, C. Screen Printing and Rheology of Pastes. (2019).
11. Schlisske, S. *et al.* Ink Formulation for Printed Organic Electronics: Investigating Effects of Aggregation on Structure and Rheology of Functional Inks Based on Conjugated Polymers in Mixed Solvents. *Adv. Mater. Technol.* **6**, (2021).
12. Ueki, M. M. & Zanin, M. Influence of additives on the dielectric strength of high-density polyethylene. *IEEE Trans. Dielectr. Electr. Insul.* **6**, 876–881 (1999).
13. Dobrynin, A. V, Jacobs, M. & Sayko, R. Scaling of Polymer Solutions as a Quantitative Tool. *Macromolecules* **54**, 2288–2295 (2021).
14. Dobrynin, A. V. & Jacobs, M. When Do Polyelectrolytes Entangle? *Macromolecules* **54**, 1859–1869 (2021).
15. Pierre-Gilles Gennes. *Scaling Concepts in Polymer Physics*. (1979).
16. Colby, R. H., Fetters, L. J., Funk, W. G. & Graessley, W. W. Effects of Concentration and Thermodynamic Interaction on the Viscoelastic Properties of Polymer Solutions. *Macromolecules* **24**, 3873–3882 (1991).
17. Abdel-Azim, A. A. A., Atta, A. M., Farahat, M. S. & Boutros, W. Y. Determination of intrinsic viscosity of polymeric compounds through a single specific viscosity measurement. *Polymer (Guildf).* **39**, 6827–6833 (1998).

18. Gandhi, K. S. & Williams, M. C. solvent effect on the viscosity of moderately concentrated polymer solutions. *J. Polym. Sci. Part C* **35**, 211–234 (1971).
19. Zakin, J. L., Wu, R., Luh, H. & Mayhan, K. G. *Generalized Correlations for Molecular Weight and Concentration Dependence of Zero-Shear Viscosity of High Polymer Solutions*. *journal of polymer science : polymer physics edition* vol. 14 (1976).
20. Ovejero, G., Pérez, P., Romero, M. D., Guzmán, I. & Díez, E. Solubility and Flory Huggins parameters of SBES, poly(styrene-b-butene/ethylene-b-styrene) triblock copolymer, determined by intrinsic viscosity. *Eur. Polym. J.* **43**, 1444–1449 (2007).
21. Vink, H. Viscosity of Polyelectrolyte Solutions. *Die Makromol. Chemie* **131**, 133–145 (1970).
22. Förster, S. & Schmidt, M. Polyelectrolytes in solution. *Adv. Polym. Sci.* **120**, 51–133 (1995).
23. Chimichi, L. & Popescu, F. Determination of intrinsic viscosity for some cationic polyelectrolytes by fedors method. **34**, 13–16 (1998).
24. Fedors, R. F. An equation suitable for describing the viscosity of dilute to moderately concentrated polymer solutions. *Polymer (Guildf).* **20**, 225–228 (1979).
25. Rizos, A. K., Spandidos, D. A. & Krambovitis, E. Light scattering characterization of synthetic MUC-1 peptides and their behavior in dilute solution. *Int. J. Mol. Med.* **12**, 559–563 (2003).
26. Dünweg, B., Reith, D., Steinhauser, M. & Kremer, K. corrections to scaling in the hydrodynamic properties of dilute polymer solutions. *J. Chem. Phys* **117**, 55 (2002).
27. Wu, C. & Zhou, S. Thermodynamically Stable Globule State of a Single Polyt(N-isopropylacrylamide) Chain in Water. *Macromolecules* **28**, 5388–5390 (1995).

CHAPTER 4:

Optimization of fully screen printed PVDF-based organic piezoelectric devices

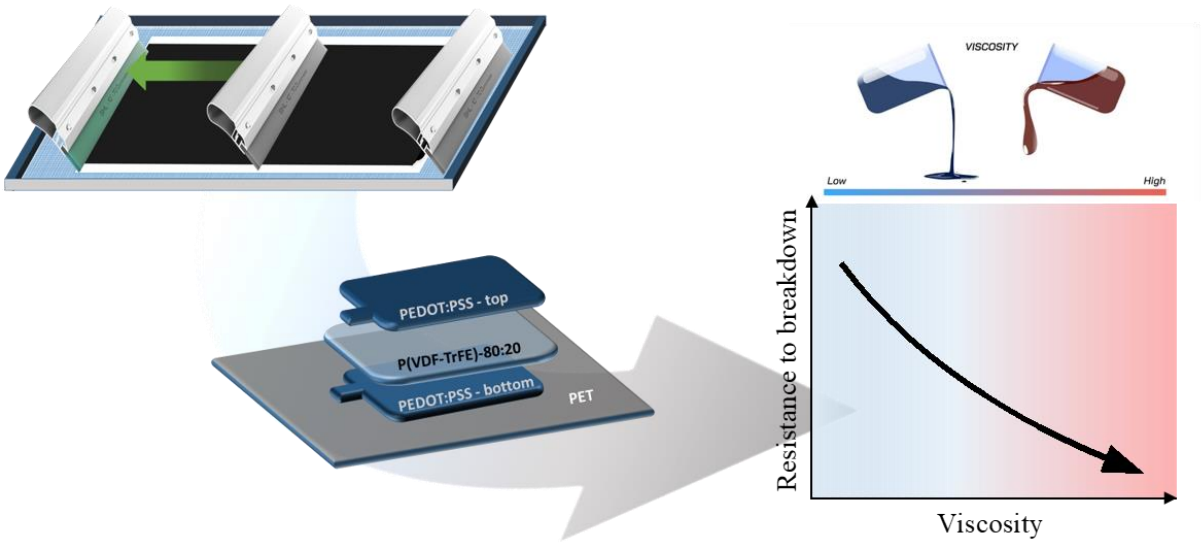

Chapter 4: Optimization of fully screen printed PVDF-based organic piezoelectric devices

In the two previous chapters, we devoted a particular attention to the behavior of inks formulated in various solvents for different compositions of P(VDF-TrFE). In this chapter, we will focus on the processing of these inks using the screen-printing technology and in agreement with industrial standards such as solvent evaporation rate and solvent toxicity. The main objective is to correlate the ink rheological properties to their printability and their electroactive properties. To do so, we based our approach on the utilization of a commercial solution, named “ink P”, containing 17 wt.% of P(VDF-TrFE)-80:20 in TEP provided by Arkema Piezotech. Several solvents of different qualities were evaluated in the previous chapter (DMSO, CP, Ac) and their effect on the chain conformation and viscosity of the formulations was studied. However, from the processing the point of view, it is hard to achieve reliable printings with very low or high boiling point inducing a very fast or slow drying. Moreover, environmental concerns limit the use of non-green solvent for such large-scale process. Consequently, the first step of this study was dedicated to the use of this “ink P” as a reference and to gauge its printability according to the specificities of the printing parameters such as the meshing geometry of the screens.

This ink was then compared to a homologous ink with a lower copolymer content, *i.e.*, 13 wt.%, in terms of ink printability, as well as with respect to the structure and morphology of the deposited films. The extracted data for inks formulated in TEP were then compared with other solvent formulations.

Accordingly, we first examined the rheological behaviors of these ink formulations using steady shear and thixotropy measurements. Then, we evaluated the printability of the inks depending on the meshing geometry which was shown to dictate the thickness and the roughness of the layers. Finally, we proposed a method to optimize the formulation and processing of these inks for screen printing purposes.

4.1 Introducing the process specificities and problematics

Screen-printing is commonly used in industry to laminate organic-based functional devices as it allows with the ever-increasing demand for mass production at low cost. The quality of deposition plays a crucial role in the performance of the final devices. Extensive research has been carried out to examine how different deposition parameters and how ink formulations impact the printing quality and dielectric performance for screen-printed inks and pastes. Due to its complexity, the screen-printing process has for long time been treated like an art without any conceptual models. The process of screen printing is represented in **Figure 60**. The ink containing the material of interest is first deposited on a fabric screen. This screen fabric, composed either of nylon or steel threads, is patterned to allow the ink flow at predetermined positions. The squeegee movement induces the impregnation of the mesh with ink and the subsequent transfer of ink onto the substrate, ultimately revealing the intended pattern.

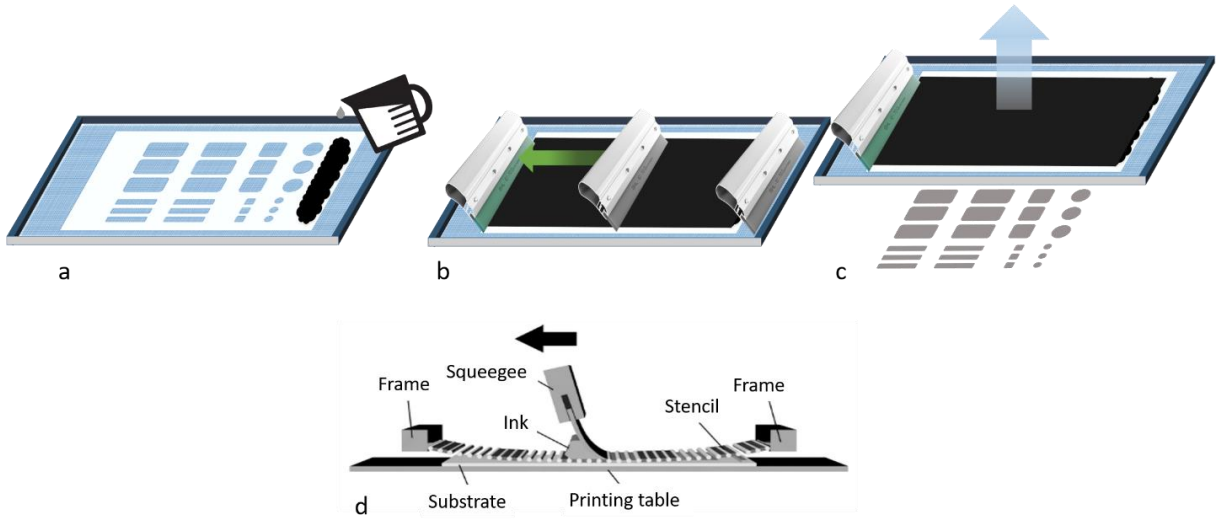

***Figure 60**. Simplified screen-printing procedure: (a) disposition of the ink on the screen (b) impregnation of the mesh and deposition on the substrate (c) removal of the screen and final pattern (d) side view of the screen printing deposition adapted from Novaković et al.*[1]

To achieve high-quality printing and ensure proper ink deposition, several key parameters must be carefully considered, as they are closely linked to the quality of the final print:

- Squeegee speed: the speed of the squeegee is a critical factor. If the speed is too high, there is a risk that the ink may not transfer correctly from the screen to the substrate, resulting in subpar prints.
- Snap-off distance: finding the right conditions for the screen to detach swiftly behind the squeegee is essential. This separation should ensure that the fabric forms a straight line from where the screen touches the substrate to where it attaches to the frame. An excessively large snap-off distance can lead to “aggressive” ink release from the mesh, potentially causing ink bridges or ink dropping onto the screen, especially when dealing with highly viscous ink.
- Ink formulation: Achieving the correct balance of solid content and rheological properties is crucial for obtaining well-defined patterns and enhancing printability.
- Meshing geometry: similar to increasing the number of pixels in a digital image to enhance its quality, in screen printing, a high-quality print can be achieved by reducing the mesh open area and thread diameter. This allows for more intricate and finely detailed prints, contributing to the overall print resolution and quality.

The optimization of this intricate process can be time-consuming due to its complexity. In this study, our primary focus was to assess how meshing geometry and ink formulation contribute to the quality of depositions. We initially determined the optimal screen geometry for the specific “inkP” formulation, which contains 17 wt.% of P(VDF-TrFE)-80:20, and its counterpart at 13 wt.%. The underlying objective was to systematically analyze the impact of decreasing the P(VDF-TrFE) content on viscosity and printability. This approach aimed to rationalize the diverse rheological behaviors observed in previous chapters, with respect to the solution concentration and solvent quality.

4.2 Ink rheological characterization

Primary rheological characterization consists of measuring the ink viscosity for different copolymer concentrations in TEP as shown in **Figure 61**.

From this first approach, we observed that the amount of polymer strongly influences the solution viscosity according to the different regimes: semi-dilute, semi-dilute with overlap of the thermal blobs, and concentrated. The zero-shear viscosity taken on the Newtonian plateau is 2.9 mPa.s for 0.1 wt.% solution while it is 16636 mPa.s for the most concentrated solution at 17 wt.%. **Figure 61**b. further highlights that, above 1 wt.% concentration, the viscosity increases exponentially as the semi dilute regime over the overlap of the thermal blob is crossed. For the concentration of interest for screen-printing, it is easy to visualize this increase by comparing the viscosity of the 17 wt.% solution (16636 mPa.s) with the viscosity of the 13 wt.% solution (4800 mPa.s). This effect is a direct consequence of the different solution regimes presented in **Figure 61**c. From the representation of the correlation length as a function of the concentration, it is indeed possible to attest of a modification of the concentration regimes. In the case of the copolymer 80:20 in TEP, the concentrated regime is achieved for c** = 14.4 wt.%, *i.e.*, at the crossover of the -1 and -0.5 slopes. This critical value being located between 13 wt.% and 17 wt.% explains the drastic viscosity change observed in **Figure 61**b.

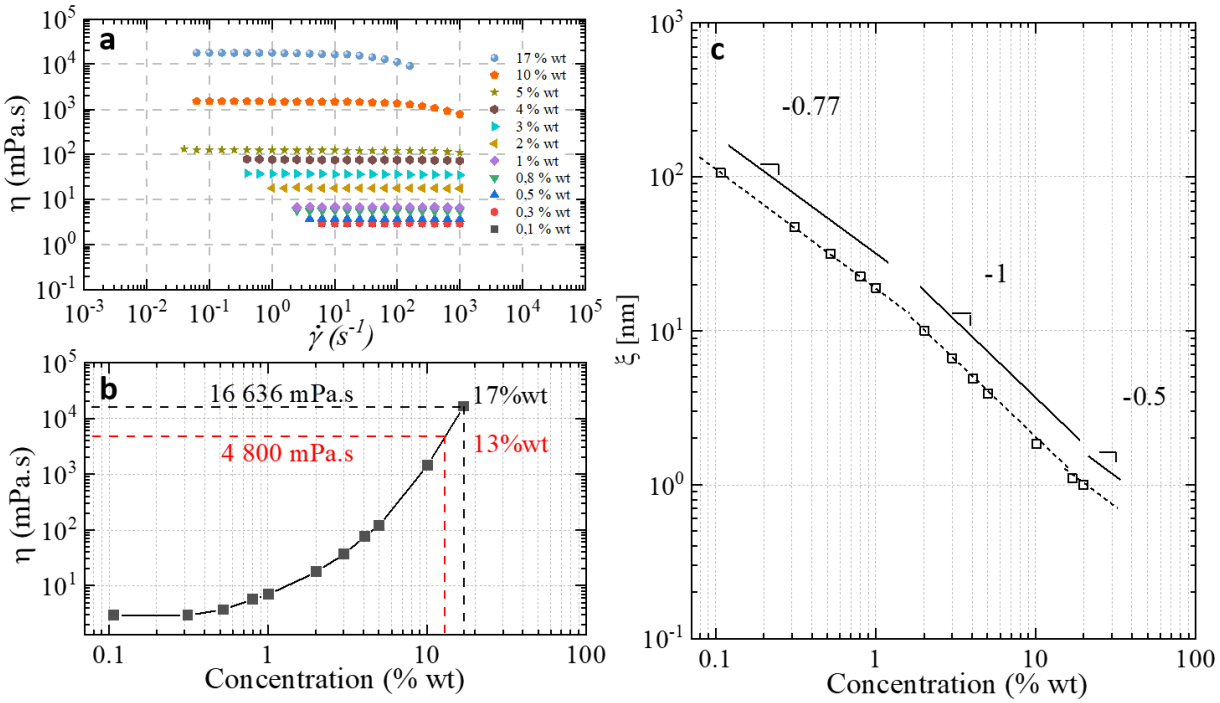

***Figure 61**. (a) Steady shear measurements of inks prepared with a different concentration in TEP. (b) Evolution of the viscosity as function of the concentration of copolymer. (c) Evolution of the correlation length, ξ, as function of the mass percentage of polymer in TEP. The different slopes correspond to the evolution of ξ for the different solution regimes corresponding to the semi-dilute, semi-dilute with the overlap of the thermal blobs, and the concentrated regimes.*

Entanglements in polymer solutions highly contribute to the rheological properties as they act as constraints for the solution flow. As the two studied concentrations are located in two distinct solution regimes, the thixotropic behavior is also expected to differ drastically. It was also reported that the meshing of the screens modified the shear applied to the inks while performing the deposition.[2,4] A three interval thixotropic test (3ITT) was performed on the two formulations and the results are presented in **Figure 62**. This procedure is designed to simulate the various stages undergone by the ink during the screen-printing process. Each interval corresponds to a specific step in the process:

- The first interval (interval 1) the ink resting on the screen prior to the printing. An oscillatory shear with a 1% strain amplitude was applied to the ink allowing the extraction of the complex viscosity η*.

- The second interval (interval 2) is representative of the printing step, where the squeegee stroke pushes the ink through the mesh onto the substrate. This step is materialized by the application of a continuous shear for 20 s.
- Finally, the third step (interval 3) represents the end of the process, when the ink is no longer subjected to external forces. This interval is simulated by a oscillatory shear with a 1% strain amplitude inorder to retrieve the complex viscosity η*.

To evaluate the effect of different meshing during the printing process, several shear values were applied to the inks during the steady shear interval (interval 2) before observing their recovery (interval 3).

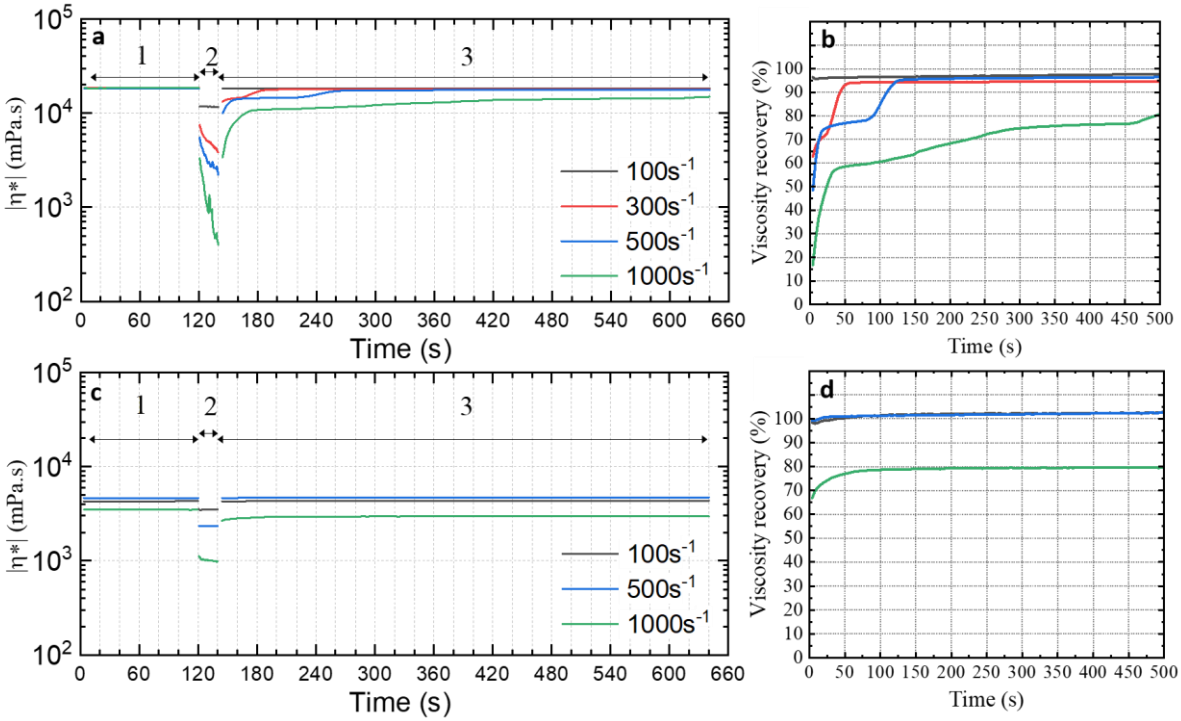

***Figure 62**. a) 3ITT measurements for different continuous shear values of ink at 17 wt.% ("ink P") and b) its viscosity recovery. c) 3ITT measurements for different continuous shear values for the 13 wt.% ink and d) its recovery. Each measurement was performed on a newly deposited ink.*

The thixotropic measurements clearly reveal a significant difference between the two inks. When we transition from interval 1 to interval 2, there is a notable drop in viscosity due to

the shear-thinning behavior of the inks. Specifically, for the 17 wt.% ink, we observe a substantial viscosity drop of 15 Pa.s at a shear rate of 1000 s^{-1}, whereas the 13 wt.% ink experiences a much smaller drop of only 2 Pa.s at the same shear rate.

The recovery of the inks is influenced by both the polymer content and the previously applied shear rate, especially for the 17 wt.% ink. During interval 3, we notice that a complete recovery is never achieved, except in the case of a run at 100 s^{-1}, where the total recovery occurs in less than ten seconds. In contrast, for the 13 wt.% ink, the recovery seems less dependent on the shear rate, and full recovery is achieved in tens of seconds. The lower absolute recovery values observed for runs at 1000 s^{-1} can be attributed to ink loss occurring at high rotation speeds, leading to an artificially lower viscosity.

The distinct behavior of these two inks can be ascribed to their shear-thinning properties. This effect becomes more prominent as the polymer concentration in the solution increases, primarily due to enhanced entanglement of polymer chains. When the ink is at a concentration of 17 wt.%, above the critical concentration, c**, it demonstrates a high level of entanglements. During high shear conditions, the process of disentanglement becomes more significant, leading to longer recovery times. This phenomenon explains the observed steps during the recovery phase, as the polymer attempts to return to its initial state. Previous studies by Ravindranath and Wang suggested that these steps result from macroscopic motion, arising from the sample recoiling when the strained entangled network yields, and not directly for abrupt change of solution viscosity.[5,6]

These observations regarding the ink recovery process underscores the critical nature of selecting appropriate printing parameters, particularly the applied shear rate, as it can substantially influence the printed device integrity. In screen printing, shear stresses are particularly predominant during the stroke and snap-off steps, which are largely influenced by the meshing geometry of the screens. To further explore this issue, we opted to assess how the geometric parameters of the screen, including the number of threads per centimeter and thread diameter, impact the behavior of these two ink formulations.

4.3 Benchmarking screen geometries with respect to the “inkP” reference

Eight different screens have been used for this study and the overall procedure for the fabrication of the electroactive devices are reported in the *Materials & Methods* section. Each screen geometry is composed of several vacant spaces of different shapes in order to create a variety of printed geometry, as shown in **Figure 63**.

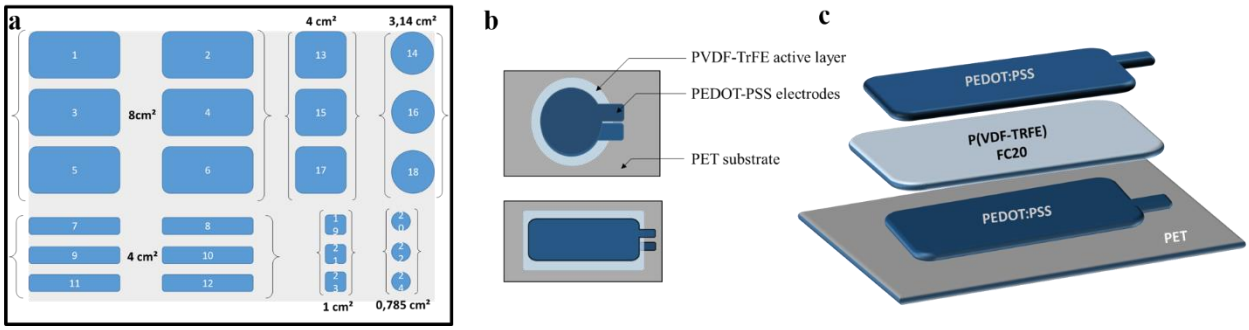

***Figure 63**. (a) Schematic representation of the screen layout comprising 24 different geometries. (b) Top view of the two device geometries fabricated on PET substrate. (c) Exploded view of a multilayer device.*

This pattern was applied on various screen geometries composed of PET wires labelled as [XX – YY], where XX corresponds to the number of threads per cm, and YY represents the diameter of the threads in microns. The various screen geometries include [180-27], [100-40], [71-48], [48-55], [32-70], [32-120], [12-140] and [27-140]. The different screen meshing can also be represented by their open area (*OA*), calculated as $OA = (1-MC \cdot d)^2$, with *MC,* the mesh count per µm and *d* the wire diameter in µm.

4.4 Influence of the screen printing parameters on the film deposition

According to previous studies aimed at predicting the volume of ink transferred from the mesh to the substrate, it is theoretically possible to evaluate the thickness of the deposition.[4] For a general understanding, the flow of a single opening of the 3D meshing structure can be represented in two dimensions as shown in **Figure 64**.

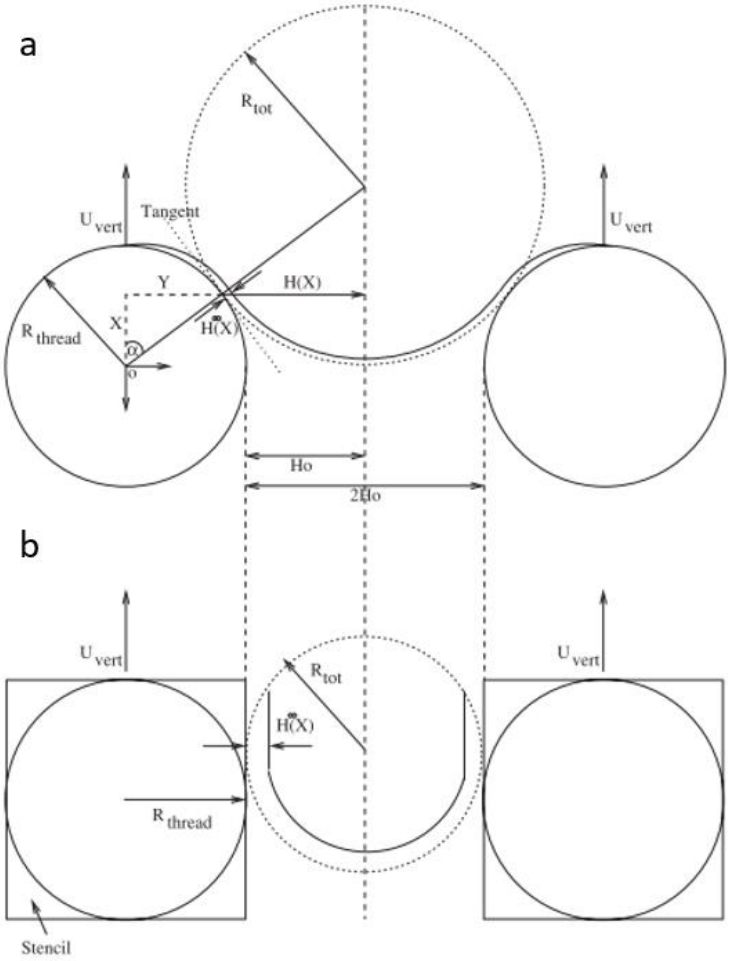

***Figure 64**. Geometry of (a) 2-D mesh and (b) stencilled portion of the mesh with a single opening reproduced from Kapur et al.*[4]

By considering the following assumptions, *i.e.*, incompressibility of the fluid, negligible body forces, no-slip boundary conditions at the surfaces of the substrate and the screen, negligible inertial forces, and a laminar flow, the maximum thickness theoretically achievable (H_{max}) is:

$$H_{max} = 2R_{thread}(2 - \pi\, R_{thread}\, M \sqrt{1 + (2R_{thread}\, M)^2}) \qquad (IV.1)$$

Where R_{thread} represents the thread radius (µm), and M the thread density (µm^{-1}).

The maximum achievable thicknesses for the screens under study have thus been calculated and are presented in **Figure 65**. In this representation, the relationship for H_{max} (maximum thickness) is then adjusted based on the solid content of the ink, expressed in weight percentage (wt.%), which corresponds to the thickness of the dried film.

$$^{wt.\%}(H_{max}) = (wt.\%) \cdot H_{max} \qquad (IV.2)$$

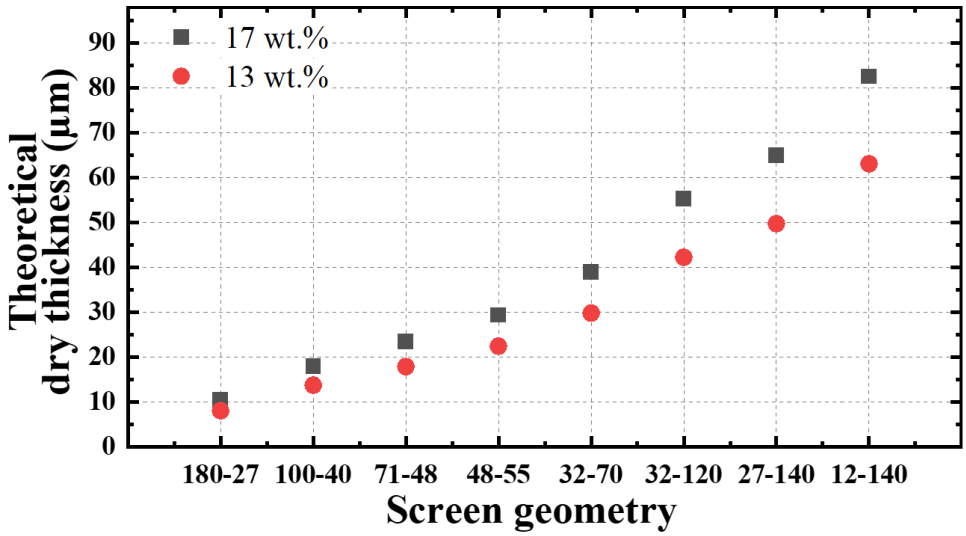

***Figure 65**. Comparison between the theoretical dried thicknesses deposited with various screen geometries for the 17 wt.% and 13 wt.% formulations in TEP.*

From this representation, it is noticeable that the dried thickness deposited is tuneable by the mesh geometry (OA and threads diameter); the minimum values of 8 µm being reached for the low OA and thread diameter screen [180-20], and the maximum thickness of 82 µm for the higher OA and thread diameter screen [12-140]. The value of the thickness is as expected affected by the solid content of polymer present in the ink as it is the only entity remaining after solvent evaporation. This statement results in a noticeable increase of the thickness according to the concentration of the ink. To asses the reliability of this model on our system, a set of deposition was performed with the various screen geometries for different ink concentrations.

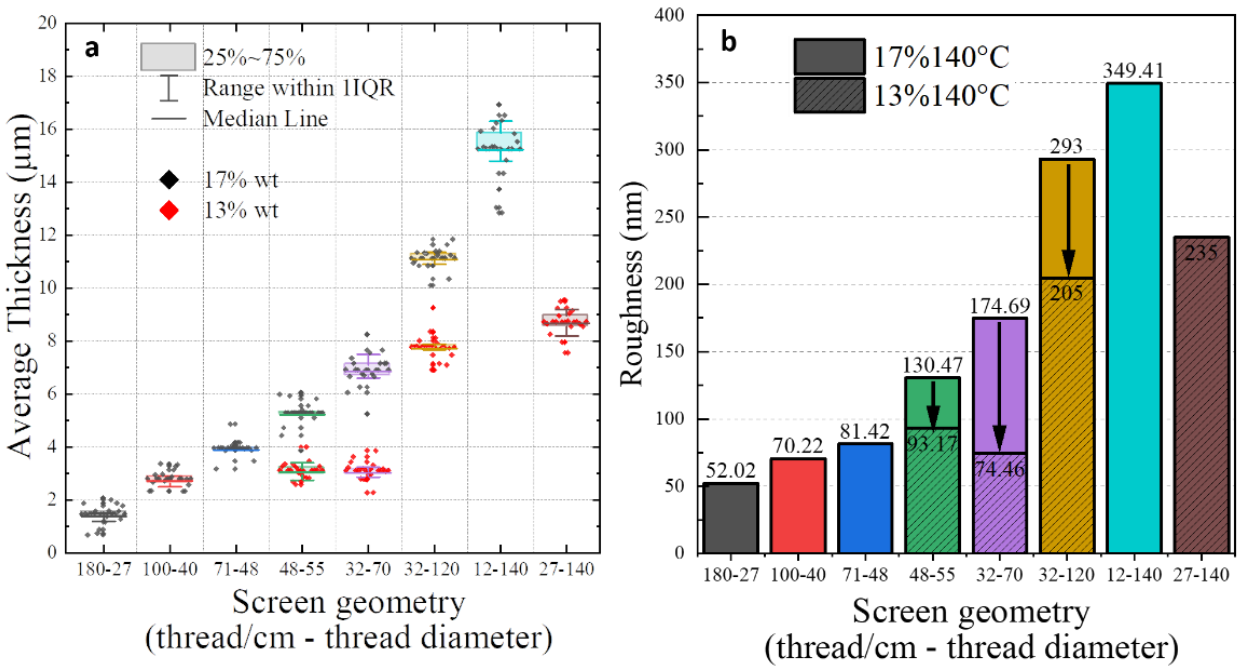

***Figure 66**. (a) Evolution of the thickness of the active layer with the (♦) 17wt.% (♦) 13wt.% solutions in TEP for different screen mesh geometries. The different screen geometries are listed in ascending order of thread diameter. Each dot represents the mean thickness of each device measured by profilometry. The colored box indicates the threshold within which 75% of thicknesses fall, the median line being the median value and the vertical line the range of values in the first quartile. (b) Roughness of the active layer as a function of the meshing used for the 17 wt.% and 13 wt.% inks.*

Irrespective of the concentration used, the thickness of the active layer material depends, as expected, on the mesh size as shown in **Figure 66**a. Screens with higher OA and thread diameter lead to an increase of the layer thickness, as previously underlined by the theoretical predictions. Interestingly, if the initial ink concentration is reduced by 4%, the thickness of the active layer is reduced by approximatively 4%. This observation suggests that the amount of ink deposited in this concentration range is only feebly dependent of the viscoelastic properties of the solutions. It is also noticeable that for wider geometries, the total thickness deposited is less consistent as the presence of outliers increases. Nevertheless, these results highlight the possibility of controlling the thickness deposited by changing the screen meshing for the printing step. Interestingly, when comparing the amount of available ink that can theoretically be deposited with the actual amount of ink transferred to the substrate, the process is not perfect. As shown in

Figure 65, the experimental values of thicknesses obtained for the different geometries are lower than that of the theoretical predictions. These discrepancies could be due to various factors, such as a bad impregnation of the mesh or a lack of adhesion with the substrate resulting in a poor ink transfer.

Another parameter of interest is the roughness of the printed layer. Roughness measurements performed on the active layers highlight the effect of the screen geometry on the surface of the samples. **Figure 66**b shows that increasing the diameter of the threads leads to an increase of the roughness, even if a similar annealing procedure was employed for all devices. The roughness of the active layer can have a negative impact on the device performance, increasing leakage and charge build-up in certain areas.[7] In the following part, we will now examine the influence of the deposition parameters on the morphological and crystalline properties of the printed layers.

4.4.1 Morphological features of the active layers

To assess the impact of the screen meshing geometry, AFM imaging was performed on the active layers. As seen in **Figure 67**, the topography of the layer on a 10x10 µm² range is independent of the screen meshing geometry. The structure is well representative of a thermally annealed P(VDF-TrFE) film with the typical fibrillar crystalline structures.[8] During the process, the annealing was performed at 140 °C to allow a complete evaporation of the solvent and to crystallize the material into the appropriated ferroelectric phase. This process also eliminates imperfections transferred from the screen to the layer, as the mobility of the freshly deposited material is still very high at such a temperature. However, it should be noted that on all the surfaces shown in **Figure 67**, the presence of holes is detected which could subsequently affect breakdown stability. The existence of these holes could tentatively be attributed to the drying process (solvent evaporation) as the vacuum is only turned on during the last 8 minutes of the drying process which lasts 20 min in total. Other works refer to the drying process as being the most impactful for surface topography and homogeneity.[9] Nevertheless, from the overall imaging of the different samples, no difference in the morphological and crystalline features at the surface can be established and associated with the meshing of the screen.

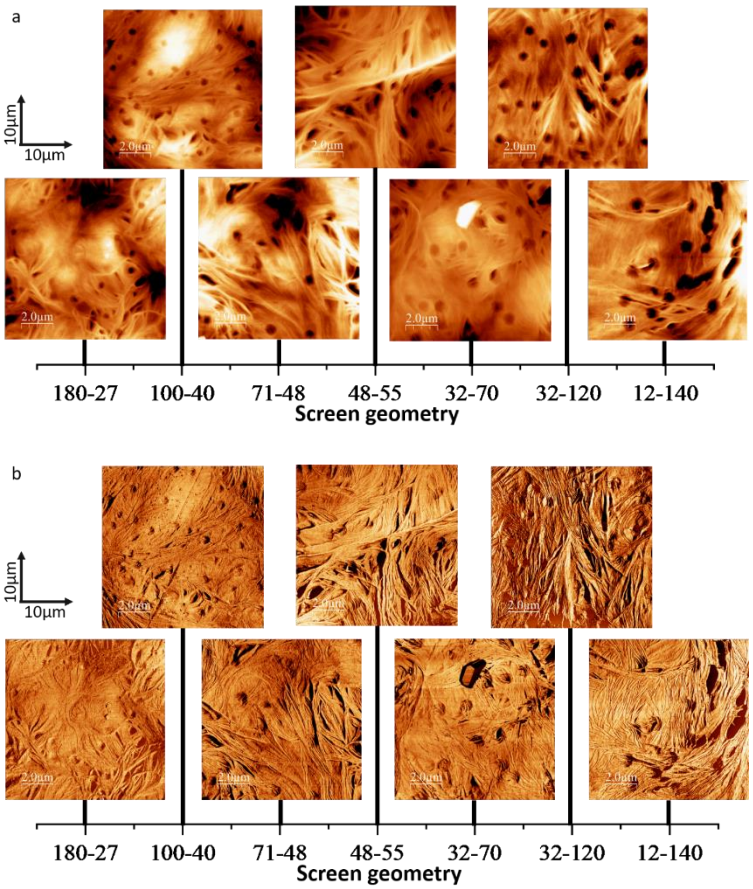

***Figure 67**. 10x10 µm² AFM images of the active P(VDF-TrFE) layers deposited via different meshing geometries with the 17 wt.% ink in TEP: (a) height (b) phase.*

To evaluate if the decrease of the viscosity has an impact on the morphology, the same measurements were performed on the 13 wt.% printed layers and the results are shown in **Figure 68**. The fibrillar structure is similar to the one observed for the 17wt.% ink. Holes are also present due to the subsequent drying process. Accordingly, from AFM imaging, we conclude that the morphology is mainly determined by the annealing process and is not affected by the meshing and the polymer concentration.

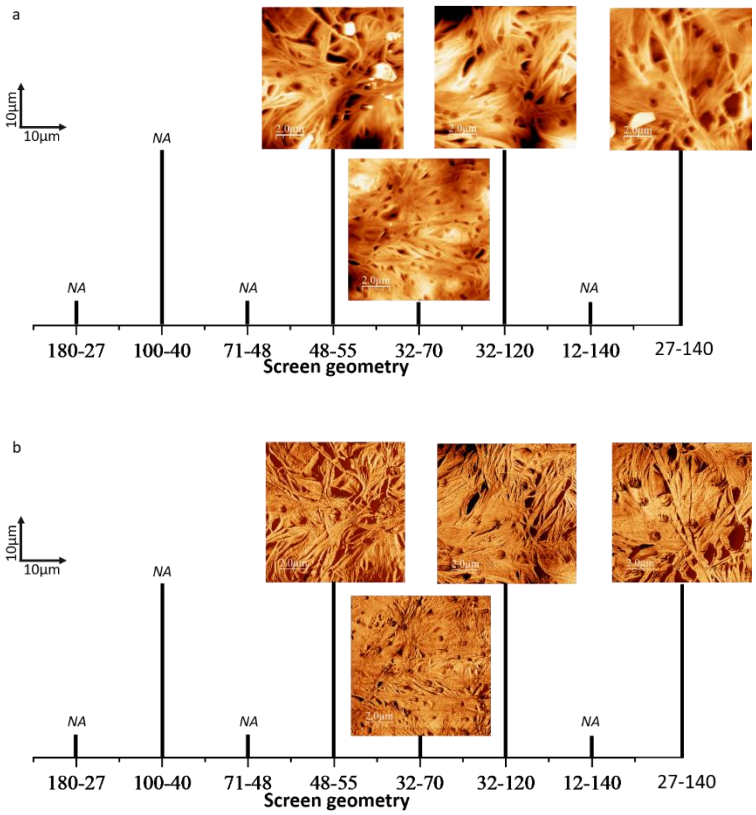

***Figure 68**. AFM 10x10 µm² images of the active P(VDF-TrFE) layers deposited via different meshing geometry for the 13 wt.% ink in TEP: (a) height (b) phase.*

Besides, we performed additional probing of the surface topography at larger scale thanks to 2D mapping profilometry. From **Figure 69**, it is apparent that the thickness of the printed layer is not homogeneous, in particular at the level of the top layer electrode which displays a higher roughness than the other layers. Interestingly, this feature shows that the use of a higher OA for the deposition of the PEDOT-PSS screen printing paste increases the thickness to the detriment of surface topography. However, a relatively good separation is obtained between the different layers, as the transitions from one material to another are sharp.

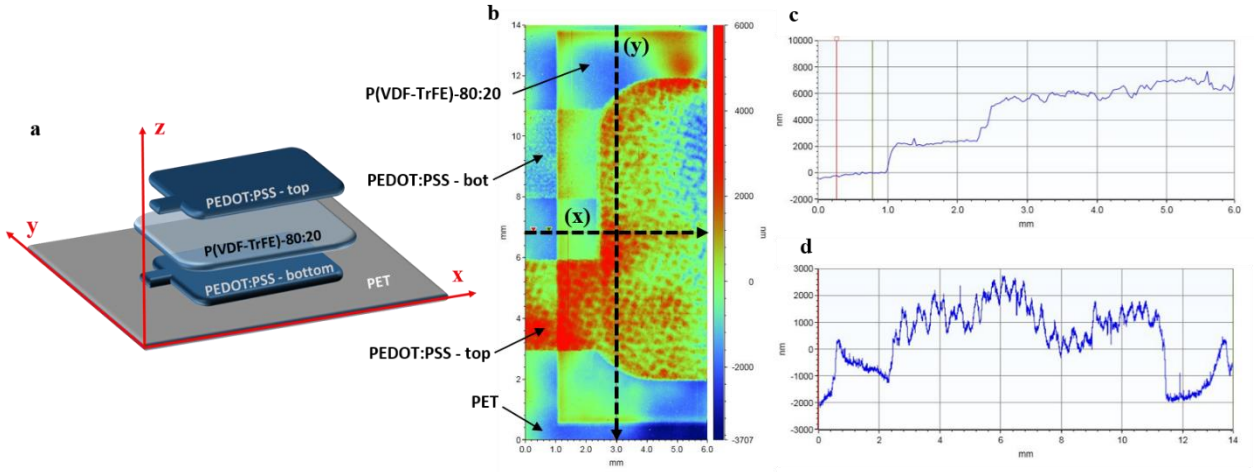

***Figure 69**. (a) Surface mapping of a device deposited with a [180-27] meshing with a 17 wt.% formulation, (b) and (c) represent the height profile corresponding to the (x) and (y) dashed arrows, respectively. All height scales are displayed in nm.*

4.4.2 Interfaces between the PEDOT:PSS electrodes and the active layer

As the devices are fabricated through several deposition processes (2 electrode layers and one P(VDF-TrFE) layer), the adhesion between the layers is crucial for the stability of the device. Inhomogeneous contact or delamination can create hot spots where charge build-up will be greater, increasing the likelihood of a short-circuit or breakdown. In this context cross-section scanning electron microscopy (SEM) images were performed to evaluate the integrity of the multilayered devices.

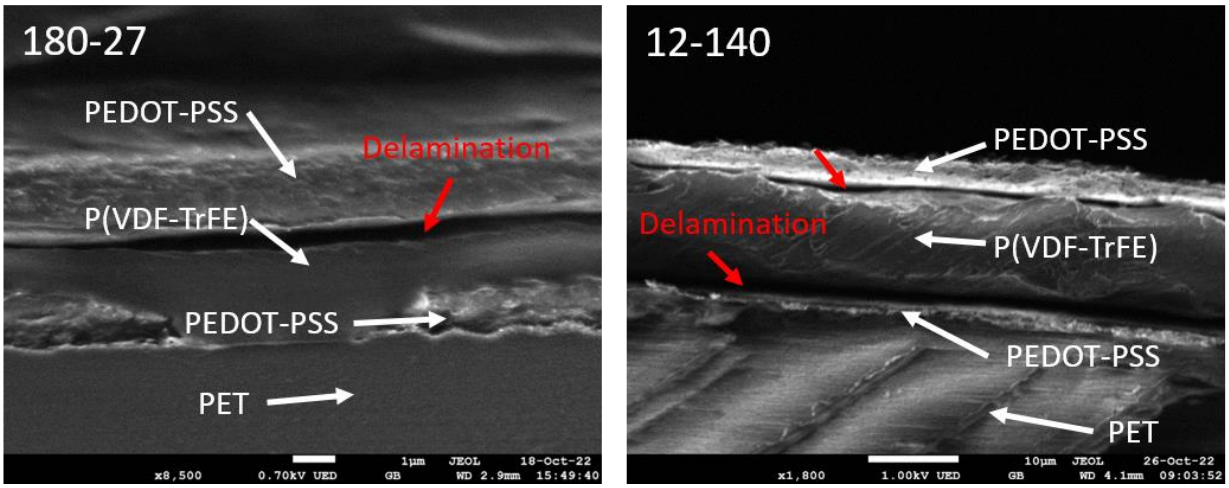

***Figure 70**. Cross-section SEM images of samples deposited with [180-27] and [12-140] screen geometries with the 17 wt.% formulation. Red arrows highlight delamination at the interface between the P(VDF-TrFE) active layer and PEDOT-PSS electrodes.*

In **Figure 70**, the different layers of the device can be distinguished. A good homogeneity within the same material, especially on the active layer, is observed. As the different layers are prepared by doing two consecutive depositions of the same material, an interface could be created leading to defectivity within the structure. Concerning the interface between the electrodes and the active layer, darker spots are identified which we associated to delamination voids between layers. The delamination can be observed on the devices deposited with the two extreme geometries (low OA [180-27] and high OA [12-140]). Accordingly, it appears that the process leading to delamination is not highly related to the screen geometry but rather to a lack of adhesion between the PEDOT:PSS electrodes and the P(VDF-TrFE) active layer.

4.4.3 Evaluation of the crystallinity of the active layers

The study of the film morphology serves as an initial indicator to evaluate the capabilities of the electroactive material. The effectiveness of the P(VDF-TrFE) layers is intricately tied to the quantity and quality of its crystalline structure. This section focuses on determining the material electroactive phases using two primary techniques, namely differential scanning calorimetry (DSC) and Fourier transform infrared spectroscopy (FTIR), as they offer direct insights into these

aspects. The goal is to compare the two formulations (17 wt.% and 13 wt.%) deposited using various screens to examine their potential impact on the crystalline composition.

To determine the crystalline nature and crystal quality, we first conducted DSC experiments on layers created using various screen geometries for both formulations. In **Figure 71**, we present the results of the first heating cycle for these different samples, wherein we observe the characteristic profile of a ferroelectric P(VDF-TrFE). The initial endothermic peak corresponds to the Curie temperature, while the subsequent one relates to the melting of the material crystalline phase. It is noteworthy that there are minimal discrepancies among the samples generated using different mesh sizes and formulations. Subsequently, we normalized the enthalpy values by referencing them to the enthalpy values obtained during the second heating cycle, effectively eliminating any influence of the sample prior thermal history. This normalization process entailed setting the enthalpy values during the second heating cycle to arbitrary but uniform values for all samples.

Upon close examination of the enthalpy values, we observed that these values consistently hover around 60 J/g, showing no discernible trend associated with the variations in meshing geometry. However, when comparing the enthalpies of the second formulation (13 wt.%) to those of the 17 wt.% formulation, we observed slightly lower enthalpy values for the 13 wt.% formulation, with the lowest value recorded for the [32-120] meshing configuration. Consistent with our earlier findings from AFM measurements, it is evident that both the meshing configuration and the formulation exhibit negligible effects on the crystallinity of the samples. This observation remains true even after the samples have undergone post-processing annealing at 140 °C.

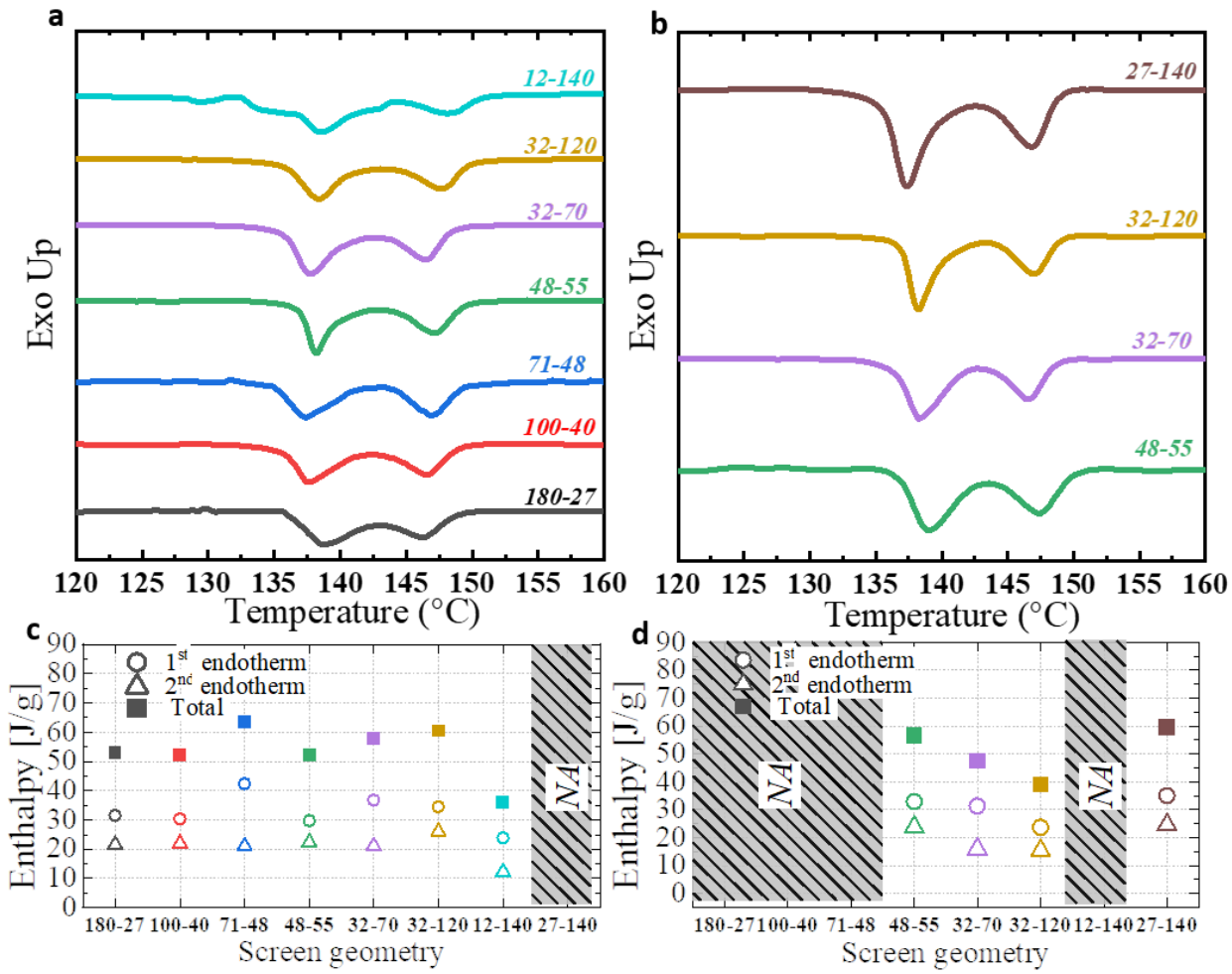

***Figure 71**. DSC thermograms obtained during the first heating cycle obtained on layers fabricated with the different mesh geometries with the (a) 17 wt.% and (b) 13 wt.% inks. (c) and (d) represent the normalized relative enthalpy values of the first endotherm, second endotherm, and total endotherm for the 17 wt.% and 13 wt.% formulations, respectively.*

DSC analysis provides a useful estimate of the electroactive phase content within the material, as reflected in the enthalpy values. However, our approach using a normalization step to qualify the crystallinity of our material falls short in delivering a precise quantitative assessment of crystallinity. To achieve a more precise and accurate determination of the crystalline phase polymorphism, FTIR emerges as a valuable alternative. In **Figure 72**, we observed that all P(VDF-TrFE) samples, deposited using various screens and subjected to annealing, exhibit nearly identical FTIR spectra. However, on the thinner samples produced with lower OA, we can discern the characteristic signature of the PET substrate, denoted by an asterisk symbol (*). Consistently, all

the samples demonstrate substantial overall crystallinity, marked by a pronounced peak at 1234 cm^{-1}, and a peak at 840 cm^{-1}, indicative of the high electroactive phase content within the material. These findings align with our expectations, affirming the high crystallinity and significant fraction of all-*trans* phase across all the samples. **Figure 72**a-b compare the samples deposited with the two formulations. At this point, our observations do not reveal any discernible differences leading us to consider a more quantitative approach. We used the treatment developed by Cai *et al.*[10], (see Chapter 1 and Figure 14c for details) to determine the amount of EA phase with a differentiation of the all-*trans* and *tttg* phase content. Accordingly, the results corresponding to each meshing geometry and formulation are displayed in **Figure 72**c-d. From this approach, we can easily confirm that the overall electroactive content is around 85% with a majority of *all*-trans content and only a few percent of *tttg* content. Once again, the two formulations displayed very similar results as the annealing step has the highest impact on the crystal formation.

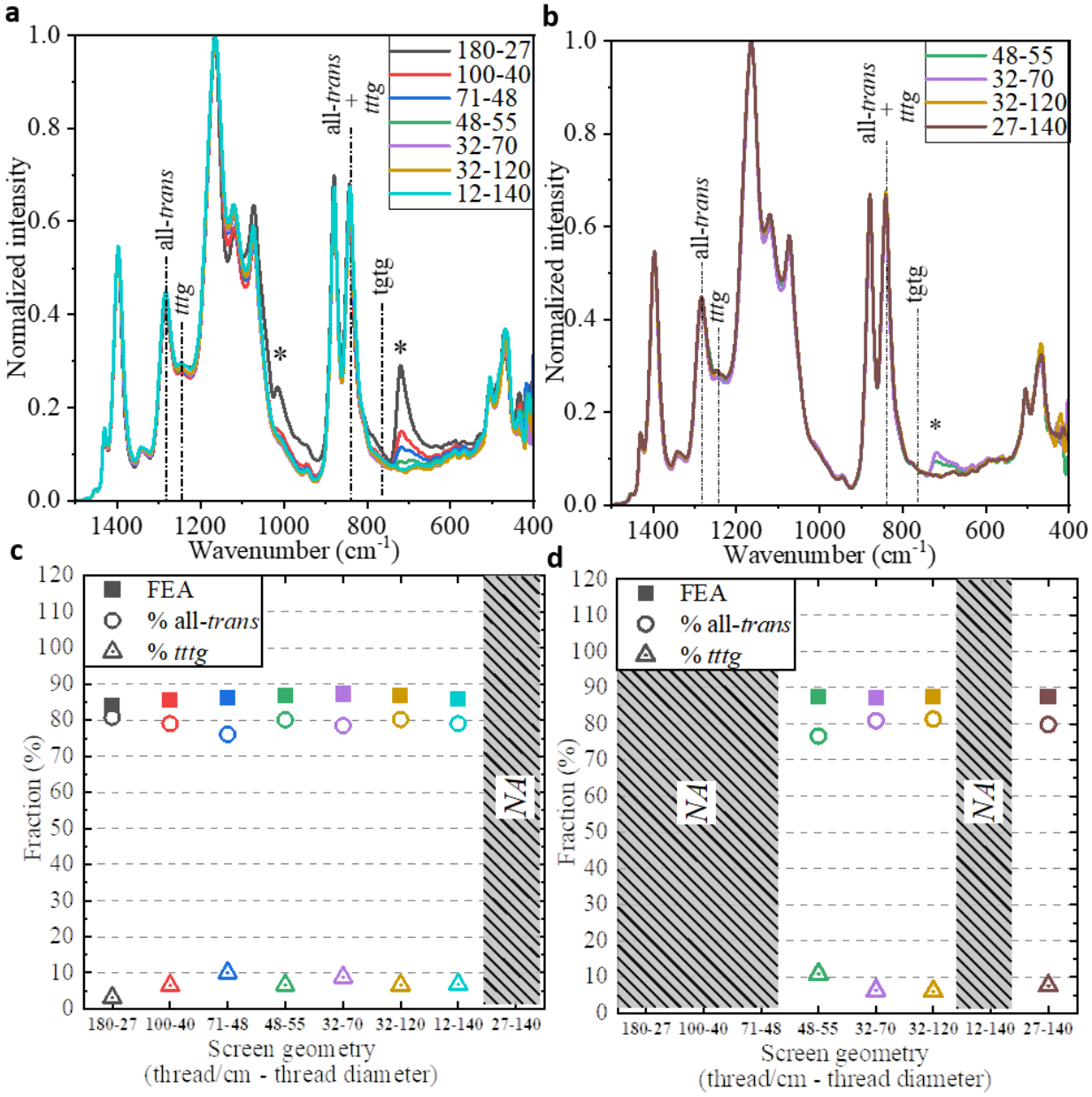

***Figure 72**. FTIR spectra of the active layers deposited with both (a) 17 wt.% and (b) 13 wt.% inks and different meshing geometries. The vibrations of interest corresponding to a specific chain conformation tg^+tg^-, all-trans and tttg that are used for the calculation of the electroactive phase are shown on the figure by the dotted lines. The vibration corresponding to the PET substrate is also highlighted by an asterisk symbol (*). (c) and (d) are the fraction of various phases determined following the treatment of Cai et al.[10] for 17 wt.% and 13 wt.% inks, respectively.*

4.4.4 Resistance to breakdown of the devices

From the manufacturer standpoint, material electroactive efficiency is a crucial criterion. However, one of the most critical parameters is the stability of the samples when subjected to an external field to induce polarization in the material. If achieving polarization without compromising the device integrity becomes unattainable, the entire process and device are compromised. Therefore, the primary objective of this section is to determine which process, encompassing screen geometry and formulation, results in the maximum polarization of the material while ensuring the absence of any breakdown or failure in the device. A maximum electric field of E_{max}=100 V/µm was appropriately chosen as the value recommended by the manufacturers to obtain a usable device.[11] To assess the stability of our devices, the following procedure was employed. An alternative voltage was applied through contact on various devices, and this voltage was normalized with respect to the median thickness of each device. As a result, the applied electric field ranged from 25 V/µm to 100 V/µm in increments of 5 V/µm. In order to reach the maximum electric field of 100 V/µm, a total of 15 polarization cycles were applied to each device.

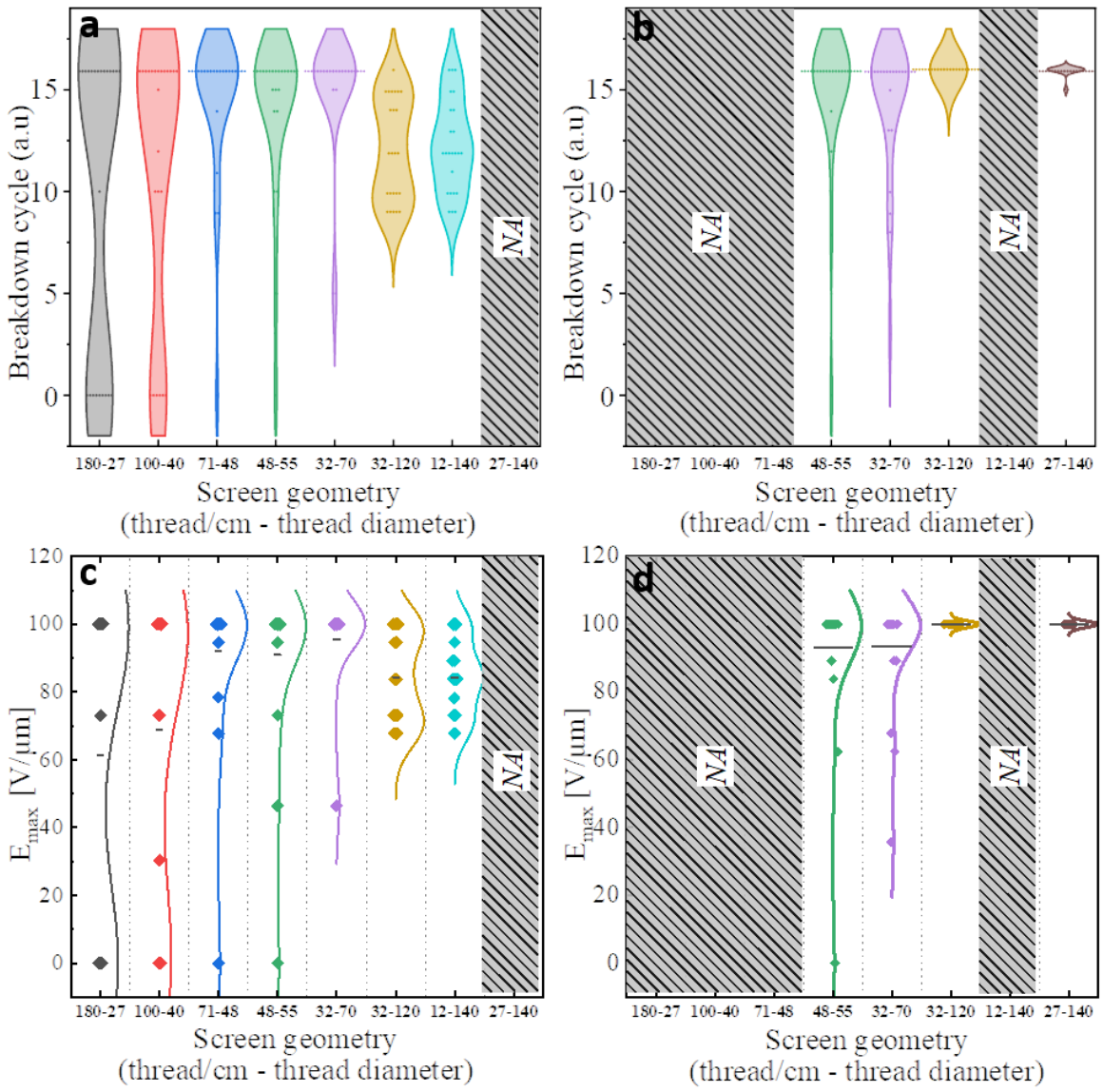

***Figure 73**. (a) and (b) violin representation of the number of maximum polarization cycles applied on a total of 24 devices for each mesh geometry for the 17 wt.% and 13 wt.% formulations in TEP, respectively. The colored surfaces represent the density function of the number of maximum cycles applied in which a cycle number equal to 0 represents a conductive sample (no polarization is possible) and a cycle equal to 16 represents an effective polarization with 15 cycles without any breakdown. (c) and (d) maximum field applied to the sample for the different meshes and the 17 wt.% and 13 wt.% formulations, respectively. Each dot represents a sample and the half-violin represents the distribution density of the E_{max} applied to the sample.*

The representation in **Figure 73** provides insight into the relationship between the number of cycles and the maximum electric field applied. Particularly interesting observations can be

made regarding the breakdown density concerning the mesh configurations used for the 17 wt.% formulation, as depicted in **Figure 73**a and **Figure 73**c. For the 17 wt.% formulation, it is evident that the number of maximum polarization cycles is directly influenced by the mesh geometry employed during deposition. When employing the low OA screen geometries, such as 180-27 and 100-40, the breakdown cycles exhibit a bimodal distribution. The first region corresponds to the 0-cycle, indicating that the device remains conductive, preventing successful polarization (making the device unsuitable for applications). The second distribution emerges at the 16^{th} cycle, signifying that these devices were successfully polarized without any breakdown. Another behavior pattern is observed for devices created using meshes with intermediate OA, such as 71-48, 48-55, and 32-70. With these configurations, devices unsuitable for polarization (0-cycle) still exist but in a smaller proportion compared to the low OA meshing. Consequently, a higher number of devices are fully polarized by the 16^{th} cycle. On the other hand, devices produced with higher OA and larger thread size meshing exhibit a different pattern. Notably, there are no instances of "0-cycle" polarization. The non-conductive devices are offset by a minimal number of fully polarized samples after 16 cycles.

From these initial observations with the 17 wt.% formulation, it becomes evident that the maximum field applied is contingent upon the chosen mesh configuration. These variations are not primarily attributed to the material internal structure (*i.e.*, morphology and crystallinity) but rather relate to the overall layer characteristics, specifically thickness and surface roughness, as detailed beforehand. Lower mesh apertures result in the deposition of thinner and smoother layers. Given the extremely thin nature of the active layer, measuring less than 4 µm, any defects at the interface, such as poor adhesion between the PEDOT and active layers, can lead to device failure. Accordingly, as attested by the AFM images, the presence of holes, likely stemming from solvent evaporation, can create conductive pathways between the electrodes, thus rendering the device inoperable. However, when these defects are minimized or absent, complete polarization becomes attainable. This phenomenon is particularly pronounced in the second group of mesh configurations. While there are still some instances of zero breakdown cycles, they are notably

reduced. Moving to the third set of meshes, there are no instances of 0-cycle breakdowns. Nevertheless, the increase in thickness and roughness may raise the likelihood of surface defects that could create shortcuts. It is crucial to note that, for the same applied electric field, materials with greater thickness necessitate higher voltage input to reach the desired polarization.

To confirm these conclusions, the response of the devices fabricated with the 13 wt.% formulation was also evaluated. In comparison to its homologous counterpart with a 17 wt.% composition, these devices demonstrated a greater occurrence of fully polarized samples and a reduced frequency of breakdowns at 0-cycle. This can be linked to the sample thickness and roughness, which indicated lower values at this concentration. Accordingly, reducing thickness appears to be advantageous as it also leads to a decrease in roughness. Besides, for screens with higher OA and thread diameter, breakdowns that can be attributed to important values of the roughness are minimized, thereby contributing to the increase in fully polarizable devices.

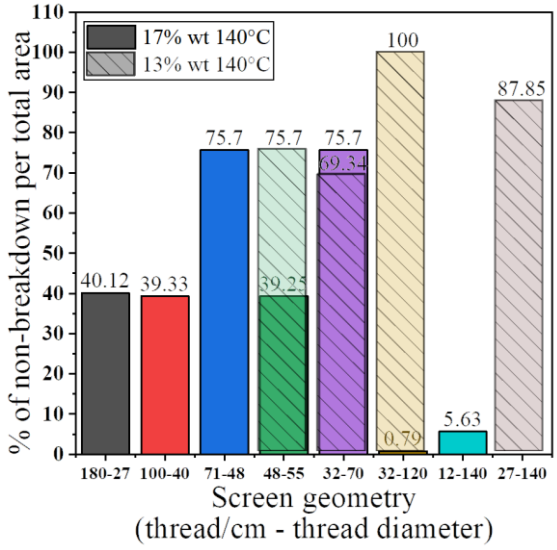

***Figure 74**. Percentage of non-breakdown according to the mesh geometry for the 17 wt.% and 13 wt.% formulations in TEP.*

The percentage of devices with no breakdowns is illustrated in **Figure 74**. This representation clearly demonstrates that the meshing influences on the occurrence of breakdowns. It also highlights a process window in which the printing process operates with a maximum efficiency in

terms of avoiding breakdowns. Furthermore, this efficiency is significantly improved by modifying the formulation to a lower copolymer content, specifically 13 wt.%. The most notable enhancement is observed in cases of high OA meshes and thread diameters, where the number of breakdowns previously affecting a substantial portion of the samples shifts to a nearly complete absence of breakdowns (e.g., screen [32-120]).

4.4.5 Influence of the thermal treatment on the breakdown density

As demonstrated previously, the ink formulation impacts the deposition and its resistance to breakdown. By reducing the ink concentration by 4 wt.%, a substantial improvement was achieved. The thermal treatment applied to the sample after deposition also plays a crucial role in influencing the properties of devices. It serves to both smoothen the film surface and enhance the content of the EA phase, thereby impacting device performance significantly. In this scope, the effect of the thermal treatment was further investigated using the 13 wt.% formulation in TEP.

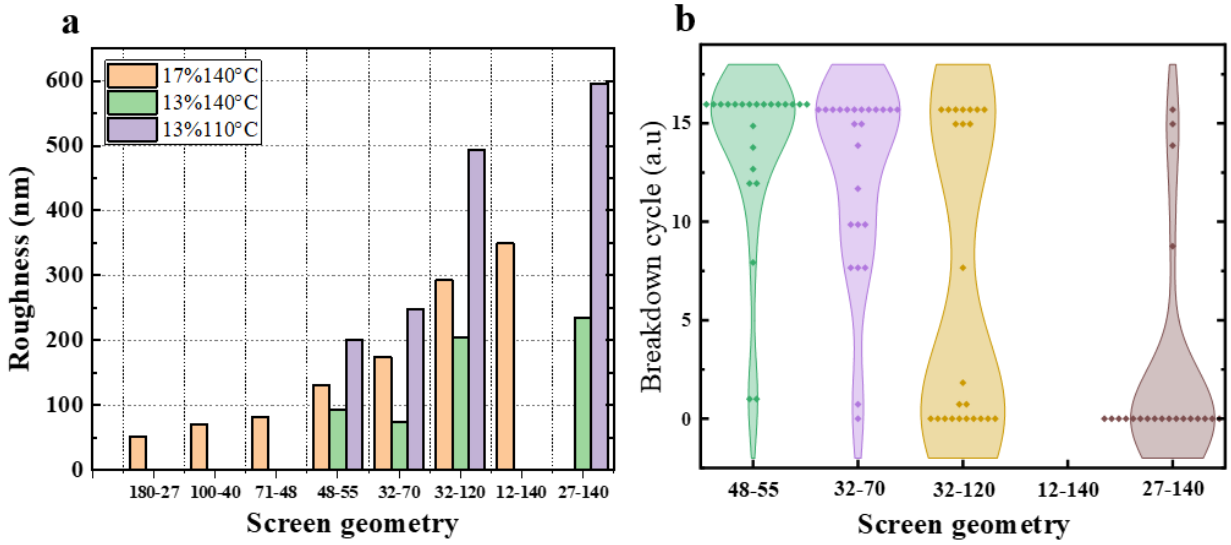

***Figure 75**. (a) Roughness measured for the different temperatures and formulations. (b) Violin representation of the number of maximum polarization cycles applied on a total of 24 devices for each mesh geometry concerning the 13 wt.% formulation annealed at 110 °C. The colored surfaces represent the density function of the number of maximum cycles applied to the device.*

The annealing temperature was adjusted to 110 °C with respect to the previous one of 140°C. Following the same procedure, measurements of thickness and roughness were conducted on devices deposited using four different screens. As anticipated, the thermal treatment had no discernible effect on the thickness, but it significantly influenced the roughness. From **Figure 75**, it is clear that the process at 110 °C considerably increases the roughness of the active layers depositions compared to the process at 140 °C for both 13 wt.% and 17 wt.% formulations. The breakdown of these devices was also altered. In the case of lower OA meshing, the roughness is comparable to that obtained with the 17 wt.% ink at 140 °C process, leading to a similar number of breakdowns and distributions over the range of cycles. However, with higher OA meshing, the roughness nearly doubles compared to the 13 wt.% at 140 °C process, resulting in a broader distribution of breakdowns and an increased occurrence of breakdowns at the 0-cycle.

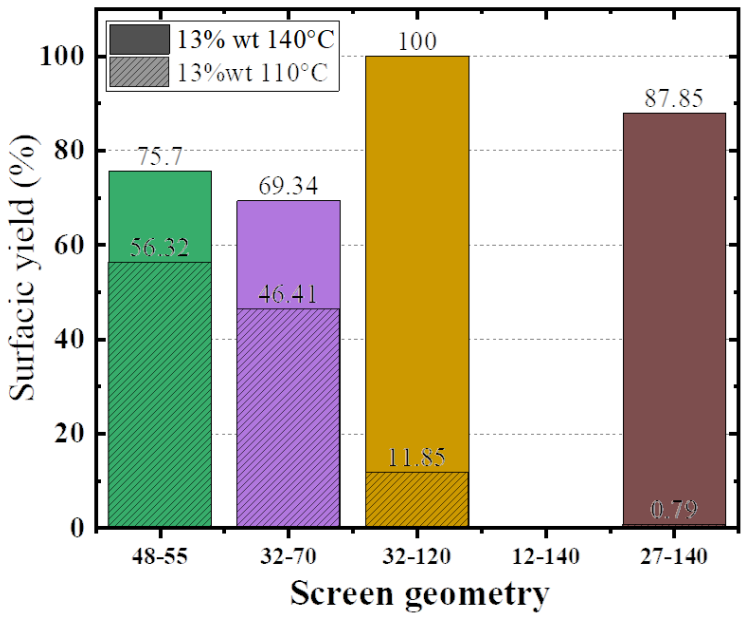

Figure 76. Surfacic yield per total area for the process at 140 °C and 110 °C.

Figure 14 illustrates the overall resistance to breakdowns. The number of breakdowns significantly increases as the surface yield decreases from 87% to less than 1% for the [27-140] screen, while the yield is notably reduced for the other screen geometries. Annealing at lower

temperatures accordingly introduces defects related to the increased roughness, ultimately leading to device failure.

4.4.6 Impact of the solvent on the resistance to breakdown

In this study, we evaluated two formulations, 17 wt.% and 13 wt.% in TEP. Most of the differences affecting the final resistance to breakdown were attributed to their rheological behavior as attested by the three-interval shearing tests, which reduced the roughness on the devices deposited with higher OA. This effect was mostly attributed to the behaviour of the ink under an applied shear. Nevertheless, the hypothesis that the solvent impacts the depositions was not dismissed. As previously established in Chapter 3, we demonstrated that the solvent affects the conformation of the polymer chains, the number of entanglements, and viscosity.

To investigate this further, we selected three systems of interest (EGDA, PC, and PGMEA) to conduct printing tests and determine their rheological properties, comparing them with inks formulated in TEP. To accomplish this, we performed a three-interval shearing test to assess the recovery of the solutions. The results presented in **Figure 77** provide insights into the recovery of various inks following the application to different shear values, as compared to the reference ink (17 wt.% in TEP). Throughout the shearing process, the recovery of the inks exhibits a consistent and smooth behavior for all compositions, with the exceptions of inks formulated in PC at 13 wt.%, in PGMEA at 17 wt.%, and in EGDA at 13wt.%, which do not display any discernible steps in their recovery profiles.

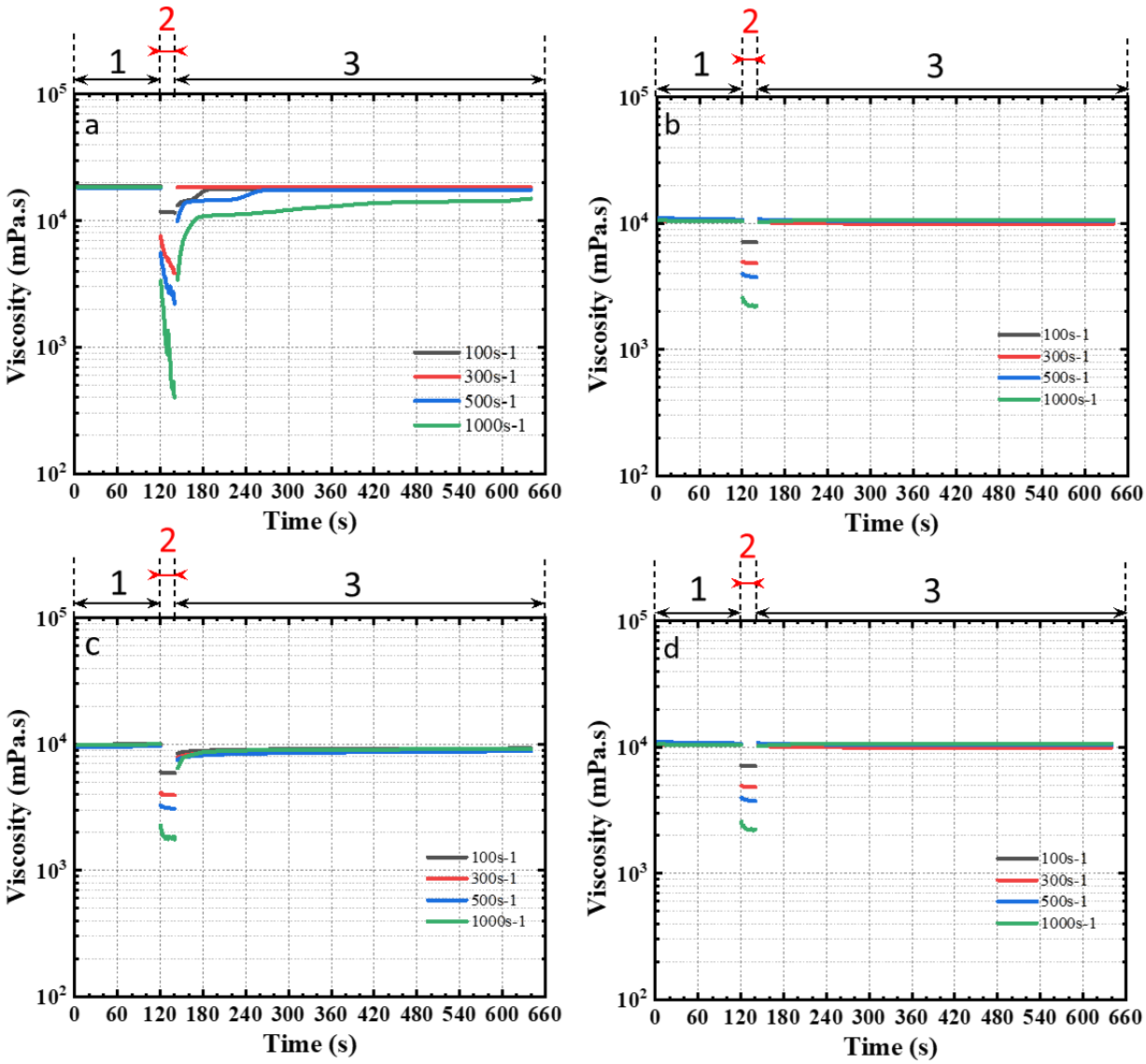

***Figure 77**. 3ITT measurements for different continuous shear values. Each measurement is performed on fresh inks of different formulations: (a) TEP 17 wt.%, (b) PC 13 wt.%, (c) PGMEA 17 wt.%, and (d) EGDA 13 wt.% The measurement procedure is explained in the method section. Each color corresponds to the shear applied to the solution during interval 2 (100 s^{-1}, 300 s^{-1}, 500 s^{-1} and 1000 s^{-1}).*

Interestingly, this particular property was identified as the primary distinction between the inks formulated in TEP at 13wt.% and 17wt.%. Consequently, it was established as the critical parameter for achieving reliable devices. Notably, during the 20 s shear step, the reference ink

exhibited pronounced shear-thinning behavior, potentially linked to a restructuration and disentanglement of the polymer chain in solution. In contrast, for the other formulations, shear-thinning behavior is observable for only a brief duration, after which the viscosity stabilizes.

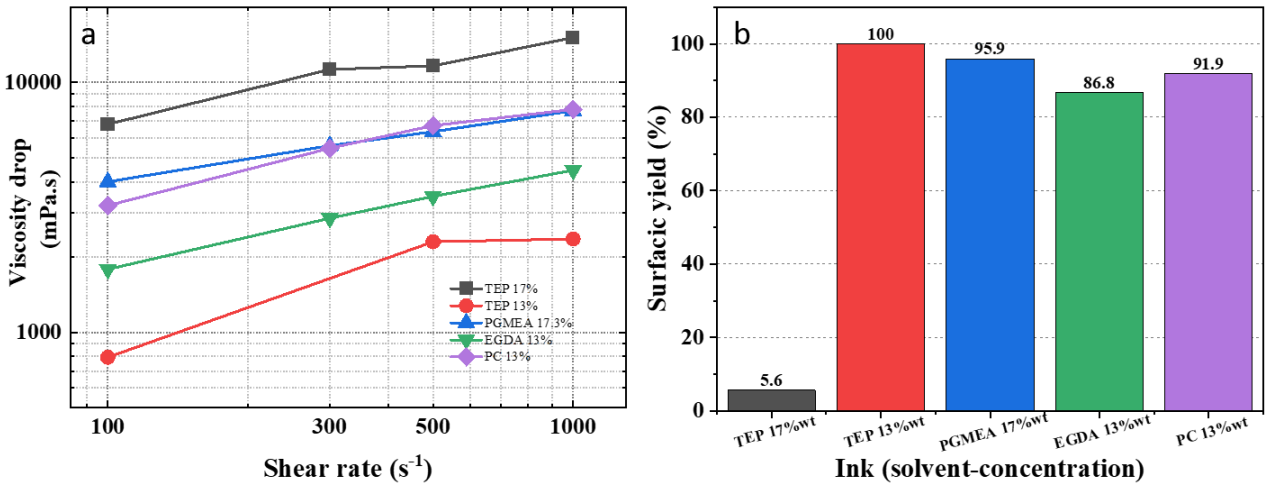

***Figure 78**. (a) Viscosity drop of the different formulations, TEP 17 wt.% and 13 wt.%, EGDA 13 wt.%, PC 13 wt.%, and PGMEA 17 wt.%, submitted to different shear rates. (b) Surfacic yield obtained for the different ink formulations deposited with a [32-120] mesh.*

The viscosity drop was reported for the various formulations in **Figure 78**a. These values indicate that the viscosity drop is less pronounced for all the formulations when compared to the reference ink. This finding implies that the ink recovery may be more uniform, reducing the likelihood of defects during deposition. To investigate this hypothesis, polarization experiments were conducted on devices deposited using the mesh geometry [32-120] with different ink formulations. The resulting surface yield is presented in **Figure 78**b. Significant improvements were observed in the number of devices that achieved full polarization without breakdown, particularly when compared to devices made with the reference ink. This observation underscores the critical role of ink formulation in ensuring device stability, which can be influenced by factors such as viscosity drop and shear response.

4.5 Conclusion

In this chapter, we conducted an extensive study focusing on the screen-printing process of P(VDF-TrFE)-based inks. Initially, we measured the rheological properties of the reference ink in TEP and its homologue of lower concentration under a shearing procedure representative of a screen-printing process. Our findings indicated that the rheological properties differ significantly depending on the ink concentration regime. As previously demonstrated in Chapter 3, the concentrated regime, situated above the critical concentration (c^{**}), exhibited irregular recovery post shearing, characterized by the appearance of recovery steps. In contrast, the other formulation in TEP, located in the semi-dilute regime above c_{th}, displayed a smoother and more homogeneous recovery after shearing. This distinctive behavior may be attributed to the relaxation and inner structure of the polymer chains in solution. In particular, the disentanglement of an entangled system under high shear induces a restructuring of the ink during the recovery time, resulting in the observed steps during the three-interval thixotropic measurement.

We then compared the two formulations based on a screen-printing process, a technique that involves transferring ink from a mesh to a substrate. The impact of the mesh geometry on our two formulations was evaluated. Interestingly, the geometry influenced the thickness and roughness of the depositions without affecting the texture, the amount of crystalline material, or the nature of the crystals (α, β, and γ). These effects were consistent across different concentrations. However, significant differences in device polarization were observed. The number of breakdowns on the devices depended on both the screen and the formulation used. An analysis of the number of polarization cycles applied to the devices before breakdown suggested that defects were primarily due to the roughness of the electroactive layer, which in turn affected adhesion with the conductive electrodes. This finding further corroborated the importance of ink rheology in the ink transfer process, ultimately influencing the reliability of the devices.

To validate our hypothesis, we formulated additional inks using different solvents of interest for our industrial partner. After thixotropic characterization and assessment of resistance

to breakdown under polarization, it became evident that ink rheology played a significant role. All the inks, with various concentrations and solvents (PC 13 wt.%, PGMEA 17 wt.%, and EGDA 13 wt.%), exhibited similar recovery without the presence of steps or significant viscosity drops during the shearing step. Consequently, as anticipated, the surface yield of the devices outperformed that of the reference ink, further confirming our initial conjecture.

4.6 Materials and methods

4.6.1 Materials

Inks, formulated in TEP, PGMEA, EGDA, and PC, with a solid content of 17 wt.% and 13 wt.% of (PVDF-TrFE)-80:20, used during the deposition, were kindly provided by Arkema Piezotech and filtered at 1 µm with PTFE filter before use. PEDOT-PSS screen printing paste Orgacon EL-P 5015 was purchased from Agfa. 125 microns PET substrates with adhesion coating in an A4 format from ADDEV Materials were used as substrates. Depositions of the electrodes and the active material were performed with a semi-automatic E2 type Ekra X5 screen-printer. A polyurethane squeegee (shore A: 70) and a steel-based counter-squeegee were used for the impression. Deposition parameters were used as follows: printing speed 20 mm/s, pressure 2 bars, snap off 1.5 mm.

Screens used for the study were provided by Koenen GmBH, with an aluminum frame consisting of 22.5° oriented PET wires reported as follows: [XX – YY] with XX corresponding to the number of threads per cm and YY the diameter of the threads in microns. Respective screens used for the different layers are shown as follows, PEDOT-PSS (bottom electrode): [190-31], PEDOT-PSS (top electrode): [100-50], PVDF-TrFE (active layer): [180-27], [100-40], [71-48], [48-55], [32-70], [32-120], [12-140] and [27-140].

4.6.2 Device fabrication

The multilayer devices were deposited on PET substrates previously thermos-stabilized at 140°C for 15 minutes. The devices were fabricated by the only use of the screen printer using the deposition parameters mentioned above. Each device is composed of several layers including two layers of PEDOT-PSS as a bottom electrode, two layers of P(VDF-TrFE)-80:20 as an active layer, and two layers of PEDOT-PSS as a top electrode. The deposition of each layer was followed by 15 minutes of thermal annealing under vacuum at 140 °C for the PEDOT-PSS electrodes and 20 minutes of thermal annealing at 140 °C comprising 8 min vacuum suction.

For each screen geometry, the deposition results in the printing of 24 distinct devices differentiating by their active area and geometry as shown in Figure 63. It is important to note that the screen and the squeegees are cleaned between each deposition cycle.

4.6.2 Device characterization

4.6.3.A Thickness and Roughness

Morphological characterization with AFM was performed with an AFM system from Bruker (Dimension Fast Scan) in tapping mode. A Bruker Dektak XT-A stylus profilometer was used to measure each device thickness and roughness.

4.6.3.B SEM

SEM imaging was performed with a JEOL 7800-E PRIME (Jeol Ltd., Japan), under low current (< 50 pA) and low voltage (≤ 1 kV) settings. Fresh cross-sections for imaging were prepared by sliding a clean surgical blade perpendicular to the surface of the sample/device. The samples were then mounted on a cross-section sample holder with conductive carbon tape and silver paste to ensure electrical contact between the sample and the holder. A conductive coating of 2 nm of platinum was then deposited on the exposed cross-sections with a magnetron sputtering

system (Leica EM ACE600). Imaging was performed with the GB mode of the microscope, at a working distance below 4 mm, using the in-column detector (UED).

4.6.3.C Polarization

A homemade thin film polarizer was used to apply an alternative voltage by contact on the different devices and normalized with the median respective thicknesses so the applied electric field goes from 25 V/µm to 100 V/µm with a 5 V/µm step.

4.6.3.D FTIR

FT-IR spectra were recorded with a Nicolet iS5, with an ATR module iD7, containing a diamond-crystal window with a sampling diameter of 1.8 mm. The spectra were recorded for a range between 4000 to 400 cm^{-1}.

4.6.3.E DSC

Differential Scanning Calorimetry was performed with a Mettler Toledo DSC 1, equipped with an intra-cooler and N_2 flux, over a temperature range of -50 °C to 200 °C and a heating rate of 10 °C min^{-1}.

4.6.3.F Ink rheological characterization

Viscosity and thixotropic behavior of the inks were characterized with an Anton Paar MCR302 rheometer with a CP50-1° geometry (cone 50 mm – 1° / plate) at 21 °C. The measurements were carried out under a solvent saturated atmosphere with the help a solvent trap. Steady shear measurements were performed by applying different shear rates in a logarithm scale from 0.01s^{-1} to 1000s^{-1}. The thixotropic behavior of the inks was evaluated using a step test of three intervals: 1st and 3rd intervals with an oscillatory deformation of 1% at a 1Hz frequency where G' and G'' represent the ink storage and loss moduli, and 2nd interval using a steady shear. The 1st, 2nd, and 3rd interval duration were set to 120 s, 20 s, and 500 s, respectively.

References

1. Novaković, D., Kašiković, N., Vladić, G. & Pál, M. Screen Printing. in *Printing on Polymers: Fundamentals and Applications* 247–261 (Elsevier Inc., 2015). doi:10.1016/B978-0-323-37468-2.00015-4.
2. Riemer, D. E. The Theoretical Fundamentals of the Screen Printing Process. *hybrid circuits* **18**, (1989).
3. Abbott, S. How to be a great Screen printer. (2008).
4. Kapur, N., Abbott, S. J., Dolden, E. D. & Gaskell, P. H. Predicting the behavior of screen printing. *IEEE Trans. Components, Packag. Manuf. Technol.* **3**, 508–515 (2013).
5. Wang, S.-Q., Ravindranath, S., Wang, Y. & Boukany, P. New theoretical considerations in polymer rheology: Elastic breakdown of chain entanglement network. *J. Rheol. (N. Y. N. Y).* **127**, 64903 (2007).
6. Ravindranath, S. & Wang, S.-Q. What Are the Origins of Stress Relaxation Behaviors in Step Shear of Entangled Polymer Solutions? *Macromolecules* (2007) doi:10.1021/ma071495g.
7. Ieda, M. Dielectric breakdown process of polymers. *IEEE Trans. Electr. Insul.* **EI**-**15**, 206–224 (1980).
8. Li, W. *et al.* Crystalline morphologies of P(VDF-TrFE) (70/30) copolymer films above melting point. *Appl. Surf. Sci.* **254**, 7321–7325 (2008).
9. Zhang, Y., Aich, B. R., Chang, S., Lochhead, K. & Tao, Y. How to process P(VDF-TrFE) thin films for controlling short circuits in flexible non-volatile memories. *Org. Electron.* **105**, 106494 (2022).
10. Cai, X., Lei, T., Sun, D. & Lin, L. A critical analysis of the a, b and g phases in poly(vinylidene fluoride) using FTIR †. *RCS Adv.* **7**, 15382–15389 (2017).
11. Piezoelectric Materials | P(VDF-TRFE) | Arkema Piezotech. https://piezotech.arkema.com/en/Products/piezoelectric-copolymers/.

Chapter 5:

Solution shearing inducing a tuning of the dielectric response of PVDF-based terpolymer thin films

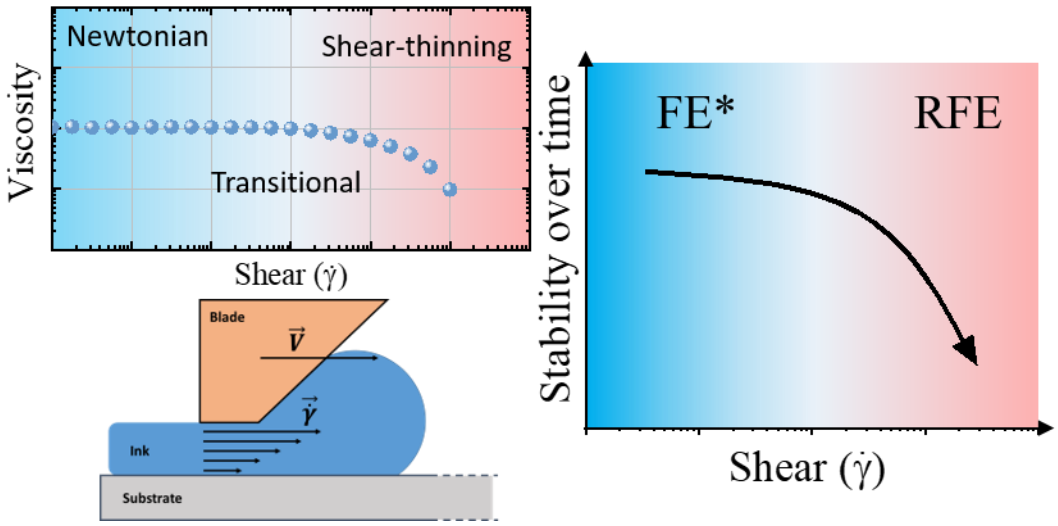

Chapter 5: Solution shearing inducing a tuning of the dielectric response of PVDF-based terpolymer thin films

In this work, we intend to explore the enhancement of the functional properties of P(VDF-TrFE-CTFE) thin films fabricated with industrially compatible printing processes. The first step consisted of the evaluation of the rheological and physical-chemical properties of terpolymer solutions (also referred to as inks) in cyclopentanone (CP). An emphasis was given to inks with higher solid content, as these yield thin films in the micrometer range, typically used in practical applications. The rheological properties were evaluated at room temperature, assessing the evolution of the viscosity as a function of the applied shear rate. Several thin films were then prepared through doctor-blading, following the obtained rheology data as a criterion for solution concentration. The depositions were performed at different shear rates, studying the effects of this deposition parameter on film property. The different fabricated films were fully characterized with different techniques, as to relate their dielectric performance to their internal structure and conformation.

By comparing the observed changes between the samples sheared at different rates, we can study the structural, morphological, and dielectric characteristics of the films and directly relate these to the deposition process.

5.1 Viscosity regimes:

A preliminary study on the rheological properties of different polymer solutions has been performed. This study allows the determination of the most adequate solution concentration to be used in thin film preparation. The rheological properties for different concentrations were assessed at room temperature (21°C) with a rotational rheometer, recording the evolution of the solution's apparent viscosity as a function of the applied shear rates.

As seen in **Figure 79**a, with steady shear measurements, non-Newtonian and shear-dependent behavior of the viscosity is observed for polymer concentrations above 5 wt.%, which results in a shear thinning behavior of the solution (at high shear). This tendency was fitted according to the Carreau-Yasuda model, which describes the transition from Newtonian to non-Newtonian behavior. Shear thinning can be linked to the appearance of overlaps and entangled regimes in solution.[1,2] These different regimes can be estimated from the measured specific viscosity as a function of solution concentration (**Figure 79**b). From the data plotted in **Figure 79**b, we can choose the most suited concentration for thin film preparation, taking into consideration that the solution must: (i) provide sufficient material availability after solvent drying; (ii) present low mass transfer due to aging on solid films[2]; (iii) and present a response that can be modulated by the deposition parameters (in this case, the applied shear).

Based on the obtained results, we have chosen to perform the depositions with a solution concentration of 15 wt.%, as the viscosity of the solution was observed to depend on the applied shear (**Figure 79**a). Three different shear rates were also used, selected according to the solution's apparent viscosity, covering three different regimes: 10 s^{-1}, 100 s^{-1}, and 1000 s^{-1}, which correspond to Newtonian, transitional, and shear thinning regimes respectively.

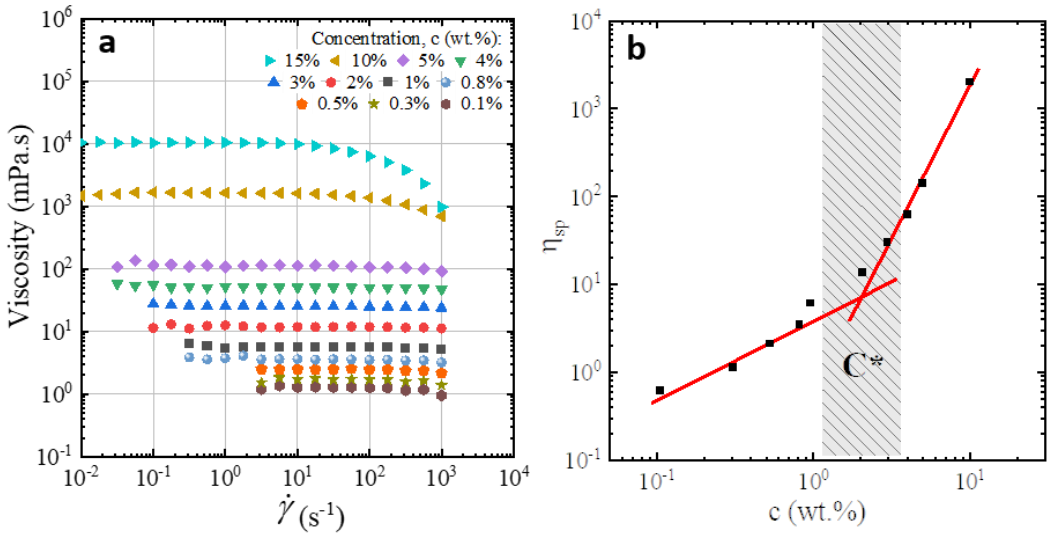

Figure 79. *(a) Viscosity measurements over a range of concentrations (from 0.1 to 15 wt.%) with each point representing a measurement at a specified shear rate. (b) Representation of the specific viscosity over the concentration reported in wt.%. The hatched area represents approximatively the region wherein the polymer starts to entangle, determined by the intersection of the extrapolation lines in red.*

5.2 Effect of the shear on the crystallinity

The crystalline structure of the prepared films was assessed with WAXS. **Figure 80**(a-c) shows the obtained diffractograms. Pattern multipeak fitting followed previous reference literature works on X-ray characterization of these terpolymer systems.[3,4] The diffractograms show two distinct regions at 16°-22° and around 40°. The main crystalline peaks are located at the first region (16°-22°), presenting contributions from different phases that form a main broad peak around 18°. The second region around 40°, which typically presents higher order diffraction peaks, is populated by amorphous halos. Interpretation of the diffraction maxima for these materials has been performed in previous works, attributing the observed peaks around 16° to 22° to the (200)/(110) diffraction planes of the pseudo-hexagonal/orthorhombic unit cell for the cases of the RFE/DFE/FE phases.[3,4,5] As seen in **Figure 80**a-c, by performing a non-linear function fit we can deconvolute the main peak into two smaller contributions that correspond to different crystalline phases, in this case, a RFE phase (RFE, red, 2θ = 18.4°), and a FE or defective-FE (FE or DFE, blue – henceforth FE*, 2θ = 19.4°). The observed peak positions are also in agreement with the reported chain structure and crystal unit cells for these phases, with the RFE phase presenting larger unit cells with longer interplanar distances, and the FE phase presenting a more compact unit cell a majority of all-*trans* chains, similarly to the β-phase in the PVDF homopolymer. The intermediate positioning of the DFE phase has been attributed to an increase of *tg* and *tttg* defects along the polymer backbone which increases the unit cell volume. From the diffractograms, we can also see a very similar peak distribution and intensity with the applied shear rate, with the main contribution arising from the RFE phase, in agreement with previous studies on the crystallization of similar PVDF terpolymers.[10,12]

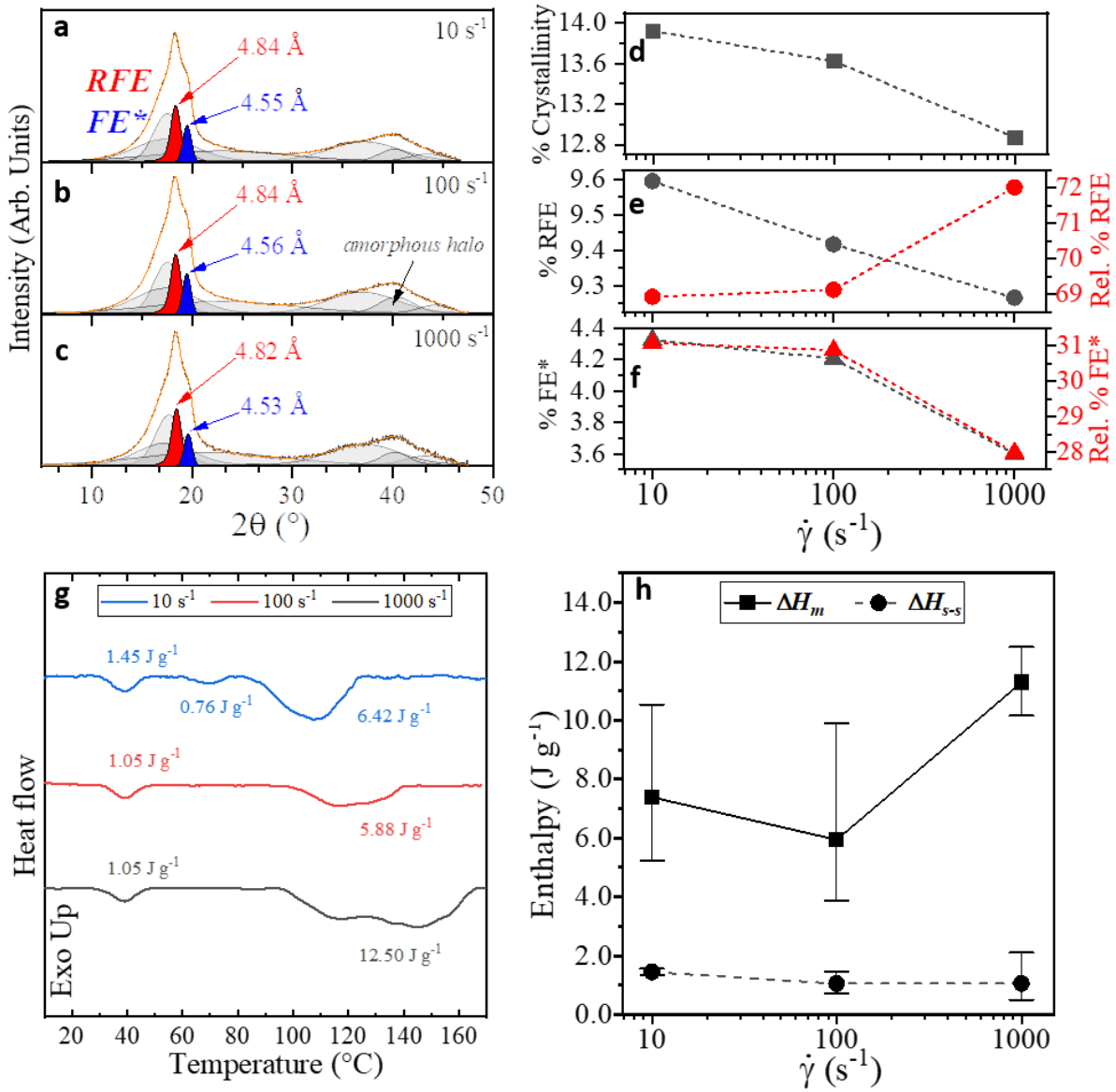

Figure 80. *(a-c) WAXS diffractograms for the different shear rates of 10 s^{-1}, 100 s^{-1}, 1000 s^{-1}, respectively, and the obtained non-linear fit (orange line). Red, and blue colored peaks refer to the RFE, and FE* phases, with their interplanar distance respectively. (d) Total sample crystallinity %χ_{tot} (■) and relative phase content, as a function of the shear rate, where (e) %χ_{RFE} and (f) %χ_{FE^*} are the percentages of relative crystallinity of the RFE, FE* in black, and the phase content reported to the relative phase content in red. (g) DSC curves (Exo. up) of the first heating ramp of the prepared samples at 10 s^{-1}, 100 s^{-1}, and 1000 s^{-1} (blue, red, and black solid lines respectively). (h) Enthalpy of melting ΔH_m (■) and enthalpy of the solid-solid transition $\Delta H_{S\text{-}S}$ (●) as a function of the applied shear rate. The values represented are extracted from three DSC measurements with the associated error bars.*

The total crystallinity and the relative phase content (χ_{tot} and χ_i respectively, where *i* stands for RFE, or FE*) can be estimated from the area ratio of the crystalline peaks (or a

selection of peaks, in the case of the phase fraction) and the total peak area – see Annex. This is shown in **Figure 80**d, as a function of the applied shear rate. The tendencies show that the sample crystallinity [$\%\chi_{tot}$ (■)] presents a dependency on the shear rate, with the highest crystallinities obtained for 10 s^{-1}. DSC was also performed, with the obtained thermograms (first heating, 10 °C min^{-1}) shown in **Figure 80**g. Several differences can be observed, highlighting the effects of deposition shear rate on the properties of the thin film. An endotherm can be observed around 40 °C, and its enthalpy shows a decrease from low to high shear rates, which can be associated with solid-to-solid transitions. The normalized enthalpies corresponding to this solid-to-solid ($\Delta H_{s\text{-}s}$) transition are plotted in **Figure 80**h, showing a decrease in enthalpy with increasing shear rate. At higher temperatures, a second endotherm can be observed, corresponding to the melting of the crystalline material. The shape, position, and magnitude of this endotherm changes with the applied shear rate. The melting enthalpy depends not only on the amount of crystalline material but also on the different crystalline phases. Phase-related enthalpy changes should be expected considering that certain phases are thermodynamically more stable than others (such as the EA phases, which typically require annealing steps or co- and terpolymerization). The enthalpy of melting plotted in **Figure 80**h, presents large discrepancies in the total crystallinity comparing with previous WAXS diffractograms, with an apparent increase observed by DSC at high shear. A phase quantification from the DSC data is difficult to obtain, given the presence of different phases with a complex relationship, with potential synergetic thermodynamic effects between them. It should also be noted that the sample sheared at 10 s^{-1} exhibits an extra endotherm around 60 °C, indicating another solid-to-solid transition of a more cohesive phase, specifically associated with the FE* phase of the material. This observation aligns with the WAXS data, which indicates a higher FE* content in this particular sample. Both the DSC and WAXS data thus suggest that high shear deposition favors the more –CTFE-rich RFE phase, most probably as a result of increased chain mobility resulting from the shear-induced chain disentanglement. This slightly higher mobility facilitates the insertion of more of the bulky CTFE groups inside the crystalline lamellae, thus increasing the proportion of RFE phase. This disentanglement may also be responsible for the more pronounced lamellar thickening observed at high shear, as evidenced by the shift to higher temperature of the melting endotherm observed in **Figure 80**g.

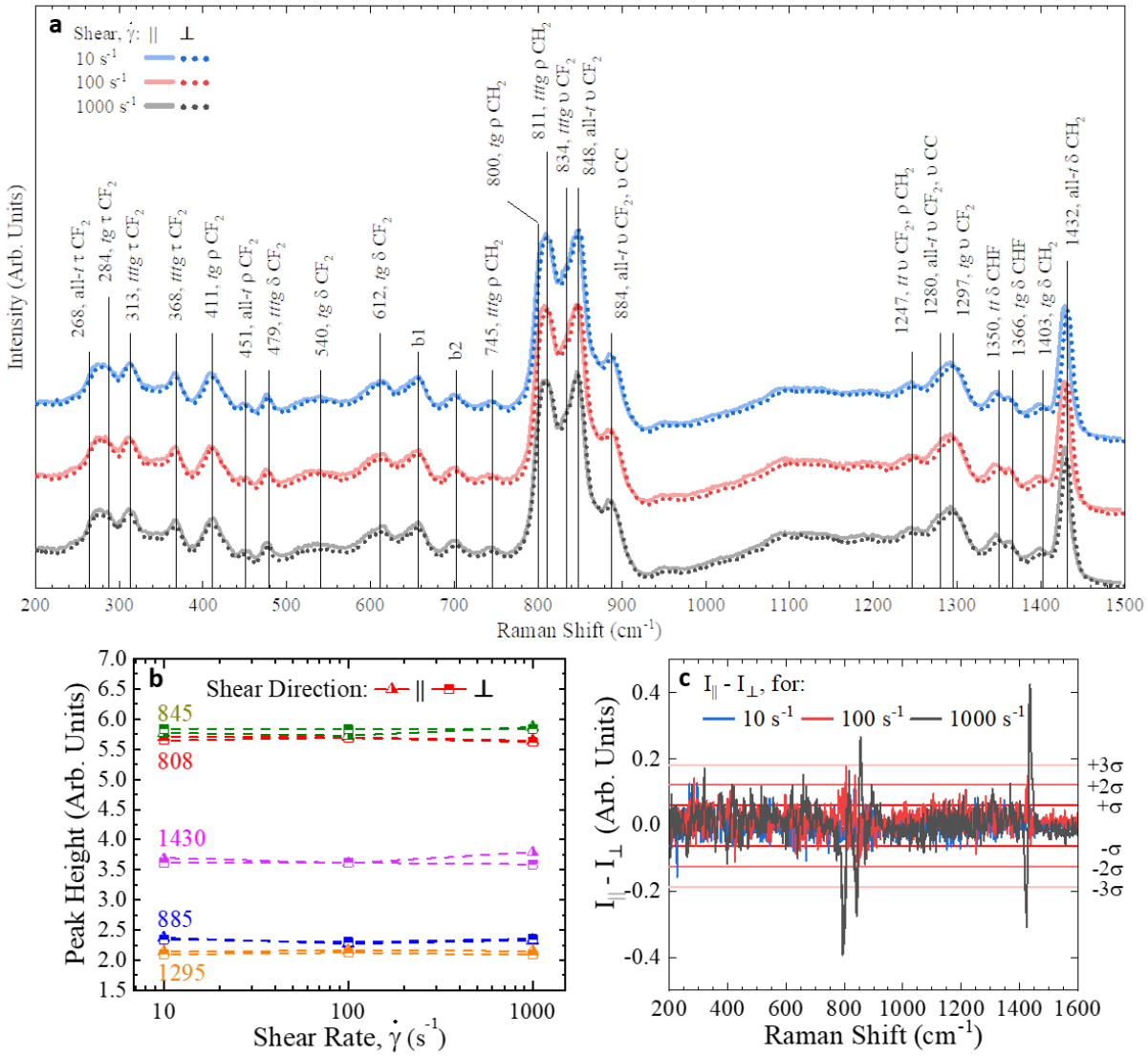

Figure 81. Raman spectroscopy as a function of deposition shear rate, $\dot{\gamma}$. (a) Film Raman spectra, measured with the laser polarization parallel (❙❙, solid lines) and perpendicular (⊥, dotted lines) to the direction of shear. (b) Peak height for a collection of five different crystalline bands *vs.* $\dot{\gamma}$, and laser polarization direction (◭ – ❙❙; ⬒ – ⊥). (c) Intensity difference between the parallel (❙❙) and perpendicular (⊥) spectra, showing spectral changes (intensity and shift). The associated error due to signal noise is also plotted (σ lines, right side). Noticeable changes are detected around 800 and 1400 cm^{-1}, especially for $\dot{\gamma}$ = 1000 s^{-1}. Vibration legend: τ, torsion; ρ, rocking; *w*, wagging; δ, deformation/bending; ν, stretching; *tt*, *trans*-segment; *tg*, gauche-segment.

Raman spectroscopy was used to assess chain structural changes arising from thin film deposition conditions. Analysis and band labeling followed previous experimental and simulation works on the determination of the Raman and FT-IR spectra of PVDF and its co- and

terpolymer family.[8,9,18,10–17] The main peaks of interest are located between 750 and 900 cm^{-1} (some ν CF_2, and ρ and τ CH_2 modes), around 1300 cm^{-1} (ν CF_2 modes), and around 1400 cm^{-1} (δ CH_2). In FT-IR spectra (**Figure S1**), the first zone of interest is also between 800 to 900 cm^{-1}, coinciding with the Raman spectra; a second zone between 1000 to 1300 cm^{-1}, where several ν CF_2 and CC modes overlap, that typically present low intensity in Raman. Lastly, around 1400 cm^{-1} (δ CH_2 modes), we find an additional mode group that is also present in Raman albeit with lower intensity compared to FT-IR (in Raman the modes between 1425 and 1430 cm^{-1} are more intense, contrary to FT-IR).

Figure 81a. shows the obtained spectra for all the thin films. Each film was measured under different laser polarization directions (parallel and perpendicular: **||** and ⊥, respectively) concerning the direction of the shear. The overlapped spectra show small intensity variations with the polarization direction (solid line – **||**; dotted line – ⊥) and the applied shear (the range between 700 and 900, around 1300, and 1400 cm^{-1}). The peak at *ca.* 808 cm^{-1} is a combination of two contributions at 800 (ρ CH_2, α, *tg* segment) and 811 (ρ CH_2, γ, *tttg* segment). Given the proximity to the 811 band, the spectra suggest a larger amount of *tttg*-segments (γ, VDF-specific) along the chain. A smaller hidden peak can also be detected at 834 (ν CF_2, γ, *tttg*), which also arises from *tttg*-segments found in PVDF samples with high γ-content. The most intense band in this region corresponds to the ~845 cm^{-1} band (ν CF_2, ρ CH2, β, all-*trans* segment), typically presenting high intensity for high-*trans* content FE and DFE phases. The position and intensity of these bands already suggest high contents of *tttg* segments. Increases in β phase content would increase the 845 cm^{-1} band along with decreases in the 808 cm^{-1} band, which is observed in P(VDF-TrFE) copolymers. The peak at 880 cm^{-1} also contains multiple contributions (from 870 to 888) from all phases associated with stretching vibrations of skeletal CC of the VDF unit, at 874 (γ), 876 (α), and 884 cm^{-1} (β). Its position suggests the highest contribution comes from all-*trans* VDF segments.

The bands around 1240 to 1300 cm^{-1} are associated to several ν CF_2 and ν CC, arising from different chain conformations. The most significant contribution in this region comes

from the band at 1297 cm^{-1}, associated to *tg*-containing segments found in α-PVDF. Contributions from the all-*trans* band at 1288 cm^{-1} are also visible as a small shoulder. The peak at 1432 cm^{-1} is associated with δ CH_2 modes from the VDF units. The position of this peak changes depending on the chain conformation: found usually at high wavenumbers around 1435 cm^{-1} for β; at 1430 cm^{-1} for α; and 1425 cm^{-1} for γ. The band was associated to all-*trans* δ CH_2, but given its position, a significant contribution from 1430 should also be expected, pointing to the presence of *tg*-defects. This is also in agreement with the remaining bands observed throughout the spectra. Lastly, the bands located between 200 up to 650 cm^{-1}, offer additional clues on the polymer conformation, with multiple visible bands associated to *tttg* and *tg*-segments. The bands associated to the *tttg* conformation are especially significant, as these bands tend to be specific to γ-PVDF, suggesting that long polymer segments present this conformation. Around 650 and 700 cm^{-1}, two additional bands were also detected (b1 and b2) which are not associated to any reported PVDF (and co- and terpolymer) bands. Their location suggests these bands may arise from Cl ν modes from the CTFE monomers, as these vibrations are typically found in this range for other chlorinated organic compounds.

The peak (band) height is shown in **Figure 81**b, for a selection of bands, with polarization directions. The band intensity is very consistent with the applied shear rate, with minor changes in polarization direction. A larger anisotropy appears to take place for a shear rate of 1000 s^{-1}, especially for the 1432 cm^{-1} band, and may point to an increase in thin film structural anisotropy for larger deposition shear rates. The 808 and 845 cm^{-1} bands also present a small degree of anisotropy, albeit less significant. In addition, the spectral difference between the two polarization directions (for each shear rate) are also plotted in **Figure 81**c, highlighting important spectral changes in these samples. As seen in the peak height plot, the samples produced with a shear rate of 1000 s^{-1} have a detectable anisotropy, observable around 800 and 1430 cm^{-1}. The band located at 1432 cm^{-1} shows the biggest change, with the band measured under perpendicular polarization shifting to lower wavenumbers, signifying an increase in *tg* defects. This is consistent with the slight increase in RFE phase content detected in WAXS for a shear rate of 1000 s^{-1}. The standard deviation of the measurement is also plotted (red

lines), extracted from the measurement background noise after baseline, showing these differences extend well beyond the signal noise. These measurements show that the deposition shear rate has resulted in a detectable structural anisotropy, which was not detected with X-ray diffraction (WAXS, 2D diffraction patterns before azimuthal integration). Fine-tuning the deposition conditions (higher shear rates or higher concentrations) and the used solvent (higher volatility) may further increase the observed structural anisotropy.

The chain conformation observed with Raman shows that the chain structure is similar between the different prepared samples, presenting all-*trans* and *tttg* segments along the chain backbone (note that modes containing CH_2 are VDF-specific). This result agrees with the tendencies observed with WAXS and DSC, that showed that the RFE phase is the majority phase in these films, presenting very small changes in crystallinity and relative phase content. FT-IR spectroscopy measurements were also performed, and are available in annex. The band analysis showed the same tendencies observed in the Raman spectra, with fairly constant band intensity across the different spectra, and presence of *tg*-containing modes, as expected in RFE systems.

5.3 Effect of the shear on the dielectric properties

The dielectric spectroscopy measurements provide insights into the real (ε_r') and imaginary (ε_r'') components of the relative permittivity as well as the loss factor (tan δ). Given that the films consist of two main crystalline phases (RFE, and FE*, as observed with WAXS), and the PE phase occurring above the T_C we can expect diverse contributions to the material's response to an applied electric field. The proportion and behavior of these phases will govern the observed dielectric response. The EA phases, represented by RFE and FE* domains, contribute to an increase in the material dielectric response. **Figure 82** illustrates ε_r', ε_r'', and tan δ for thin films produced at various shear rates across a temperature range of -40 to 70 °C. In **Figure 82**a, a maximum permittivity can be observed for all samples around 55 °C during the heating cycle, corresponding to the Curie transition, which for the case of PVDF-based terpolymers is much broader and occurs at lower temperatures than in β-PVDF and other FE PVDF

copolymers. Despite the increase in RFE content for higher shear rates, the measured response is decreased for the 100 s^{-1} sample, most probably due the disentanglement remaining limited at this shear rate when compared to 1000 s^{-1}. The maxima of ε_r'' at -15°C and 50°C describe the T_g and the Curie temperature for all the samples (**Figure 82**b). For 100 s^{-1}, the value obtained at the Curie temperature during the heating cycle is lower than the remainder of the samples leading to maximum values in the following order $\varepsilon_{r\,(100)} < \varepsilon_{r\,(10)} \approx \varepsilon_{r\,(1000)}$. Sample total crystallinity and phase quality is consequently noted to be a factor that affects the magnitude of the measured response. The data clearly shows that the dielectric response of the produced films has a direct dependency not only on the crystallinity of the material but also on the relative phase content.

The effect of the shear is more readily observable during the cooling ramp as the maximum ε_r' and ε_r'', follow the same trend as the total crystallinity (DSC, **Figure 80**h) with: $\varepsilon_{r\,(100)} < \varepsilon_{r\,(10)} < \varepsilon_{r\,(1000)}$. On the **Figure 82**c, the dielectric loss (tan δ) of the material is unaffected by the change in the deposition shear with a clear observation of the T_g and T_C at equal values as observed in graphs **Figure 82**a and b.

During cooling, the response of the material exhibits significant changes. The maximum value of ε_r' shifts to lower temperatures with a wider range threshold where the material's solid-to-solid transition occurs. The maximum value of the permittivity changes substantially, with an increase of the permittivity by a value of 10. The highest ε_r'' value observed in the material during the heating ramp also indicates a shift in the location of the peak, accompanied by a significant increase in its absolute value. The values of crystallinity align with the complexity of the signal as the ε_r maxima follow the previously determined crystallinity percentage trends, with $\varepsilon_{r\,(100)} < \varepsilon_{r\,(10)} < \varepsilon_{r\,(1000)}$. The thermal hysteresis inherent to the FE phase is also observed here, from the difference of the signal during the cooling ramp, which is formed primarily due to the low temperature of crystallisation. The limited polymer chain mobility afforded at room temperature is insufficient to insert the bulky CTFE groups inside the crystalline lamellae, thus favouring the crystallisation of the denser all-*trans*-rich FE phase.

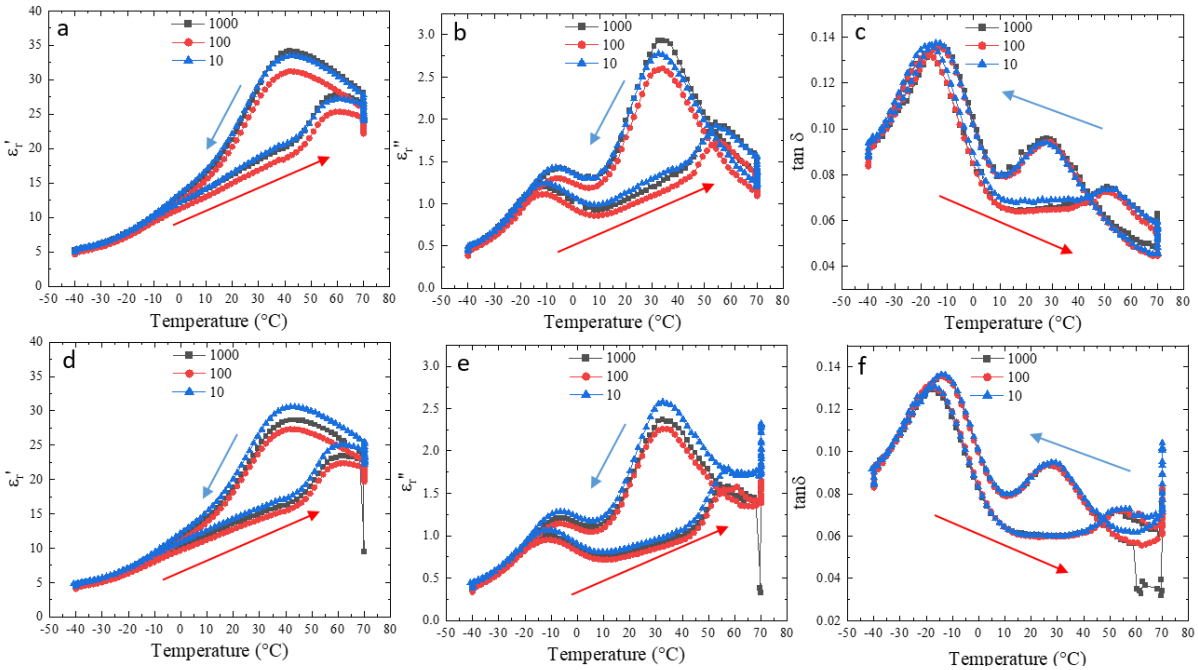

Figure 82. *(a) relative permittivity real (ε_r') and (b) imaginary part (ε_r''), and (c) the loss factor (tan δ) of the samples sheared at 10 s^{-1} (▲), 100 s^{-1} (●), and 1000 s^{-1} (■), over a temperature range of -40°C to 70°C. (d) ε_r', (e) ε_r'', and (f) tan δ measurements performed on one-week aged samples. Red and blue arrows show the measurements performed during heating and cooling, respectively.*

The samples stability was assessed by remeasuring their dielectric performance after one week. Interestingly, the permittivity was seen to decrease with no shift in the transition temperatures. Consequently, the aging of the sample has an effect on the properties of the material as the ε_r' decreased by 8%, 12%, and 16% for the $\varepsilon_{r\,(10)}'$, $\varepsilon_{r\,(100)}'$ and $\varepsilon_{r\,(1000)}'$, respectively. This point rises further concerns on the stability of the material's crystallinity deposited at different shears. Notably, the samples sheared at 10 s^{-1} exhibited the highest permittivity values, suggesting superior stability over time. This behavior can be attributed to different effects, namely: the predominant presence of a more cohesive FE*; higher crystalline content that hinders long range rearrangements[2]; but also to a higher entanglement density contributing to anchor the structure over time.

5.4 Conclusion

In this work, we have analyzed how the deposition process of P(VDF-TrFE-CTFE) terpolymer thin films affects the material properties and structure. The deposition was performed with the doctor-blade method, controlling the deposition shear rate. X-ray diffraction and calorimetry hinted at crystallinity and phase changes with applied shear rate. Through disentanglement of the polymer solution at high shear an increase in chain mobility was obtained, allowing the inclusion of the CTFE in the crystal. Consequently, a more relaxor phase was obtained at high shear. In agreement with WAXS, Raman and FT-IR spectroscopy revealed the presence of similar crystallinity for the samples with the appearance of a slight anisotropy for the highly sheared samples. Dielectric spectroscopy also revealed that, although high shear deposition favors the more sought-after RFE phase, it also decreases the structural and performance stability over time. This observation suggests that higher chain mobility is achieved. Therefore, low-shear deposition (at onset of melting temperature, see *Pouriamanesh* et al.[2]) should be favored for highly crystalline and stable phases. The higher content in FE phase observed at low shear may even be beneficial to the dielectric properties, as we have recently shown that some amount of chains in all-*trans* conformation in RFE-rich compositions can act as starting points decreasing the energy required for dipole rotation.[19] These results highlight the effects of the deposition conditions on the final properties of the films, providing alternative steps for the modulation of the material response without resorting to post-processing techniques (such as mechanical stretching). Nevertheless, it is important to note that variations in the deposition process will most likely affect the final properties of the material, requiring good control of the different parameters. Other factors, such as solvent evaporation rate, ambient temperature, solution temperature, or even relative humidity (especially for very hygroscopic solvents), are parameters that will influence polymer behavior inside the solution and should also be investigated, to understand their effects on thin film fabrication and optimize material properties.

5.5 Materials and methods

5.5.1 Materials

P(VDF-TrFE-CTFE) powder was kindly provided by Arkema Piezotech with a composition of 61.3%-28.4%-10.3%, as stated by the manufacturer. Cyclopentanone (CP) was chosen as the solvent for this study and was purchased from Sigma-Aldrich.

5.5.2 Polymer Solutions

For this work, 15wt.% solutions were prepared by dissolving the polymer powder in CP. The mixtures were magnetically stirred at 300 rpm on a hot plate for 24 hours at room temperature (25 °C), until a fully transparent solution was obtained. When the viscosity of the solution increased, the stirring was reduced to 100 rpm and the temperature was slightly increased to 30°C for a few hours.

5.5.3 Thin Film Deposition

Polymer thin films were deposited on glass substrates with a doctor blade deposition system. The glass substrates were cleaned before film deposition with a standard substrate cleaning procedure: subsequently rinsed in acetone, isopropanol, and deionized water for 15 min each under sonication, followed by drying with pressured air. During deposition, a constant gap of 100 µm was kept between the blade and the substrates. A variation on the deposition shear rate was performed by changing the blade speed and using 1, 10, and 100 mm s^{-1}, yielding shear rates of 10, 100, and 1000 s^{-1} respectively. The films were then stored and annealed in a vacuum oven at 30 °C, under constant vacuum, for 24 hours, to remove any traces of the used solvent. The absence of the solvent was confirmed with FT-IR spectroscopy, and no traces were found after 24 hours. Thin films used in FT-IR and Rama spectroscopy, DSC, AFM, X-ray diffraction, and profilometry were prepared on 75×26 mm glass substrates. The prepared thin films were separated from the glass substrate through immersion in deionized

water, which gradually detached the films from the substrate without introducing stress or deformation. AFM and profilometry measurements were performed directly on the prepared films, without detaching them from the substrates. Dielectric spectroscopy was performed on thin films deposited on specially prepared 15×15 mm glass substrates that required previous electrode deposition (see below, Dielectric Spectroscopy).

5.5.4 Dielectric Spectroscopy and Sample Hysteresis

Permittivity measurements were performed with a broadband dielectric spectroscopy system, and a Solartron 1260 A impedance analyzer, with an alternating voltage signal of 1 V, at a frequency of 1 kHz (additional information is provided in the SI). Sample temperature was controlled with a Linkam LTS 350 temperature-control system from -40 to 70°C. To perform the measurements, several electrical contacts were deposited on 15×15 mm glass substrates (bottom electrode, Cr and Ag), followed by thin film deposition according to the previous section, and then by another set of contact electrodes (top electrode, Ag). The electrode deposition process is also available in the SI. Sample polarization hysteresis was also measured, by recording several polarization hysteresis loops with a TF Analyzer 2000E from aixACCT Systems, applying a triangular wave signal, with a frequency of 100 Hz, at room temperature.

5.5.5 FT-IR and Raman Spectroscopy

FT-IR and Raman spectroscopy were used to analyze the molecular structure and conformation of the prepared polymer films. FT-IR spectra were recorded with a Nicolet iS5, with an ATR module iD7, containing a diamond-crystal window with a sampling diameter of 1.8 mm. The spectra were recorded for a range between 4000 to 400 cm^{-1}, with an in-built ATR spectral correction. Raman spectra were obtained with an XploRa spectrometer from Horiba Instruments, coupled with an Olympus microscope. The measurements were performed with a linearly polarized laser (λ = 532 nm), at magnifications of 50 to 100× (sampling diameter of 15 to 10 μm). No spectral modifications from the laser intensity were detected. The samples

were measured twice with the direction of applied shear parallel and perpendicular to the laser polarization, investigating the potential effects of shear rate on molecular orientation. The different spectra were recorded at room temperature for ranges between 200 and 1600 cm^{-1}.

5.5.6 Structural Characterization

Differential Scanning Calorimetry (DSC) was performed with a Mettler Toledo DSC 1, equipped with an intra-cooler and N_2 flux, over a temperature range of -50 °C to 200 °C and a heating rate of 10 °C min^{-1}. The crystalline structure of the produced films was assessed with Wide Angle X-ray Scattering (WAXS) in transmission at atmospheric pressure and room temperature, using a MicroMax-007 HF, Rigaku Nanoviewer, with a 2D detector (λ = 1.54189 Å, Cu Kα), and a range of 1° to 47°. The sample-to-detector distance was 148 mm. The obtained 2D diffraction patterns were then azimuthally integrated and exported into a 1D diffraction pattern.

5.5.7 Additional Characterization

Profilometry was used to determine thin film thickness, using a Bruker Dektak XT-A stylus profilometer. The sample average thickness was found to be around 5 µm. Viscosity measurements were performed with an Anton Paar MCR302 rheometer with a CP50-1° geometry (cone 50 mm – 1° / plate) at 21°C. The measurements were carried out under a solvent saturated atmosphere with the help a solvent trap. Different shear rates were applied in a logarithm scale from 0.01 s^{-1} to 1000 s^{-1}.

Annex chapter 5:

1. Dielectric Spectroscopy

Analysis of the dielectric properties of the different thin films was performed with a Solartron 1260 A impedance analyzer, with an external temperature control system. Measurements were performed with an alternating voltage signal of 1 V, with a signal frequency of 1 kHz, and a well-defined temperature profile ramp. This technique allows the measurement of the Capacitance (C) and loss factor [$\tan(\delta) = \frac{\varepsilon''}{\varepsilon'}$]. The relative permittivity (or dielectric constant of the material) is then calculated using the following equation:

$$D = \varepsilon_0 \mathrm{E} + \mathrm{P} = \varepsilon_0 \varepsilon_r \mathrm{E} \qquad (S\textit{V-1})$$

$$C = \varepsilon_0 \varepsilon_r \frac{A}{l} \qquad (S\textit{V-2})$$

Where ε_0 is the permittivity of free space; ε_r is the relative permittivity of the material; *l* is the thickness of the thin film (distance between the electrodes); and *A* is the effective surface area of the measurement. Additionally, the relative permittivity, ε_r, can be further decomposed as follows:

$$\varepsilon_r = \varepsilon'_r + i\varepsilon''_r \qquad (S\textit{V-3})$$

Where ε'_r and ε''_r are the real and imaginary parts of the relative permittivity, respectively.

2. Electrode Deposition

Thin metallic electrodes were deposited on 15×15 mm glass substrates to create contact electrodes for dielectric spectroscopy and polarization hysteresis measurements. A PLASSYS thermal evaporation system was used, operating under high vacuum (4×10^{-6} mBar). The bottom electrodes were deposited directly onto the glass substrate, consisting of a single strip of 10 nm Cr layer for adhesion, followed by 100 nm of Ag. The polymer thin films were then deposited on top of these electrodes, following the procedure mentioned in the main

text. The top electrodes (perpendicular to the bottom electrode) were deposited in the same system, consisting of 5 strips of 100 nm of Ag. The overlap of the bottom and top electrodes generated 5 active sampling zones, with an area of around 2 mm^2. The deposition rate was adjusted during the process to minimize sample temperature increase. The sample temperature reached a maximum of 40 °C. Access to the bottom electrode was achieved by solvating a small surface of the prepared film exposing the electrode surface. A conductive silver paste was used to improve the electric contact between the Ag contacts and the tungsten measurement probes.

3. FT-IR and Raman Spectroscopy

FT-IR measurements utilize unpolarized IR light and result in an average of the observed vibrations. Raman spectroscopy is complementary to FT-IR and gives additional information about other Raman-active vibration modes. Deposition anisotropy can also be investigated with Raman spectroscopy by exploiting the direction of the linearly polarized laser with respect to the film deposition direction.

A suitable spectral rescaling factor is required to establish comparisons between the different measured spectra and remove intensity variations from shifts in the sampling area or variations in sample thickness. The best approach to is to perform a standard normal variate (SNV) transformation. The obtained data is scaled by multiplying it with the average value, and dividing by the standard deviation:

$$I_{SNV}(k)=I_{exp}(k)\times\frac{\overline{Iexp}}{\sigma_{Iexp}} \qquad (SV\text{-}4)$$

All the data were treated with an SNV transformation. When applicable, background fitting was performed with 2nd to 4th order polynomials. Smoothing was applied for functions with very high noise, with sampling windows around 5 to 6, and 2nd order polynomials, using the Savitzky-Golay method.

4. FT-IR Spectra Analysis

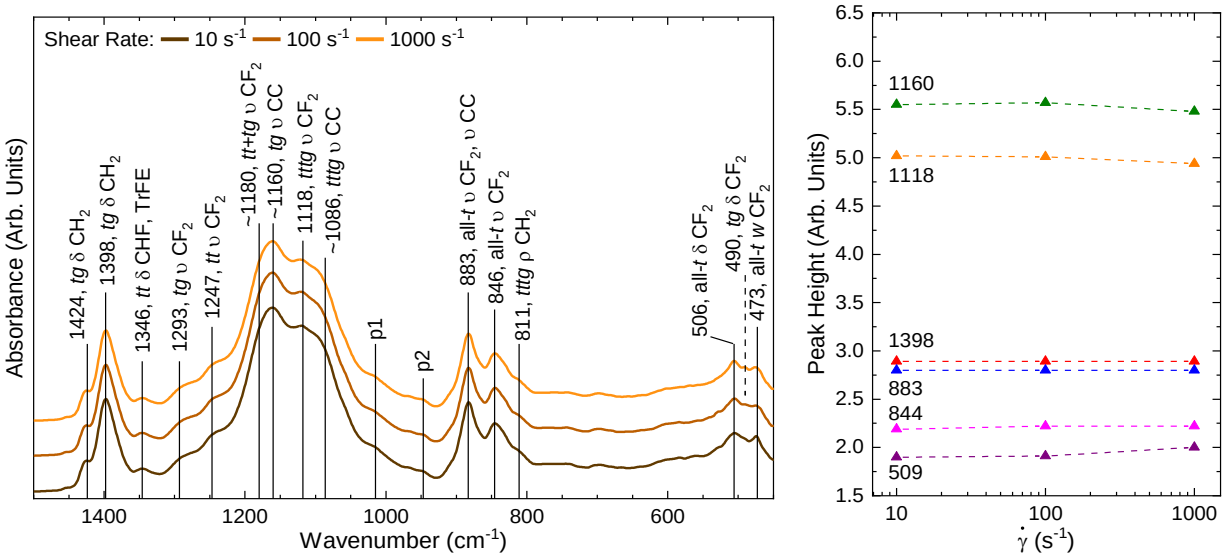

FigureS5- 1*. FT-IR spectra for the different shear rates, with the respective peak height and position.*

FT-IR spectroscopy served as a complementary characterization to the Raman spectroscopy measurements. Important to note that several bands detectable in FT-IR and Raman spectroscopy are present in more than one of the PVDF polymorphs, becoming a matter of debate and confusion when performing band assignment. These bands typically originate from *tt* or *tg* segments that are found in β and γ, and in γ and α respectively. The spectra shown in **FigureS5- 1**a reveal several bands of interest. The 506 cm^{-1} is associated with δ CF_2 in the β phase, but some works have also associated this peak with the γ phase, both originating from the *tt*-segments. The peaks at 846 and 883 cm^{-1} are also present. Around this zone, we can observe peak broadening and shoulders that correspond to other vibration modes associated with *tg* and *tttg* conformations (such as the 811, arising from *tttg*-segments associated to γ-VDF). The peaks between 1000 and 1300 cm^{-1} have multiple band contributions, with considerable broadening, hindering the assignment to specific phases or deciphering the nature of the vibrations. The band at 1118 cm^{-1} is associated with a ν CF_2 mode from *tttg* segments; the peak at ~1160 cm^{-1} has the mode ν CC from *tg*-segments as the closest match.

Hidden contributions at 1086 and 1180 are also associated to *tg* and *tttg*-containing chain segments (revealed with 2nd derivative). Contributions from the all-*trans* to ν CF_2 modes typically appear at higher wavenumbers, from 1200 cm^{-1} upward. However, the band around 1280 cm^{-1} (appearing as a small shoulder in Raman) associated to an all-*trans* chain cannot be discerned, with the surrounding bands being more intense and also associated to *tg*-containing segments (1247 and 1293). At the end of the spectra, we see the peak at 1398 cm^{-1}, which is complementary to the Raman peak at 1430 cm^{-1}, arising from *tg* segments. The peak at 1425 cm^{-1} is still visible in FT-IR as a small shoulder. The reverse takes place in Raman, with the peak at 1398 cm^{-1} appearing as a small shoulder and shifted to 1400 cm^{-1}. Analyzing the changes in peak height and position (**FigureS5- 2**), we observe that the band intensity is approximately constant for the selected shear rates. Nevertheless, the detected modes further validate the different observations from Raman and the remaining techniques, revealing the presence of *tg* and *tttg*-containing segments associated to the majority RFE phase. The all-trans modes can also be attributed to the FE/DFE minority phase.

5. Wide Angle X-ray Scattering Analysis

The Fityk open source software was used to perform non-linear curve fitting. The fitting was obtained with a combination of Gaussian and Voigt functions, respectively, for the amorphous and crystalline contributions. The total crystallinity of the sample was extracted using the ratio of the total area attributed to the crystalline peaks over total area:

$$\%Crystallinity_{\ total} = \frac{total\ Area\ of\ the\ crystalline\ phases}{Total\ area} \qquad (SV\text{-}5)$$

The percentage of each phase (P, RFE, and FE*) was calculated using the following equation:

$$\%Crystallinity_{\ i} = \frac{Area\ of\ the\ i\ cristalline\ peak}{Total\ area} \qquad (SV\text{-}6)$$

Where i denotes the phase of interest (P, RFE, or FE*).

6. Polarization

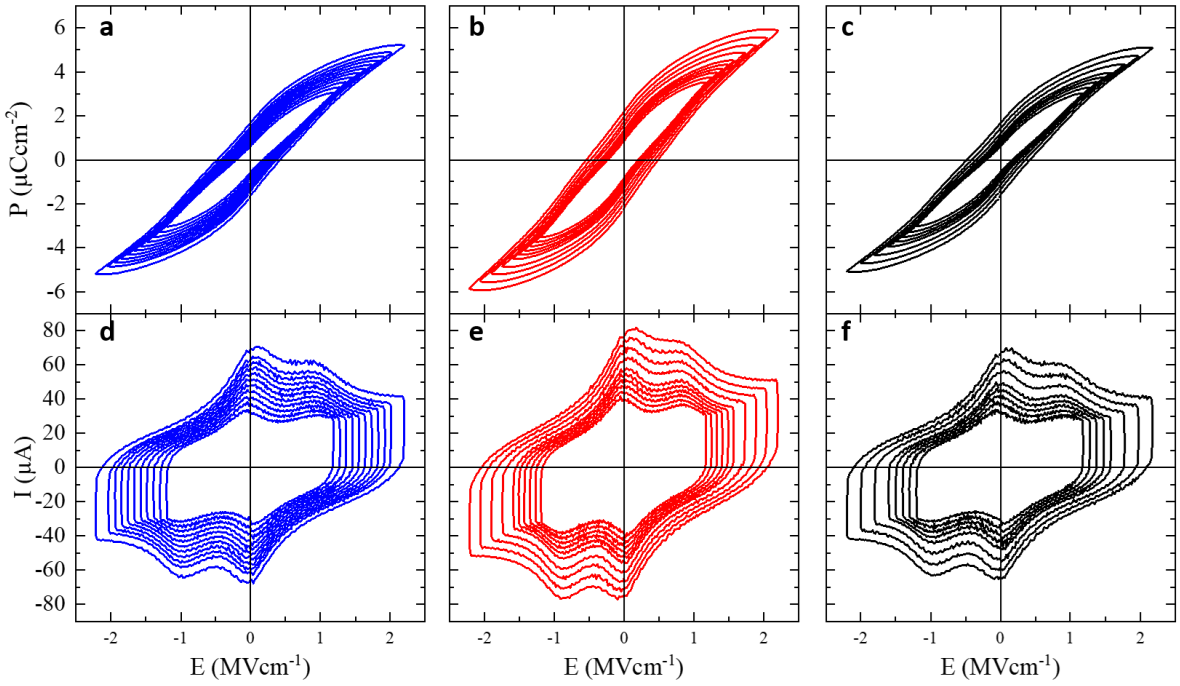

FigureS5- 2*. Hysteresis loops of Polarization* vs. *Electric field and the associated Current* vs. *Electric field for samples produced with shear rates of 10 s^{-1} (a and d), 100 s^{-1} (b and e), 1000 s^{-1} (c and f).*

Sample polarization hysteresis was recorded to obtain the overall response of the material (shown in **FigureS5- 2**) with an applied electric field. All the produced samples exhibited a narrow hysteresis loop with a low remanent polarization. At low polarization fields, a RFE behavior can be observed, with gradual loop opening and an evolution towards a more ferroelectric behavior that could also be due to an increase of the leakage current. Interestingly, the same behavior is also observed for samples produced with lower shear rates. This behavior suggests that the detected FE* phase may be a DFE phase, which would explain the initially observed narrow shape of the hysteresis loop and the low remanent field. The changes observed at higher fields can be explained by the poling effect of the measurement, potentially converting DFE phases into a fully FE phase, decreasing conformation defects. From this data, at higher polarization fields the thin films are expected to be composed primarily of a FE phase with minor contributions from the RFE phase. The observed behavior is consistent with the X-ray structural analysis and Raman/FT-IR spectroscopy

References

1. Phanibhusan, R.-C. & Deuskar, V. D. *Effect of Solvent, Concentration, and Molecular Weight on the Rheological Properties of Polymer Solutions**.
2. Pouriamanesh, N., Le Goupil, F., Stingelin, N. & Hadziioannou, G. Limiting Relative Permittivity 'Burn-in' in Polymer Ferroelectrics via Phase Stabilization. *ACS Macro Lett.* **11**, 410–414 (2022).
3. Bargain, F. *et al.* Thermal behavior of poly(VDF-ter-TrFE-ter-CTFE) copolymers: Influence of CTFE termonomer on the crystal-crystal transitions. *Polymer (Guildf).* **161**, 64–77 (2019).
4. Bargain, F., Thuau, D., Hadziioannou, G., Domingues Dos Santos, F. & Tencé-Girault, S. Phase diagram of poly(VDF-ter-TrFE-ter-CTFE) copolymers: Relationship between crystalline structure and material properties. *Polymer (Guildf).* **213**, 123203 (2021).
5. Yang, L. *et al.* Relaxor ferroelectric behavior from strong physical pinning in a poly(vinylidene fluoride- co -trifluoroethylene- co -chlorotrifluoroethylene) random terpolymer. *Macromolecules* **47**, 8119–8125 (2014).
6. Thuau, D. *et al.* High and Temperature-Independent Dielectric Constant Dielectrics from PVDF-Based Terpolymer and Copolymer Blends. *Adv. Electron. Mater.* **6**, (2020).
7. Florian Le Goupil, Konstantinos Kallitsis, Sylvie Tencé-Girault, Naser Pouriamanesh, Cyril Brochon, Eric Cloutet, Thibaut Soulestin, Fabrice Domingue Dos Santos, Natalie Stingelin, G. H. Enhanced Electroncaloric response of Vinylidene fluoride-based polymers via one-step molecular engineering. *Adv. Funct. Mater.* **31**, (2021).
8. Resende, P. M., Isasa, J.-D., Hadziioannou, G. & Fleury, G. Deciphering TrFE Fingerprints in P(VDF-TrFE) by Raman Spectroscopy: Defect Quantification and Morphotropic Phase Boundary. *Macromolecules* (2023) doi:10.1021/ACS.MACROMOL.3C01700.
9. Tashiro, K., Kobayashi, M. & Tadokoro, H. *VibrationalSpectraandDisorder-OrderTransitionofPoly(vinylidenefluoride)FormIII*. *Macromolecules* vol. 14 https://pubs.acs.org/sharingguidelines (1981).
10. Kobayashi, M., Tashiro, K. & Tadokoro, H. Molecular Vibrations of Three Crystal Forms of Poly(vinylidene fluoride). *Macromolecules* 158 (1974).
11. Gregorio, R. Determination of the , and Crystalline Phases of Poly(vinylidene fluoride) Films Prepared at Different Conditions. *J Appl Polym Sci* **100**, 3272–3279 (2005).
12. Arrigoni, A. *et al.* P(VDF-TrFE) nanofibers: Structure of the ferroelectric and paraelectric phases through IR and Raman spectroscopies. *RSC Adv.* **10**, 37779–37796 (2020).
13. Milani, A. Joint Experimental and Computational Investigation of the Structural and Spectroscopic Properties of Poly(vinylidene fluoride) Polymorphs. *Phys. Chem. B* (2015).
14. Thakur, A. Temperature Raman Studies of Freestanding and Flexible Thin Films of CdS-doped PVDF. *Polym. Compos.* (2018).
15. Martins, P. Electroactive phases of poly(vinylidene fluoride):Determination, processing and applications. *Prog. Polym. Sci.* (2014).

16. Lin, Y. Studies on the electrostatic effects of stretched PVDF films and nanofibers. *Nanoscale Res. Lett.* (2021).
17. Tashiro, K. *et al.* High-Electric-Field-Induced Hierarchical Structure Change of Poly(vinylidene fluoride) as Studied by the Simultaneous Time-Resolved WAXD/SAXS/FTIR Measurements and Computer Simulations. *Macromolecules* acs.macromol.0c02567 (2021) doi:10.1021/acs.macromol.0c02567.
18. Cai, X., Lei, T., Sun, D. & Lin, L. A critical analysis of the a, b and g phases in poly(vinylidene fluoride) using FTIR †. *RCS Adv.* **7**, 15382–15389 (2017).
19. Le Goupil, F. *et al.* Double-Bond-induced Morphotropic Phase Boundary leads to Enhanced Electrocaloric Effect in VDF-Based Polymer Flexible Devices. **14**, 26 (2023).

Chapter 6:

Conclusions and perspectives

Chapter 6: Conclusions and perspectives:

This thesis was dedicated to unraveling the behavior of PVDF-based copolymers in solutions for the development of printed electroactive films.

Taking into account the lack of studies on the solvation behavior of fluorinated polymers, **Chapter 2** established the relationships between P(VDF-TrFE) composition, chain conformation in the solvated state, and rheological behavior. In particular, we demonstrated drastic modification of chain conformation in DMSO with respect to the TrFE content, inherent to the interplay between the solvent dipolar moment and the insertion of TrFE units. Various characterization techniques confirmed an elongation of the chain with the addition of TrFE units, followed by a subsequent chain collapse at a critical composition of 50 mol.% of TrFE.

Chapter 3 focuses on the P(VDF-TrFE):(80-20) composition, renowned for its particularly interesting ferroelectric properties. It explores the effects of solvent polarity and chemical nature on the viscosity of concentrated solutions, revealing that solution viscosity is primarily driven by solvent-polymer interactions. Light scattering experiments further reveal the consequences of these interactions on chain conformation, establishing key conclusions on the behavior of P(VDF-TrFE):(80-20) chains. Indeed, we demonstrated that P(VDF-TrFE):(80-20) chains behave as in theta conditions, with the dipolar moment of fluorine atoms canceling monomer attraction.

In **Chapter 4**, taking advantages of the previous studies related to the behavior of P(VDF-TrFE) in solution, we implemented this material into inks to fabricate devices through a screen printing deposition process. By analyzing the rheological behavior of inks under a simulated printing process, we were able to reveal significant differences in the viscoelastic behavior of the inks depending on concentration regime and applied shear. Following, a mapping of the screen meshing used for the printing process was performed and showed that shear-induced structural modification of the deposited layers are linked to device performance and stability. Accordingly, this study further established that the ink concentration regime, depending on solvent quality, is a sensitive criterion.

Finally, in **chapter 5**, we delved into the deposition process of P(VDF-TrFE-CTFE) using blade coating as the chosen deposition technique. A comprehensive exploration of shear rate, identified earlier as a critical parameter influencing the quality of deposited layers, was undertaken. Various deposition speeds were systematically employed to fabricate P(VDF-TrFE-CTFE) layers. The study revealed that the viscoelastic behavior of the P(VDF-TrFE-CTFE) solution during deposition (*i.e.*, Newtonian, transitional, and shear thinning behaviors) had a discernible impact on the deposited layers. Notably, these changes were intricately linked to alterations in crystalline polymorphism.

In this study, a thorough characterization of different polymer compositions was established. However, the single-chain conformation was elucidated in the appropriate dilute regime, and the structuration of the chains or potential self-organization in semi-dilute or concentrated regimes was not evaluated. SAXS/WAXS and light scattering characterizations could be employed for this purpose, providing insights into the origin of the observed destructuration during thixotropic tests. Factors such as the insolubilized fraction of the polymer, aggregates, and crystallinity in solution could be investigated to enhance printability and achieve final film homogeneity and desired properties.

The screen-printing process is complex, with multiple parameters influencing its outcome. Few systems were studied, emphasizing the importance of initial viscosity and the concentrated regime. Further understanding of solvent evaporation and the drying process could be advantageous. Given the diversity of printing techniques, specific rheological parameters are necessary. Our study delineates a clear pathway to investigate parameters that align with the ink's requirements.

Finally, the dependence of shear could be further explored by optimizing certain points. Increasing the concentrations of deposited solutions could enhance shear thinning and disentanglements. Exploring simpler systems, such as PVDF or PVDF-based copolymers with high concentrations deposited at elevated temperatures to induce structure quenching, could increase crystal anisotropy.